



NUCLEAR CHARGE DISTRIBUTION IN THE ASYMMETRIC FISSION OF ^{238}U

Jean-Louis GALINIER

NUCLEAR CHARGE DISTRIBUTION IN
THE REGION OF ASYMMETRIC FISSION
OF ^{238}U BY PROTONS OF ENERGY 20-65 MeV

by

Jean-Louis Galinier

A thesis submitted to the Faculty of Graduate
Studies and Research in partial fulfilment of
the requirements for the degree of
Doctor of Philosophy

Department of Chemistry
McGill University
Montreal, Quebec
CANADA

October 1973



JEAN-LOUIS GALINIER

1977

ABSTRACT

Ph.D.

Jean-Louis Galinier

Chemistry

NUCLEAR CHARGE DISTRIBUTION IN THE REGION OF ASYMMETRIC FISSION OF ^{238}U BY PROTONS OF ENERGY 20-85 MeV

The independent formation cross sections of ^{148}Pm and ^{150}Pm and the cumulative formation cross sections of ^{146}Ce , ^{146}Pr , ^{147}Nd , ^{149}Nd , ^{149}Pm , ^{151}Nd , ^{151}Pm , ^{153}Sm , ^{155}Sm , ^{156}Sm , and ^{157}Eu produced in the fission of ^{238}U by protons of energy 20-85 MeV have been measured radiochemically. The independent cross sections of ^{146}Pr , ^{149}Pm , and ^{151}Pm have been estimated from the cumulative yields. Excitation functions were constructed and the energy at which their maxima was reached was observed to decrease with proton energy when compared to increasing neutron-to-proton ratio of the products.

The cumulative cross sections have been used to provide a better definition of the heavy wing of the mass distribution. The fractional independent yields deduced from the independent cross sections have enabled the construction at each incident energy of charge dispersion curves representative of the $A = 146-151$ mass region. With increasing incident energy, the most probable charge Z_p moves toward stability with a rate of displacement slower than that observed in heavy products of lower mass. The full-width at half-

maximum of the curves broadens with increasing bombarding energy while remaining narrower than in the case of neighbouring lower masses, thus confirming a mass region dependence suggested by other workers. The estimated total number of neutrons emitted during very asymmetric mass divisions induced at medium energy was found to be lower than in less asymmetric fission processes.

The results in this mass range appear to be consistent with a growing contribution of direct interaction mechanisms leading to low-energy deposition events with increasing bombarding energy.

RESUME

Ph.D.

Jean-Louis Galinier

Chimie

DISTRIBUTION DE CHARGE DANS LA FISSION ASYMETRIQUE DE ^{238}U INDUITE PAR PROTONS DE 20 A 85 MeV

Les sections efficaces de formation indépendante de ^{148}Pm et ^{150}Pm , et les sections efficaces de formation cumulative de ^{146}Ce , ^{146}Pr , ^{147}Nd , ^{149}Nd , ^{149}Pm , ^{151}Nd , ^{151}Pm , ^{153}Sm , ^{155}Sm , ^{156}Sm et ^{157}Eu produits au cours de la fission de ^{238}U induite par protons d'énergies comprises entre 20 et 85 MeV ont été mesurées par voie radiochimique. Les sections efficaces de formation indépendante de ^{146}Pr , ^{149}Pm et ^{151}Pm ont pu être déduites à l'aide des rendements cumulatifs mesurés. Les fonctions d'excitation des produits indépendants atteignent leur maximum à une énergie incidente qui décroît corrélativement à un accroissement du rapport neutron-proton des nucléides correspondants.

Les sections efficaces cumulatives ont servi à mieux définir la partie de la distribution de masse située au niveau des masses élevées. Les rendements indépendants déduits des sections efficaces indépendantes ont permis, pour chaque énergie incidente, la construction des courbes de distribution de charge s'appliquant à la région de masse $A = 146-151$. La charge la plus probable Z_p se déplace vers

la ligne de stabilité au fur et à mesure que l'énergie croît. Toutefois, ce déplacement est moins marqué que celui observé dans le cas de produits lourds de masse moins élevée. Les largeurs à mi-hauteur des distributions croissent avec l'énergie incidente tout en restant plus étroites que dans le cas de produits de fission voisins de masse moindre. Ceci confirme l'influence de la masse sur la largeur des distributions, comme l'ont déjà suggéré plusieurs auteurs.

L'estimation du nombre total de neutrons émis à moyenne énergie au cours de divisions en masse à caractère très asymétrique conduit à des valeurs inférieures à celles calculées dans le cas d'événements moins asymétriques.

Les résultats dans ce domaine de masse sont en accord avec l'hypothèse d'une contribution importante des mécanismes d'interaction directe conduisant à de faibles dépôts d'énergie d'excitation.

ACKNOWLEDGEMENTS

I would like to express my sincere gratitude to Professor L. Yaffe for suggesting the subject of this dissertation and for his constant interest, understanding and encouragement during the course of this work.

I am indebted to the members of the Radiochemistry group, past and present, for their collaboration in various ways, in particular to Dr. J.J. Hogan, Dr. J-C. Brodovitch, Dr. S. Sarkar, Messrs. K.I. Burns and C.F. Lau, and Mr. N. Attas for his assistance during the summer months of 1972.

Special thanks are due to Dr. M. Dikšić for many valuable discussions and moral support and Dr. H. Guérin for friendly help during the final stages of this work.

I wish to thank Dr. S.K. Mark for permission to use the Foster Radiation Laboratory Synchrocyclotron and Mr. R.H. Mills for his cooperation in carrying out the irradiations.

I would like also to record my appreciation to Ms. Renée Charron for the excellent work she did in typing this thesis.

Finally, I am equally grateful to the Canada Council for the award of a Fellowship during 1971-1974 and to the Chemistry Department for providing demonstratorship throughout the period of this work.

TABLE OF CONTENTS

	<u>Page</u>
ABSTRACT.....	1
ACKNOWLEDGEMENTS.....	v
TABLE OF CONTENTS.....	vi
LIST OF FIGURES.....	ix
LIST OF TABLES.....	xiii
A. INTRODUCTION.....	1-65
I. DISCOVERY.....	1
II. NATURE OF THE FISSION PROCESS.....	1
III. ELEMENTS OF A COMPLETE THEORY.....	5
IV. NUCLEAR MODELS.....	7
a) Adiabatic models.....	7
b) Non-adiabatic models.....	19
V. FISSION PARAMETERS AND THEIR MEASUREMENTS.....	25
a) Chemical methods.....	25
b) Mass spectrometric methods.....	29
c) Physical methods.....	31
VI. LOW AND MEDIUM ENERGY FISSION.....	33
a) Mass distribution.....	33
b) Charge distribution.....	42
c) Neutron emission in fission.....	56
VII. PURPOSE OF THE PRESENT STUDY.....	63
B. EXPERIMENTAL PROCEDURES.....	66-94
I. PREPARATION OF TARGETS.....	66

	<u>Page</u>
II. IRRADIATIONS.....	69
III. CHEMICAL PROCEDURES.....	70
a) Separation of rare earths.....	70
b) Separation of cerium.....	77
c) Copper chemistry.....	83
d) Standardization of carrier solutions..	84
IV. ACTIVITY MEASUREMENTS.....	86
a) 30 cc Ge(Li) detector.....	87
b) NaI (Tl) scintillation detector.....	91
C. TREATMENT OF DATA.....	95-109
I. ANALYSIS OF SPECTRA: PEAK INTEGRATION.....	95
II. DECAY-CURVE ANALYSIS.....	97
III. CROSS SECTION CALCULATIONS.....	100
a) General equation.....	100
b) Calculation of disintegration rates at the end of bombardment.....	103
D. RESULTS.....	110-155
I. CUMULATIVE CROSS SECTIONS.....	110
II. INDEPENDENT CROSS SECTIONS.....	114
a) ^{148}Pr , ^{150}Pr	114
b) ^{146}Pr , ^{151}Pr	114
c) ^{149}Pr	126
III. TOTAL CHAIN YIELDS.....	127
IV. FRACTIONAL INDEPENDENT YIELDS.....	133
V. ERROR ANALYSIS.....	149

	<u>Page</u>
E. DISCUSSION.....	156-194
I. EXCITATION FUNCTIONS.....	156
II. HEAVY WING OF THE MASS DISTRIBUTION.....	160
III. CHARGE DISTRIBUTION.....	162
a) Construction of the charge dispersion curves.....	162
b) Charge dispersion parameters and their correlation.....	179
IV. CALCULATION OF THE TOTAL NUMBER OF NEUTRONS EMITTED.....	190
SUGGESTIONS FOR FUTURE WORK.....	193
SUMMARY AND CONTRIBUTION TO KNOWLEDGE.....	196
APPENDIX A.....	199
REFERENCES.....	203

LIST OF FIGURES

		<u>Page</u>
Figure 1	Scission configuration in the fission process and neutron emission.....	3
Figure 2	Potential energy function for deformations leading to fission.....	17
Figure 3	a) LDM fit to experimental masses b) Total shell correction to nuclear ground states.....	20
Figure 4	Yield-mass curve for ^{235}U fission at 14MeV and thermal energy.....	34
Figure 5	a) Mass yield curves for thermal fission of various targets b) Average mass of the light and heavy products.....	36
Figure 6	Fission-product distribution of ^{238}U irradiated with protons.....	40
Figure 7	Gaussian charge distribution.....	54
Figure 8	a) Neutron yields vs fragment mass b) Neutron yields in ^{233}U and ^{238}U proton fission.....	58
Figure 9	Target assembly and end of cyclotron probe.....	68
Figure 10	Radiochemical group separation of rare-earths - Flowchart.....	74
Figure 11	Radiochemical separation of cerium - Flowchart.....	80
Figure 12	Radiochemical separation of copper - Flowchart.....	85

		<u>Page</u>
Figure 13	Black diagram of the detector system used	
	a) Ge(Li) solid-state detector	
	b) NaI (Tl) scintillation detector.....	88
Figure 14	Photopeak efficiency of 30 cc Ge(Li) detector.....	93
Figure 15	Excitation function for the cumulative formation of ^{146}Ce	115
Figure 16	Excitation function for the cumulative formation of ^{146}Pr	116
Figure 17	Excitation function for the cumulative formation of ^{147}Nd	117
Figure 18	Excitation function for the cumulative formation of ^{149}Nd	118
Figure 19	Excitation function for the cumulative formation of ^{149}Pm	119
Figure 20	Excitation function for the cumulative formation of ^{151}Nd	120
Figure 21	Excitation function for the cumulative formation of ^{151}Pm	121
Figure 22	Excitation function for the cumulative formation of ^{153}Sm	122
Figure 23	Excitation function for the cumulative formation of ^{155}Sm	123
Figure 24	Excitation function for the cumulative formation of ^{156}Sm	124
Figure 25	Excitation function for the cumulative formation of ^{157}Eu	125
Figure 26	Excitation functions for the independent formation of ^{148m}Pm and ^{150}Pm	129

		<u>Page</u>
Figure 27	Excitation function for the independent formation of ^{146}Pr	130
Figure 28	Excitation function for the independent formation of ^{151}Pm	131
Figure 29	Excitation function for the independent formation of ^{149}Pm	132
Figure 30	Heavy side of the mass distribution at 20 MeV.....	136
Figure 31	Heavy side of the mass distribution at 25 MeV.....	137
Figure 32	Heavy side of the mass distribution at 30 MeV.....	138
Figure 33	Heavy side of the mass distribution at 35 MeV.....	139
Figure 34	Heavy side of the mass distribution at 40 MeV.....	140
Figure 35	Heavy side of the mass distribution at 45 MeV.....	141
Figure 36	Heavy side of the mass distribution at 50 MeV.....	142
Figure 37	Heavy side of the mass distribution at 55 MeV.....	143
Figure 38	Heavy side of the mass distribution at 60 MeV.....	144
Figure 39	Heavy side of the mass distribution at 65 MeV.....	145
Figure 40	Heavy side of the mass distribution at 70 MeV.....	146
Figure 41	Heavy side of the mass distribution at 77 MeV.....	147

	<u>Page</u>
Figure 42	Heavy side of the mass distribution at 85 MeV..... 148
Figure 43	Fractional independent yields of ^{148}Pm , ^{149}Pm and ^{150}Pm 151
Figure 44	Fractional independent yields of ^{146}Pr . 152
Figure 45	Fractional independent yields of ^{151}Pm . 153
Figure 46	Incident energies at which the excita- tion functions reach their maximum..... 159
Figure 47	Charge distribution at 20 MeV..... 166
Figure 48	Charge distribution at 25 MeV..... 167
Figure 49	Charge distribution at 30 MeV..... 168
Figure 50	Charge distribution at 35 MeV..... 169
Figure 51	Charge distribution at 40 MeV..... 170
Figure 52	Charge distribution at 45 MeV..... 171
Figure 53	Charge distribution at 50 MeV..... 172
Figure 54	Charge distribution at 55 MeV..... 173
Figure 55	Charge distribution at 60 MeV..... 174
Figure 56	Charge distribution at 65 MeV..... 175
Figure 57	Charge distribution at 70 MeV..... 176
Figure 58	Charge distribution at 77 MeV..... 177
Figure 59	Charge distribution at 85 MeV..... 178
Figure 60	a) Variation of the FWHM with energy b) Displacement of the most probable charge with energy..... 180
Figure 61	Variation of N/Z_p with mass..... 185
Figure 62	Variation of FWHM with mass..... 189

LIST OF TABLES

	<u>Page</u>
Table I Absolute efficiencies for gamma-rays of nuclides studies - 30 cc Ge(Li) detector	92
Table II Decay properties of the observed nuclides.....	98
Table III $^{65}\text{Cu}(p, pn)^{64}\text{Cu}$ cross sections.....	101
Table IV Fission product decay chains.....	104
Table V Cumulative formation cross sections of ^{146}Ce , ^{146}Pr , ^{147}Nd , ^{149}Nd	111
Table VI Cumulative formation cross sections of ^{149}Pm , ^{151}Nd , ^{151}Pm , ^{153}Sm	112
Table VII Cumulative formation cross sections of ^{155}Sm , ^{156}Sm , ^{157}Eu	113
Table VIII Independent formation cross sections of ^{148}Pm , ^{149}Pm , ^{150}Pm , ^{146}Pr , ^{151}Pm	128
Table IX Parameters for the heavy side of the mass distribution.....	134
Table X Total chain yields used in fractional chain yields calculations.....	137
Table XI Fractional independent yields used in charge dispersion curves.....	150
Table XII Parameters of charge dispersion curves.	165
Table XIII Total number of neutrons emitted in the proton fission of ^{238}U at medium energies.....	193
TABLE A-I Charge dispersion data for A = 96.....	200
TABLE A-II Charge dispersion data for A = 136.....	201
TABLE A-III Charge dispersion data for A = 141.....	202

A. INTRODUCTION

I. DISCOVERY

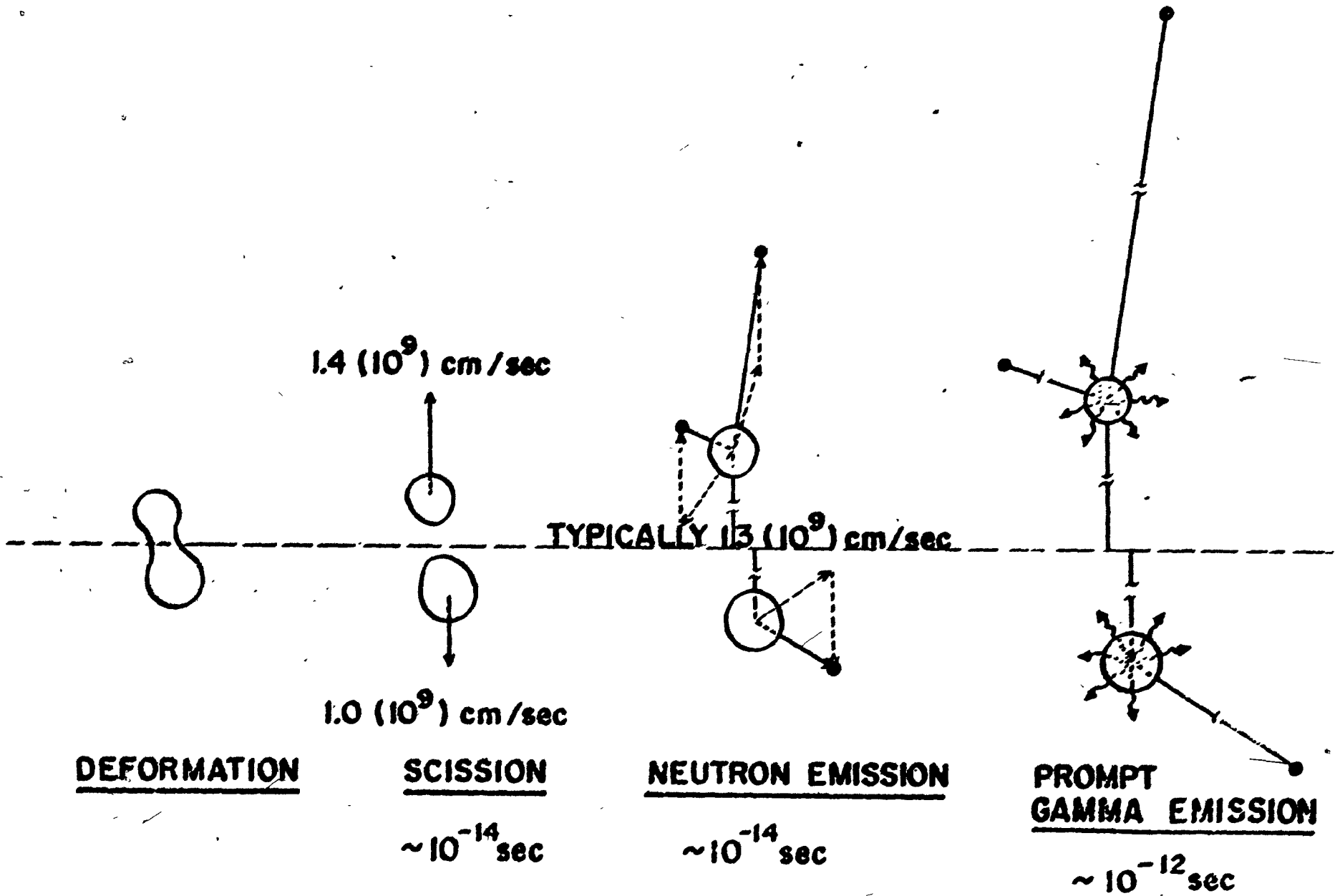
The discovery of nuclear fission was the unexpected outcome of the efforts of Fermi and his collaborators to produce transuranic elements by means of the irradiation of natural uranium with neutrons (Fe 34). Many radioactive species were found to be produced and believed, at first, to be the result of the β^- decay of the resultant nucleus, i.e. transuranic elements. The establishment by Hahn and Strassman (Ha 39) of the chemical identity of these elements, among others barium and lanthanum, forced the consideration of another type of formation. The fact that these products had a mass roughly equal to half that of the target led Meitner and Frisch (Me 39) to the conclusion that the products originated from the splitting of this nucleus. To describe this process, they proposed the term nuclear "fission".

Fission has now become a branch of nuclear physics, one of the most complex, and yet it has developed almost independently from it. In spite of numerous theoretical proposals, there is to date no comprehensive theory capable of reproducing in a complete fashion those features that can be observed experimentally. However, partial successes have been achieved by means of various models and empirical rules.

II. NATURE OF THE FISSION PROCESS

When ^{235}U is bombarded with thermal neutrons, the

FIGURE 1: Scission configuration in the fission process and neutron emission.



period required by a medium-energy particle to travel a distance comparable to the nuclear diameter, typically 10^{-22} sec.

- 3) The transition state nucleus oscillates through many shapes and the lifetime is of the order of 10^{-15} sec. for thermal-neutron capture. This is the point where the potential energy of the system has reached its maximum.
- 4) The deformation increases and the nucleus reaches a point where the configuration is that of two separate fragments (scission point). This transition is rapid (10^{-21} to 10^{-20} sec.) and corresponds to a decrease in potential energy. A small particle (mostly prompt neutrons) may be emitted.
- 5) Under the influence of the Coulomb repulsion, the excited primary fragments are accelerated. They reach approximately 90% of their final kinetic energy in 10^{-20} sec. These fragments have approximately the same neutron-to-proton ratio as the initial nucleus and hence are highly neutron-rich.
- 6) The primary fragments undergo de-excitation, by neutron emission (10^{-15} to 10^{-18} sec.) until the remaining excitation energy falls below the binding energy of the last neutron, then by γ -ray emission (10^{-11} sec.). They are now the secondary fission fragments or primary fission products (Z_1A_1), (Z_2A_2).

- 7) Although primary products are in their ground states, they still are in the great majority quite far from the β stability line and hence are radioactive. β^- decay occurs which sometimes populates a neutron-unstable level to give delayed-neutron emitters. This process is very slow ($> 10^{-3}$ sec.).

Fission products can be classified into three groups:

- 1) Independently-formed products (shielded nuclides): these are shielded from formation by a stable or extremely long-lived precursor. They are either primary fragments or the product of neutron and γ -de-excitation of primary fragments.
- 2) Cumulatively-formed products: they result from both independent formation and β^- decay of their precursors.
- 3) Semi-shielded products: these are partially shielded from formation by radioactive decay by a precursor whose half-life is long enough to allow chemical separation of the daughter product before appreciable decay of the parent has taken place.

The first and third type of products are studied by radiochemists to determine nuclear charge distributions in fission. The second, usually the last member in the radioactive decay chain, is studied to determine the mass distribution in fission.

III. ELEMENTS OF A COMPLETE THEORY

A complete knowledge of internucleonic forces would

lead to an exact Hamiltonian for the energy of the nucleus and one could write:

$$H = \sum_1^A \frac{P_i^2}{2M} + \frac{1}{2} \sum_i \sum_{i \neq j}^A V_{ij} + E \cdot M \tag{A.2}$$

where: P_i is the momentum of the i th particle
 V_{ij} is the exact potential of the interaction of the i th and j th particle
 $E \cdot M$ is a term which allows for the existence of the electromagnetic field.

The solution of Schrödinger's equation making use of this Hamiltonian would, in principle, explain all nuclear phenomena, including fission. Firstly, it is necessary to know the form of the potential V_{ij} and also how this potential varies as a function of the deformation coordinates. Secondly, the knowledge of the dependence of the kinetic energy part of the Hamiltonian on the time derivatives of these same deformation coordinates is required. Once the potential and kinetic energy variation is known, it is possible to carry out formally a complete dynamical calculation, starting from a given set of initial conditions. However, in the present case, the solution of the equations of motion is complicated by the fact that a collection of nuclei may exist in a wide variety of initial conditions. Furthermore, the calculation of average quantities such as fission rates, the kinetic energy and excitation energy distribution of the fragments, where a huge number of nuclei

are involved, renders necessary the use of statistical mechanics. Finally, considering the complexity of a system like, for example ^{236}U , where 708 internal degrees of freedom are involved, it is not surprising that a complete solution to the problem of fission, by means of a formal approach developed from first principles, remains out of reach of most known methods.

An alternative method that overcomes many of the difficulties inherent in more fundamental approaches consists of constructing a nuclear model which yields a much simpler Hamiltonian. The models of nuclear fission currently utilized are divided into two main categories (Fr 66):

- adiabatic models - these have been developed under the assumption that the coupling between the collective and the internal motions is weak. This condition is met in the liquid-drop model.
- non-adiabatic models where the coupling is strong. This is the basis on which the statistical model rests.

IV. NUCLEAR MODELS

a) Adiabatic models

i) Liquid-drop model (LDM)

Following the suggestion of Meitner and Frisch, Bohr and Wheeler (Bo 39) were the first to give an extensive treatment of the fission process envisaged as the division of

a charged liquid drop. The basis for this model is similar to that for the Weizsäcker semi-empirical mass equation (We 35). The nucleus is assimilated to a uniformly charged sphere of incompressible matter whose shape represents a balance between the nuclear forces, which translate into surface tension, and Coulombic repulsive forces. Thus, the liquid-drop model in its simplest form describes the potential energy changes associated with shape distortions in terms of the interplay of the two factors mentioned above. If the electrostatic forces become greater than the restoring surface tension forces, the drop may divide into two or more fragments.

In the case of small distortions of a sphere, the radius, R , can be written as:

$$R(\theta) = R_0 [1 + \alpha_2 P_2(\cos\theta)] \quad (\text{A.3})$$

where θ is the angle of the radius vector
 α_2 is a parameter describing the amount of quadrupole distortion
 R_0 is the radius of the undistorted sphere
 P_2 is a Legendre polynomial

The surface and Coulomb energies are given by Bohr and Wheeler as:

$$E_s = E_s^0 (1 + \frac{2}{5} \alpha_2^2), \quad E_c = E_c^0 (1 - \frac{1}{5} \alpha_2^2) \quad (\text{A.4})$$

where E_s^0 and E_c^0 are the surface and Coulomb energies of

undistorted spheres, and α_2 is as defined above. In order for the charged liquid-drop to be stable against small deformations, the decrease in Coulomb energy $\Delta E_C = -\frac{1}{5} \alpha_2^2$ must be smaller than the increase in surface energy $\Delta E_S = \frac{2}{5} \alpha_2^2$. The drop will become unstable when $|\Delta E_C|/\Delta E_S = 1$, i.e. when $E_C^0/2E_S^0 = 1$. This ratio defines the fissility parameter and may be expressed in terms of the mass number A and the nuclear charge Z of the nucleus (Gr 54):

$$x = Z^2/50.13A \quad (\text{A.5})$$

typical values of x are 35.56 for ^{238}U and 38.11 for ^{252}Cf . Above $Z = 125$, this simple liquid-drop model would predict spontaneously fissioning nuclei, i.e. nuclei which are expected to fission in a time comparable to a nuclear vibrational period.

For larger deformations, as those encountered beyond the saddle point, it becomes necessary to include higher-order polynomials than are given in Eq. (A.2). The drop shape may be described in terms of an expansion in Legendre polynomials:

$$R(\theta) = \frac{R_0}{\lambda} [1 + \sum_{n=1}^{\infty} \alpha_n P_n(\cos(\theta))] \quad (\text{A.6})$$

where λ is a scale factor required to ensure that the volume remains constant. The three coordinates α_2 , α_3 and α_4 represent the fission, mass-asymmetry, and necking degrees of freedom. In this expression, even values of n give shapes

that are axially symmetric and symmetric towards reflection through the central plane perpendicular to the axis, whereas odd values of n still give axial symmetry but do not give reflection symmetry. The appropriate variations of the coefficients a with time will generate a series of shapes which is meant to reproduce the actual sequence leading to the scission point.

Many other types of representations have been used also, depending on the type of configurations studied. For shapes close to a spheroid (ellipsoid of revolution) one may describe the nucleus in terms of a perturbed spheroidal expansion (Jo 70, Sw 56, Sw 58). The two extreme cases obtained in this representation consist of an infinitely long needle and an infinitely thin disc and therefore this parametrization is unable to describe the later stages of the fission process, due to the absence of formation of a neck. Configurations close to the scission point are well described by perturbed Cassinian ovals (Pa 71, Ad 71). Shapes such as two touching spheres are however better reproduced by means of a two-center parametrization (Ha 68, Wo 69, Mo 70a). This method, however excellent for describing separate nuclei, is impractical for a single nucleus because of a cusp in the nuclear surface in the region where the spheroids interact. This cusp can be removed by adding to the equation of the two spheroids an additional function which connects smoothly the two outer spheroids (Mo 71, Mu 72).

Mapping of potential energies based on such a treatment involves of course, a great deal of arbitrariness in that the initial shapes from which calculations are carried out are chosen intuitively as the best mathematical approximations to a certain type of configuration which is believed to be representative either of the saddle point or of the scission point. Furthermore, simple liquid-drop calculations do not take into account the dynamic aspect of the fission process. Therefore, the goal of the method remains limited to the estimation of static properties of certain shapes of deformed nuclei.

Applications of the LDM model have basically yielded three types of information:

- values of nuclear masses.
- fission barriers.
- most probable modes of fission.

In the first case, Myers and Swiatecki (My 66) were able to reproduce the mass decrements of 97 β -stable nuclides in what remains probably the best illustration of the qualities of the method. However, one observes systematic deviations between calculated and experimental values, especially pronounced in the region of the so-called magic nuclei (see following section). In some cases, nuclei appear to be as much as 13 MeV more bound than predicted by the LDM average fit (Br 72).

Fission threshold energies obtained by Androsenko et al. (An 69) by an analysis based upon observed fission

cross sections have been compared to the predictions of the liquid-drop model for fissioning actinide nuclei of masses 232-245. These experimental barriers are seen to decrease slightly with increasing mass number of the fissioning nuclei, whereas the LDM predicts a rather sharp decrease over this mass range. A quantitative fit would require the use of unrealistic fissility parameters.

One of the first extensive investigations of equilibrium configurations has been performed by Cohen and Swiatecki (Co 62, Co 63). The drop, assumed axially symmetric, was parametrized using the classical Legendre polynomial expansion with $n = 18$. The different terms of the potential energy were calculated by numerical integration and for a given value of the fissility parameter. The total energy was made stationary with respect to small changes in the deformation parameters. The appearance of the shapes changes from dumbbell-like for $x < 0.67$ to cylinder-like for $x > 0.67$. Configurations were found to be stable against asymmetry down to $x = 0.39$. Using a different mathematical approach, Strutinsky et al. (St 64) have arrived at the same conclusion. This result constitutes one of the major failures of the LDM theory since this model was originally developed in the hope that it would provide an explanation for the asymmetric mass distribution encountered in low-energy fission - the overwhelming majority of equilibrium-configuration studies point to the fact that no asymmetric equilibrium configuration exhibits a lower energy than the symmetric.

Certain refinements to the LDM have been introduced, like modifications for a diffuse surface, a non-uniform charge distribution, compressibility and curvature-dependent surface tension. Among those of relevance to fission are corrections which are dependent on distortion. Strutinsky (St 64) has investigated some of these effects and the overall result is that predicted barriers are lowered. However no quantitative statement has been made. Nix (Ni 67) has introduced a correction for barrier curvature based upon considerations of surface diffuseness. This modification has not significantly altered the previous conclusions.

ii) Shell model

This model was initially developed by Mayer (Ma 48, Ma 49) in order to explain the gaps observed in the energy-level structure of certain nuclei where certain combinations of neutrons and protons (like for example 2, 8, 20, 50, 82 and 126) give rise to an exceptional stability. By analogy with the atomic structure terminology, these combinations are called shells and sub-shells. Each particle in the nucleus is considered as independent and the interaction between particles is a small perturbation on the interaction between particle and the potential field. A review of the various types of potentials used in single-particle calculations has been given by Nix (Ni 72). A pairing correction

which arises from the short-range interaction of correlated pairs of nucleons should also be added (Be 59). In the framework of this model, shells are interpreted as large distinct groups of degenerate single-particle states in a spherical nuclear field (Br 72). This approach has provided a basis for a microscopic theory where collective excitations found in nuclei are described as the result of a coherent motion of the shell-model particles. Its extension to non-spherically symmetric average fields by Nilsson (Ni 55) has led to the correct prediction of the ground-state spins and low-excitation spectrum for most of the even-odd nuclei. Conversely, Mottelson and Nilsson (Mo 59) have successfully applied this model to the evaluation of nuclear ground-state deformations estimated from the sum of single particle energies.

Attempts have been made to extend such a treatment to larger deformations, such as those encountered in the fission process. The extent to which shells play a role in the fission act seemed to be clearly demonstrated by the structure in the dependence of neutron yields on fragment mass, first observed by Fraser and Milton (Fr 54). This led Terrell (Te 62, Te 65) to the conclusion that the neutron yields are closely related to the deformabilities of the nascent fragments. In particular, the minimal value of ν observed for fragments with $A \approx 130$ originating from the thermal fission of ^{233}U , ^{235}U , ^{239}Pu , ^{252}Cf was immediately

related to the presence of a doubly magic shell $Z = 50$,
 $N = 82$.

Johansson (Jo 61) was the first to show that the shell-structure of the deformed nucleus determines to some extent the features of the mass distribution, in view of a linear relationship between the mass ratio of the most probable fission fragments and the degree of octupole deformation calculated at saddle point for fissioning nuclei ranging from ^{227}Ac to ^{252}Cf . Quantitative agreement was obtained by the same author in the case of the peak-to-valley ratio of the mass distribution of ^{236}U and ^{240}Am for excitation energies below 10 MeV.

Anomalies in the spontaneous fission half-lives have also been interpreted in terms of shell effects. This was suggested by an absence of correlation with the fissility parameters, contrary to what one would normally expect, considering the smooth dependence of the barrier height with those predicted by the LDM. The half-lives for a given element decrease with x for the heavier isotopes of each element, as for example the anomalously short half-lives of nuclides with $N > 152$ such as ^{154}Fm , ^{256}Fm and ^{257}Fm . This fact has been attributed to a shell closure at $N = 152$.

The existence of spontaneous isomers (Po 62) has been linked to structures in the fission barrier caused by the presence of shells that increase the stability of a deformed nucleus in its ground state, thus lowering the

potential energy and creating a depression in the fission barrier (Gu 68) (see Fig. 2).

However, analyses of this type, based entirely upon the single-particle model, cannot be expected to describe in an adequate fashion the nuclear deformation energy. Although they yield reasonably good results for moderate quadrupole deformations, more complex deformations require the incorporation of the bulk properties of the nucleus in addition to the single-particle structure, if one expects to draw quantitative conclusions.

One alternate solution consists of combining a macroscopic approach, such as the LDM, which describes the smooth trend of the potential energy, with a microscopic approach, such as the single-particle model, which reproduces the local fluctuations. This method was first developed in 1967 by Strutinsky (St 67).

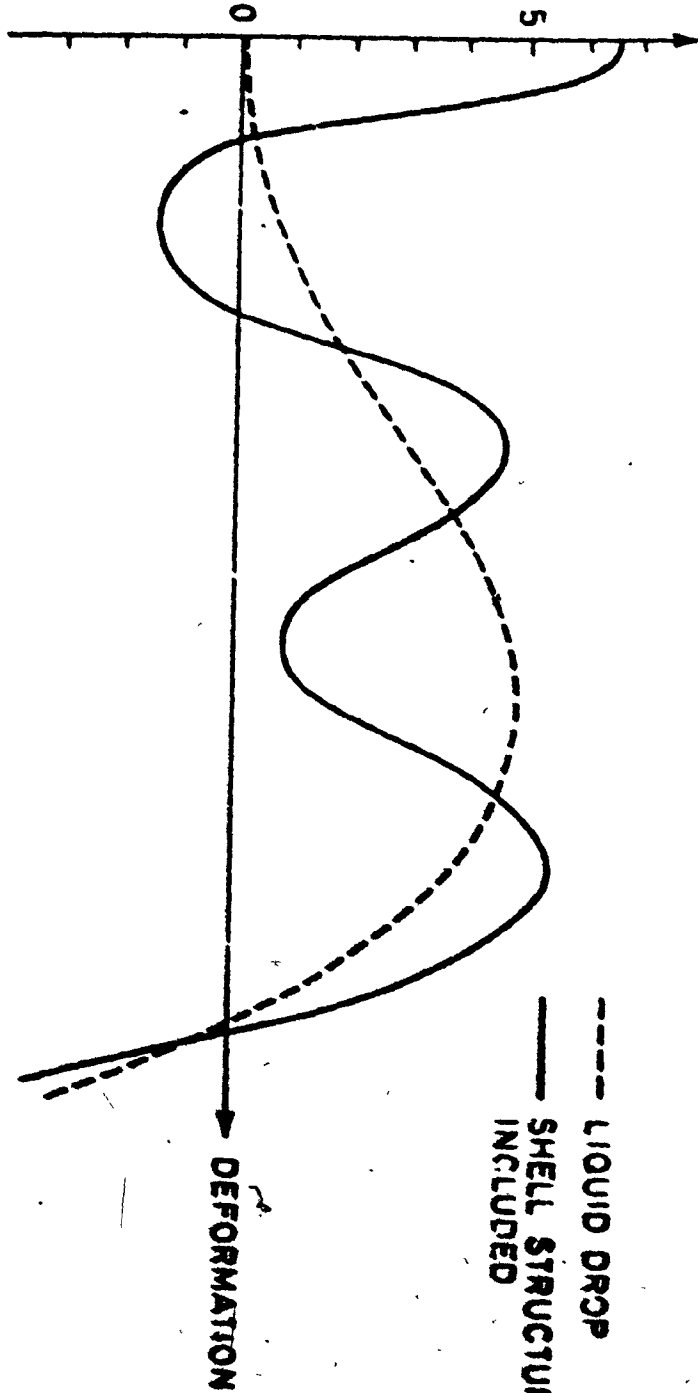
iii) Macroscopic-microscopic approach

The calculation of the nuclear potential energy of deformation by means of this approach is usually performed in five steps. These have been summarized by Strutinsky (St 67) in the following way:

- 1) Specify nuclear shape.
- 2) Calculate macroscopic (liquid-drop) energy, E_{LDM} .
- 3) Generate single-particle field felt by nucleons.
- 4) Solve Schrödinger equation for single-particle energies.

FIGURE 2: Potential energy function for deformations leading to fission. The deformation parameter labels the path towards fission, as indicated by the shapes at the top of the figure. The shapes at the first and second minima correspond to those observed in the ground states and in the shape isomers in nuclei in the region of uranium. After Bohr and Mottelson (Bo 73).

POTENTIAL ENERGY (MeV)



--- LIQUID DROP
— SHELL STRUCTURE INCLUDED



FISSION
⇌

- 5) Calculate microscopic (shell and pairing) corrections δP .

The total potential energy is then given by the sum of the energy of step 2 and the correction of step 5. This method is also known as the shell-correction method. The dependence of the pairing strength on deformation can be also included in the same manner. The total energy becomes:

$$E = E_{LDM} + \sum_{Pn} (\delta U + \delta P) \quad (A.7)$$

where the corrections for neutrons and protons are treated separately.

Mustapha et al. (Mu 72, Mu 73) have applied this method to potential energy surface calculations by using the two-center potential of Mosel and Schmidt (Mo 71). Their results show that the minimum energy path leads to most probable fission modes of heavy nuclei in agreement with those observed experimentally, provided the potential surface plays the dominant role. For instance, the most probable mass ratio for ^{236}U fission centers around 146/96, whereas the calculations predict a mass distribution peaked at symmetry for ^{210}Po and ^{202}Pb . Möller et al. (Mö 70b) have been able to reproduce the two-hump fission barriers of a number of heavy nuclei ranging from ^{226}Ra to ^{252}Fm . However, the theoretical barrier heights are found to be too high compared with the experimental values.

An interesting application of the method is the

prediction of fission barriers of super-heavy nuclei as yet undiscovered. The calculations of Nilsson (Ni 69) carried out with a Woods-Saxon single-particle potential show that the nuclide with $Z = 114$ and $N = 184$ is predicted to have a fission barrier of about 9 MeV which would make it stable towards spontaneous fission. Some of the lighter $Z = 114$ isotopes may also have spontaneous fission half-lives long enough so that they might exist in nature, provided they were produced in nucleosynthesis.

Myers and Swiatecki (My 67) have used a shell correction to the LDM in a somewhat different manner by using a simple short-range alternating function chosen to be Gaussian. This idea is the result of the observation that the shell effects are associated with degeneracies characteristic of the spherical shapes and should disappear in distortions away from the sphere.

Strutinsky (St 67) has calculated the total shell-correction energies to the nuclear ground-state masses. These corrections are in good agreement with the deviations observed between the LDM fit of Myers and Swiatecki (My 66) and experimental masses (Fig. 3).

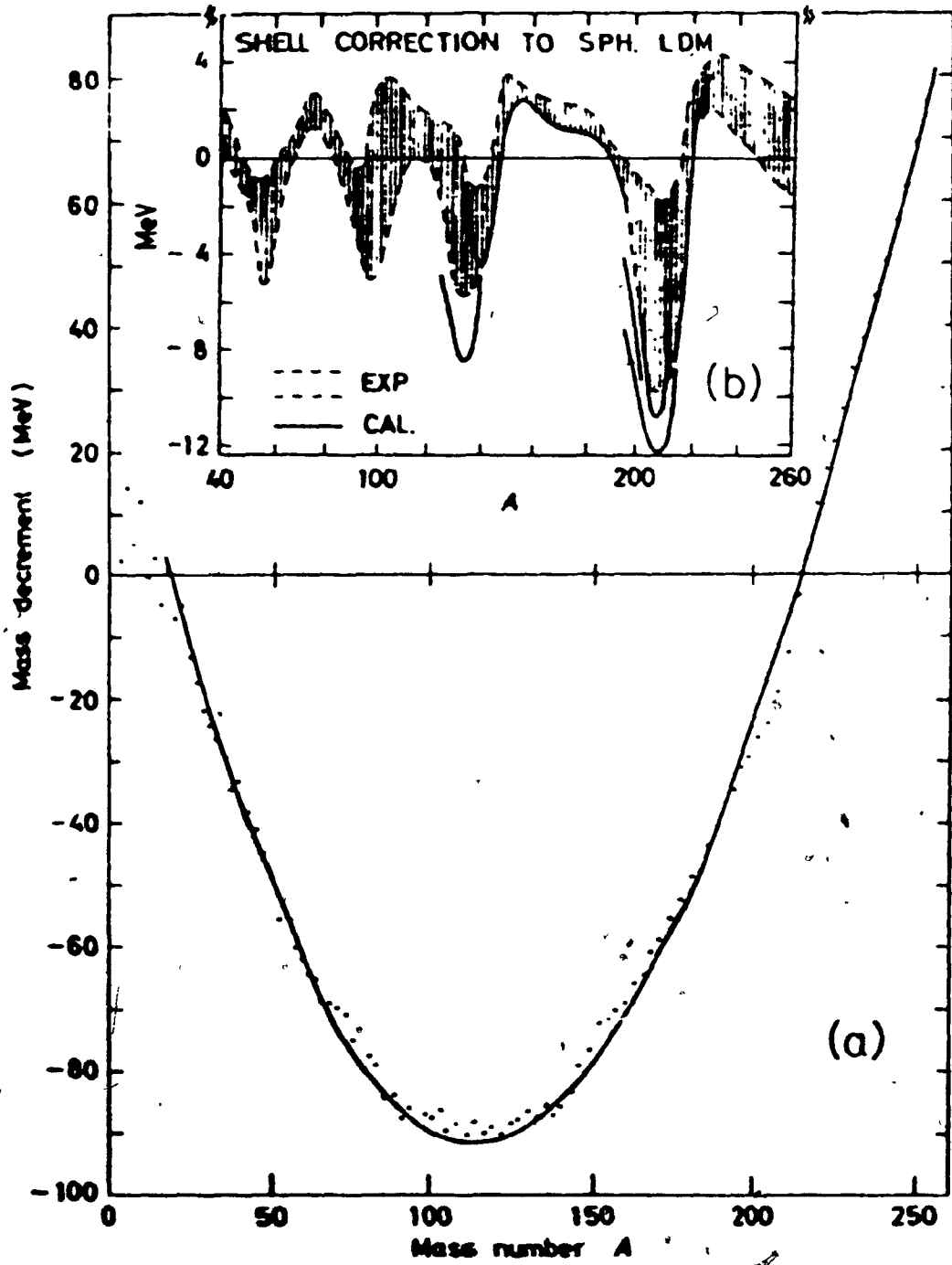
b) Non-adiabatic models

i) Channel theory of fission

A. Bohr (Bo 56) suggested that low-energy fission may be understood in terms of the energy levels of the

FIGURE 3: a) Experimental nuclear masses as compared with the LDM fit used by Myers and Swiatecki (My 66).

b) The total shell-correction energy to the nuclear ground-state masses as calculated in Strutinsky (St 67) are compared to the deviations of experimental masses from an LDM mass law referring to spherical nuclei.



transition nucleus defined in the LDM formalism, and that observable features such as angular distributions of the resulting fragments were determined by the characteristics (spin and parity among others) of the levels through which the fission act proceeds. This treatment was first put forward for cases where the excitation energies involved are comparable to the fission barrier (5 to 6 MeV for actinides). One of the premises on which the theory rests consists in the assumption that the transition nucleus is thermodynamically cold, i.e. that most of the excitation energy of the fissioning nucleus goes into deformation energy during the passage from the initially excited nucleus to the highly deformed configuration at saddle point. Consequently, the spectrum of excited states at the top of the fission barrier is expected to be analogous to that of a normal nucleus near its ground state. Secondly, the descent from saddle to scission is so rapid compared to the average lifetime of the transition nucleus that the final characteristics of the fission fragments, though strongly dependent on several other factors, are nevertheless influenced by those of the transition states at the saddle point. At higher excitation energies, the compound nucleus states exhibit a very high density with level spacing of the order of eV, but their number makes it possible to study their properties using statistical assumptions. In both cases, the properties of the fission process can be accounted for by a limited number of reaction alternatives (channels) even though

the number of fragment pairs is very large in the binary fission of a heavy nucleus. In the particular case of angular distribution studies, this treatment has generally led to a good agreement between experiment and theory to the extent that results obtained from fission-fragment angular distributions have sometimes been used to extract information about nuclear structure and nuclear reaction mechanisms. This point has been developed mainly by Halpern and Strutinsky (Ha 58), Strutinsky (St 61a) and Griffin (Gr 59, Gr 62).

ii) Statistical theory of fission

The fundamental assumption on which this theory is based is that the fission process is considered to be a slow one, so that instantaneous thermal equilibrium will be established at any moment of the process. This implies that a strong coupling exists between the collective and the internal (single-particle) motions (Sw 65) and that the model is essentially a combination of the liquid-drop model and the single-particle model at high energy. Fong (Fo 64) has based an argument for the validity of the statistical model, even for low-energy fission, on an estimated descent from saddle to scission point that is about five times longer than the characteristic nuclear transit time and ten times longer than the nuclear relaxation time. Wilets (Wi 64), however, points out that this argument is not valid for the case of the ground or first few excited states of the transition-state nucleus

where these highly correlated states deviate appreciably from the gas model on which the argument for statistical equilibrium is based.

The statistical model of fission was given serious consideration first by Fong (Fo 53, Fo 56). This author assumes that the relative probabilities of different scission configurations (characterized by mass, charge, deformation and kinetic energy of the nascent fragments) is proportional to the number of quantum states associated with them and therefore, the relative probability of occurrence of fission modes is proportional to the density of quantum states at the moment just before scission. In the original calculations, the dependence of the level density in the nascent fragments on excitation energy is exponential, and as a consequence, the probability for different mass splits is very sensitive to the mass defects of the deformed fragments, which in turn are likely to be strongly dependent on the shell structure of the final fragments. The statistical model is therefore capable, in principle, of accounting for the tendency of asymmetric mass splits at low energy, and also for the disappearance of this mode with increasing energy, since a given shell effect becomes relatively less important.

The application of this theory to the calculation of the mass-yield curve from the fission of ^{235}U by thermal neutrons resulted in an exceptional agreement with the experimental results (Fo 56). In particular, asymmetric fission was found to be favored over symmetric fission by a

factor of the order of 10^3 . However, a most-probable mass ratio around 132/104 was predicted, instead of 140/96, as found experimentally, and fine structures in the $^{235}\text{U}+n$ mass distribution were also not reproduced. A similar calculation carried out in the case of thermal fission of ^{239}Pu yielded a four-humped mass distribution. These discrepancies have often been considered a major objection of a fundamental nature against the statistical theory despite the existence of other evidence such as reasonably good agreement between calculated and experimental charge distribution (Wi 67), kinetic energy and prompt neutron distribution (Fo 63), ternary fission rate (Fo 71) and alpha-particle angular distribution (Fo 70). They have been partly attributed to the fact that the shell effect on energy was calculated by treating the deformed fragments as if undeformed (Fo 74a).

In a recent work, Fong (Fo 74a) has been able to obtain complete agreement between calculated and experimental mass-yield curves of $^{235}\text{U}+n$ by introducing in his calculations the potential-energy surface calculated by Mustapha et al. (Mu 73) and the Strutinsky prescription (St 67). The results indicate that asymmetric fission modes, centered around the mass ratio 140/96, are favored energetically.

Numerous attempts have been made to use a statistical approach to account for one or another feature of fission properties. Unlike the original Fong treatment, which was

free of arbitrary parameters, the later applications have been employing adjustable parameters at some point. By using this approach, Newson (Ne 61) was able to reproduce the mass distributions obtained in ^{233}U , ^{235}U , and ^{239}Pu with thermal neutrons, ^{238}U and ^{232}Th with 2.8 MeV neutrons, and ^{226}Ra with 11 MeV protons. Erba et al. (Er 63, Er 64) have used a slightly modified theory in that they have related the probability of fission to the states in the final nucleus rather than to the states at saddle point. They also used free parameters. They obtained good agreement with experimentally determined mass and kinetic energy distributions obtained from $^{235}\text{U}+n$. The reasonableness of the parameters obtained in this case may be some measure of the validity of the statistical model.

V. FISSION PARAMETERS AND THEIR MEASUREMENTS

a) Chemical methods

Since the early days of fission studies, most of the yield determinations have been carried out by means of radiochemical techniques. They consist in the isolation of various elements produced as a result of fission and they call for specific chemical reactions whose purpose is to separate a given element, or several elements belonging to the same group, from the bulk of fission products. Such a method implies that the various isotopes of an element will behave in an identical fashion as far as the chemistry is concerned

and, as a consequence, chemical yields determinations carried out on a particular nuclide will apply to all of its isotopes. This technique constitutes a very sensitive means of selection of fission products. Provided their decay characteristics are known, their identity may be easily established on the basis of such parameters as half-lives and emitted gamma-rays. Their measured activities may be related to the true disintegration rates and the yields of production are determined using the classical laws of radioactive decay (see experimental section).

However, the radiochemical method remains confined to the study of radioactive species whose half-lives are long enough so that the relevant chemical separations can be performed before complete decay has occurred. Several ingenious procedures have been devised where the time required for isolating short-lived species with half-lives of the order of tens of seconds can be reduced to as little as a few seconds. An extensive review of these methods has been given by Amiel (Am 68b) and more recently by Herrmann (He 69).

The most commonly used technique consists of dissolving the fission source and subjecting it to various chemical separations after the addition of appreciable quantities of stable isotopes of the elements concerned, compared to those of the radioactive elements produced. The operations involved consist mostly in coprecipitations and solvent extractions. The chemistry is performed after complete isotopic

exchange has occurred between the stable carrier atoms and their radioactive homologues so that both species participate to the same extent in any given chemical reaction. Besides their role as a carrier, the stable isotopes serve in the determination of chemical yields. This is done with the help of classical analytical methods such as gravimetry, calorimetry, flame spectrophotometry, etc.

A second category of separations involves the use of ion-exchange resins, with or without carrier being added to the original sample solution. In the latter case, chemical yields may be determined by use of radioactive tracers. Finally, coprecipitation and ion-exchange may be combined in the course of the same chemical separation.

In some instances, catcher foils surrounding the fission source have been used to collect the recoiling fragments, thus avoiding the necessity of having to dissolve the original source, an operation which sometimes proves to be time-consuming. This method has been used by Sugarman et al. (Su 47) to estimate the mass numbers of 4.5-sec. ^{89}Br and 55.6-sec. ^{87}Br delayed-neutron emitters. Aluminum absorbers were used to isolate and rapidly measure the activity of these nuclides. Emanation methods based on the diffusion properties of long-chain fatty acid salts of heavy metals (Ha 49) have also proved very useful in the case of scarce isotopes or whenever repeated irradiations were necessary. Wahl (Wa 58) has applied this technique with a great deal of success to

the measurement of the fractional cumulative yields of such short-lived nuclides as 1.84-sec. ^{92}Kr , 9.0-sec. ^{91}Kr , 33-sec. ^{90}Kr and 3.2-min. ^{89}Br produced in thermal-neutron irradiation of ^{235}U .

The two main requirements in radiochemical separations are high purity and high yield of the final sample, the former being of prime importance whenever activity measurements call for a method which does not permit energy discrimination of the emitted radiations, like for example in beta-activity measurements. The advent of high-resolution gamma spectroscopy with the help of Ge(Li) and Si(Li) detectors however has made this requirement less stringent in the case where suitable gamma-radiations pertaining to the nuclides under study could be isolated. The degree of acceptable purification may be assured by following the decay of selected gamma-rays and comparing the half-lives found to those reported in the literature. Analyses of this type have been carried out by direct activity measurements performed on the fission source itself, without any chemical separation. Miller (Mi 70) has tentatively identified 45 fission products resulting from the proton fission of natural uranium using a Ge(Li) detector of 4.0 cm^2 active area and a 5 mm depletion depth coupled to a 1600-channel analyzer. Among those products, one third have been quantitatively determined by resolution of their decay curves.

b) Mass spectrometric methods

They possess two main advantages as compared to radiochemistry:

- i) stable isotope yields can be measured in addition to radioactive species. This is of particular importance in fission from moderately and highly excited nuclei where the contribution of independently-formed stable nuclides to their overall cumulative yields is no longer negligible as compared to what one observes in fission at thermal energies.
- ii) in addition to a high intrinsic precision, this technique has the advantage of eliminating the usual radiochemical problems of decay-curve resolution, knowledge of the decay schemes and counting corrections which sometime yield large errors in cross-section measurements.

Thode and Graham (Th 47) were the first to utilize this method and they applied it to the measurement of Kr and Xe yields produced from the thermal-neutron fission of ^{235}U . This study was extended to ^{233}U and ^{235}U by Fleming et al. (Fl 54) and Wanless and Thode (Wa 55). Since then, Thode, Tomlinson and co-workers (Fi 59, Th 60, Fa 62) have determined practically all the major cumulative yields produced in slow-neutron fission. More recently, McHugh and Michel (Mc 68) have measured the relative cumulative yields for the majority of

nuclides in the mass range 83-90 and 131-153 produced in ^{232}Th fission induced by 20-57 MeV alpha particles.

Apart from the area of rare gases, this method has encountered a great deal of success with elements of low-ionization potential such as alkali elements. Its sensitivity is illustrated by the work of McHugh (Mc 66) on isotopic ratio measurements of $^{86}\text{Rb}/^{87}\text{Rb}$ produced in ^{235}U thermal fission where the yield of ^{86}Rb , which is shielded, is very low compared to the high cumulative yield of ^{87}Rb . Friedlander, Friedman, Gordon, and Yaffe (Fr 63) made a very detailed study of the stable or long-lived isotopes of Rb and Cs produced in the fission of ^{238}U by 100 MeV to 6.2 GeV protons. A similar work has been extended to other elements produced in ^{238}U fission. Rudstam (Ru 65) studied the yields of $^{118-135}\text{I}$ at 590 and 18 GeV. Brandt (Br 65) has reported cross-sections and range measurements of $^{74-84}\text{Br}$ at the same energies. Hagebø (Ha 67) investigated $^{115-131}\text{Sb}$ produced at 159 MeV and 18.2 GeV. Chu et al. (Ch 71) have measured rare-earth products from ^{238}U fission by 28-GeV protons, extending their previous measurements to a mass region where radiochemical measurements prove to be difficult.

So far the above mentioned examples have utilized mass-spectrometry as a mass-selective step to otherwise conventional radiochemical procedures. The introduction of on-line mass-spectrometers directly connected to the beam of accelerators or reactors has made possible the detection of fission products of practically any half-lives from milli-

seconds to stability (Kl 69). There is a distinct advantage in using this technique in high-energy nuclear reaction studies since these result in products that lie very far both on the neutron-deficient and the neutron-excess side of the stability valley (Mi 59). Up to now, only alkali elements have been investigated. Following the method of Klapisch (Kl 67), the heated ion source of the mass-spectrometer is directly bombarded by a beam of particles. Rapid extraction of the reaction products occurs through high-temperature diffusion. These products recoiling out of the target are stopped by thin graphite slabs interspersed with thin foils of the target element. Na, K, Rb and Cs are then separated from the other elements by preferential diffusion through the heated graphite. This method has enabled Klapisch and co-workers to measure the isotopic yields of all known Rb and Cs isotopes produced in ^{238}U and ^{232}Th at 150 MeV (Am 68a, Ch 71), at 10 GeV (Kl 68) and 24 GeV (Ch 70a). A similar technique has been recently applied at McGill where Lee et al. (Le 75) have determined the same isotopic distributions at 80 and 100 MeV. Ion-source experiments are underway to extend this technique to elements other than alkali metals.

c) Physical methods

They have enabled the study of dynamic properties of the fission process due to the fact that, in some cases, the phenomena observed can be related to the primary fission

fragments. Physical measurements may be classified into three principal categories as far as fission studies are concerned: time-of-flight measurements, X-ray experiments, and β -decay energy measurements.

The time-of-flight technique consists of measuring the time necessary for a fragment to travel a known distance. The information yields directly the velocity of the fragments and provided their masses are known, one can deduce their kinetic energy. This approach has been used by Milton and Fraser (Mi 62) to determine the kinetic energy of fission fragments produced in the thermal-neutron fission of ^{233}U , ^{235}U and ^{239}Pu .

X-ray measurements performed directly on fission fragments have been made possible by continued improvement in X-ray detector technology. Their good resolution has enabled reliable assignments to specific elements of X-ray transitions arising from internal conversion associated with the de-excitation of the primary fragments. Of the various methods in this line, X-rays measured in coincidence with fragment kinetic energies has probably been studied the most (Gl 65, Wa 70, Re 71). The main disadvantage, however, is that the technique does not give specific properties of individual fragments. Yields, for example, are averaged over several isotopes, but these data have nevertheless been analyzed to extract properties such as charge and mass distribution.

The number of β particles emitted in the decay of

a specific mass chain can lead to the determination of the most probable charge, as shown by Armbruster et al. (Ar 64). They studied the system $^{235}\text{U} + n_{\text{th}}$. The β -decay energy of the individual products was determined following their mass separation, and this energy was converted into chain length by means of a mass formula.

A more up-to-date technique involving the use of solid-state detectors consists of measuring in coincidence the energy lost by a fragment by passage through a thin detector and its kinetic energy. The response from the first detector is proportional to v^2/Z^2 , where v and Z are the velocity and the charge of the fragment respectively. This information combined with the knowledge of the kinetic energy provides a means of identification of the charge and the mass of the fragment.

In spite of their growing importance as a tool for the study of fission reactions, physical methods remain hampered by a poor mass resolution as compared to radio-chemical techniques.

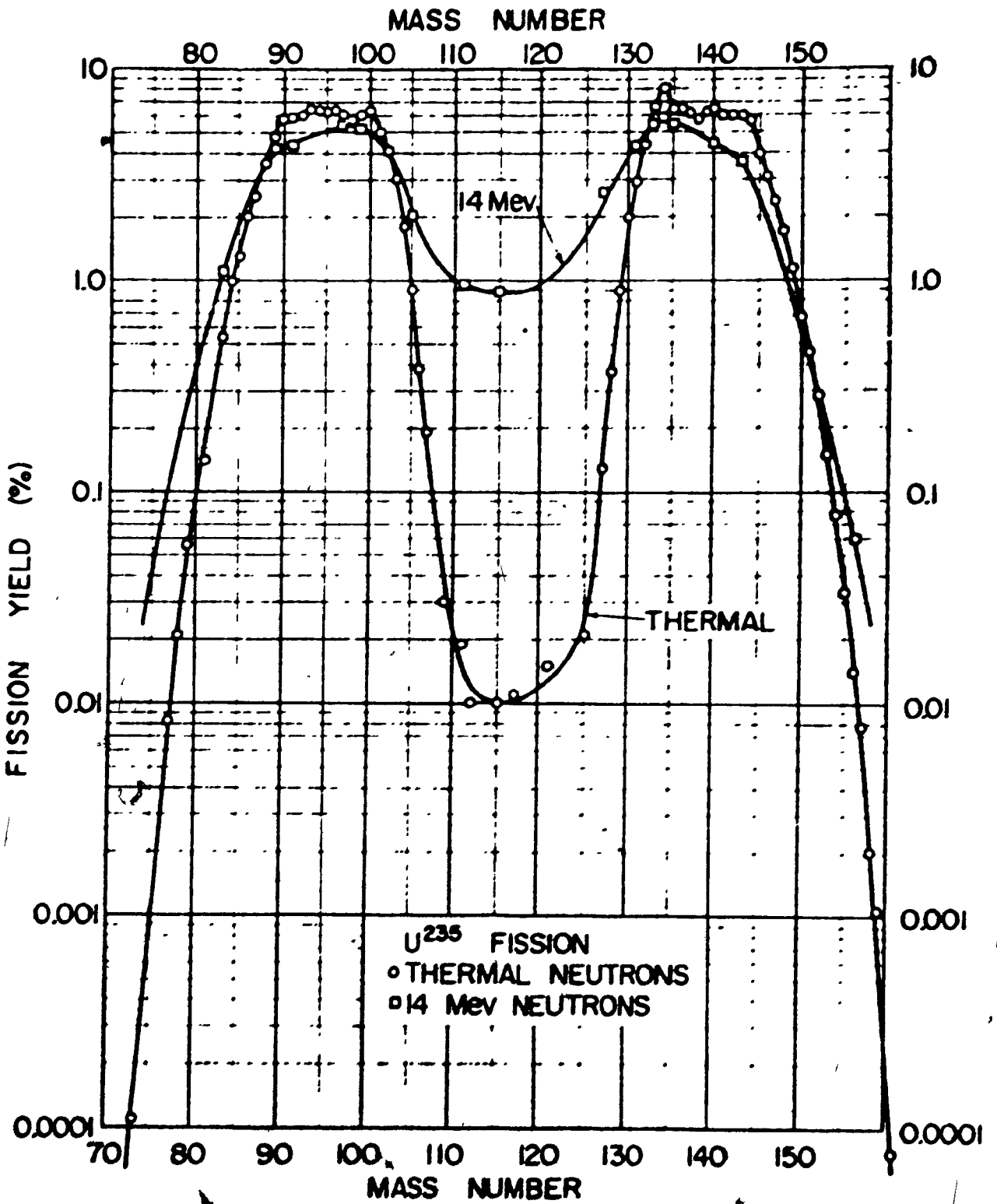
VI. LOW AND MEDIUM ENERGY FISSION

a) Mass distribution,

i) Fission at thermal energies

The distribution of the cumulative chain yields of different fission chains versus the mass numbers of those

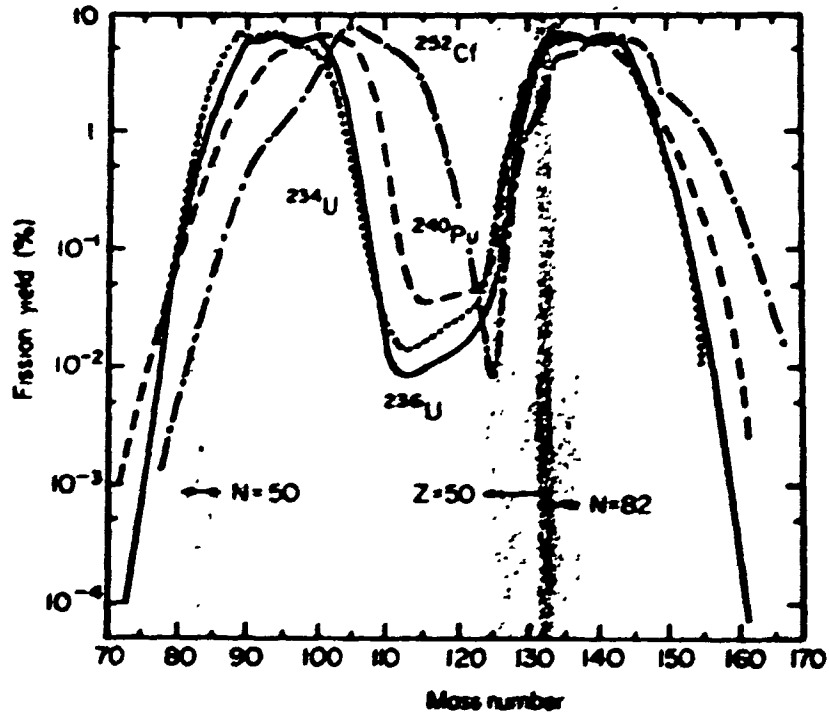
FIGURE 4: Yield-mass curve for fission of ^{235}U induced by thermal and 14 MeV neutrons. After Hyde (Hy 60).



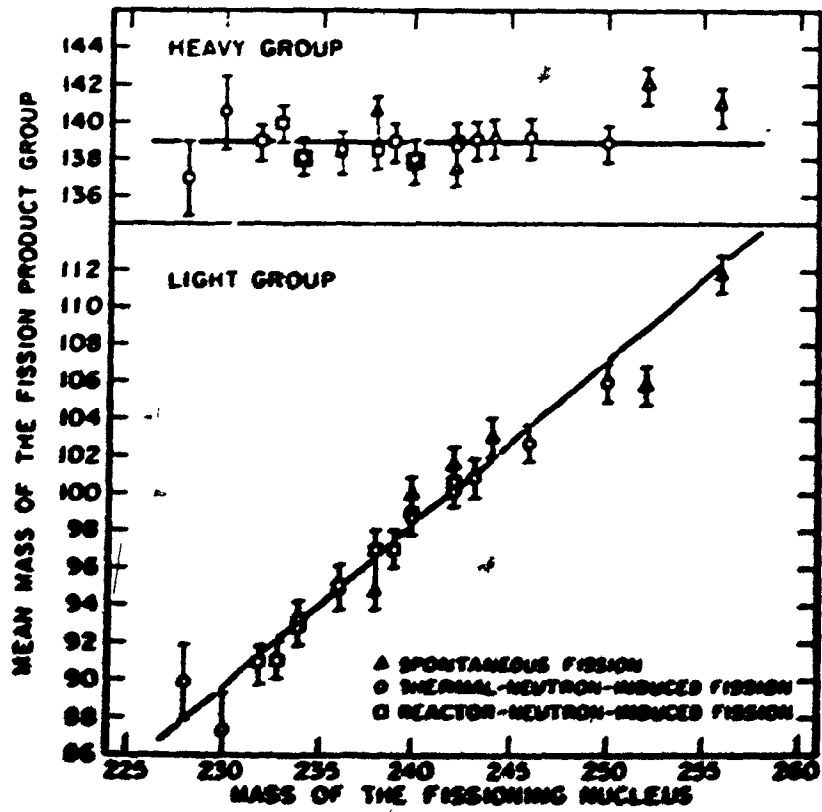
chains constitutes the mass distribution of fission products. Low-energy fission (spontaneous fission and fission induced by thermal neutrons) results in about 200 neutron-rich nuclides distributed over approximately 40 elements spanning a mass range 65-160. Among those products, half of them exhibit half-lives smaller than 100 seconds. These neutron-rich products undergo negative beta-decay along isobaric chains and, in general, the cumulative yield of the last member of those chains, which in most cases lies next to the line of stability, is representative of the total chain yield of the chain having the same mass number. As stated before, this information is principally gained by radiochemical or mass spectrometric procedures, the latter being believed to be somewhat more accurate. Absolute yields may be calculated from the measured cumulative cross-sections by normalizing their sum to 200%, assuming all the chains of significant yields have been measured and that fission is predominantly binary. Figure 4 shows an example of the mass-yield curve obtained by fission of ^{235}U by thermal neutrons and 14-MeV neutrons. The curves which are symmetric about mass 115 indicate that, at thermal energy, asymmetric mass splits are favored by a factor of ~ 600 over symmetric mass divisions. The maxima of the curve lie respectively near mass 97 and 139 for the light and heavy wing. At 14 MeV, the increase in excitation energy results in a decrease of the peak-to-valley ratio while the maxima remain approximately stationary. The rise in the valley is also accompanied by a slight broadening

FIGURE 5: a) Fission product mass-yield curves for thermal-neutron induced fission of ^{233}U , ^{235}U and ^{239}Pu , and spontaneous fission of ^{252}Cf . Shaded areas indicate approximate positions of nuclear shell edges. Curves are denoted by the symbol of the fissioning nucleus. After Wahl (Wa 65).

b) Average masses of the light and heavy fission product groups as function of the masses of the fissioning nucleus. After Flynn (Fl 72)



- a -



- b -

of the wings.

The effect of target composition on mass-yield distributions has been investigated by numerous authors. A recent review of experimental results for spontaneous and thermal-neutron induced fission of a number of nuclei ranging from ^{228}Th to ^{258}Fm has been given recently by Hoffman and Hoffman (Ho 74). The following general trends may be noted from their tabulation. a) On one hand, the mean mass of the heavy-fragment group remains nearly constant at mass 140 ± 1 for A_f between 230 and 246, although deviations of 1 or 2 mass units are seen between mass 250 and 256 (Fig. 5b). On the other hand the mean mass of the light wing shows a linear increase with A_f , with variations again apparent in the region $A_f = 250$ to 256. One notices that for ^{258}Fm , the most probable split becomes symmetric. b) The symmetric yield for thermal-neutron induced fission has a minimum around ^{235}U . For lighter or heavier nuclei, the symmetric yield goes up (Fig. 5a). c) The full-width at tenth-maximum of the light and heavy fragment groups have been found to increase linearly as a function of increasing A_f from 19 mass units for ^{228}Th (n_{th}, f) to 27 mass units for ^{252}Cf (sf) (Vo 67).

The early radiochemical investigations indicated that the mass-yield curves were smooth. However, the mass-spectrometric work of Thode and co-workers (Th 47) established the existence of spikes in the double-humped distribution leading for example to a yield of ^{134}Xe about 35 percent higher

than had been expected from the smooth trend in ^{235}U thermal fission. This particular feature was later confirmed by Unik et al. (Un 74) with the help of coincidence measurements of fission fragments using gold-surface barrier silicon detectors. In both pre- and post-neutron mass distributions, the fine structures were found to be especially pronounced in the case of ^{229}Th (n_{th}, f), ^{235}U (n_{th}, f) and ^{248}Cm (sf). In particular, there appears to be a marked tendency for divisions in which the heavy fragment contains respectively 52, 54 and 56 protons in the case of Pu, Cm, and Cf, complementary with 42 protons in the light fragment. However, it is not clear that $Z = 42$ in the light fragment is a governing factor in mass division since the same spikes on the heavy side of the mass distribution appear for Th and U whereas the non-complementary $Z = 42$ fragments are produced in very low yields (Un 74).

The fine structures in the final mass distribution are slightly displaced towards lower masses with respect to the spikes in the initial distribution as a result of post-fission neutron emission. The fact that they are also more pronounced has been attributed to variations in neutron-emission probability with mass of the primary fragment (Te 62). Thomas and Vandebosch (Th 64) have suggested that the fine structures in the kinetic-energy distribution of the fragment pairs were responsible for those observed in the mass distribution as a result of energetically preferred even-even configurations due to the pairing energy which depresses the

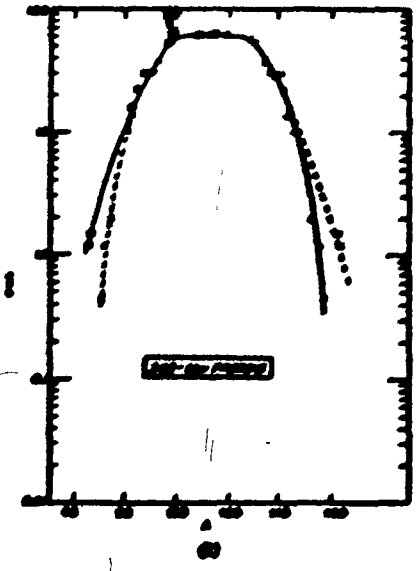
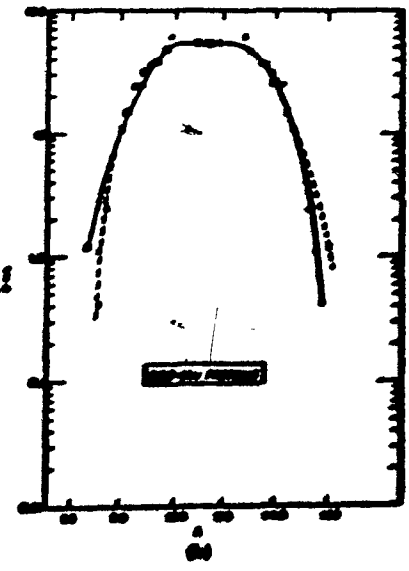
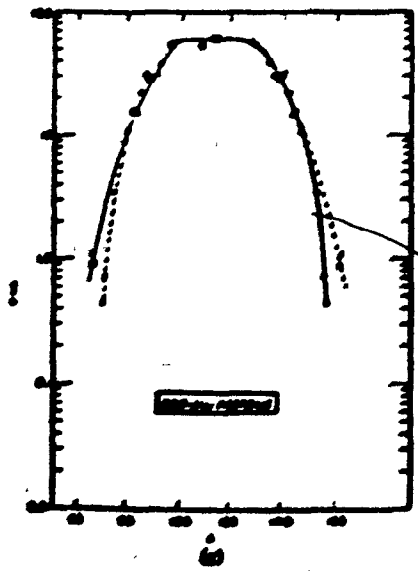
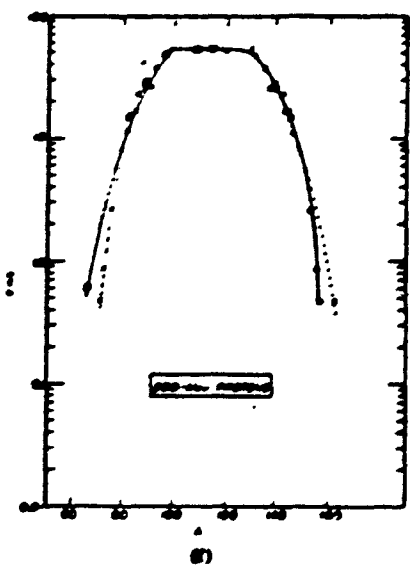
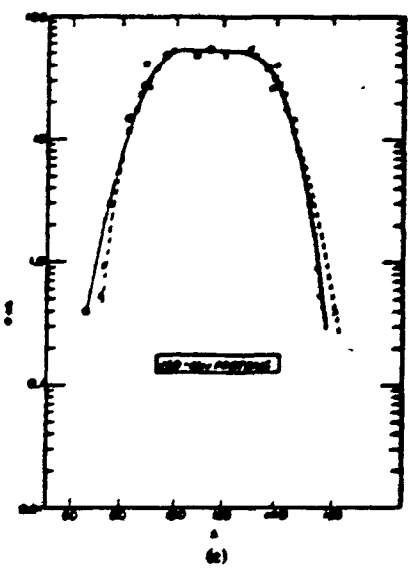
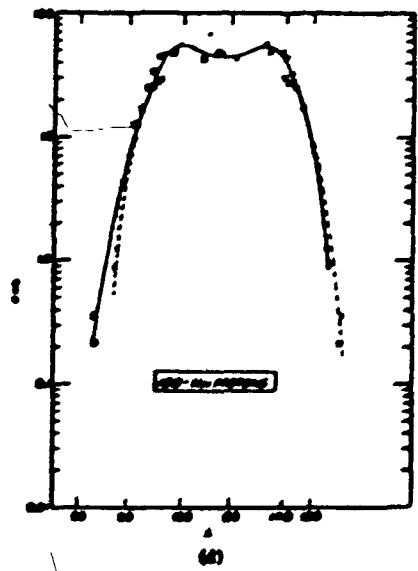
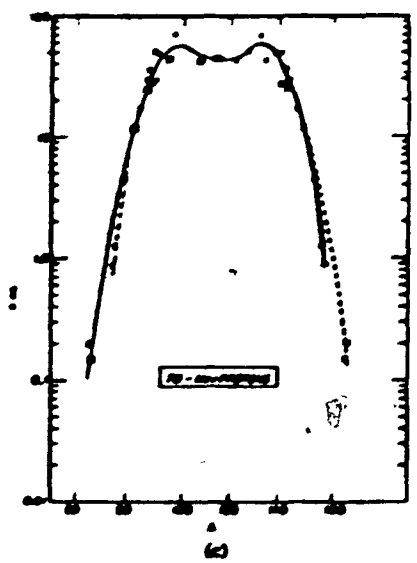
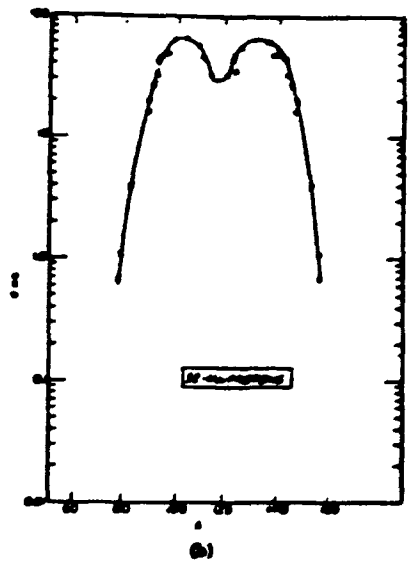
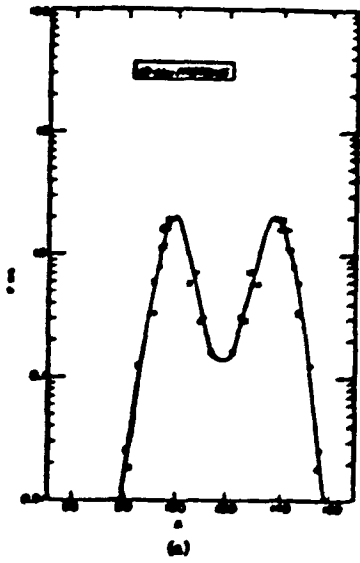
surface energy for odd-mass fragments below that for even-even. However, no satisfactory explanation consistent with all experimental observations has been proposed as yet.

ii) Fission above thermal energies

The data at higher energies are more scarce. So far, the most extensive studies involving excitation energies above 10 MeV have dealt with the fission of ^{238}U . Stevenson et al. (St 58) have reported the mass distribution of ^{238}U fission products at 10 to 340 MeV. Similar works have also been performed by Choppin and Meyer (Ch 66) at proton energies 7.1 to 12.0 MeV, Baba et al. (Ba 71) with protons of energies ranging between 13 and 55 MeV, Pappas and Hagebø (Pa 66) and more recently Haldorsen et al. (Ha 74) at 170 MeV. The results of Stevenson appear on Figure 6. They show a continuation of the trend already noticed on Figure 4, namely that with increasing incident energy, the distribution becomes broader and the two humps eventually disappear to give a single-humped curve above 200-MeV proton energy. The steep rise in the probability of symmetric fission with increasing energy appears to be consistent with the two-mode-fission hypothesis introduced by Turkevitch and Niday (Tu 51) by which a second high-energy component centered at symmetry superimposes itself over the low-energy asymmetric distribution. This seems to find further support in the results of Croall and Cuninghame (Cr 69) on the fission of ^{232}Th by 13 to 53 MeV protons, and those of Rao (Ra 72) on the same

FIGURE 6: Fission-product distribution of ^{238}U irradiated with protons.

Legend = ● Stevenson et al. (St 58)
■ Hicks and Gilbert (Hi 55)
▲ Lindner and Osborne (Li 56)
x reflection points



target with 14.8 MeV neutrons. These studies reveal the appearance of a third hump centered in the valley of the mass distribution and although symmetric fission is no longer negligible, the asymmetric mode remains predominant within their energy range. At 155 MeV, however, Galin (Ga 67) has shown by physical method that symmetric fission accounts for $\sim 75\%$ of all the fission events.

The two-mode-fission hypothesis has been most fruitfully applied by Ford (Fo 60), Hicks et al. (Hi 62), Britt et al. (Br 63), Choppin and Meyer (Ch 66) to explain quantitatively the change in the patterns of mass distribution. However, it appears difficult to invoke this theory in the case of ^{226}Ra where asymmetric and symmetric fission have been found to be equally likely at 11 MeV-proton bombarding energy.

Perry and Fairhall (Pe 71) have studied the primary fission-fragment mass distributions obtained for deuteron-induced fission of radium. They conclude that the first-chance fission of ^{228}Ac at 24-MeV excitation energy is symmetric. These two examples seem to be evidence in favor of a "many-mode" fission process suggested by Unik and Huizenga (Un 64) where differences in the structure of fissile nuclei are associated with corresponding differences in the pattern of mass-yield distribution. Möller and Nilsson (Mö 71) have elaborated on this idea by treating the problem in terms of saddle shapes. An explanation could be that the fission barrier has two maxima at some asymmetric deformation.

Symmetric fission then occurs between the maxima and asymmetric fission occurs around the outside of the maxima. The result of symmetric fission of ^{228}Ac raises the question whether the barrier shape goes from symmetric to asymmetric for a 1-unit change in A. This has not received any satisfactory explanation as yet.

b) Charge distribution

In a complete description of the fission process, one must consider the distribution of charge as well as mass between the fission fragments and how this is related to the nuclear structure of the fissioning nucleus and of the primary fragments. If we consider a single mass split, there are several possible charge divisions and a detailed characterization of this process requires a knowledge of the independent yield of each isobar of that particular mass chain, namely the charge dispersion along that chain. Numerous studies have been concerned with measurements of that nature in order to establish the most probable charge Z_p , and the distribution of Z_p as a function of the mass of the primary fragments.

Until recently, most of the experimental data on nuclear charge division were obtained by radiochemical determinations of independent yields, even though the quantities of interest in fission theories are those of the primary fragments. As mentioned earlier, independent yields can be determined either if the adjacent isobar is stable, or

if it possesses a sufficiently long half-life so that its contribution to the species of interest can be measured. Also, some information about charge division can be obtained from cumulative yields for a species that lies far enough from the line of beta stability so that its cumulative yield is significantly less than the total yield for that mass.

i) Charge dispersion curves

Various methods of constructing the charge dispersion curves have been proposed. The first attempt is due to Glendenin et al. (Gl 51) who obtained charge dispersion curves by plotting the independent yields versus the $(Z - Z_p)$ of the products. The Z_p values were calculated with the help of a prescription which will be described in a subsequent paragraph (Equal charge displacement postulate). Among other things, the calculation of Z_p requires the knowledge of Z_A , charge of the stable member of the isobaric chain under consideration, a quantity which is known to present discontinuities near the shell edges. There has been to date no theoretical treatment which has been able to show how the Z_A values of all possible fragments pairs can influence the saddle configuration of the fissioning nucleus.

In order to circumvent this difficulty, Wahl (Wa 58) proposed an empirical method based on the determination of Z_p from a plot of independent yields versus Z of the products. Further work of this author (Wa 62, Wa 65) showed that the charge dispersion curves constructed in this fashion could be

represented by a Gaussian distribution. Such distributions have later been extensively used and found further support. In this description, the probability of formation of a product with a given atomic number Z , within a particular mass chain is $P(Z)$ and assumed to be given by the Gaussian equation:

$$P(Z) = A \exp[-(Z-Z_p)^2/c] \quad (A.8)$$

The constant c reflects the relative width of the Gaussian function and has been found to have about the same value of ~ 0.8 for many decay chains produced in the fission of ^{235}U by thermal neutrons (Wa 69). The maximum amplitude of the function is given by A which is related to c :

$$A = (\pi c)^{-1/2} \quad (A.9)$$

A Gaussian charge distribution may also be represented in cumulative form which gives unity for the sum of fractional independent yields in a decay chain. The fractional cumulative yield of a number of a decay chain with charge Z is given by the equation:

$$P(n) = (2\pi\sigma^2)^{-1/2} \int_{-\infty}^{Z+1/2} \exp\left[-\frac{(n-Z_p)^2}{2\sigma^2}\right] dn \quad (A.10)$$

$$= \frac{1}{2} + \frac{1}{2} \left[f\left(Z-Z_p + \frac{1}{2\sigma}\right) \right] \quad (A.11)$$

where $f(X)$ is a normal probability integral given by:

$$f(X) = (2\pi)^{-1/2} \int_{-X}^{+X} \exp(-a^2/2) da \quad (\text{A.12})$$

σ and c are related through the relationship:

$$C = 2(\sigma^2 + 1/12) \quad (\text{A.13})$$

This type of treatment applies to ideal cases where several independent yields belonging to the same chain can be measured. Unfortunately, there are very few mass chains where it has been possible to determine more than two independent yields of adjacent isobars. An example of such a chain is $A = 93$ where the independent yields of ^{93}Rb , ^{93}Sr , and ^{93}Y as well as the cumulative yield of ^{93}Kr have been determined (Wa 65). In actual cases, one needs to measure independent yields distributed over a certain mass range, an extreme case being isotopic distribution. To correlate this type of data, Friedlander et al. (Fr 63) observed that their results could be better represented in terms of N/Z , neutron-to-proton ratio, rather than a $Z-Z_A$ plot. There are however two implicit assumptions when one uses N/Z as a parameter: (i) for any value of A , the total chain yield must be assumed to be the same in the mass range under consideration, otherwise independent yields have to be corrected, provided the mass-yield curve is defined in this region, (ii) the most probable value of N/Z , N/Z_p , has the same value for different mass chains. However, Hogan and Sugarman (Ho 69) have concluded, with the help of the data of Pappas and Hagebö (Pa 66), that isotopic dispersion

curves may be compared to classical isobaric charge dispersion curves if one corrected for the slope of the mass yield curve and the variation of N/Z_p with A . The latter correction, however, can only be performed in certain mass regions where the variation of N/Z_p is known. Miller has shown (Mi 70) that if one uses isotopic plots to get charge dispersion curves, the widths are larger than what one would observe with true isobaric plots. An alternate solution consists of choosing a mass range as narrow as possible in order to minimize the effects of the variation of N/Z_p on the width of the charge dispersion.

ii) Postulates of charge division

Various empirical prescriptions have been used in order to correlate experimental data. We will review briefly those of interest in the field of charge distribution studies. They do not constitute a theory as such but they often have been found to be useful as a way of comparing results obtained for a variety of fissile nuclei subjected to excitation energies varying from thermal excitation up to hundreds of MeV.

1) Equal-charge-displacement hypothesis (ECD)

This postulate assumes that the difference between the most probable charge Z_p of a given mass chain and the charge of the most stable isobar Z_A will be equal for the light and heavy complementary fragments:

$$(Z_p - Z_A)_l = (Z_p - Z_A)_h \quad (A.14)$$

This was suggested on empirical grounds by Glendenin et al. (Gl 51) from charge-division data for low-energy fission. This rule may be reformulated as:

$$Z_P = Z_A - \frac{1}{2} [Z_A(A_1) + Z_A(A_2) - Z_P] \quad (\text{A.15})$$

where Z_P is the charge of the fissioning nuclide.

This formulation however involves some arbitrariness as it requires calculations of Z_A , and additional prescriptions had to be used. As stated earlier, difficulties were encountered near the shells, and this fact led to a discontinuous plot of the valley of stability, as proposed by Pappas et al. (Pa 55). The postulate accounts for the observed charge division at low energy if Z_P is assumed to cross gradually from one curve $Z_P = f(A)$ to the other in the vicinity of shell discontinuities in the Z_A function.

2) Unchanged charge distribution (UCD)

If one ignores nuclear polarizability and if the nucleus is expected to divide within a time short enough so that charge rearrangements do not take place before scission, the ratio of neutrons to protons N/Z should be the same in both fragments of a pair, and identical to that of the fissioning nucleus (Go 49). The value of Z_P could be calculated using the relationship:

$$Z_P = \frac{Z_A}{A} A \quad (\text{A.16})$$

where:

Z_F = charge of the fissioning nucleus.

A_F = mass of the fissioning nucleus.

ν_T = total number of neutrons emitted by both fragments.

Among other consequences, one would expect the most probable charge division to be one where the difference between $(N/Z)_A$ corresponding to the valley of stability and N/Z of the primary fragment is larger for the light fragments than for the heavy, due to increasing values of $(N/Z)_A$ of the most stable isobar with increasing mass. This fact would translate into longer beta-emitter chains for the light fragment than for the heavy complement, a conclusion which is at variance with the hypothesis on which the ECD is based. The UCD rule has been found to hold at energies above thermal excitation if one takes into account neutron evaporation before fission.

3). Minimum potential energy (MPE)

This postulate due to Present (Pr 47) states that the nuclear charge distributes itself between fragments such that a minimum is achieved between the nuclear potential energy and the Coulomb energy. Various formulations have since been proposed (Fo 56, NÖ 66), but the calculations are all strongly dependent on the mass equations and shell corrections used. Wing and Fong (Wf 67) and Armbruster (Ar 70)

have carried out charge-division calculations based on this rule by minimizing the potential energy or maximizing the energy release of the nascent fragments in the vicinity of the scission point. This led to the prediction of chain lengths of the light fragments which are shorter than those of the heavy fragments.

iii) Previous work

Most of the charge dispersion measurements at thermal energy have been carried out by Wahl and co-workers (Wa 62, Wa 65, Wa 69, Fo 74b) who studied ^{235}U fission by thermal neutrons. Their results, along with others obtained in the thermal-neutron-induced fission of ^{233}U and ^{239}Pu and in the spontaneous fission of ^{242}Cm and ^{242}Cf have been summarized by Umezawa et al. (Um 70). The independent yields were fitted for each mass chain to a Gaussian distribution. The first results of this type of analysis showed that the width of the charge-dispersion curves thus obtained with ^{235}U were constant within experimental uncertainties and equal to $C = 0.80 \pm 0.14$ (Wa 69). The near constancy of these widths has led to the assumption of a universal charge dispersion curve applicable to all mass chains which, as a consequence, enabled a deduction of the most probable charge for any mass chain for which a single independent yield has been determined. A plot of Z_p values calculated in this fashion shows qualitatively that the light products receive a larger fraction of the available charge than would be expected if the charge-to-

mass ratio of the fissioning nucleus were preserved in the fragments (UCD). On the other hand, the Equal Charge Displacement postulate seems to account qualitatively for the observed divisions if Z_p is assumed to cross gradually from one curve to another at the points where Z_A exhibits discontinuities resulting from the shell effects. The data available for ^{233}U and ^{239}Pu thermal-neutron fission and ^{242}Cm and ^{252}Cf spontaneous fission show also a general trend consistent with the ECD postulate (Um 70). The average value of $Z_p(A_H) - Z_p(\text{UCD}) = -[Z_p(A_L) - Z_p(\text{UCD})]$ was found to be -0.44 for mass numbers 92-95 and 141-144 and -0.45 for the other mass numbers for which Z_p was determined radiochemically (Wa 69). However, caution must be exercised if one wants to calculate independent yields for all the nuclides produced in thermal fission of ^{235}U by using the "normal" distribution of Wahl. The correlation of these "normal" yields with experimental values shows an enhancement of the yields of even-Z nuclides and a depression of odd-Z nuclides, particularly in the mass region below $A_H = 134$ and above $A_L = 102$. Amiel and Feldstein (Am 74) have found even- and odd-Z yields for thermal fission of ^{235}U to be well represented by distribution 25% higher and lower, respectively, than Wahl's normal distribution. They found the neutron-pairing effect, which was expected to be as high as for protons, to be only $\pm 8\%$ in the heavy peak, and not observable in the light mass peak.

Other results obtained by physical measurements are, in general, in good agreement with the radiochemical data.

Reisdorf (Re 68) has determined the mean primary nuclear charges of fragments from thermal-neutron fission of ^{235}U by means of K X-rays measurements in coincidence with the light fragments in the mass range 88-105. The deviation from the UCD prediction was found to be 0.54 ± 0.14 charge unit, and independent of mass in the range studied. However, no closed-shell effect on the primary charge was found. This may be attributable to the fact that the structures seen in the radiochemical data are introduced by anomalies in the neutron emission rather than by the primary charge division. The effect of post-fission-neutron emission should also have repercussions on the width of the charge dispersion curves. Fragment distributions are expected to have narrower width than the products, due to the removal of fluctuations in the number of neutrons emitted. This fact has been verified by Reisdorf et al. (Re 71). They found the average charge dispersion for thermal fission of ^{235}U to be narrower, corresponding to $C = 0.40 \pm 0.05$, than that determined radiochemically after neutron emission.

The problem of charge distribution in medium-energy fission has now been the object of studies mostly with proton irradiation of various target nuclei. The McGill team has contributed a great deal to the accumulation of data in the energy range 20-85 MeV after this type of study was initiated by the work of Pate, Foster and Yaffe (Pa 58a) on the isotopic distribution of iodine produced in ^{232}Th fission by 8-87 MeV protons. This was followed by similar studies of ^{238}U fission

by Davies and Yaffe (Da 63), Parikh et al. (Pa 67), Khan et al. (Kh 70), Miller and Yaffe (Mi 70), Umezawa et al. (Um 71), Tracy et al. (Tr 72), Dikić et al. (Di 74), and Sarkar (Sa 75). Charge dispersion studies of ^{232}Th fission products have been extended to other mass regions by Benjamin et al. (Be 69), McGee et al. (Mc 71), Tracy et al. (Tr 72), and Holub and Yaffe (Ho 73). Systems like $^{235}\text{U} + \text{p}$ have been studied by Khan et al. (Kh 70), Saha et al. (Sa 71) and Tracy et al. (Tr 72), $\text{p} + ^{233}\text{U}$ by Tomita and Yaffe (To 69) and Marshall and Yaffe (Ma 73), $\text{p} + ^{237}\text{Np}$ by McGee et al. (Mc 72), $\text{p} + ^{239}\text{Pu}$ by Saha and Yaffe (Sa 70). Studies utilizing different projectiles have been carried out by McHugh and Michel (Mc 68) who investigated charge distribution resulting from the fission of ^{232}Th by 20-57 MeV alpha particles, and Choppin et al. (Fr 68a, Fr 68b) with ^{232}Th and ^{238}U irradiated with 9.5 to 11.5 MeV deuterons. The results obtained at McGill up to 1969 have been summarized by Yaffe (Ya 69).

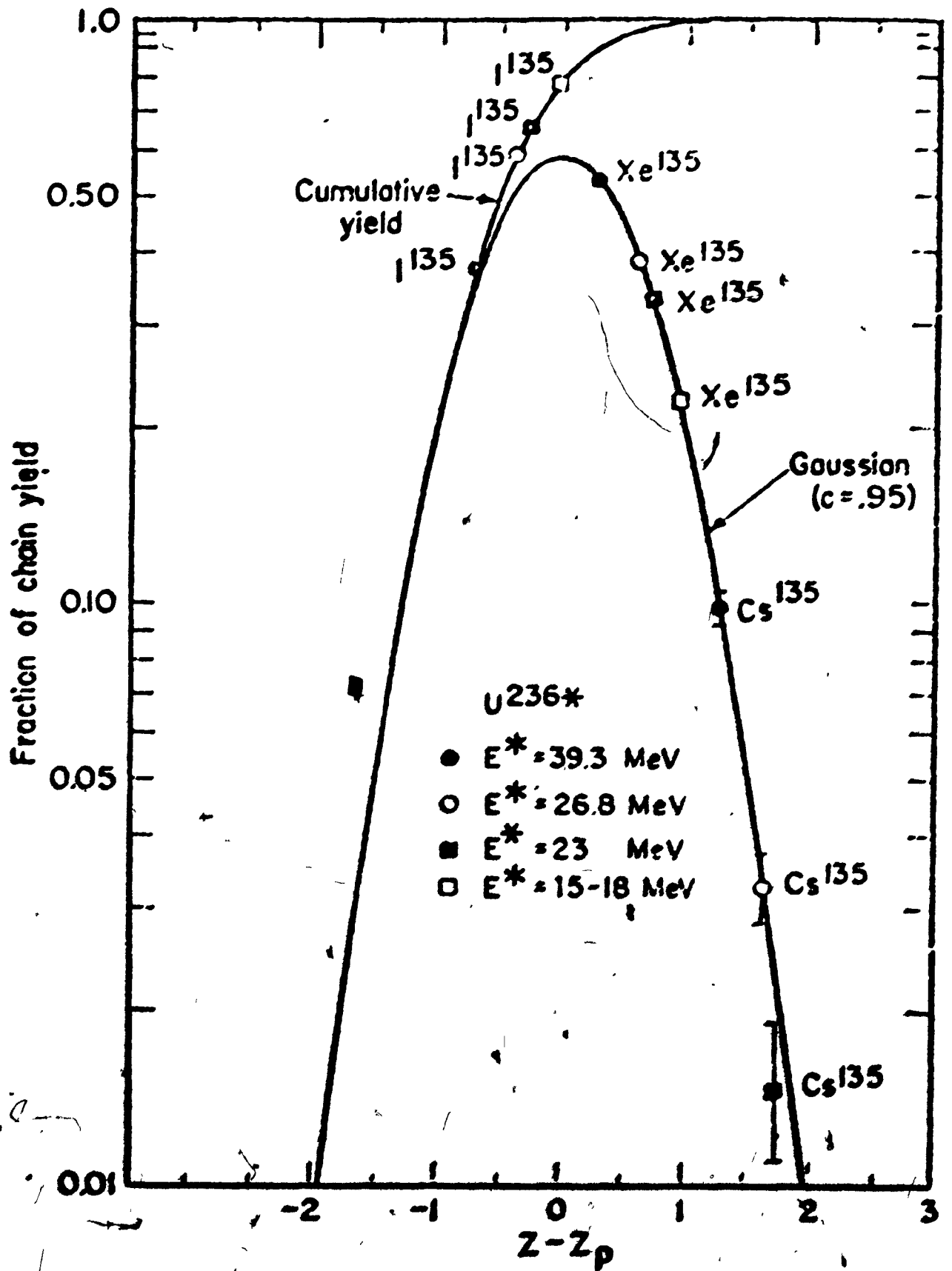
The charge-dispersion curves plotted using the cross-sections against N/Z of the corresponding products, rather than $(Z-Z_A)$ to avoid shell-edge discontinuities, show the following trends:

- 1) The position of the peak of the charge-dispersion curves shifts towards beta-stability with increasing incident energy, due to neutron-emission from the fissioning nucleus and the fission fragments as well. One notices however different behaviours in the light-mass and the heavy-mass region, the variation of Z_p being more ac-

centuated for the heavy products than for the light. For ^{238}U , Khan et al. (Kh 70) report a variation of Z_p of 0.47 charge unit in the vicinity of $A = 96$ as compared to 0.65 charge unit for $A = 135$ (D1 74). In the symmetric-mass region, Sarkar (Sa 75) found a variation of Z_p intermediate between these two.

- 2) The full width at half maximum (FWHM) of the curves obtained in the heavy-mass region remain essentially constant with increasing energy up to 40-45 MeV with ^{238}U and ^{232}Th (see Fig. 7) whereas there is a regular increase with targets of lower N/Z values. Above 45 MeV, full-width at half-maximum (FWHM) increases regardless of the target. Light-mass products on the other hand display FWHM which increase very slightly with energy (Ma 73) or do not vary (Mc 72) within the 20-85 MeV energy range. For the same target and bombarding energy, the charge dispersion appears to be larger for light-mass products, as for example FWHM = 2.9 Z units for $A = 96$ (Ma 73) as compared to 2.5 Z units for $A = 130-134$ (To 69) at 50 MeV for ^{233}U .
- 3) Effect of target composition: in the heavy mass region, the displacement of the most stable charge from stability shows a marked dependence on the neutron-to-proton ratio of the target, the higher the N/Z of the target, the larger the $(Z_A - Z_p)$ of the products for the same bombarding energy. For the light mass products, the $(Z_A - Z_p)$ values obtained for ^{235}U , ^{238}U and ^{232}Th do not show significant

FIGURE 7: Gaussian charge-distribution curve that best fit the fractional yield data of the mass-135 chain resulting from the ^4He -induced fission of ^{232}Th . After McHugh and Michel (Mc 68).



differences. This observation suggests that the variation introduced by differing targets is absorbed by the heavy fission fragment. In the case of FWHM, it is not clear whether there is any systematic correlation or not, between the experimental values obtained at a given bombarding energy for different targets, except that the data for ^{235}U are consistently smaller than those of ^{233}U , ^{238}U , ^{239}Pu , ^{232}Th , and ^{237}Np .

The values of Z_p deduced from charge-dispersion curves have been compared to those calculated using the various postulates described in the preceding section. In general, the experimental Z_p cannot be reproduced by either the ECD or the UCD rule, but lie in between those expected on the basis of these postulates. In the case of ^{239}Pu a very good agreement with the UCD mechanism was observed for $A = 136$. However, it has been pointed out (Sa 70) that, because of the assumptions involved as to how the excitation energy is shared between the fragments, it is very difficult to identify the mechanism on the basis of such an agreement. If one assumes that the heavy fragment receives 1.5 times the excitation energy it would normally receive in proportion to its mass, the experimental values no longer agree with either postulate but lie closer to ECD. Recently, Tracy et al. (Tr 72) have claimed on the basis of their result at 40 MeV and 60 MeV on ^{238}U that the mechanism of charge division is not markedly different from that operating at thermal energies, i.e. ECD. Lee et al. (Le 75) have also concluded that their

results at 80 and 100 MeV were consistent with ECD.

c) Neutron emission in fission

As we have already seen, the fission of a heavy nucleus is always accompanied by neutron emission. At thermal energies and in spontaneous fission, initially there is a unique excited nucleus which decays predominantly by fission. The emitted neutrons are those resulting from the break-up of the excited nucleus (scission neutrons) and those subsequently evaporated during the de-excitation of the fragments. These two categories of neutrons constitute the post-fission neutrons.

One of the most interesting aspects of neutron emission is the striking variation of neutron yields as a function of fragment mass. Since the neutrons are emitted from fully accelerated fragments, there is a strong angular correlation between the two. This makes possible an experimental determination of the neutron yield as a function of fragment mass. The first evidence for a structure in the dependence of neutron yield on fragment mass was obtained by Fraser and Milton (Fr 54) for neutron fission of ^{233}U . Their study revealed that the number of neutrons emitted by two complementary fragments are unequal, most of the neutrons being emitted by the heavier light fragments and by the heavier heavy fragments and that there is a considerable variation in neutron yield through each peak of the mass distribution. The total neutron yield shows also, but to a much lesser

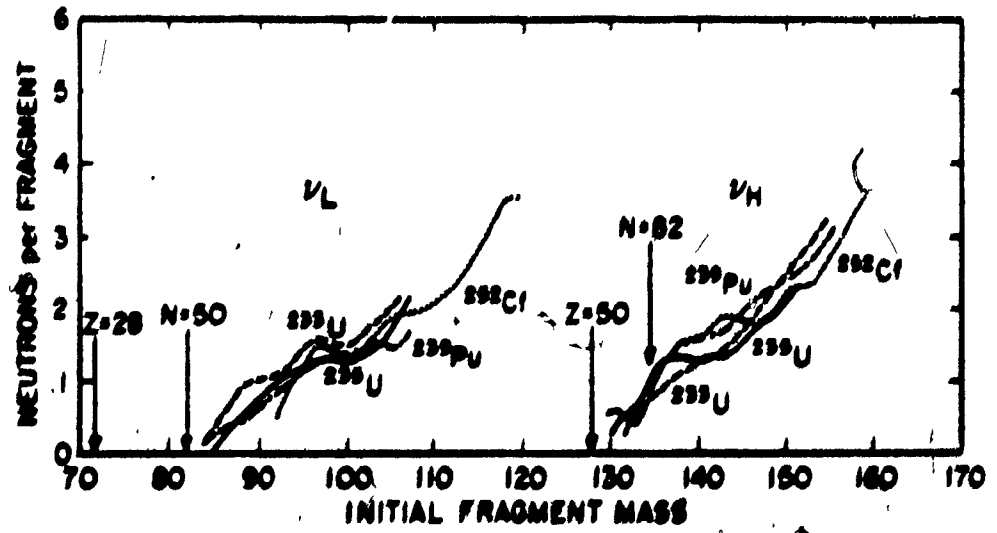
extent, a dependence on mass ratio.

The dependence of neutron yield on mass ratio may also be determined by a comparison of initial (primary fragments) and final (products) mass yields. This type of study has been carried out by Terrell (Te 65) for ^{233}U , ^{235}U , ^{239}Pu , and ^{252}Cf (see Figure 8a). The similarity of the neutron yields for a given fragment originating from these different systems has led Terrell to the conclusion that the neutron yields are closely related to the deformabilities of the nascent fragments. The low yields at $Z = 60$ and $N = 50$ may be explained by the fact that closed-shell nuclei are resistant to deformation and hence the fragments will evaporate less neutrons as a consequence of deformation energy being converted into excitation energy.

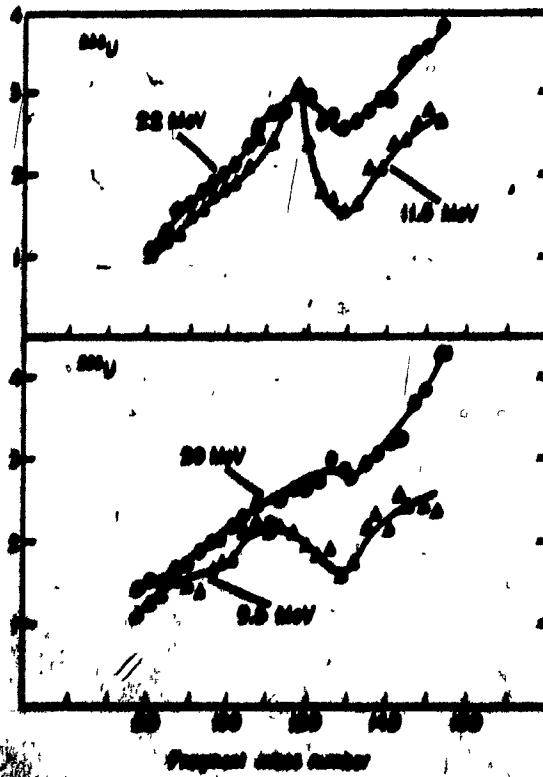
The strong saw-toothed variation of neutron yield versus fragment mass vanishes rapidly with increasing excitation energy as shown by Burnett et al. (Bu 71) for 8.5 and 13-MeV proton-induced fission of ^{233}U and Bishop et al. (Bi 70) for 11.5 and 22-MeV proton-fission of ^{238}U . The largest change occurs near mass 130, the trend being to wash out the dip in the neutron-versus-fragment-mass curve with increasing excitation energy (Fig. 8b). If fragment shells are responsible for the low neutron yields around mass 130 at low excitation energy, then this trend is consistent with other observations that shell effects tend to disappear with increasing excitation energy, thus causing the number of neutrons emitted by a fragment to follow the linear increase

FIGURE 8a: Neutron yields as a function of fragment mass for four types of fission as determined from mass-yield data. The approximate initial fragment masses corresponding to various magic numbers are shown. After Terrell (Te 62).

FIGURE 8b: Dependence of neutron yield on fragment mass for proton-induced fission of ^{233}U and ^{238}U . The incident proton energy is indicated for each curve. After Bishop et al. (Bi 70).



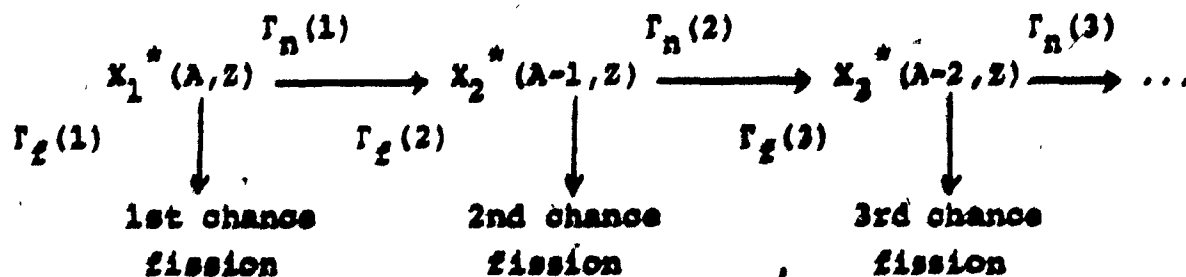
- 21 -



- b -

with mass predicted by the liquid-drop calculations of Nix and Swiatecki (Ni 65). It is also interesting to note that, essentially, the increase in excitation energy manifests itself in the heavy fragment, this being probably due to the fact that it receives a more equal share of the deformation energy at scission configuration

When fission is induced by a projectile whose interaction with the target nucleus gives rise to excitation energies beyond the binding energy of the last neutron, de-excitation may occur by means of neutron emission prior to the fission act (pre-fission neutrons). Let us consider at this point cases where the incident particle is captured and where excitation energies are sufficiently low so that proton emission may be neglected as a result of the Coulomb barrier. The decay of the compound nucleus $X_1^*(A, Z)$ may be schematized as follows:



In this de-excitation chain, the initial nucleus can either fission or emit a neutron to give $X_2^*(A-1, Z)$. Depending on its excitation energy, X_2^* can again undergo a similar process. At each step of the chain, fission will compete with neutron evaporation until the residual excitation energy falls

below the binding energy of the last neutron, at which point fission or γ -ray emission become the only alternate means of de-excitation. The relative probabilities of fission and neutron emission are given respectively by Γ_f and Γ_n , fission and neutron widths. Huizenga and Vandenbosch (Hu 62) have derived an analytical expression for the value of the fission branching ratio $G = \Gamma_n/\Gamma_f$ based on the Fermi-gas model of the nucleus:

$G =$

$$\frac{2\pi r_0^2 g}{h^2} \frac{4A^{2/3} a_f (E - B_n)}{a_n [2a_f^{1/2} (E - E_f)^{1/2} - 1]} \exp[2a_n^{1/2} (E - B_n)^{1/2} - 2a_f^{1/2} (E - E_f)^{1/2}] \quad (A.17)$$

where:

- A is the mass of the nucleus
- r_0 the nuclear radius parameter
- a_n and a_f the level-density parameters at equilibrium deformation and at the saddle point
- E_n and E_f the neutron binding energy and the fission threshold
- m the mass of the neutron
- g the spin degeneracy of the neutron
- E the excitation energy
- and B_n the binding energy of the neutron.

From this expression, one can see that the magnitude

of the variation of Γ_n/Γ_f with excitation energy is directly related to the difference between E_f and E_n and the relative values of a_n and a_f . The excitation energy dependence of Γ_n/Γ_f becomes very difficult to investigate when the fission threshold and the neutron binding energy are approximately the same, like in heavy nuclei. Although a strong excitation energy dependence of Γ_n/Γ_f for the less fissionable elements has been observed, and there is evidence for the heavier nuclei that there are smaller variations at low energies which correlate with the difference $(E_f - E_n)$, the excitation energy dependence of Γ_n/Γ_f for the heavier elements at higher energies is rather unclear. A number of results indicate that Γ_n/Γ_f for the heavier elements does not vary much with excitation energy.

The relative probabilities of fission and neutron emission can also be determined by radiochemical measurements. The method consists of measuring radiochemically the reaction yield of the nuclides near the target nucleus, thereby determining the cross section for the reaction which did not involve fission throughout all stages of the de-excitation process. Studies of this kind have been made by Lindner and Turkevitch (Li 60) for 340-MeV protons on ^{232}Th and ^{238}U , by Lafort, Simonoff, and Tarrago (Le 61) for 82-MeV and 150-MeV protons on ^{232}Th , by Pate and Poskanzer (Pa 61a) for 680-MeV and 1.8-GeV protons on ^{232}Th , ^{235}U , and ^{238}U .

When fission is induced in heavy nuclei by high energy (> 100 MeV) protons, the reaction takes place in two

stages. In the first stage, the incident particle interacts with a single nucleon in the struck nucleus, due to the fact that the associated wave length is of the order of the inter nucleonic distance (See 47). The partners of this collision may make more collisions with other nucleons and a nucleonic cascade is developed, whose exact nature depends on the probability and the kinematics of each collision. At incident energies above the pion production threshold, inelastic collisions must also be considered and will have an appreciable effect on the propagation of the cascade. There is a fairly high probability that many of the cascade nucleons and pions will escape from the nucleus. The generation of such a cascade may be computed by the Monte-Carlo method in a rather straightforward manner since the impulse approximation allows one to use elementary particle scattering data as input information. Each nucleon-nucleon collision is characterized by its own probability distribution for occurrence, energy, and angular distribution of the collision partners, and cross section for pion production. A random choice is made at every point in the calculation where a decision must be made, as for example the position of the first collision partner and the choice of a neutron or a proton as a collision partner. If each random choice is weighted according to its probability of occurrence, and if a large number of events are calculated, the net result should be characteristic of the overall process. In particular, such a method allows for the calculation of the average excitation energy of the cascade nuclei. Calculations

of this type have been performed for the system $^{238}\text{U}+p$ with the aid of the code of Metropolis et al. (Me 58) and more recently the STEPNO code of Chen et al. (Ch 68).

The emission of neutrons in the fast intranuclear cascade is not believed to be related to the subsequent fission process and the de-excitation of the cascade nucleus proceeds as described at the beginning of this section.

In addition to the experimental methods mentioned previously, there is another type of experimental measurement from which one can deduce information about Γ_n/Γ_p . It consists in the determination of the relative numbers of prefission and postfission neutrons from the angular correlation of the neutrons with respect to the fragment direction. The prefission neutrons are essentially isotropic with respect to the fragment direction, while the postfission neutrons are strongly correlated with the fragment direction. This technique has been applied to proton-induced fission of ^{238}U at 155 MeV by Cheifetz et al. (Ch 70b). They concluded that the nearly equal fraction of prefission and postfission neutrons is inconsistent with the assumption that Γ_n/Γ_f is independent of excitation energy but is qualitatively consistent with the energy dependence given by Eq. (A.17).

VII. PURPOSE OF THE PRESENT STUDY

The present investigation was undertaken in order to extend the work on energy dependence of charge distribution

in the fission of ^{238}U by protons of 20-85 MeV to the heavy side of the mass distribution (rare-earth region of fission products).

Previous studies on ^{238}U have been carried out in this laboratory by Khan et al. (Kh, 70), Sarkar (Sa 75), Miller and Yaffe (Mi 73), Dikšić et al. (Di 74) and Parikh et al. (Pa 67), involving respectively fission products in the following mass regions: $A = 90-93$, $111-117$, $122-131$, $130-135$ and $139-143$. With the exception of the work of Umezawa (Um 71) in the energy range 13-55 MeV, there has been very little experimental data in the mass region beyond $A = 143$, this situation being partly due to the fact that the complete radiochemical separation of individual rare-earth-fission products calls for delicate and lengthy operations often incompatible with the short half-lives encountered in this mass region. The advent of high-resolution Ge(Li) detectors has now made possible the use of simplified chemical procedures where rare-earths can be separated as a group and information on separate nuclides can be extracted on the basis of their decay properties. This method has been utilized in the present dissertation to study fission products covering the mass region 146-157.

We have determined the independent formation cross-sections of ^{146}Pr , ^{148}Pr , ^{149}Pr , ^{150}Pr , ^{151}Pr and the cumulative formation cross-sections of ^{146}Ce , ^{146}Pr , ^{147}Nd , ^{149}Nd , ^{149}Pr , ^{151}Nd , ^{151}Pr , ^{152}Sm , ^{155}Sm , ^{156}Sm , ^{157}Eu . The

independent cross sections were used to construct charge-dispersion curves while the cumulative cross sections have been useful in providing a better definition of the heavy wing of the mass distribution in the 20-85 MeV range.

One of the main purposes of this study was to verify if the narrow widths of the charge distribution curves previously reported by Parikh (Pa 67) for $A = 139-143$ are typical of very asymmetric fission events, a fact which might not be consistent with increased neutron evaporation in the heavier wing. It was also of interest to see if the behaviour of the most probable charge followed similar trends as those observed in lighter heavy products.

B. EXPERIMENTAL PROCEDURES

I. PREPARATION OF TARGETS

The target material used consisted of uranium foils of natural composition (99.28% ^{238}U). The thicknesses used varied depending on the type of experiment performed. For irradiations, where long-lived nuclides (i.e. with half-lives greater than one hour) were studied, a thickness of 134 mg/cm² was used. Whenever shorter half-lives were investigated, a smaller thickness of 54 mg/cm² was utilized, the reason for that being two-fold. Firstly, the chemical separations needed to be performed in a minimum amount of time and the use of a thinner target reduces significantly the time necessary for its dissolution. Secondly, the counting rates resulting from the whole group of rare earths are usually quite high, especially when short-lived nuclides are still present. A smaller superficial density will result in a lower activity level which is preferable in view of the possible dead-time losses during activity measurements.

Prior to irradiation the uranium foils were cleaned in dilute HNO_3 in order to remove the oxide layer and sequentially rinsed with distilled water, ethanol, and acetone. The foils were dried under vacuum at room temperature in order to prevent further oxidation. Thicknesses were determined by weighing a known area prior to the preparation of the targets. A foil of natural copper (20.9% ^{65}Cu) of 99.99% purity was used in order to monitor the proton beam by means of the

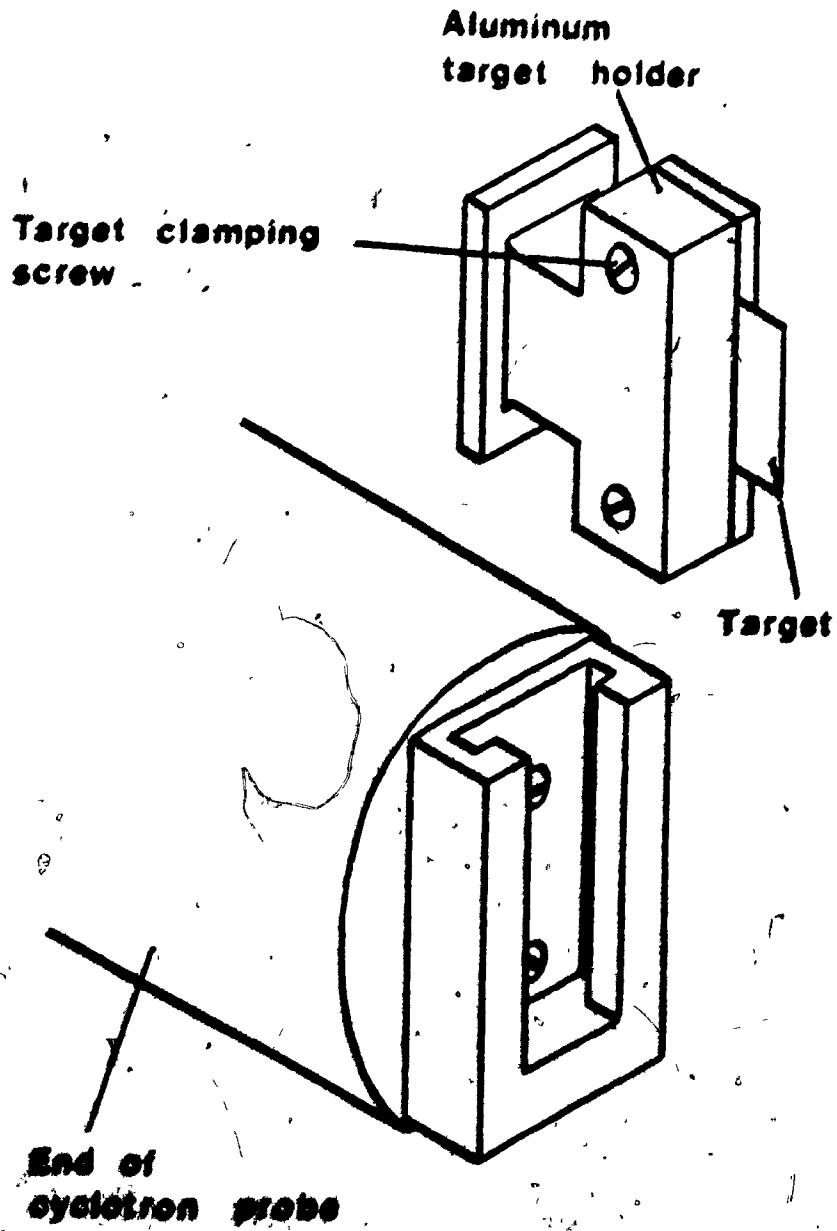
reaction $^{65}\text{Cu} (p, pn) ^{64}\text{Cu}$. A superficial density of 44 mg/cm^2 was used throughout the series of irradiation.

The target assembly consisted of a stack of five foils:

- the uranium target sandwiched between two similar foils whose role is to compensate for recoil losses inside the master target.
- one copper monitor target. The recoil losses in the monitor foil were considered to be negligible so that there was no necessity of sandwiching it between two foils of the same material.
- an aluminum foil separating the copper and uranium targets in order to prevent the former from contamination by fission products.

The 5-foil assembly was carefully trimmed with scissors on three sides in order to insure equal exposure to the proton beam in the copper and uranium targets. The stack was clamped in a target holder of the model shown in Figure 9 and wrapped with a 10 mg/cm^2 thick aluminum foil which acted as an absorber of fission products to avoid contamination of the cyclotron chamber. The target assembly was then attached to the end of the water-cooled probe of the cyclotron (Fig. 9).

FIGURE 9: Target assembly and end of cyclotron probe.



II. IRRADIATIONS

The target bombardments were carried out at the McGill synchrocyclotron at the Foster Radiation Laboratory at energies ranging from 20 to 85 MeV. The irradiations were performed using the internal beam at energy intervals of 5 MeV or 10 MeV, depending on the nature of the fission products being investigated. The incident energy was determined by setting the leading edge of the target assembly at a proper radius with the help of the energy-versus-radius calibration data provided by the Foster Radiation Laboratory team (Po 64). The foil stack was placed in such a way that the copper-monitor foil was the first to intercept the proton beam in order to be bombarded exactly at the nominal energy [the excitation functions of (p,pn) reactions are more sensitive to small energy changes than that of fission products]. The beam-energy degradation inside the target assembly was calculated using the table of Williamson and Boujot (Wi 62). At 20 MeV, where the degradation is at a maximum, it was calculated to be 0.70 MeV in the copper foil, 0.20 MeV in the aluminum catcher and 0.55 MeV and 1.40 MeV in each of the uranium foils used, corresponding to an overall degradation of 1.65 MeV and 2.50 MeV at the level of the master target. These values are well within the uncertainties in the nominal bombarding energy resulting from uncertainties in radius estimation. A value of ± 2 MeV was adopted all throughout the bombarding energy

range.

The duration of irradiations was dependent on the half-lives and the fission yields investigated. They lasted for example 30 minutes in the case of ^{148}Pm , ^{150}Pm determinations and 5 minutes when ^{146}Ce was the product of interest.

III. CHEMICAL PROCEDURES

a) Separation of rare earths

i) General

The most elegant technique for the separation of rare earths from a mixture of fission products is the isolation of the lanthanides as a group by solvent extraction, followed by an individual separation by ion exchange. Among the selective extractants capable of separating tripositive rare-earth ions from other elements, the monoacidic organo-phosphorus compounds, among which bis(2-ethylhexyl)phosphoric acid (HDEHP), have received the most attention (Ko 69). During the extraction process, one hydrogen in the weakly acidic extractant is replaced by a metal ion and the reaction is mainly ionic. As a consequence, this process is efficient only if performed in a weakly acidic medium and requires rather stringent pH conditions (0.01N HCl or HNO_3). In the present work, the dissolution of the uranium targets necessitates the use of strong acids and consequently the strongly acidic solution of fission products does not lend itself to treatment by HDEHP unless one is prepared to include a time-consuming pH adjustment

step. Secondly, NDENP has proved efficient only in cases of carrier-free separations, a fact which rules out the use of a carrier for chemical yields determination and obtaining a final solid sample.

The chemical procedure adopted here is based essentially on the method of Nume and Martens (Nu 51). The rare-earth group is isolated by fluoride precipitation in the presence of zirconium, strontium and barium hold-back carriers, and purified by several cycles of hydroxide precipitations. This method which has shown itself to be selective enough when activity measurements are carried out by γ -activity measurement is however not recommended for the estimation of rare-earth activities by β -counting. As stated previously, the use of high resolution γ -spectrometry has made possible the choice of such a simplified procedure without encountering major problems of contamination by foreign elements. The time necessary to run a separation is only ~ 40 minutes, which allows, in particular, the detection of 24.2-m ^{146}Pr and 22.2-m ^{155}Sm , the shortest half-lives investigated in this series of experiments. Yttrium, which exhibits a similar chemical behaviour, is also co-precipitated. However, yttrium isotopes produced in medium-energy fission of ^{238}U are mostly β^- emitters and the prominent γ -rays, i.e. the 202-keV and 482-keV γ -line of $^{90\text{m}}\text{Y}$, 551-keV γ -line of 49.7-m $^{91\text{m}}\text{Y}$ and 267-keV γ -line of 10.2-h ^{93}Y do not interfere with the selected γ -rays emitted by the rare-earth group. Furthermore, the

difference in half-lives precludes the possibility of a wrong assignment. Therefore, no separation of yttrium from the lanthanides was attempted, in view of the fact that this additional step would have involved repeated precipitations or the inclusion of a time-consuming cation-exchange separation.

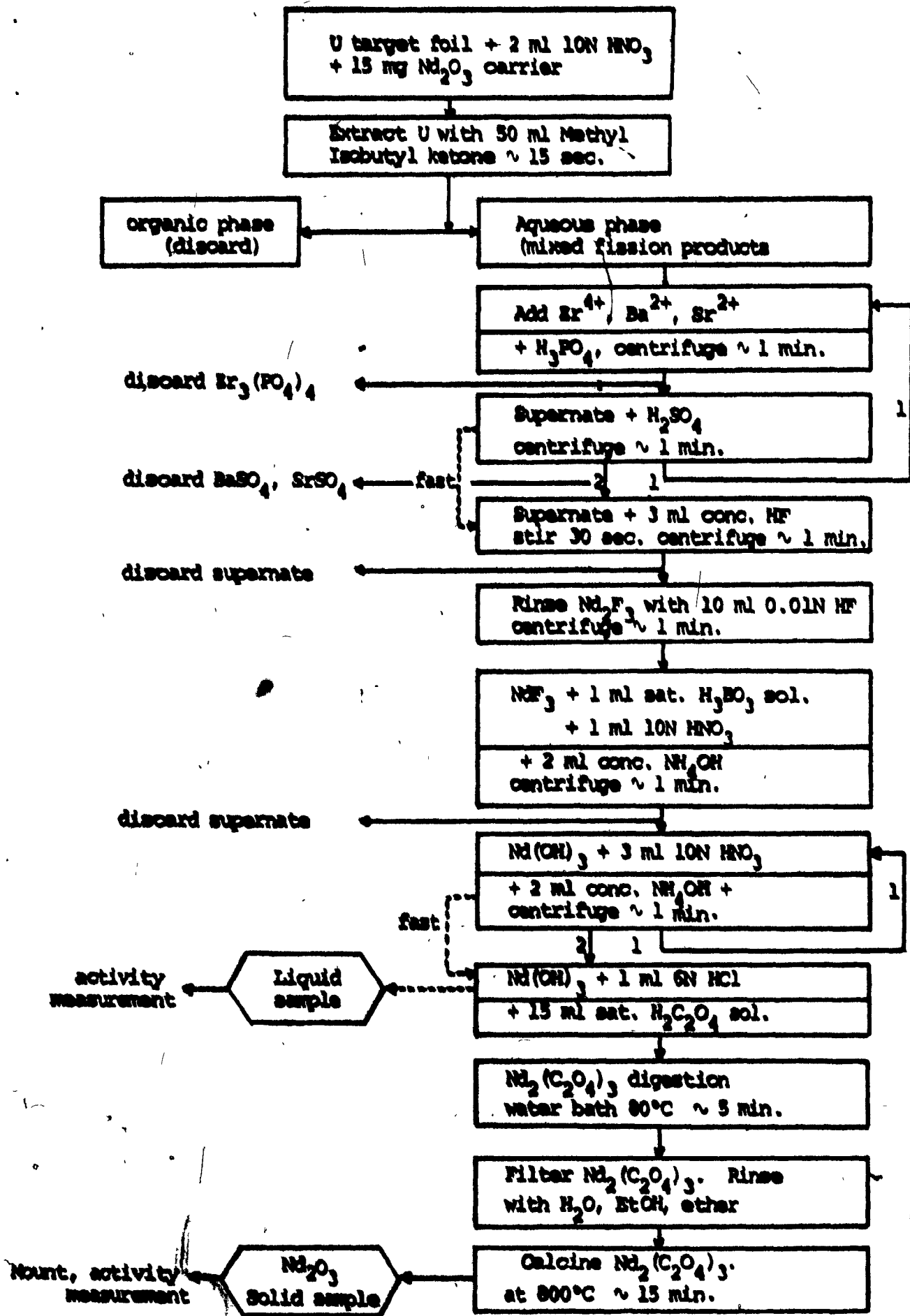
ii) Procedure

Neodymium was chosen as the carrier common to all the rare-earths investigated in this work (Pr to Eu) on the basis of the fact that the solubility products of the fluorides and hydroxides of adjacent elements do not differ greatly, as reported by Stevenson and Nervik (St 61b).

To the target solution in 10N HNO₃, 1 ml of 15 mg Nd₂O₃/ml of standardized carrier solution was added. The mixture was boiled for 1 minute and adjusted to a volume of 10 ml by further addition of 10N HNO₃. The solution was then transferred to a 150-ml separatory funnel containing 50 ml of hexone previously equilibrated with 10N HNO₃ to extract the bulk of uranium prior to the first precipitation. The aqueous solution was shaken for 15 seconds, then was transferred to a 40-ml centrifuge tube containing 1 ml each of 10 mg/ml of Ba(NO₃)₂, Sr(NO₃)₂·4H₂O, and Zr(NO₃)₂·2H₂O solution acting as hold-back carriers. Zr₃(PO₄)₄ was precipitated by addition of 5 drops of concentrated H₃PO₄ to remove zirconium activities which otherwise would be extensively precipitated during the subsequent fluoride precipitation

step. The solution was centrifuged, the supernate transferred to a second test tube, and BaSO_4 and SrSO_4 were precipitated with 5 drops of concentrated H_2SO_4 . After centrifugation, the phosphate and sulphate scavengings were repeated. The resulting solution was then transferred to a 40-ml Teflon tube and treated with 3 ml of concentrated HF. The fluoride suspension was stirred for 30 seconds, centrifuged for 2 minutes and the supernatant discarded. NdF_3 was rinsed with 10 ml of 0.1N HF solution, then dissolved with 1 ml of H_3BO_3 and 1 ml of 10N HNO_3 , and adjusted to 10 ml with distilled water. $\text{Nd}(\text{OH})_3$ was subsequently precipitated with 2 ml of concentrated NH_4OH solution, centrifuged and then dissolved in 3 ml of 10N HNO_3 . The hydroxide precipitation was repeated twice and the final precipitate dissolved in 1 ml of 6N HCl . The solution was diluted to 10 ml with distilled water, 15 ml of saturated $\text{H}_2\text{C}_2\text{O}_4$ were added and the solution was heated in a water bath for 5 minutes to help coagulate the $\text{Nd}_2(\text{C}_2\text{O}_4)_3$ precipitate which forms. The precipitate was transferred on to a No:42 Whatman filter, sequentially rinsed with distilled water, ethanol, and ether and calcinated at 800°C for 15 minutes. Nd_2O_3 was cooled and powdered with a glass rod and the powdered Nd_2O_3 was then transferred with ethanol on to a weighed glass fiber filter circle 2.4 cm in diameter fitted on a ground-off Hirsch funnel set-up. The wall of the chimney was rinsed with ethanol and ether. Nd_2O_3 was dried at 110°C for 10 minutes, cooled, weighed, mounted on a cardboard sample

**FIGURE 10: Radiochemical group-separation of rare-earths.
Flowchart.**



holder and covered with Mylar for gamma ray measurements. The measured chemical yields were of the order of 50-70%.

iii) Rapid group separation

The study of 12.4-m ^{151}Nd required a more rapid chemical separation than the one outlined in the preceding paragraph. In particular, it appeared that if liquid samples could be prepared, the sample preparation time could be reduced considerably. The procedure adopted in this case was similar to the general group separation with, however, a single zirconium and barium-strontium scavenging cycle as well as a single $\text{Nd}(\text{OH})_3$ precipitation. The hydroxide precipitate was dissolved with 10 ml of 6N HCl and rapidly transferred to a 20 ml glass bottle which was immediately sealed and used as the final sample for activity measurements. This method is also described in Figure 10. This rapid procedure thus enabled the first activity measurements to be taken ~ 20 minutes after the end of irradiation, this time interval including the transfer from the cyclotron to the location of measurement. The bottles were positioned and held in place with a plastic holder which centered the bottles with respect to the detector.

In this series of measurements, the activities of ^{151}Nd were measured against those of ^{149}Nd which played the role of an internal monitor.

iv Validity check of neodymium used as a common carrier

The separation described in section a.ii) assumes that the chemical yield of neodymium determined by gravimetry is applicable to all the rare-earths involved. However, the slightly higher water solubility of $\text{Pr}(\text{OH})_3$ (2.7×10^{-20}) as compared to that of $\text{Nd}(\text{OH})_3$ (1.9×10^{-21}), $\text{Sm}(\text{OH})_3$ (6.8×10^{-22}) and $\text{Eu}(\text{OH})_3$ (3.4×10^{-22}) [units are gram molecules per 10^6 liters] might be responsible for small differences in yields. Also, no quantitative data exist on the solubility of rare-earth fluorides and, in the case of promethium, no measurements have been carried out on macro quantities for both compounds.

Tracer experiments have been carried out using the following nuclides prepared by proton bombardment of natural Nd_2O_3 : 2.68-h ^{150}Pm by (p,n) reaction of ^{150}Nd (3.6%), 2.46-h ^{141}Nd by (p,pn) reaction and 2.04-h ^{138}Pr by (p,2p2n) reaction on ^{142}Nd (27.1%). The bombardment was carried out at 50 MeV where these nuclides are produced in comparable amounts.

Four aliquots of the tracer solution were subjected to a complete group-separation. The final Nd_2O_3 was then transferred to a 20 ml bottle, dissolved in 10 ml of HNO_3 and activity measurements were performed on the liquid samples. Two aliquots of the tracer solution were used as reference samples and their activity measured under the same geometric conditions. The decay of the three nuclides was followed and their respective activities at the end of bombardment was determined by standard procedures. The activity ratios show

that:

- the ratio of $^{150}\text{Pm}/^{141}\text{Nd}$ activities is equal, within statistical uncertainties, in both the reference and the processed samples.
- the ratio of $^{138}\text{Pr}/^{141}\text{Nd}$ activities is $\sim 3\%$ lower in the processed samples than in the unprocessed. This corresponds to a depletion in praseodymium which might be due to differences in hydroxide and/or fluoride solubilities, and/or the fact that Pr^{3+} ions have a larger ionic radius as compared to that of heavier rare-earths because of the contraction of the size of the aqueous ions with increasing nuclear charge. In subsequent chemical yield calculations, this correction was applied to Pr yields, while those of Pm to Eu were taken equal to that of neodymium.

In the case of the fast group separation, which involves less precipitation-dissolution cycles, no significant difference was observed between yields.

b) Separation of cerium

1) Procedure

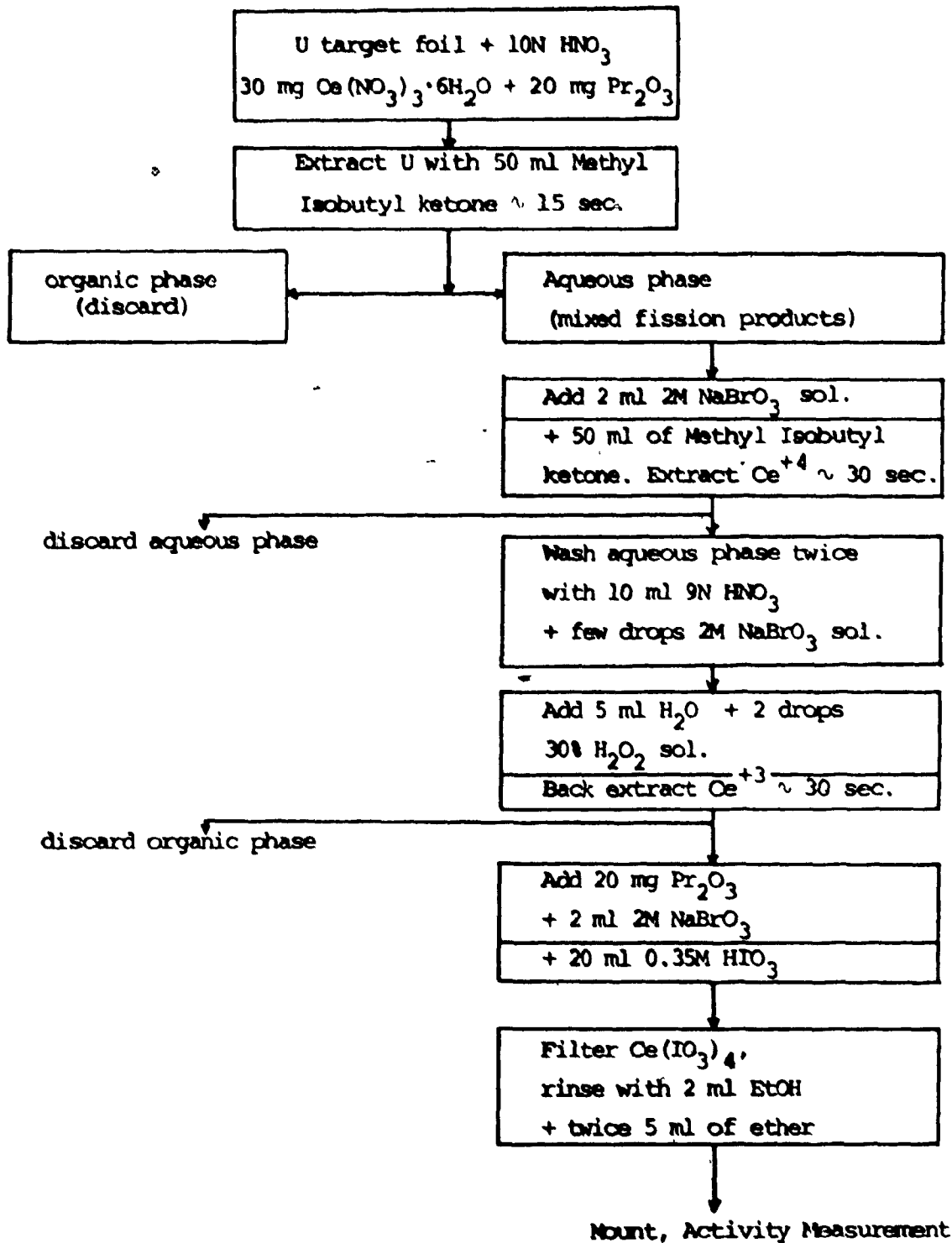
A rapid separation method, essentially based on the procedure of Glendenin et al. (Gl 55) was used in order to isolate in a short time $14.2\text{-m } ^{146}\text{Ce}$ from the bulk of

fission products and the other rare earths. The procedure makes use of the fact that cerium, unlike the other trivalent rare earths, is easily oxidized into Ce^{+4} and that Ce^{+4} may be selectively extracted from strong nitric acid media by methyl isobutyl ketone. The chemical separations were performed at the Foster Radiation Laboratory, immediately following the irradiations. The uranium targets were dissolved in a minimum amount of preheated 10N HNO_3 , preferably to HCl in order to avoid the presence of chloride ions which might hamper the subsequent oxidation of cerium. The solution was carefully boiled to dryness after addition of 1 ml of standardized cerium carrier solution (30 mg $Ce(NO_3)_3 \cdot 6H_2O/ml$) in order to promote exchange between the carrier and radioactive cerium. The solid residue was dissolved with 1 ml of praseodymium hold-back carrier solution (20 mg Pr_2O_3/ml) and adjusted to a volume of 10 ml by addition of 10N HNO_3 . The solution was transferred to a 150-ml separatory funnel containing 50 ml of methyl isobutyl ketone previously equilibrated with 10N HNO_3 and shaken for 15 seconds. This step, prior to cerium oxidation, has been included in order to free the solution from uranium which otherwise might follow cerium and contaminate the final cerium sample with weighable amounts. The aqueous solution was transferred to a second separatory funnel containing 2 ml of 2N $NaBrO_3$ solution acting as the oxidizing agent. This was followed by the addition of 50 ml of methyl isobutyl ketone pretreated with

10M HNO_3 and the mixture was shaken for 30 seconds. The time at the middle of this step was recorded and taken as that of separation of cerium from the other fission products. The aqueous phase was discarded and the organic phase was washed twice with 10 ml of 9M HNO_3 containing a few drops of sodium bromate solution. Cerium was then back-extracted in the form of Ce^{+3} by shaking the methyl isobutyl ketone with 5 ml of water containing 2 drops of 30% H_2O_2 solution which reduces Ce^{+4} into Ce^{+3} and the aqueous solution was transferred to a 50-ml centrifuge tube.

The procedure of Glendenin calls finally for a precipitation of cerium oxalate which may be used as the chemical form in which the final sample is mounted for activity measurements. However, this step is quite time consuming as it requires warming of the solution and a 5 minutes digestion of the precipitate. It was found more convenient to include as a final step of reoxidation of Ce^{+3} into Ce^{+4} followed by a precipitation of cerium as cerium iodate, after the method of Boldridge and Hume (Bo 51). Apart from being faster than the oxalate precipitation, this step introduces an additional oxidation cycle which improves decontamination from the other rare earths. The solution of Ce^{+3} , after the H_2O_2 reduction, was treated with 2 ml of 2N NaBrO_3 solution in the presence of 20 mg of Pr_2O_3 hold-back carrier and 20 ml of 0.35N HIO_3 were added. The $\text{Ce}(\text{IO}_3)_4$ precipitate forms instantly. The solution was centrifuged and the supernate discarded. The

FIGURE 11: Radiochemical separation of cerium. Flowchart.



precipitate was washed with 2 ml of EtOH and filtered with suction on a No:42 Whatman ashless filter paper attached to a ground-off Hirsch funnel. The cerium iodate was finally rinsed twice with 5 ml of ether and mounted immediately on a cardboard sample holder covered with 1.75 mg/cm^2 Mylar. In this procedure, the time elapsed between the end of irradiation and the final ceric iodate precipitation was 5-6 minutes typically.

Chemical yield determinations were carried out by a gravimetric method after the activity measurements were completed. The Mylar cover was carefully removed from the sample and rinsed with EtOH, the rinsings being recovered in a previously weighed porcelain crucible. EtOH was evaporated under an infra-red heat lamp and the sample was transferred to the crucible. $\text{Ce}(\text{IO}_3)_4$ was ignited for 1 hour at 800°C and cerium was weighed as CeO_2 using a precision balance. The chemical yield ranged between 60% and 80%.

ii) Praseodymium-cerium decontamination

In this work, the inclusion of a separate chemical separation for cerium was undertaken in order to determine the cumulative cross-section of ^{146}Ce whose knowledge, combined with that of the cumulative cross section of ^{146}Pr determined from the group separation described in the preceding paragraph, will lead to an estimation of the independent cross section of ^{146}Pr . The chemistry used here was originally devised for

the separation of 284.4-days ^{144}Ce from fission products after short-lived activities, such as those of praseodymium isotopes in particular, had decayed. In this work, 24.2-m ^{146}Pr is present at each step of the separation, either as a directly formed fission product or as the decay product of ^{146}Ce . In order to avoid additional uncertainties on ^{146}Pr independent cross-sections resulting from the use of two different decay schemes, ^{146}Ce activities were determined via the activity of the decay product ^{146}Pr . It was therefore necessary to determine to what extent praseodymium would follow cerium at those steps in the chemistry where cerium is separated from the other rare earths.

Tracer experiments have been carried out with 137.5-day ^{134}Ce and 4.41-hour ^{139}Pr produced respectively by (p,pn) and (p,2n) reaction on ^{140}Ce , by 20 MeV-proton irradiation of natural CeO_2 . In this case, the target material acts also as cerium carrier in the subsequent chemical procedures. A solution of 20 mg/ml of Pr_2O_3 was used as praseodymium hold-back carrier and the effect on the Pr-Ce contamination factor of the relative amounts of Pr_2O_3 and CeO_2 present in the initial sample was investigated for those steps involving cerium oxidation. We found that:

- no measurable amounts of Pr activities follow Ce during the methyl isobutyl ketone extraction, even without adding Pr hold-back carrier.
- when the $\text{Ce}(\text{IO}_3)_4$ precipitation is performed

in the absence of Pr_2O_3 , 35% of Pr activity follows the iodate precipitate. The decontamination factor can be slightly improved when Pr_2O_3 is added before the final precipitation. We found that the contamination drops down to 15% when the ratio $\text{Pr}/\text{Ce} = 2$. Further addition of Pr_2O_3 does not improve decontamination significantly. One has to note, however, that in spite of this poor decontamination factor, the correction to be applied to the measured ^{146}Pr activities amounts to 2% at the most, due to the short time interval (1-2 minutes) which separates the solvent extraction from the iodate precipitation. The time of solvent extraction and iodate precipitation was recorded in order to estimate the amount of ^{146}Pr which accumulates during this time interval and subtract it from that resulting from ^{146}Ce decay after the final precipitation.

c) Copper chemistry

The radiochemical processing of Cu monitor foils, derived from the procedure of Kraus and Moore (Kr 53). The copper foil was weighed on an analytical balance prior to chemical treatment and dissolved in 2 ml of concentrated HCl and a few drops of H_2O_2 which promotes the oxidation of copper into Cu^{2+} . The target material itself acts as the carrier.

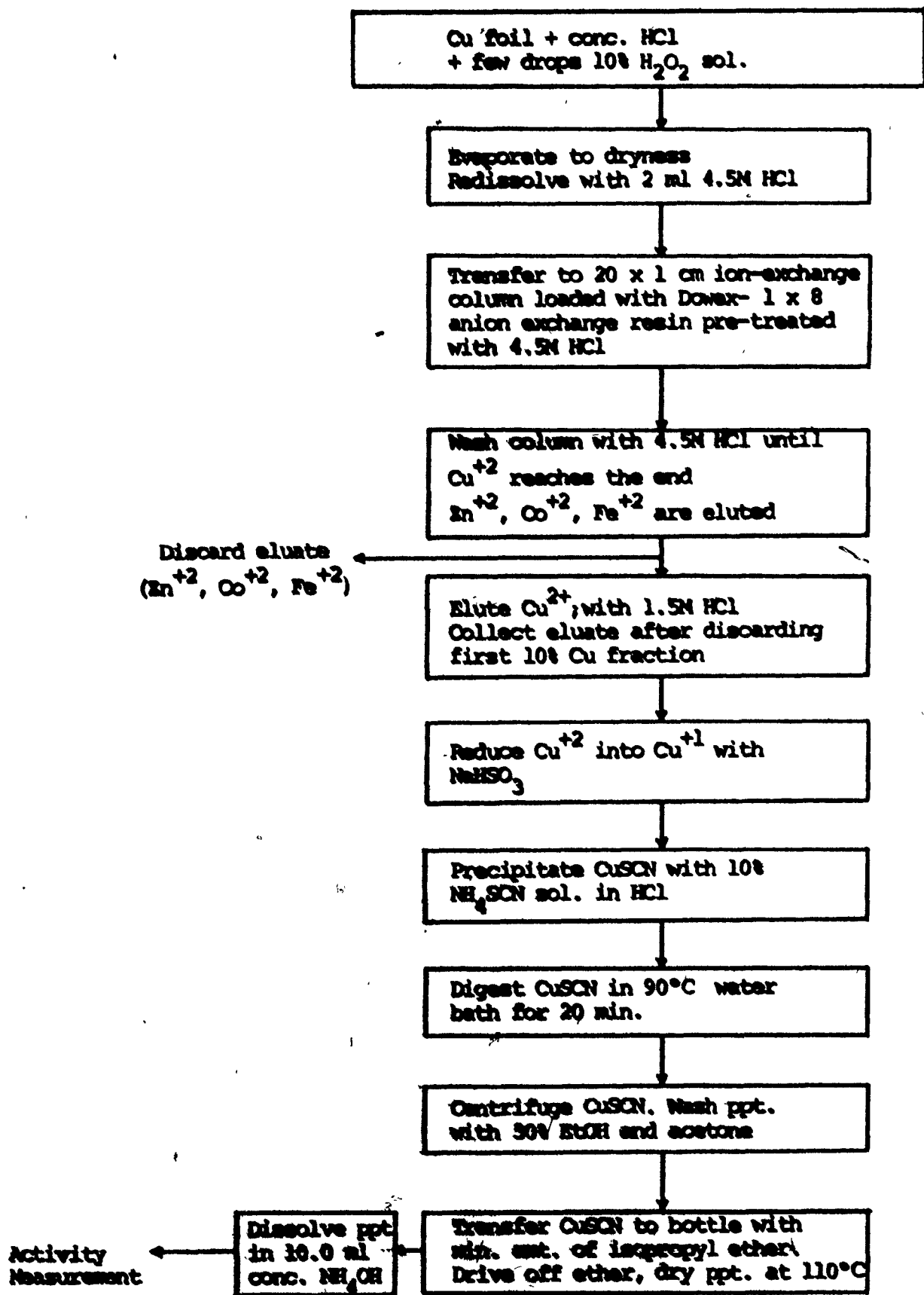
After complete dissolution, the copper chloride solution was evaporated to dryness and redissolved with 2 ml of 4.5N HCl. The new solution was transferred to the top of a Dowex-1X8 anion-exchange resin column (mesh size 100-200) about 20 cm long and 1 cm in diameter, the resin having been pre-equilibrated with 4.5N HCl. The column was washed continuously with 4.5N HCl to free it from zinc, cobalt and iron till the yellow copper band is ready for elution. Copper is then eluted with 1.5N HCl and the middle fraction of this eluate is retained. The solution is diluted to a volume of about 5 ml by addition of distilled water and Cu^{2+} was reduced to Cu^{1+} with NaHSO_3 and precipitated as CuSCN by adding dropwise a 10% NH_4SCN solution from dilute HCl solution until no more thiocyanate formed. The precipitate was digested for 20 minutes over a 90°C water bath, centrifuged, washed with 30% ethanol and acetone, and transferred with a minimum amount of isopropyl ether to a previously tared glass bottle. The ether was evaporated under an infra-red lamp and CuSCN was dried at 110°C for about 30 minutes and weighed.

The precipitate was finally dissolved in 10 ml of concentrated NH_4OH and ^{64}Cu activity was determined in this liquid sample form. The percentage recovery of copper is usually high and varies between 80% and 90%.

d) Standardisation of carrier solutions

The neodymium carrier solution was prepared by dis-

FIGURE 12: Radiochemical separation of copper. Flowchart.



solution of 1.5 g high purity Nd_2O_3 in 3N HCl and the solution was made up to a volume of 100 ml with the acid. 5.0 ml of this solution were pipetted into a 40-ml conical centrifuge tube and 15 ml of saturated $\text{H}_2\text{C}_2\text{O}_4$ solution were added. After heating for 5 minutes on a 80°C water bath, the precipitate was filtered under vacuum through a No:42 Whatman filter paper, transferred to a weighed porcelain crucible and ignited at 800°C for 1 hour. After cooling, the precipitate was weighed as Nd_2O_3 . The results of five replicate determinations agreed within $\sim 0.6\%$.

The cerium carrier solution was prepared by dissolving 30 g of $\text{Ce}(\text{NO}_3)_3 \cdot 6\text{H}_2\text{O}$ in 1000 ml of H_2O . 5 ml of this solution were pipetted into a 100-ml beaker and 50 ml of saturated $(\text{NH}_4)_2\text{C}_2\text{O}_4$ were added. The precipitate was heated on a water bath until it had coagulated, then cooled in an ice bath for 15 minutes and filtered through a No:42 Whatman filter paper. After a 30 minute ignition at 800°C , the precipitate was weighed as CeO_2 . Five standardizations, with results agreeing within 0.5% have been carried out.

IV. ACTIVITY MEASUREMENTS

All the rare-earth activities investigated in this work were measured by following the decay of characteristic gamma rays on a 30-cc Ge(Li) crystal detector. The 511-keV annihilation photons of the ^{64}Cu monitor samples were detected with a NaI(Tl) crystal.

a) 30-cc Ge(Li) detector

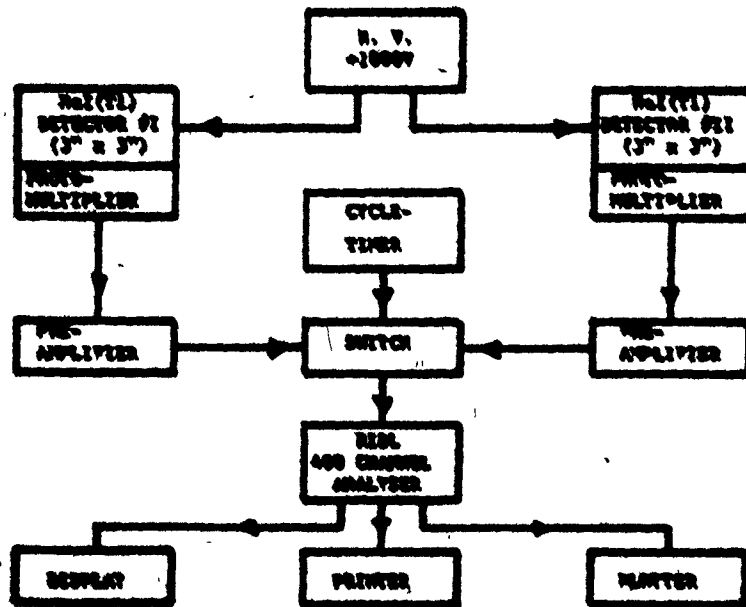
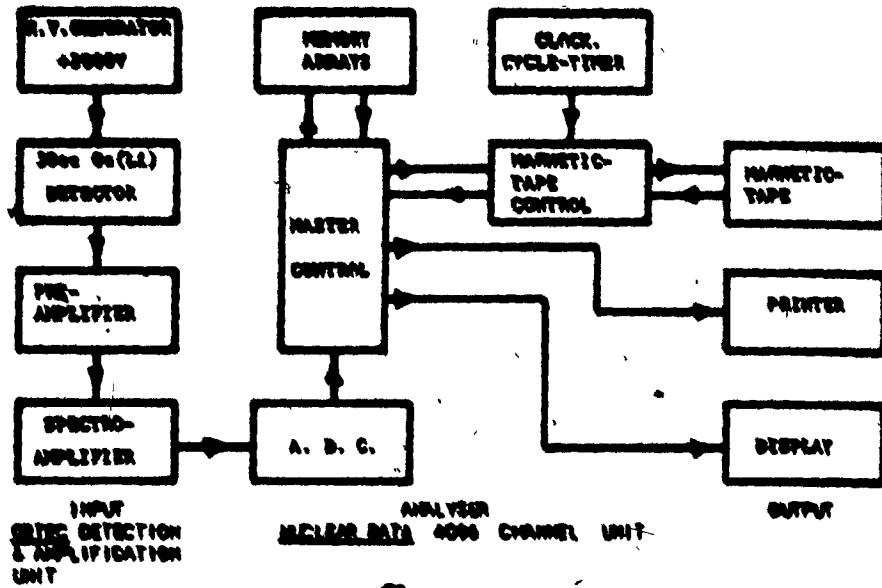
i) Description

The detector consisted of a 30-cc crystal of lithium-drifted germanium (ORTEC model 8001-0536) contained in a cryostat maintained at liquid nitrogen temperature. The operating voltage bias was +2000 volts. A preamplifier (ORTEC model 120-2F) was mounted directly on the detector and the signals were amplified by a spectroscopy amplifier (ORTEC model 451). The pulses were fed to an Analog-to-Digital Converter unit, part of a Nuclear Data 4096 channel analyser. In order to reduce the background arising from environmental radioactivity, the whole system was placed inside a thick lead shielding, the inside of which was lined with a copper foil and a lucite sheet to reduce gamma back scattering. The duration and time interval between counts could be programmed by means of an interval clock and a cycle timer. The information was then stored automatically on magnetic tape for subsequent computer analysis. Each spectrum was recorded with the time and duration of count and a tagword number for retrieval purposes. At the end of each measurement, the memory was automatically erased, the tagword number increased by one unit and a new cycle started. A block diagram of the system is shown in Figure 13a.

The detector could be used either on "clock-time" or "live-time" mode. In the second case, the system self-corrects for dead-time losses. In all our experiments, the

FIGURE 13: Block diagram of the detector systems used:

- a) Ge(Li) solid state detector.
- b) NaI(Tl) scintillation detector.



measurements were performed on live-time and the activity detected was kept to a level such that the indicated dead-time never exceeded 30%. This was achieved by varying the distance between sample and detector.

The resolution of the set-up, in the energy range pertinent to this work, was found to be 1.4% for the 122-keV γ -line of ^{57}Co , 0.6% for the 356-keV γ -line of ^{133}Ba and 0.4% for the 570-keV γ -line of ^{207}Bi corresponding to a full-width at half-maximum of the peaks of ~ 2.2 keV.

ii) Efficiency calibration

The 30-cc Ge(Li) detector has been calibrated for both energy and absolute photopeak efficiency over an energy range of 100 to 2000 keV by Fowler (Fo 72). The primary calibration has been made at a distance such that errors due to source geometry and summing effects (like β - γ summation γ ray cascades) are reduced to a negligible error. The shape of the low portion of the efficiency curve has therefore been determined at a distance of 108.0 mm from the detector using ^{182}Ta and ^{133}Ba point sources. These nuclides have been chosen for the accuracy with which the relative intensities of their emitted gamma-rays are known. The measurements were carried out using a thick plastic absorber (9.4 mm) in order to prevent possible β - γ summation. Absolute efficiency determinations have been made at the same distance using a set of International Atomic Energy Agency

(IAEA) standard point sources (^{241}Am , ^{137}Cs , ^{60}Co , ^{54}Mn , ^{22}Na , ^{88}Y) and the ^{182}Tm data have been normalized to that of the IAEA standards (Fo 72) by means of a least-square fit using the Oak Ridge General Least Square Program (ORGLS) (Bu 62).

In actual experiments, the radioactive sources used for cross-section determinations are spread sources of ~ 0.5 cm in diameter, or in some cases, liquid sources. It was therefore necessary to investigate in more details the effect of source geometry on the efficiency. A liquid source of ^{133}Ba (obtained from New England Nuclear : NEN) was prepared in identical geometric conditions (10 ml) as the rare earth samples used in ^{151}Nd experiments. Activity measurements have been made at various distances corresponding to the different shelves in the sample holder in order to determine efficiency ratios with respect to the reference shelf (108° mm) so that the activity of samples with low emission rates, measured on shelves closer to the detector, could be converted to equivalent ratios of the calibrated distances.

The liquid ^{133}Ba source was then converted into a spread solid source (same geometry of the samples) by precipitation of barium chromate and the same operation was repeated. It is to be noted that the activity of the ^{133}Ba source need not be known, since it has been shown by Fowler (Fo 72) that, at distances greater than 75.0 mm, there is no difference in the efficiency for point or extended sources.

A listing of the results obtained for the various

nuclides in this study is given in Table I. Figure 14 shows the calibration curve as determined at 108.0 mm by Fowler. The points are the IAEA and the normalized ^{182}Ta data. The solid line is the curve calculated by ORGLS least-square fit. The probable error of efficiencies above ~ 300 keV has been calculated to be $\sim 2\%$, while at lower energies it increases to about 8% at 100 keV (Fo 72).

b) NaI(Tl) scintillation detector

The scintillation detection system used in the measurement of the activity of the copper monitor samples consisted of a 3" x 3" thallium-activated sodium iodide crystal (Harshaw Chemical Company) hermetically sealed in an aluminum can and optically coupled to a photomultiplier (RCA 6342-A). The detection assembly was shielded from the background radiation by a lead housing. The inside of the lead shielding was lined with iron and copper to alternate the fluorescent radiations from lead.

The output pulses from the preamplifier were fed to a 400-channel Pulse Height Analyzer (Nuclear Chicago Corporation Model 34-12B, RIDL) and the spectrum of the stored data was printed out with a digital print-out system. In the actual measurement set-up, two identical detection systems and their preamplifier could send pulses to the analyzer alternatively through a switch. An external cycle-timer could trigger the switch and the analyzer. The arrangement is shown

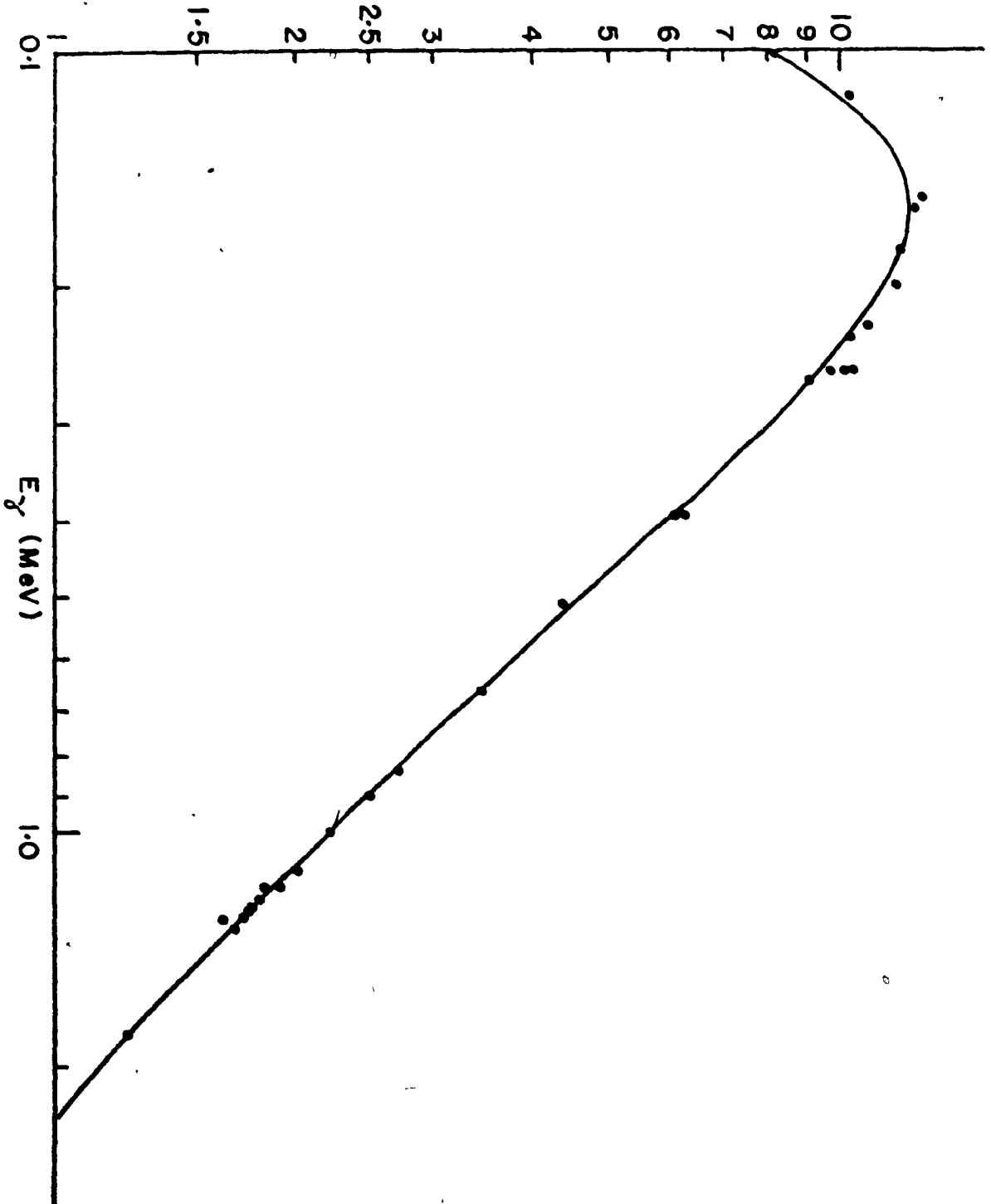
TABLE I: Absolute efficiencies for gamma-rays of nuclides studied - 30-cc Ge(Li) detector

Nuclide	Gamma-ray energy (keV)	Detector-to-sample distance	E_{sp}	E_{liq}
^{147}Nd	91.1	20.7 mm	7.10×10^{-3}	---
^{153}Sm	103.2	20.7 mm	8.71×10^{-3}	---
^{155}Sm	104.3	75.0 mm	1.80×10^{-3}	---
		153.5 mm	5.78×10^{-4}	---
^{151}Nd	117.0	75.0 mm	---	1.57×10^{-3}
		153.5 mm	---	5.65×10^{-4}
^{156}Sm	204.0	20.7 mm	1.09×10^{-2}	---
^{149}Nd	211.3	20.7 mm	1.08×10^{-2}	---
		75.0 mm	2.19×10^{-3}	1.58×10^{-3}
		153.5 mm	7.09×10^{-4}	5.69×10^{-4}
^{149}Pm	286.0	20.7 mm	8.28×10^{-3}	---
^{150}Pm	333.9	20.7 mm	7.03×10^{-3}	---
		75.0 mm	1.43×10^{-3}	---
^{151}Pm	340.0	20.7 mm	6.94×10^{-3}	---
^{157}Eu	373.0	20.7 mm	6.31×10^{-3}	---
^{146}Pr	453.6	75.0 mm	1.01×10^{-3}	---
		153.5 mm	3.28×10^{-4}	---
^{148m}Pm	550.0	20.7 mm	3.60×10^{-3}	---

FIGURE 14: Absolute photopeak efficiency of 30-cc. Ge(Li) detector measured at a distance of 108.0 mm. The plotted data are IAEA standards and ^{182}Ta data normalized to the IAEA data. After Fowler (Fo 72).

PHOTOPEAK EFFICIENCY

$\times 10^4$



on Figure 13b.

The resolution of the crystal was found to be 7.6% for the 661-keV gamma ray of ^{137}Cs . The efficiency of the detection system for the 511-keV gamma ray was determined by Newton et al. (Ne 73) using a liquid ^{22}Na standard source obtained from New England Nuclear Corporation. The standard sample was measured under geometrical conditions identical to those for the ^{64}Cu samples prepared for monitoring the proton beam. The choice of ^{22}Na was dictated by the fact that the maximum energy of its positrons ($\beta_{\text{Max}}^+ = 0.545 \text{ MeV}$) is not very different from that of the positrons emitted by ^{64}Cu ($\beta_{\text{Max}}^+ = 0.656 \text{ MeV}$). The contribution of the 1.27-MeV γ -radiation of ^{22}Na to the 511-keV annihilation peak by pair production was assumed to be negligible.

The analyser has a provision for dead-time losses corrections. However, Newton et al. (Ne 73) have found that, as the dead time rises above 8%, the live timer error becomes significant. Therefore, all the activity measurements were performed after substantial decay of ^{64}Cu had occurred so that the data were collected below 8% indicated dead time.

C. TREATMENT OF DATA

This chapter describes the procedures utilized to convert the gross data, which consist of gamma-ray spectra, to formation cross-sections of the nuclides studied.

I. ANALYSIS OF SPECTRA: PEAK INTEGRATION

The photopeak areas, which represent the total activity at a particular time, for a given measurement period and a given γ -transition, were determined by summation over the number of channels defining the peaks of interest, followed by subtraction of the background. All the data recorded on magnetic tape were processed using the McGill Computing Centre IBM 360-75. Due to the large number of peaks present in each spectrum, specially at times of measurement within one hour from the end of bombardment, no attempt was made to perform a primary analysis with the aid of a program which locates the peak positions. Each selected peak was visually located with the help of the channel number-versus energy relationship determined with standard sources prior to each series of activity measurement. In spite of the complexity of the spectra, it was possible to isolate the various peaks of interest without noticeable interference from neighbouring γ -rays (except for the 103.2-keV and 104.3-keV γ -lines of ^{153}Sm and ^{155}Sm which have been treated as a single peak, and the two components subsequently resolved using a procedure described in the following paragraph).

A simple summation program, which commands the reading of the tape, performs peak integration, prints and punches out results, has been used (Br 71). Input parameters consisted of the tagword number of the spectrum to be processed and the limits of the peaks defined by two channel-windows on each side which serve also for background determination. The program integrates the total number of disintegrations between these limits and subtracts the background. This background was taken as a straight line computed by a linear weighted least-square method through the points in the adjacent channel-windows. The variance of the total number of disintegrations was taken as its weighting factor (St 65). The standard deviation on the activity of a peak was taken as the square root of the total peak area plus the background (true peak area + twice the background). The output consisted of the time at the end of measurement, its duration, the number of recorded disintegration and the corresponding standard deviation. The format of the punched output was chosen such as to match the input format for the program used in decay-curve analysis (see following section).

For data collected with the NaI(Tl) detector, peak integration was done manually. A trapezoidal background was subtracted from the total peak area. The straight line defining the lower limit of the peak was that passing through an average background on each side of the peak. The standard deviation of the peak area was calculated with the same expres-

sion as above.

The apparent emission rate, R^0 , was then corrected for detector efficiency, gamma ray abundance, chemical yield to give the absolute disintegration rate D^0 :

$$D^0 = R^0 \times \frac{1}{E} \times \frac{1}{I_\gamma} \times \frac{1}{C \cdot Y} \quad (C.1)$$

where E: detector efficiency for a specific source-detector geometry.

I_γ : number of γ -rays emitted per disintegration.

C·Y: chemical yield.

The values I_γ for the various nuclides pertaining to this work are shown in Table II, along with the half lives used in subsequent calculations.

II. DECAY-CURVE ANALYSIS

The decay data were analyzed with the Brookhaven National Laboratory least-squares program CLSQ (Cu 63). This program, which was originally written to treat decay data obtained with gas-flow beta counters, uses a least-square procedure to compute the activity at some arbitrary initial time and is capable of resolving up to ten components. At a given time t , the observed disintegration rate is the sum of the contribution of the m components ($m \leq 10$):

TABLE II: Decay properties of the observed nuclides

Nuclide	Mode of formation *	Half-life	Radiation detected	Emitted radiation per disintegration	Ref.
^{146}Ce	c	14.2 m	453.6 keV from daughter	0.77	Le 67
^{146}Pr	c	24.2 m	453.6 keV	0.77	"
^{147}Nd	c	10.99 d	91.1 keV	0.28	"
$^{148\text{m}}\text{Pm}$	i	41.3 d	550.0 keV	0.95	"
^{149}Nd	c	1.73 h	211.3 keV	0.27	"
^{149}Pm	c	53.1 h	286.0 keV	0.026	Ch 70c
^{150}Pm	i	2.68 h	333.9 keV	0.71	Le 67
^{151}Nd	c	12.4 m	117.0 keV	0.40	"
^{151}Pm	c	28.4 h	340.0 keV	0.21	"
^{153}Sm	c	46.5 h	103.2 keV	0.28	"
^{155}Sm	c	22.2 m	104.3 keV	0.73	"
^{156}Sm	c	9.4 h	204.0 keV	0.20	"
^{157}Eu	c	15.2 h	373.0 keV	0.14	"
^{64}Cu	(p,pn)	12.74 h	511 keV	0.38	"

* c = cumulative product

i = independent product

$$A(t) = \sum_{j=1}^m [I_j \exp(-\lambda_j t) + V(t)] \quad (C.2)$$

where I_j is the initial activity of the j th component and $V(t)$ is the residual at time t due to statistical fluctuations and experimental errors. For each observation of $A(t)$, there is an equation of the form of (C.2) which is linear with respect to the initial activity. A least-squares solution for the I_j 's is obtained by minimizing the squares of the properly weighted residuals. Each point was weighted by the value of the standard deviation and the origin of time was taken as that of the end of bombardment (plus half the duration of the counting interval in the case of short-lived nuclides). Besides providing the activities at the origin of time, this program also gives the half-lives of the nuclides corresponding to the best fit as defined above.

A second program, based on the same principle, was used to analyse the copper monitor data obtained with the NaI(Tl) detector, as in the original work of Newton et al. (Ne 73). In this linear least-squares treatment based on the mathematical method of Von Holdt (Vo 59), there is no provision for a variable half-life and half-life values must be given as input data.

III. CROSS SECTION CALCULATIONS

a) General equation

The observed disintegration rate of a species A at the end of bombardment, D_A^0 , can be calculated according to the expression:

$$D_A^0 = I n_T \sigma_A (1 - e^{-\lambda_A t_0}) \quad (C.3)$$

where

- I: beam intensity of the bombarding particles (number of particles per second).
- n_T : superficial density of the target material (number of atoms per cm^2).
- σ_A : formation cross section of species A (cm^2).
- λ_A : decay constant of nuclide A (in sec^{-1}).
- t_0 : duration of bombardment (in seconds).

The determination of I is achieved by monitoring the beam with a known reaction. As stated before, the reaction $^{65}\text{Cu}(p, pn)^{64}\text{Cu}$ was used for this purpose. The cross sections at the different bombarding energies used in this work are listed in Table 3. Those labelled with an asterisk have been interpolated from the original values of Newton et al. (Ne 73).

The disintegration rate at the end of bombardment of ^{64}Cu , D_N^0 , can be calculated from a relation similar to (C.3):

TABLE III: $^{65}\text{Cu}(p, pn)^{64}\text{Cu}$ cross sections

E_p (MeV)	σ_{mb}	Ref.
20	285.0	Ne 62
25	429.1	Ne 73
30	408.7	"
35	249.7	"
40	244.6	"
45	194.5	"
50	186.6	"
55	178.2*	"
60	169.7*	"
65	162.5*	"
70	155.3*	"
77	156.9	"
85	141.1*	"

*interpolated values

$$D_M^0 = I n_M \sigma_M (1 - e^{-\lambda_M t_0}) \quad (C.4)$$

where the subscript M refers to the monitor.

By exposing an equal area of the monitor and the target foils to the same beam, the intensity I will be identical in equations (C.3) and (C.4). Therefore, the formation cross section of A may be determined relative to the known monitor cross section by combining these two equations:

$$\sigma_A = \sigma_M \frac{n_M D_A^0 (1 - e^{-\lambda_M t_0})}{n_T D_M^0 (1 - e^{-\lambda_A t_0})} \quad (C.5)$$

The number of atoms in a given area is related to its weight by:

$$n = \frac{W}{A.W.} \times Ab \times \mathcal{N} \quad (C.6)$$

where

W: weight of the foil.

A.W: atomic weight of the target nuclide.

Ab: isotopic abundance of the target nuclide.

\mathcal{N} : Avogadro's number.

Substituting (C.5) for the monitor and the target into (C.4), one obtains:

$$\sigma_A = \sigma_M \frac{D_M^0}{D_A^0} \times \frac{Ab_M}{Ab_T} \times \frac{A.W_T}{A.W_M} \times \frac{N_M}{N_T} \times \frac{(1 - e^{-\lambda_M t_0})}{(1 - e^{-\lambda_T t_0})} \quad (C.7)$$

b) Calculation of disintegration rates at the end of bombardment

i) Case 1

Equation (C.6) may be applied directly to calculate the independent cross sections of shielded nuclides and the cumulative yields of nuclides with short-lived precursors. This situation is encountered in this work in the case of ^{148m}Pm and ^{150}Pm (independent), and ^{151}Nd and ^{157}Eu (cumulative). (see Table IV for details on the various decay chains involved in this study). The precursors of ^{155}Sm and ^{156}Sm have been assumed to be short-lived since no data on half-lives exist so far in the literature. In any case, half-lives are likely to be short enough so that saturation rates are reached in a time short compared to a 30 minutes irradiation period.

ii) Case 2

When the parent decays with a half-life which is not short compared to that of its daughter and/or the duration of irradiation, its contribution to the observed cumulative yield of its daughter has to be evaluated. Consider a chain $A \rightarrow B \rightarrow C$ (stable) with A having a short-lived precursor. The amount of A present at the end of bombardment, may be expressed by a relation similar to (C.3).

$$N_A^0 = \frac{\sigma_A I n_T}{\lambda_A} (1 - e^{-\lambda_A t_0}) \quad (\text{C.8})$$

TABLE IV: Fission product decay chains (Ho 72)

Element Mass	⁵⁷ La	⁵⁸ Ce	⁵⁹ Pr	⁶⁰ Nd	⁶¹ Pm	⁶² Sm	⁶³ Eu
146	8.3s	→ 14.2m	→ 24.2m	→ <u>stable</u>			
147	< 10s	→ 70s	→ 12m	→ 10.99d	→ 2.62y	→ 1.07.10 ¹¹ y	
148 ^m	13s	→ ~ 43s	→ 2.0m	→ <u>stable</u>	41.3d	→ .10 ¹⁵ y	
149	v.short?	→ 1s?	→ 2.3m	→ 1.73h	→ 53.1h	→ > 1.10 ⁶ y	
150		v.short?	→ 12.4s	→ <u>stable</u>	2.68h	→ <u>stable</u>	
151		v.short?	→ 4s	→ 12.4m	→ 28.4h	→ 93y	→ <u>stable</u>
153				v.short?	→ 5.4m	→ 46.5h	→ <u>stable</u>
155					v.short?	→ 22.2m	→ 4.8y
156					v.short?	→ 9.4h	→ 15.2d
157					v.short?	→ 83s	→ 15.2h

y = year

h = hour

s = second

d = day

m = minute

At any time t during irradiation, the net rate of production of B is:

$$\frac{dN_B}{dt} = \sigma_A \text{In}_T (1 - e^{-\lambda_A t}) + \sigma_B \text{In}_T - \lambda_B N_B \quad (\text{C.9})$$

The first group of terms appears due to parent nuclide A, the second term is from the independent formation of nuclide B, and the last term takes care of the decay of the daughter nuclide B. At the end of bombardment, the amount of B present is:

$$N_B^0 = \text{In}_T \frac{(1 - e^{-\lambda_B t_0})}{\lambda_B} (\sigma_A + \sigma_B) - \text{In}_T \frac{(e^{-\lambda_A t_0} - e^{-\lambda_B t_0})}{\lambda_B - \lambda_A} \sigma_A \quad (\text{C.10})$$

where σ_A is the cumulative cross section of species A and σ_B the independent cross section of nuclide B.

After the end of the bombardment, the amount of B growing from N_A^0 in a time t is:

$$\frac{\lambda_A N_A^0}{\lambda_B - \lambda_A} \cdot (e^{-\lambda_A t} - e^{-\lambda_B t}) \quad (\text{C.11})$$

Therefore, at time t , the disintegration rate of B, after substituting N_A^0 in (C.10) one obtains:

$$D_B^t = \text{In}_T \left\{ (1 - e^{-\lambda_B t_0}) \cdot e^{-\lambda_B t} \cdot (\sigma_A + \sigma_B) - \frac{\lambda_B (e^{-\lambda_A t_0} - e^{-\lambda_B t_0})}{\lambda_B - \lambda_A} \cdot e^{-\lambda_B t} \sigma_A + \frac{\lambda_B (1 - e^{-\lambda_A t_0})}{\lambda_B - \lambda_A} (e^{-\lambda_A t} - e^{-\lambda_B t}) \sigma_A \right\} \quad (\text{C.12})$$

In this work, whenever the rare-earths were treated as a group, no parent-daughter separation occurred. Therefore (C.12) applies to the observed disintegration rates all throughout the period of activity measurements. Secondly, the data used in decay-curve analysis are those collected at a time when complete decay of the precursors of the nuclides of interest have taken place, i.e. when terms in $e^{-\lambda_A t}$ have disappeared. Therefore, the extrapolation of the decay curves to the time of the end of bombardment yields the following expression for the observed disintegration rate of B, D_B^{o1} :

$$D_B^{o1} = \text{In}_T \left\{ (1 - e^{-\lambda_B t_0}) (\sigma_A + \sigma_B) + \frac{\lambda_B (1 + e^{-\lambda_B t_0})}{\lambda_B - \lambda_A} \sigma_A \right\} \quad (\text{C.13})$$

The second part in this expression represents a corrective term to the first one which otherwise is identical to equation (C.3), with $(\sigma_A + \sigma_B)$ as the cumulative cross section for nuclide B. This correction had to be taken into account in the case of the $^{146}\text{Ce} - ^{146}\text{Pr}$ pair. In all other cases investigated in this work, the differences in half-lives were large enough to treat the last member of the decay chains as one having a short-lived precursor as in b-i), without introducing significant errors in cross-section calculations.

It has to be noted that equation (C.12) is applicable only to cases where either all the numbers of a decay chain are chemically separated with the same yield or the short-lived precursors have decayed completely. For ^{146}Pr - cumulative cross

section measurements, following group chemistry of the rare earths, the targets were processed after a cooling period of about ~ 1 hour, in order to allow the decay of ^{146}Ce ($> 94\%$) to take place. This precaution is made necessary by the fact that cerium, as a fission product, might exist in the +4 oxidation state.

iii) Case 3: Cerium-praseodymium separation

The calculation of the disintegration rate of ^{146}Pr formed by decay of its precursor ^{146}Ce becomes slightly complicated by the fact that during the last stage of the chemical separation (iodate precipitation), some of the ^{146}Pr which has grown from ^{146}Ce after the cerium solvent extraction follows the cerium fraction.

Let t_0 be the duration of bombardment, t_1 the time of the first Ce - Pr separation (solvent extraction) and t_2 the time of the second Ce - Pr separation (iodate precipitation) A and B refer to ^{146}Ce and ^{146}Pr respectively.

At time t_1 , following the extraction, the amount of ^{146}Ce present in the cerium fraction is

$$N_A^{t_1} = N_A^0 \cdot e^{-\lambda_A t_1} = I n_T \frac{(1 - e^{-\lambda_A t_0})}{\lambda_A} \cdot e^{-\lambda_A t_1} \sigma_A \quad (\text{C.14})$$

the amount of B following A has been found to be negligible (section B III-b).

At time t_2 , just before the iodate precipitation,

the number of atoms of ^{146}Ce is:

$$N_A^{t_2} = \text{In}_T \frac{(1 - e^{-\lambda_A t_0})}{\lambda_A} \cdot e^{-\lambda_A t_2} \sigma_A \quad (\text{C.15})$$

The amount of ^{146}Pr which has grown from ^{146}Ce during the time interval $(t_2 - t_1)$ is expressed by:

$$N_B^{t_2} = \frac{\lambda_A N_A^{t_1}}{\lambda_B - \lambda_A} [e^{-\lambda_A(t_2 - t_1)} - e^{-\lambda_B(t_2 - t_1)}] \sigma_A \quad (\text{C.16})$$

At time t_2 just after the ceric iodate precipitation, a fraction of species B follows A. Let α be this fraction ($\alpha = 0.15$ as determined in section III-b of experimental procedures). At a time $t > t_2$, the amount of B present is therefore made up of two parts: that grown from ^{146}Ce after the second Ce - Pr separation, and that coming from contamination by ^{146}Pr formed during the time interval $(t_2 - t_1)$.

$$N_B^t = N_A^{t_2} \frac{\lambda_A}{\lambda_B - \lambda_A} [e^{-\lambda_A(t - t_2)} - e^{-\lambda_B(t - t_2)}] + \alpha N_B^{t_2} \cdot e^{-\lambda_B(t - t_2)} \quad (\text{C.17})$$

By substituting $N_A^{t_2}$ and $N_B^{t_2}$ in (C.17) one gets:

$$N_B^t = In_{T^0} \sigma_A \frac{(1 - e^{-\lambda_A t_0})}{\lambda_B - \lambda_A} \left\{ [e^{-\lambda_A(t-t_2)} - e^{-\lambda_B(t-t_2)}] \cdot e^{-\lambda_A t_2} \right. \\ \left. + \alpha [e^{-\lambda_A(t_2-t_1)} - e^{-\lambda_B(t_2-t_1)}] \cdot e^{-\lambda_A t_1} \cdot e^{-\lambda_B(t-t_2)} \right\} \quad (C.18)$$

At a time when ^{146}Ce has totally decayed, the term $e^{-\lambda_A(t-t_2)}$ vanishes in (C.18). The extrapolated disintegration rate of B, D_B^0 , at the end of bombardment is obtained by multiplying (C.18) by λ_B and the decay factor $e^{+\lambda_B t}$:

$$D_B^0 = In_{T^0} \sigma_A \frac{\lambda_B (1 - e^{-\lambda_A t_0}) e^{+\lambda_B t_2}}{\lambda_B - \lambda_A} \left\{ \alpha \cdot [e^{-\lambda_A(t_2-t_1)} - e^{-\lambda_B(t_2-t_1)}] \cdot e^{-\lambda_A t_1} \right. \\ \left. - e^{-\lambda_B t_2} \right\} \quad (C.19)$$

D. RESULTS

I. CUMULATIVE CROSS SECTIONS

The cumulative formation cross sections at each incident energy have been calculated as explained in the preceding chapter from the decay scheme data given in Table II, the monitor cross sections presented in Table IV, the efficiency of the detector shown in Table I, the chemical yields and the duration of bombardment. In the case of ^{146}Pr , an additional parent-daughter factor was applied due to incomplete saturation of the precursor ^{146}Ce . A correction arising from cerium contamination was also incorporated in the final cross section calculations using the contamination factor determined in Chapter B (section III-b). The cumulative yields for production in the fission of ^{238}U at incident energies 20-85 MeV of the cumulatively-formed nuclides studied in this work are shown in Tables V to VII. The values quoted for these cross sections are in most cases the result of several determinations. They were obtained by taking the average of these measurements and the associated errors represent the maximum amplitude between replicates.

Whenever a single experiment was performed, the error quoted has been calculated by taking the maximum % error determined from replicate measurements at other energies. The systematic errors have not been included in the error bars shown and these will be discussed in a subsequent section. The data given in Table V through VII, along with data from

TABLE V: Cumulative formation cross sections*

σ_{mb} E_p (MeV)	^{146}Ce N/Z=1.5172	^{146}Pr N/Z=1.4745	^{147}Nd N/Z=1.4500	^{149}Nd N/Z=1.4833
20	11.7 ± 2.3 (1)	15.2 ± 1.7 (2)	15.9 ± 1.8 (2)	9.40 ± 0.7 (2)
25	10.5 ± 1.6 (2)	15.0 ± 1.7 (1)	16.7 ± 1.4 (2)	9.50 ± 0.9 (2)
30	13.8 ± 1.4 (2)	20.2 ± 1.4 (2)	18.1 ± 2.5 (1)	11.8 ± 0.7 (3)
35	10.1 ± 2.0 (1)	17.5 ± 1.6 (2)	20.8 ± 2.5 (2)	12.5 ± 1.1 (2)
40	12.3 ± 1.8 (2)	18.7 ± 0.9 (2)	21.0 ± 1.9 (2)	12.1 ± 0.9 (3)
45	9.9 ± 2.0 (1)	18.3 ± 1.1 (2)	18.5 ± 2.5 (1)	12.2 ± 1.4 (2)
50	5.7 ± 1.2 (2)	17.2 ± 0.8 (3)	16.6 ± 2.3 (1)	13.9 ± 0.8 (4)
55	7.4 ± 1.5 (1)	17.6 ± 1.2 (2)	20.4 ± 2.8 (2)	14.0 ± 1.7 (2)
60	6.4 ± 0.8 (2)	15.8 ± 1.3 (2)	19.2 ± 1.7 (2)	11.9 ± 0.7 (3)
65	4.7 ± 0.9 (1)	15.6 ± 1.8 (1)	15.5 ± 2.2 (1)	10.7 ± 0.9 (2)
70	4.4 ± 0.9 (2)	13.8 ± 0.9 (3)	13.7 ± 0.6 (2)	9.5 ± 1.0 (2)
77	6.1 ± 1.2 (1)	13.7 ± 1.4 (2)	11.8 ± 1.5 (2)	6.8 ± 0.7 (2)
85	3.6 ± 0.4 (2)	9.6 ± 1.1 (2)	11.4 ± 1.7 (2)	6.5 ± 0.9 (3)

*The numbers in brackets give the number of determinations

TABLE VI: Cumulative formation cross sections*

σ_{mb} E_p (MeV)	$^{149}_{Pm}$ N/Z=1.4426	$^{151}_{Nd}$ N/Z=1.5167	$^{151}_{Pm}$ N/Z=1.4754	$^{153}_{Sm}$ N/Z=1.4677
20	12.3 ± 1.3 (2)	4.3 ± 0.6 (2)	7.1 ± 0.8 (2)	3.3 ± 0.2 (2)
25	12.4 ± 1.8 (2)	4.9 ± 0.9 (1)	7.2 ± 0.6 (2)	5.0 ± 0.6 (1)
30	15.4 ± 1.4 (3)	5.2 ± 0.4 (2)	7.7 ± 0.9 (3)	-----
35	16.4 ± 1.5 (2)	5.1 ± 1.0 (1)	7.9 ± 0.5 (2)	6.7 ± 0.9 (1)
40	16.0 ± 1.2 (3)	5.0 ± 0.7 (2)	7.8 ± 1.1 (3)	7.2 ± 0.6 (2)
45	16.4 ± 1.8 (2)	5.2 ± 1.0 (1)	8.1 ± 0.7 (2)	6.4 ± 0.9 (1)
50	18.9 ± 1.7 (4)	4.8 ± 0.9 (2)	8.5 ± 0.6 (4)	-----
55	19.0 ± 2.2 (2)	4.8 ± 0.9 (1)	8.3 ± 1.1 (2)	5.9 ± 0.8 (1)
60	16.3 ± 1.8 (3)	4.3 ± 0.4 (2)	6.7 ± 1.2 (3)	-----
65	14.7 ± 0.9 (2)	4.2 ± 0.7 (1)	6.9 ± 0.5 (2)	-----
70	13.5 ± 1.5 (2)	4.5 ± 0.8 (1)	6.3 ± 0.9 (2)	6.0 ± 0.8 (2)
77	10.1 ± 1.3 (2)	4.4 ± 0.7 (2)	5.9 ± 0.6 (2)	6.2 ± 0.9 (2)
85	9.6 ± 1.1 (3)	3.2 ± 0.6 (2)	4.2 ± 0.5 (3)	4.3 ± 0.5 (2)

*The numbers in brackets give the number of determinations

TABLE VII: Cumulative formation cross sections*

σ_{mb} E_p (MeV)	^{155}Sm N/Z=1.5000	^{156}Sm N/Z=1.5161	^{157}Eu N/Z=1.4921
20	2.2 ± 0.4 (2)	1.9 ± 0.3 (2)	1.1 ± 0.2 (2)
25	2.4 ± 0.5 (1)	2.7 ± 0.6 (1)	1.0 ± 0.3 (1)
30	3.7 ± 0.5 (2)	3.5 ± 0.4 (2)	1.2 ± 0.3 (2)
35	-----	-----	-----
40	3.1 ± 0.3 (2)	2.3 ± 0.3 (2)	1.8 ± 0.2 (2)
45	-----	2.2 ± 0.5 (1)	1.8 ± 0.6 (1)
50	3.0 ± 0.2 (3)	2.2 ± 0.3 (2)	1.9 ± 0.3 (2)
55	-----	1.8 ± 0.4 (1)	1.5 ± 0.5 (1)
60	3.2 ± 0.5 (2)	1.6 ± 0.4 (2)	1.4 ± 0.4 (2)
65	-----	-----	-----
70	1.9 ± 0.4 (1)	1.9 ± 0.5 (1)	1.9 ± 0.6 (1)
77	2.4 ± 0.5 (1)	1.8 ± 0.2 (2)	1.2 ± 0.2 (2)
85	1.7 ± 0.2 (3)	1.6 ± 0.4 (1)	1.3 ± 0.3 (1)

*The numbers in brackets give the number of determinations.

Stevenson et al. (St 58), Pappas and Alstad (Pa 61) and Baba et al. (Ba 71) for ^{147}Nd , ^{149}Pm , ^{150}Pm , ^{151}Pm , ^{153}Sm , ^{156}Sm , and ^{157}Eu were used to construct the excitation functions shown in Figures 15 to 25 inclusively.

II. INDEPENDENT CROSS SECTIONS

a) ^{148m}Pm , ^{150}Pm : the independent yields of these two-shielded nuclides have been determined in the straight-forward manner outlined above. Excitation functions are shown on Figures 27 and 28.

b) ^{146}Pr , ^{151}Pm : independent cross sections have been inferred by subtracting the cumulative cross sections of ^{146}Ce and ^{151}Nd from those of their daughter nuclides. The error on the estimated independent yields was calculated by taking the square root of the sum of the squares of the uncertainties on both cumulative yields of the ^{146}Ce - ^{146}Pr and ^{151}Nd - ^{151}Pm pairs. This procedure, however inaccurate, was felt to provide a rather reliable estimate of the independent yields concerned, specially in the case of ^{146}Pr , where activity measurements have been carried out on the same nuclide (^{146}Pr) for both members of the pair, thus eliminating factors of error arising from the measurement of two different activities (via uncertainties in decay schemes and efficiency of the detector). For ^{151}Pm , an additional 15% uncertainty was added to the error bars on the fractional independent yields used in the construction of the charge dispersion curves.

FIGURE 15: Excitation function for the cumulative formation of ^{146}Ca .

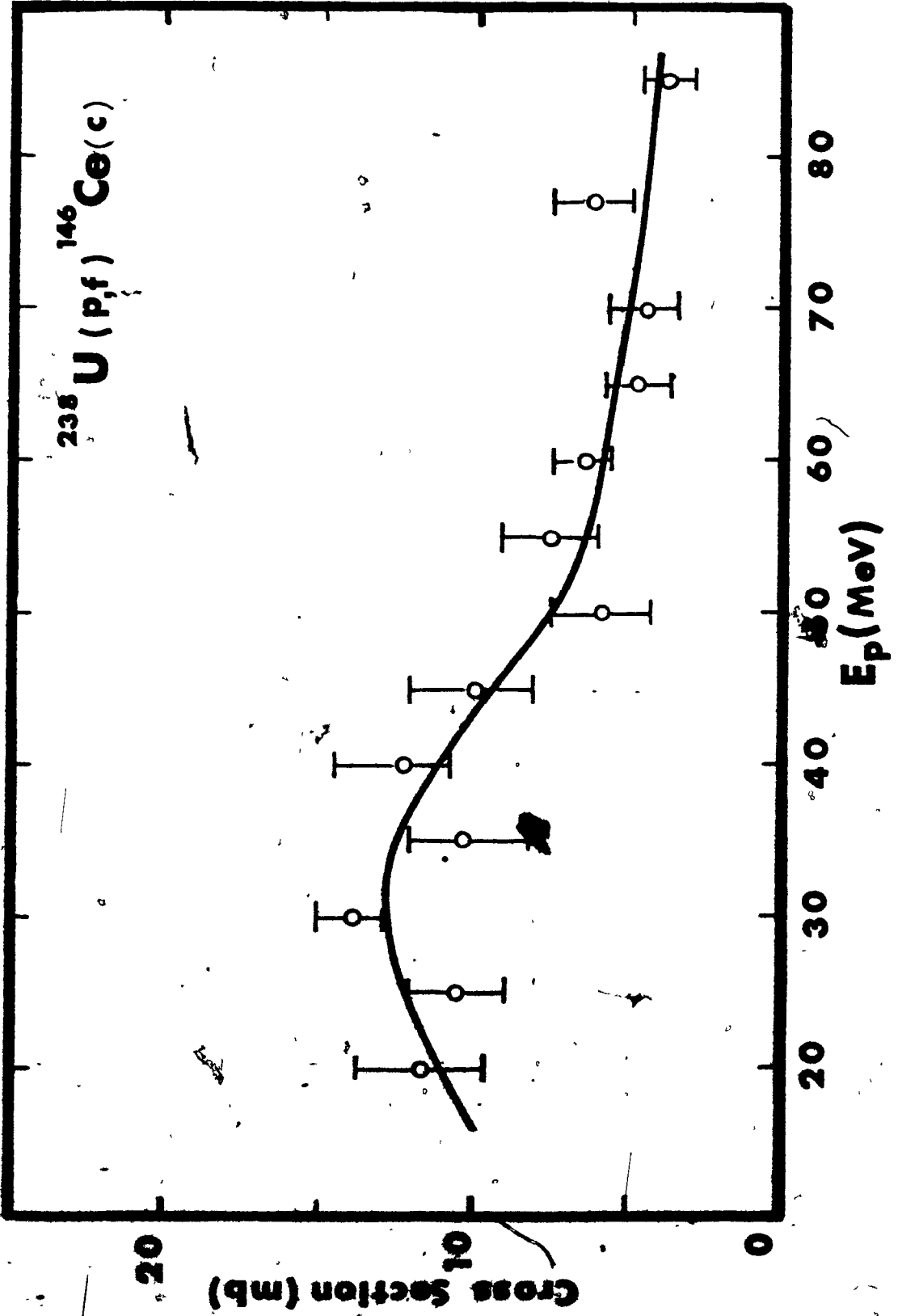


FIGURE 16: Excitation function for the cumulative formation
of ^{146}Pr .

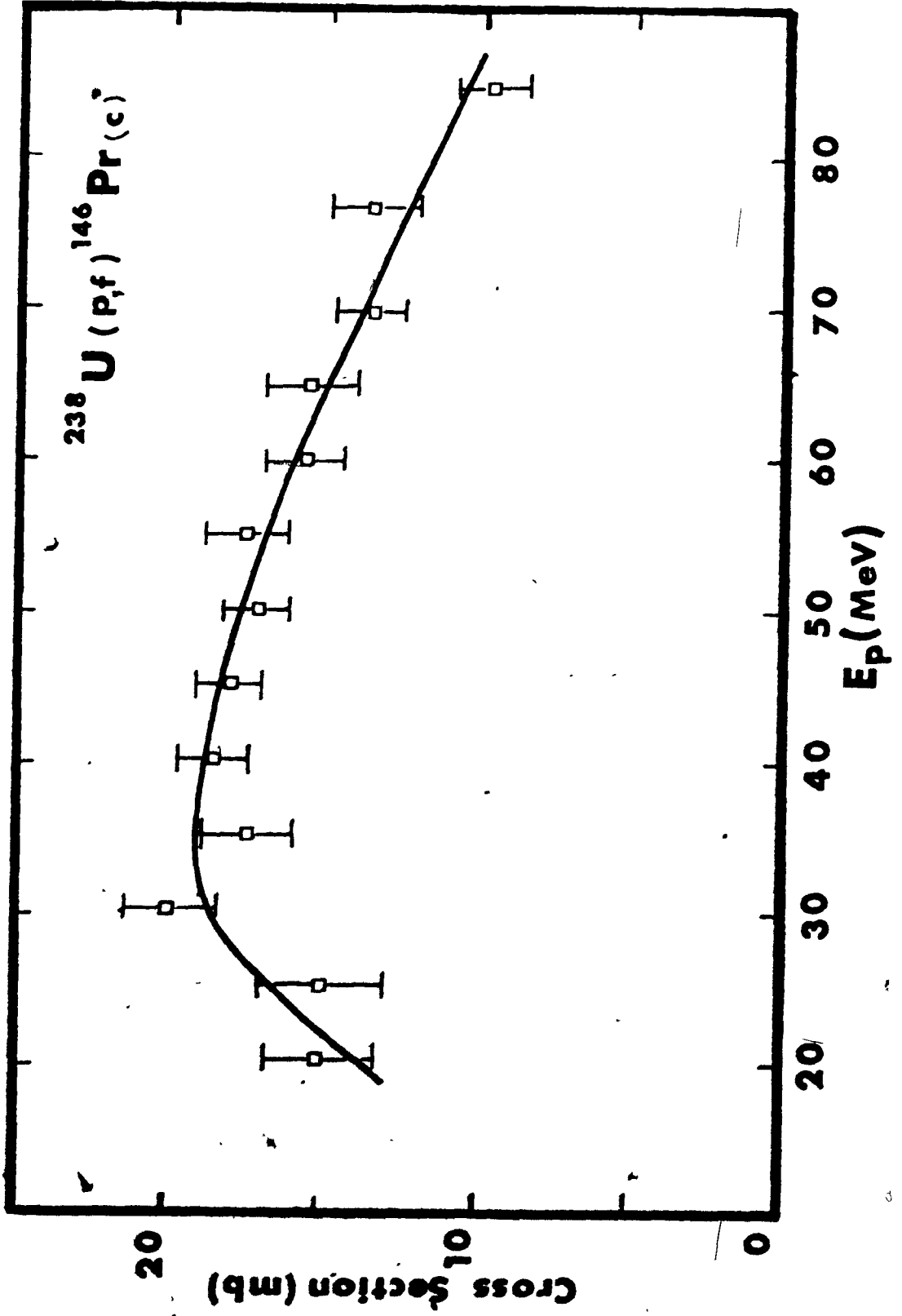


FIGURE 17: Excitation function for the cumulative formation of ^{147}Nd .

- This work
- Stevenson et al. (St 58)
- ▲ Baba et al. (Ba 71)
- △ Pappas and Alstad (Pa 61)

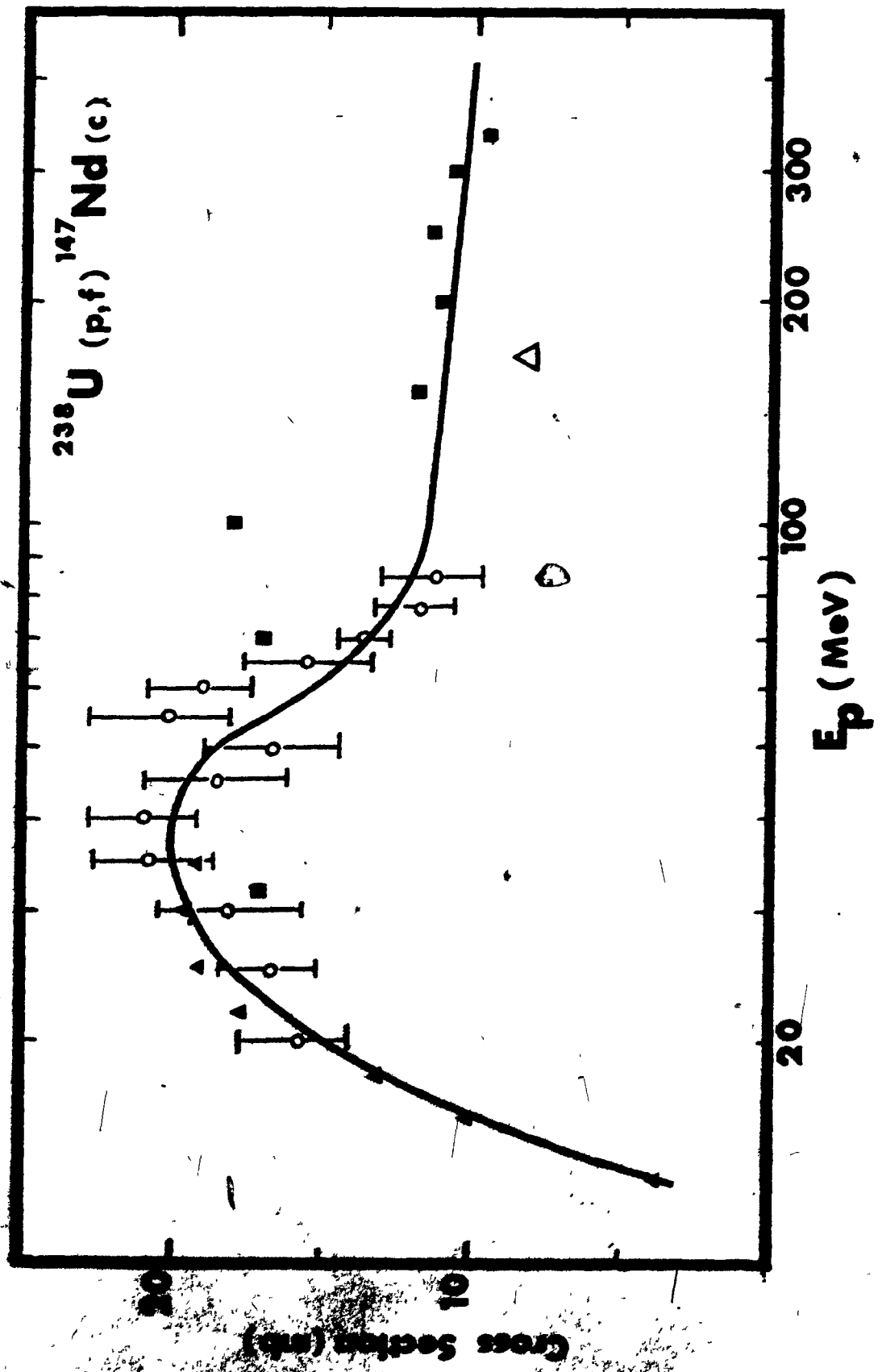


FIGURE 18: Excitation function for the cumulative formation
of ^{149}Nd .

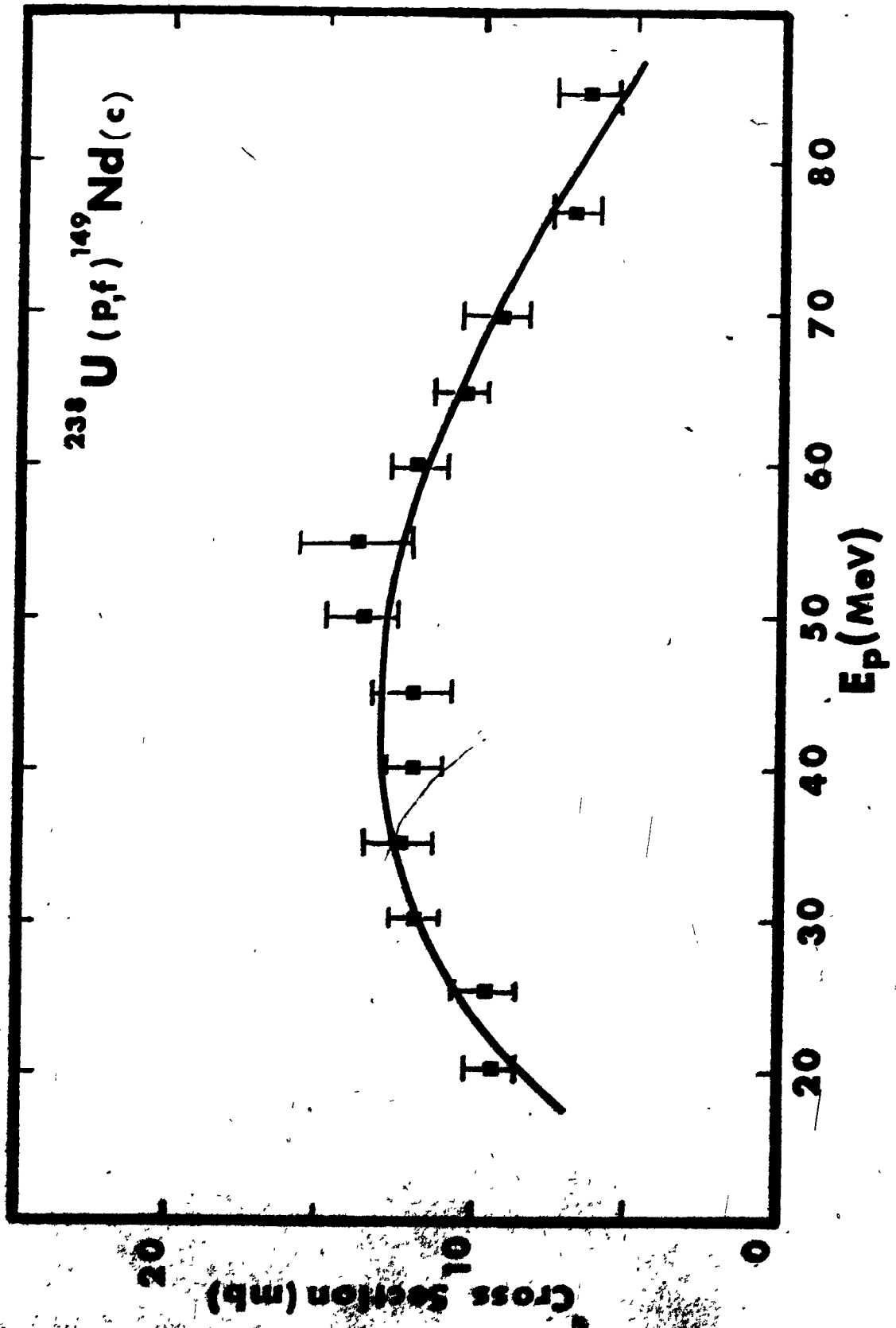


FIGURE 19: Excitation function for the cumulative formation
of ^{149}Pm .

□ This work

▼ Pappas and Alstad (Pa 61)

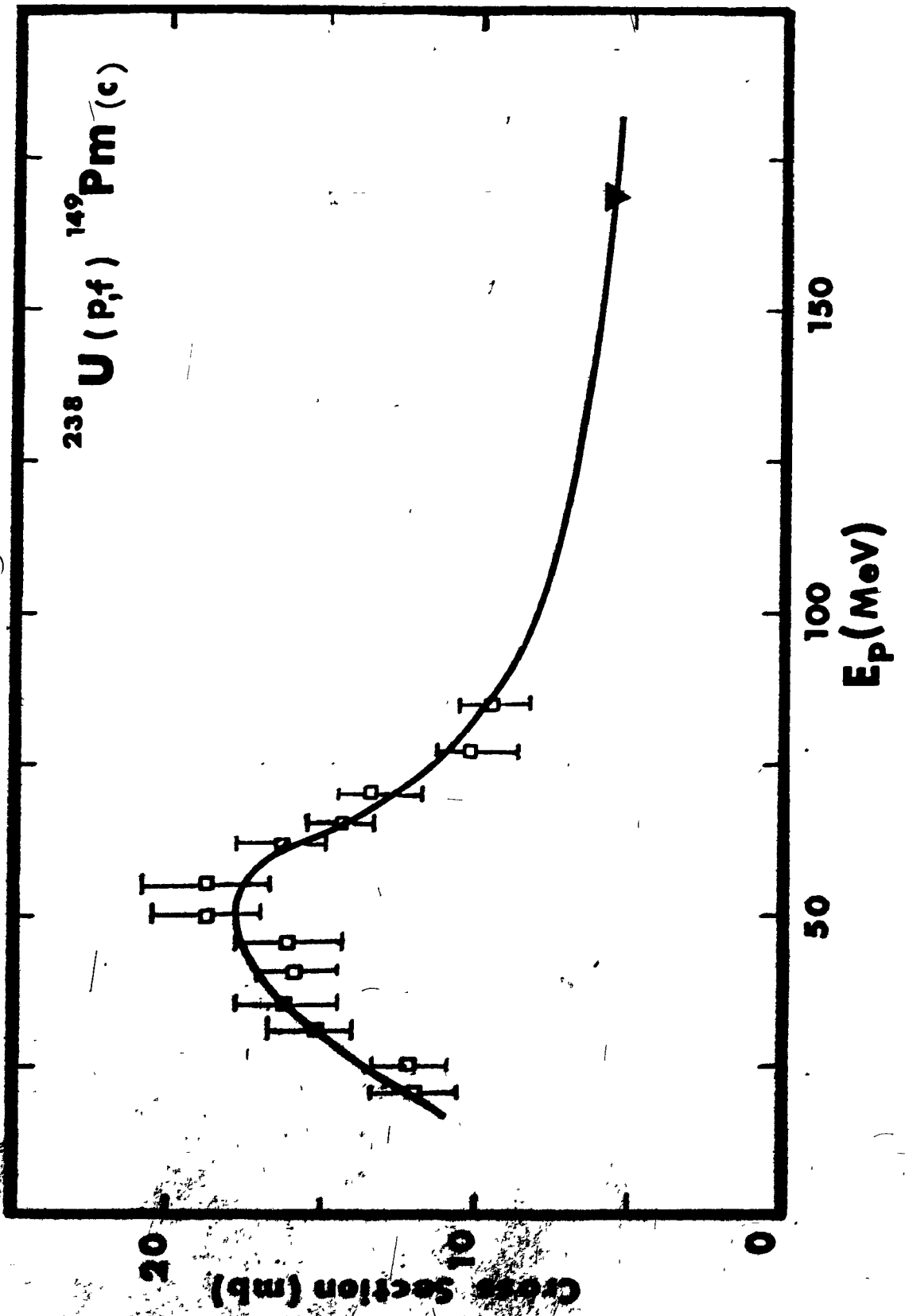


FIGURE 20: Excitation function for the cumulative formation
of ^{151}Nd .

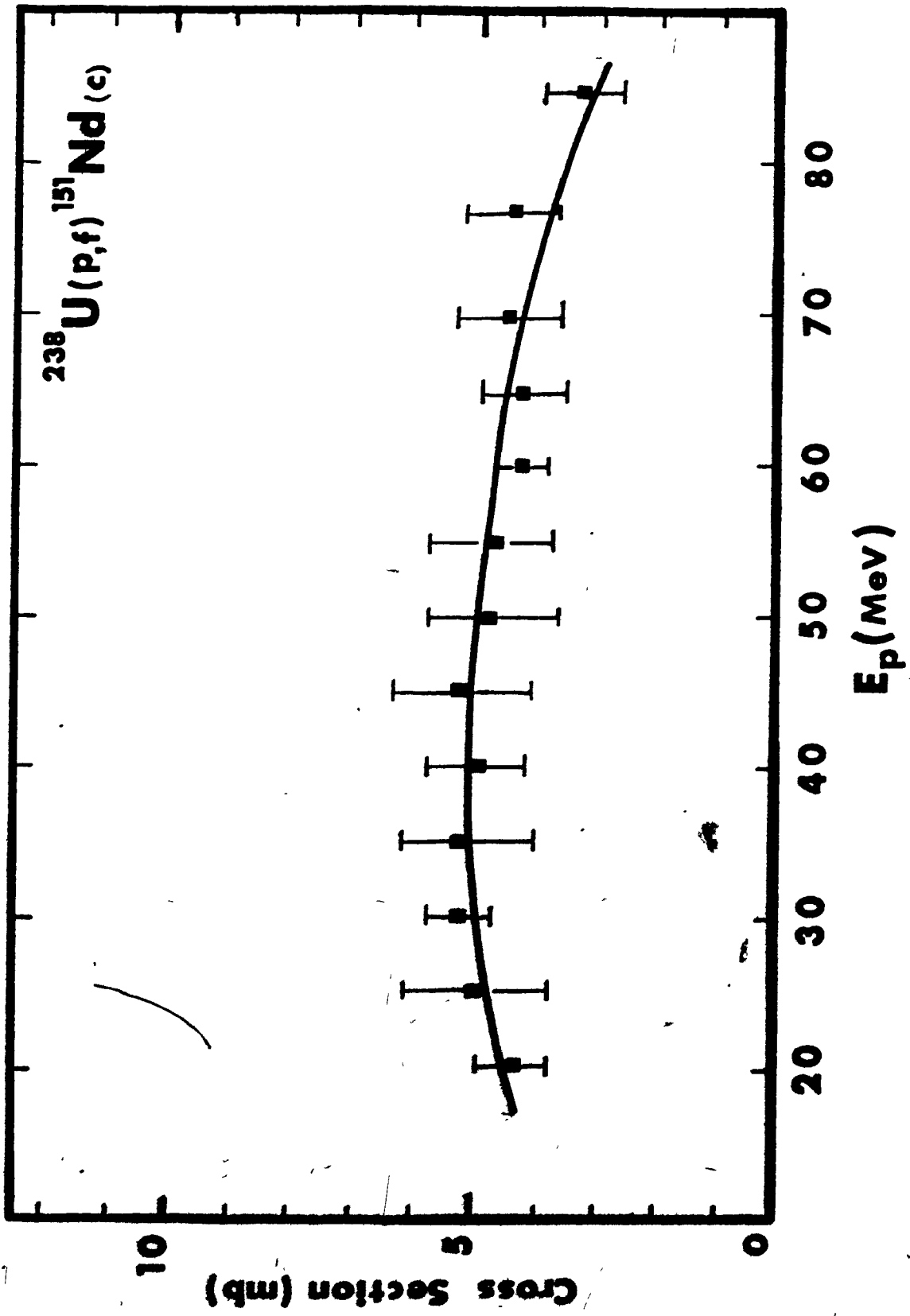


FIGURE 21: Excitation function for the cumulative formation
of ^{151}Pm .

□ This work

▼ Pappas and Alstad (Pa 61)

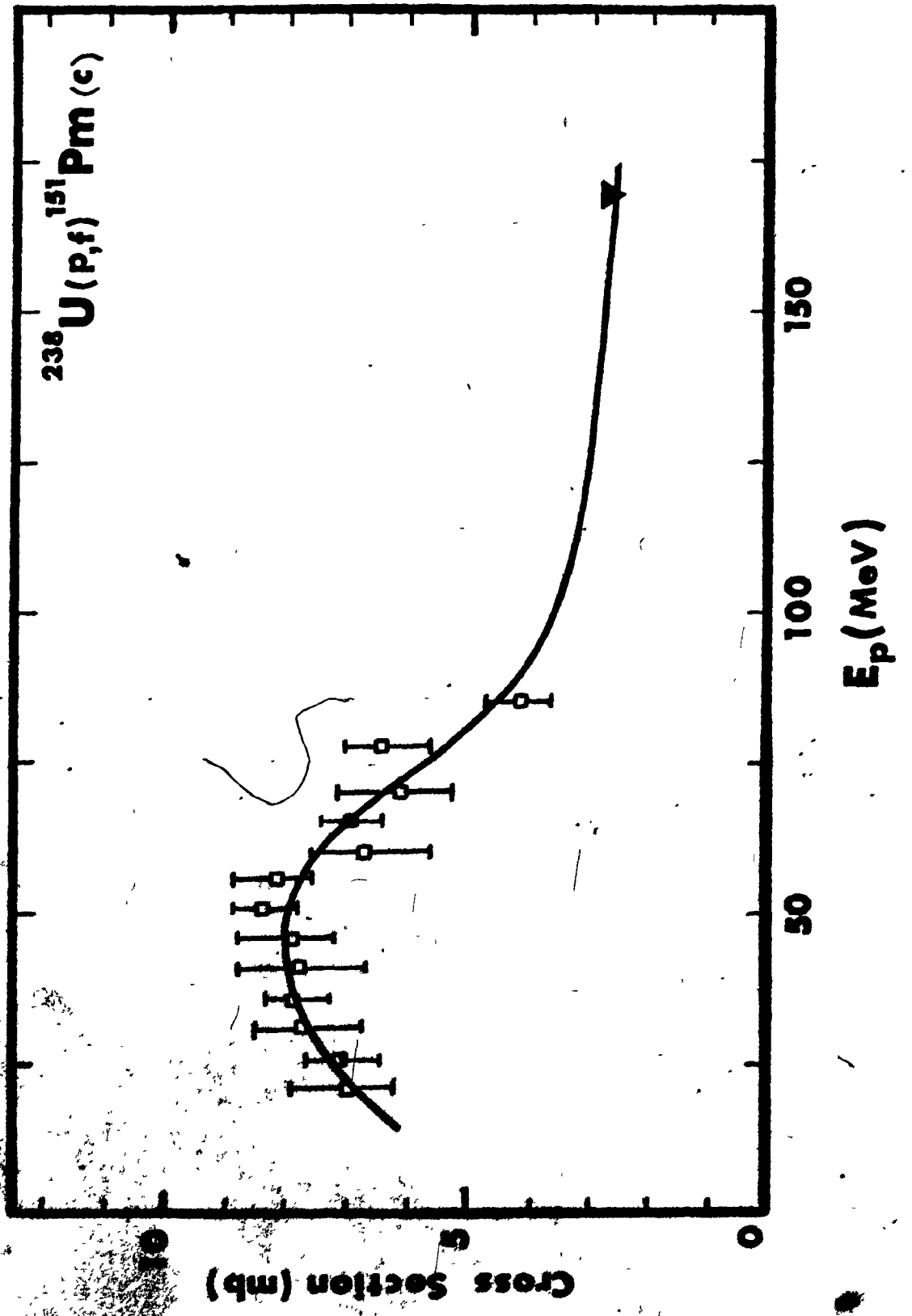


FIGURE 22: ^p Excitation function for the cumulative formation
of ^{153}Sm .

- This work
- Stevenson et al. (St 58)
- ▲ Baba et al (Ba 71)
- ▲ Pappas and Alstad (Pa 61)

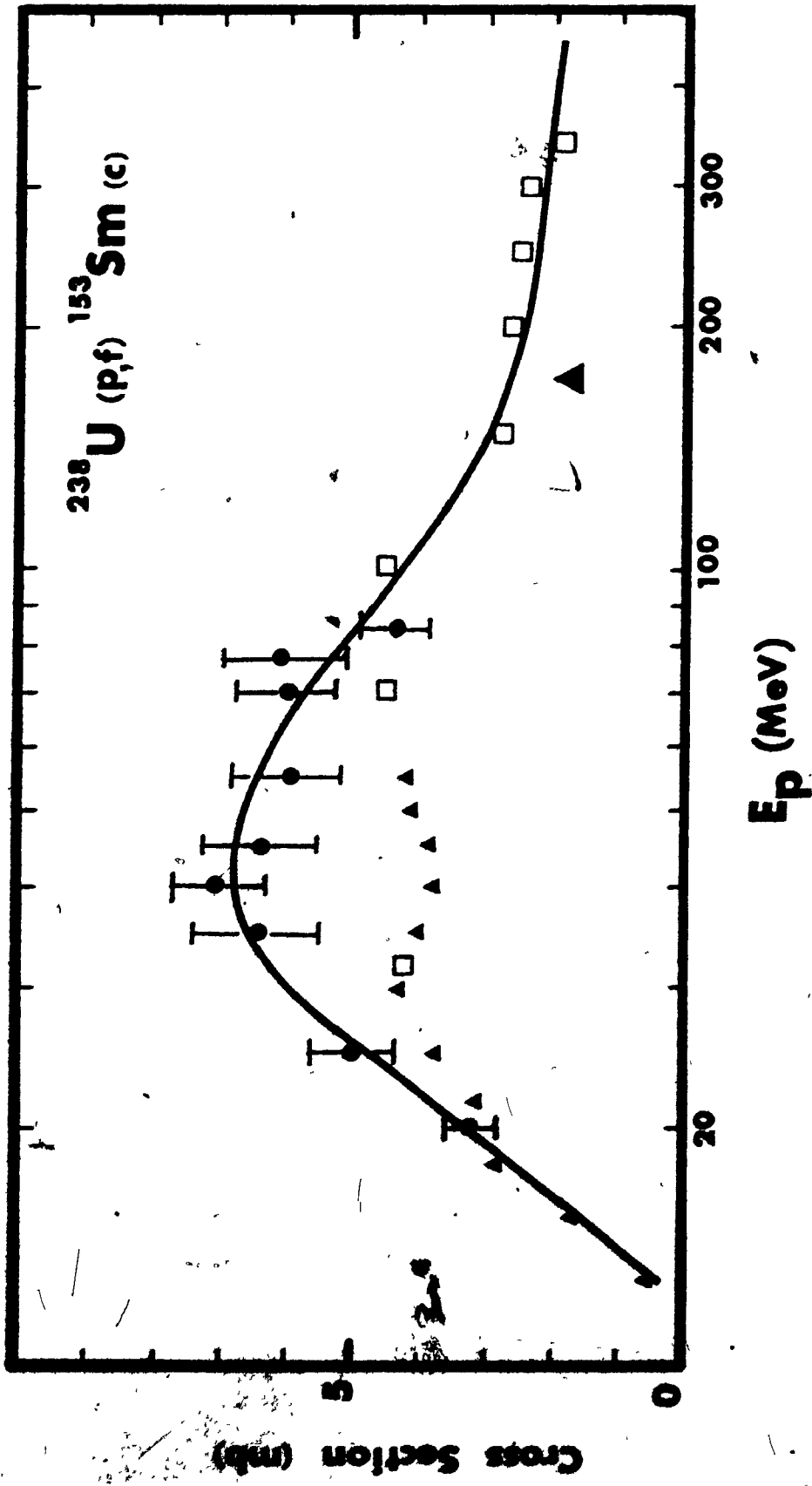


FIGURE 23: Excitation function for the cumulative formation
of ^{155}Sm .

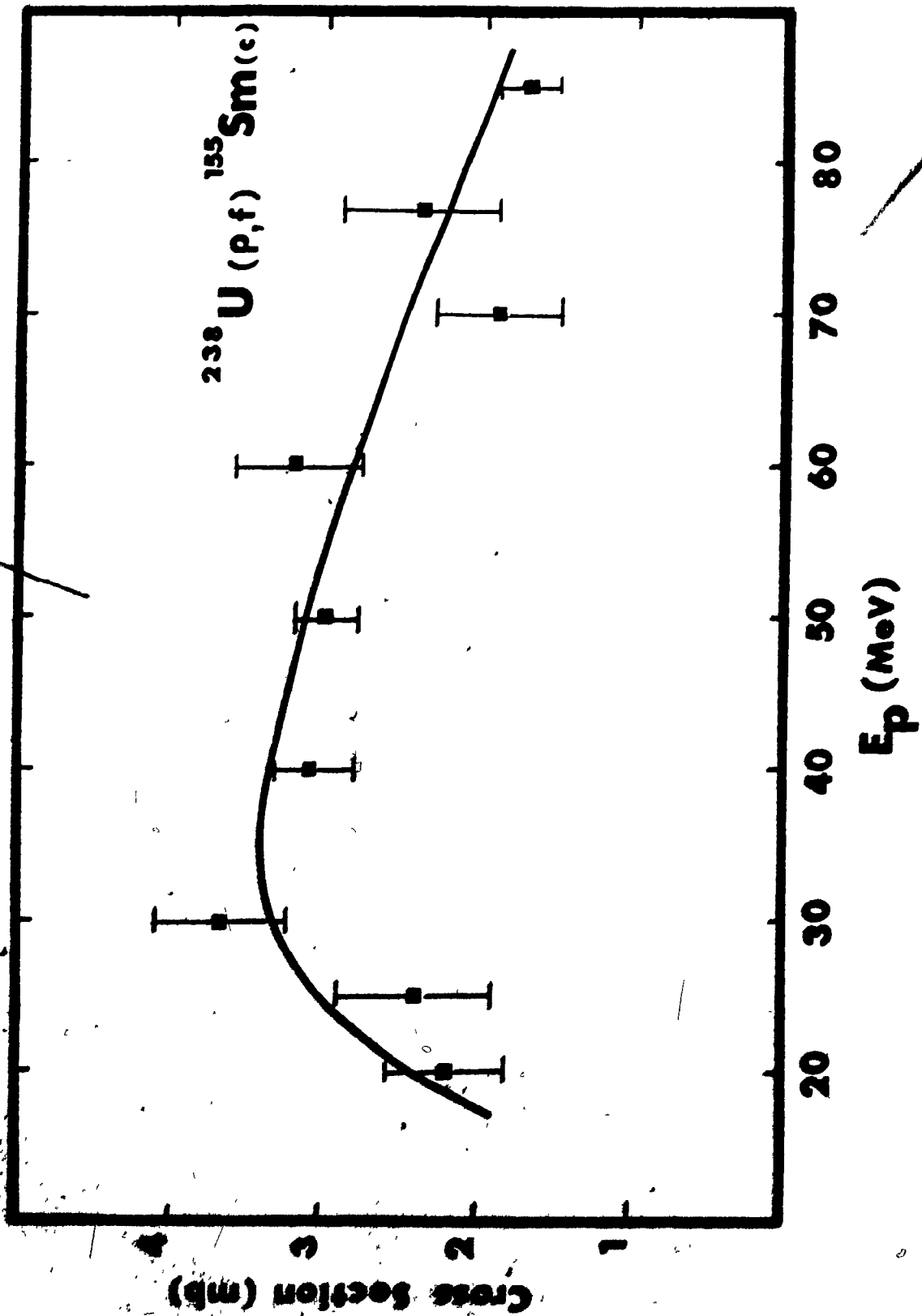
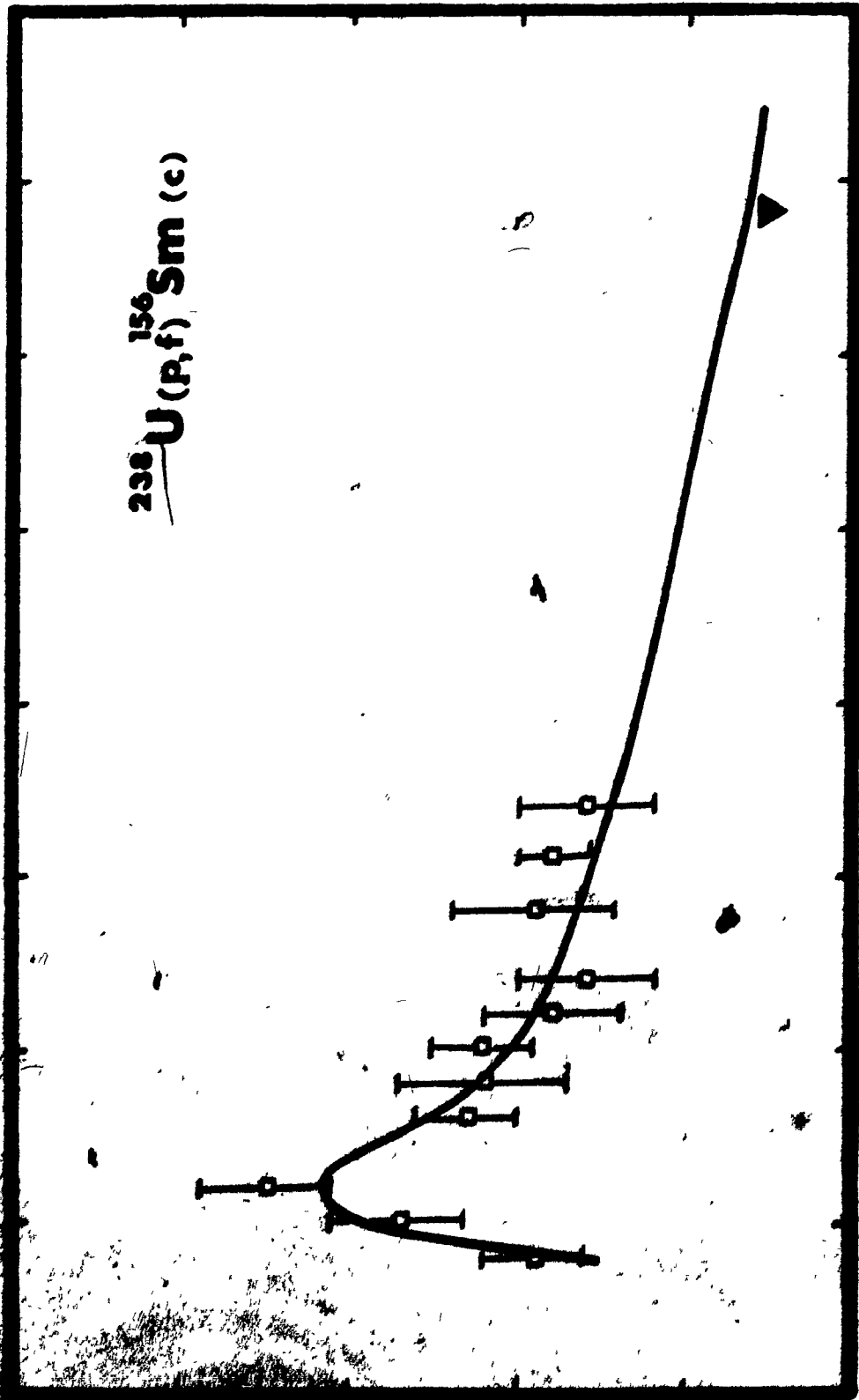


FIGURE 24: Excitation function for the cumulative formation of ^{156}Sm .

□ This work

▼ Pappas and Aistad (Pa 61)

$^{238}\text{U}(p,f)^{156}\text{Sm}(c)$



150

100

50

E_p (MeV)

Cross-section (mb)

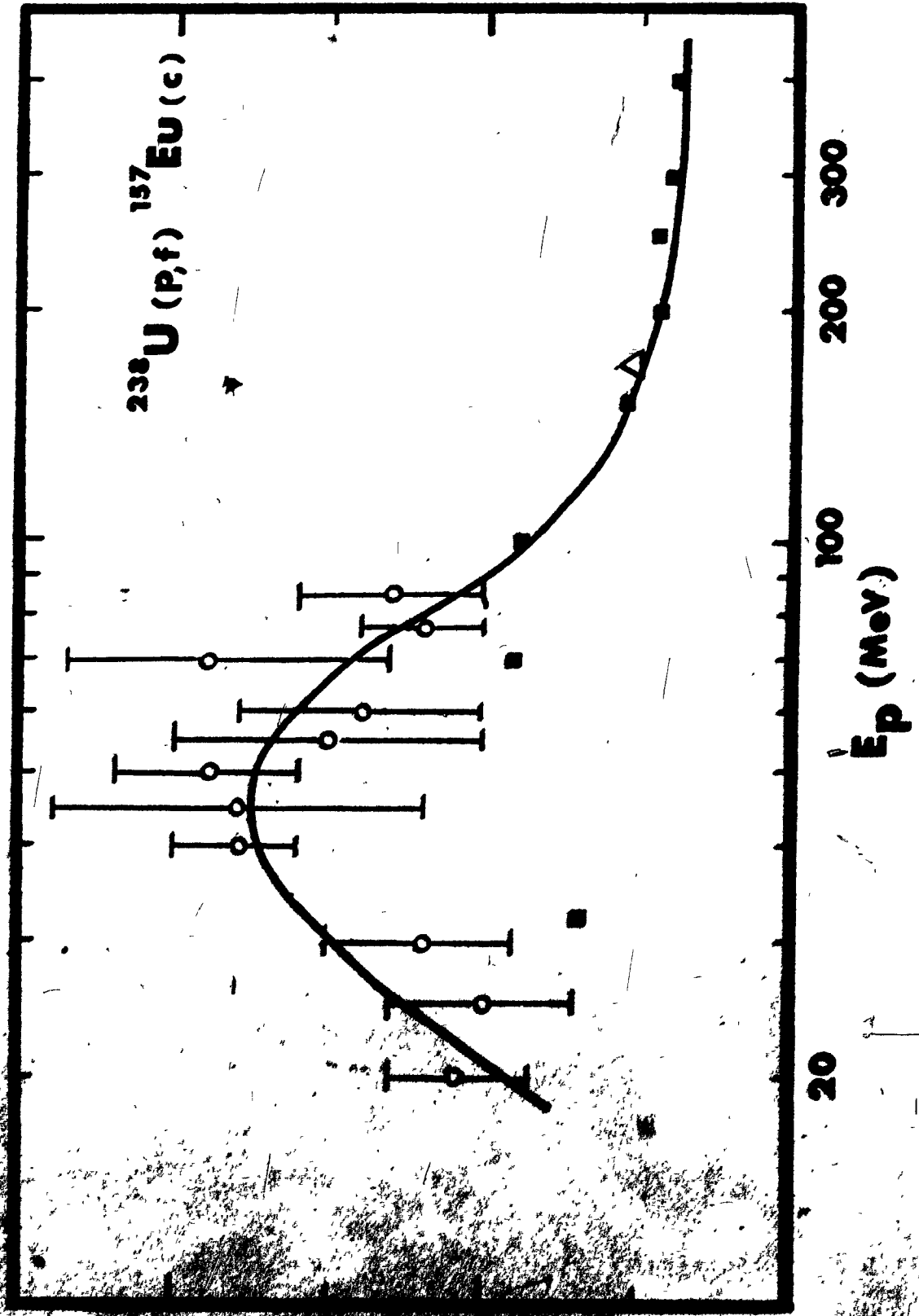
FIGURE 25: Excitation function for the cumulative formation
of ^{157}Eu .

○ This work

■ Stevenson et al. (St 58)

△ Pappas and Alstad (Pa 61)

$^{238}\text{U}(p,f)^{157}\text{Eu}(c)$



c) ^{149}Pm : the application of a straightforward subtraction procedure is no longer possible. Unlike in the previous case, ^{149}Nd and ^{149}Pm cumulative yields are almost identical within the bombarding energy range used in this work, since ^{149}Pm is a rather neutron-deficient nuclide. However, the values of ^{149}Nd and ^{149}Pm obtained show surprisingly large differences which lead to ^{149}Pm independent cross sections which are far too high to be in accord with the charge distribution systematics. This situation might partly arise from the fact that ^{149}Pm activity measurements have been carried out through its 286-keV γ -ray, whose abundance is only 2.6% (Ch 70c). A 10% error on this value would result, for example, in a ~ 2 mb increase on the cumulative cross section of ^{149}Pm at 55 MeV. The following approach was therefore adopted to estimate the independent cross sections. The cross section ratio of $^{149}\text{Pm}(c)/^{149}\text{Nd}(c)$ was determined in each sample used in this series of measurements. A value of 1.304 was found at 20 MeV, which was then used as a normalization factor for all others found at higher energy, based on the assumption that at 20 MeV almost all of mass 149 chain is distributed over ^{149}Nd and its precursors (except for a 0.04 mb contribution from ^{149}Pm as determined from charge dispersion curves constructed with the other independent yields).

These estimated $^{149}\text{Pm}(i)$ cross sections have subsequently been used only as a guide for the determination of the final charge distribution curves, by being assigned a 50%

error. No significance beyond that of a rough estimate should be placed on the values quoted.

All independent yields determined in this work are shown in Table VIII and the corresponding excitation functions appear on Figures 26 to 29.

III. TOTAL CHAIN YIELDS

The cumulative cross sections determined in this work in the mass range 146-151 have been corrected to total chain yields using a first estimate of the charge dispersion obtained with the help of the independent formation cross sections of ^{146}Pr , ^{148}Pm , ^{150}Pm , ^{149}Pm and ^{151}Pm . For masses higher than $A=151$, no such correction has been attempted, since the charge dispersion parameters determined for lighter products may not apply to this mass range. The cumulative yields of ^{153}Sm , ^{155}Sm , ^{156}Sm and ^{157}Eu have therefore been used as lower limits for total chain yields of the corresponding masses.

Our data, along with other published in the literature, are shown on Figures 32 through 44. The portion of the mass distribution covering the mass range 132-161 has been found to be well described by Gaussian distribution (Ba 71). This assumption has been used here to perform a least-squares fit, using the ORGLS program already mentioned in the experimental procedures section. The results of such a treatment are shown in Table IX. The position of the maximum of the heavy side of

TABLE VIII: Independent formation cross sections (in millibarns)*

	^{148}Pm N/Z=1.4262	$^{149}\text{Pm}^a$ N/Z=1.4426	^{150}Pm N/Z=1.4590	$^{146}\text{Pr}^b$ N/Z=1.4746	$^{151}\text{Pm}^c$ N/Z=1.4754
20	-----	0.04 ± 0.02	0.15 ± 0.03 (2)	3.5 ± 0.8	2.8 ± 0.5
25	-----	0.04 ± 0.02	0.22 ± 0.05 (2)	4.5 ± 0.9	2.3 ± 0.5
30	-----	0.05 ± 0.03	0.31 ± 0.04 (2)	6.4 ± 0.7	2.5 ± 0.3
35	-----	0.12 ± 0.06	0.47 ± 0.12 (1)	7.4 ± 1.6	2.8 ± 0.6
40	-----	0.21 ± 0.10	0.80 ± 0.22 (3)	6.4 ± 1.0	2.8 ± 0.6
45	-----	0.42 ± 0.20	1.20 ± 0.30 (1)	8.4 ± 1.8	2.9 ± 0.6
50	0.15 ± 0.04 (1)	0.54 ± 0.27	1.69 ± 0.42 (1)	11.5 ± 2.5	3.7 ± 0.7
55	0.12 ± 0.03 (2)	0.62 ± 0.31	1.50 ± 0.15 (4)	10.2 ± 2.1	3.5 ± 0.8
60	0.16 ± 0.04 (2)	0.64 ± 0.32	1.53 ± 0.22 (2)	9.4 ± 1.4	2.4 ± 0.5
65	0.25 ± 0.06 (1)	0.61 ± 0.30	1.49 ± 0.18 (2)	10.9 ± 2.7	2.7 ± 0.5
70	0.31 ± 0.05 (2)	0.88 ± 0.44	1.75 ± 0.14 (2)	9.4 ± 2.0	1.8 ± 0.4
77	0.39 ± 0.10 (1)	0.97 ± 0.48	2.18 ± 0.17 (4)	7.6 ± 1.7	1.5 ± 0.3
85	0.49 ± 0.08 (2)	0.88 ± 0.44	2.54 ± 0.23 (2)	6.0 ± 1.0	1.0 ± 0.2

*The numbers in brackets give the number of determinations.

a = best estimated values (see text for details)

b = $\sigma_{\text{ind}}^{146}\text{Pr} = \sigma_{\text{cum}}^{146}\text{Pr} - \sigma_{\text{cum}}^{146}\text{Ce}$

c = $\sigma_{\text{ind}}^{151}\text{Pm} = \sigma_{\text{cum}}^{151}\text{Pm} - \sigma_{\text{cum}}^{151}\text{Nd}$

FIGURE 26: Excitation functions for the independent formation
of ^{148m}Pm and ^{150}Pm .

● ○ This work

◇ Pappas and Aistad (Pa 61)

10

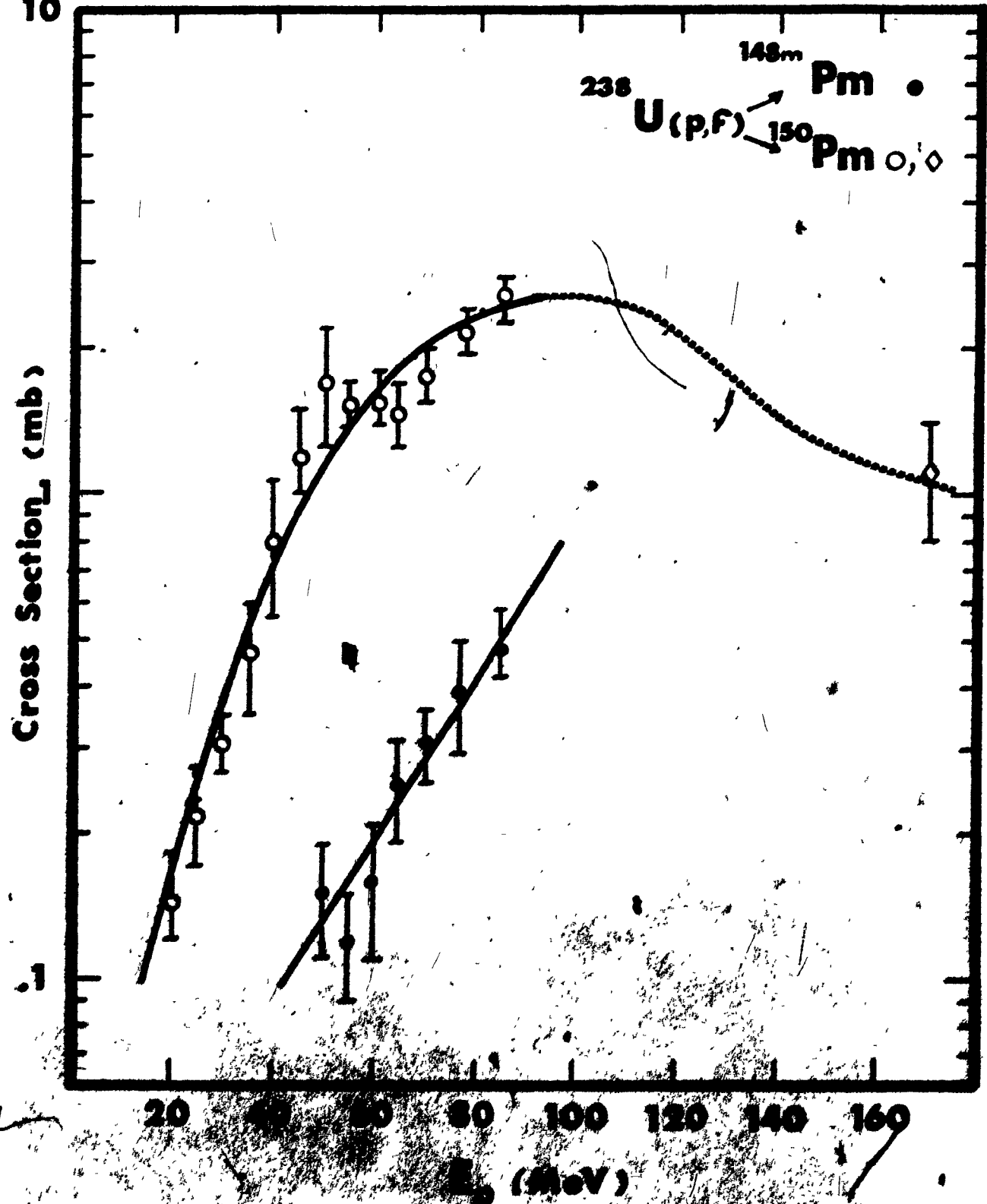


FIGURE 27: Excitation function for the independent formation
of ^{146}Pr .

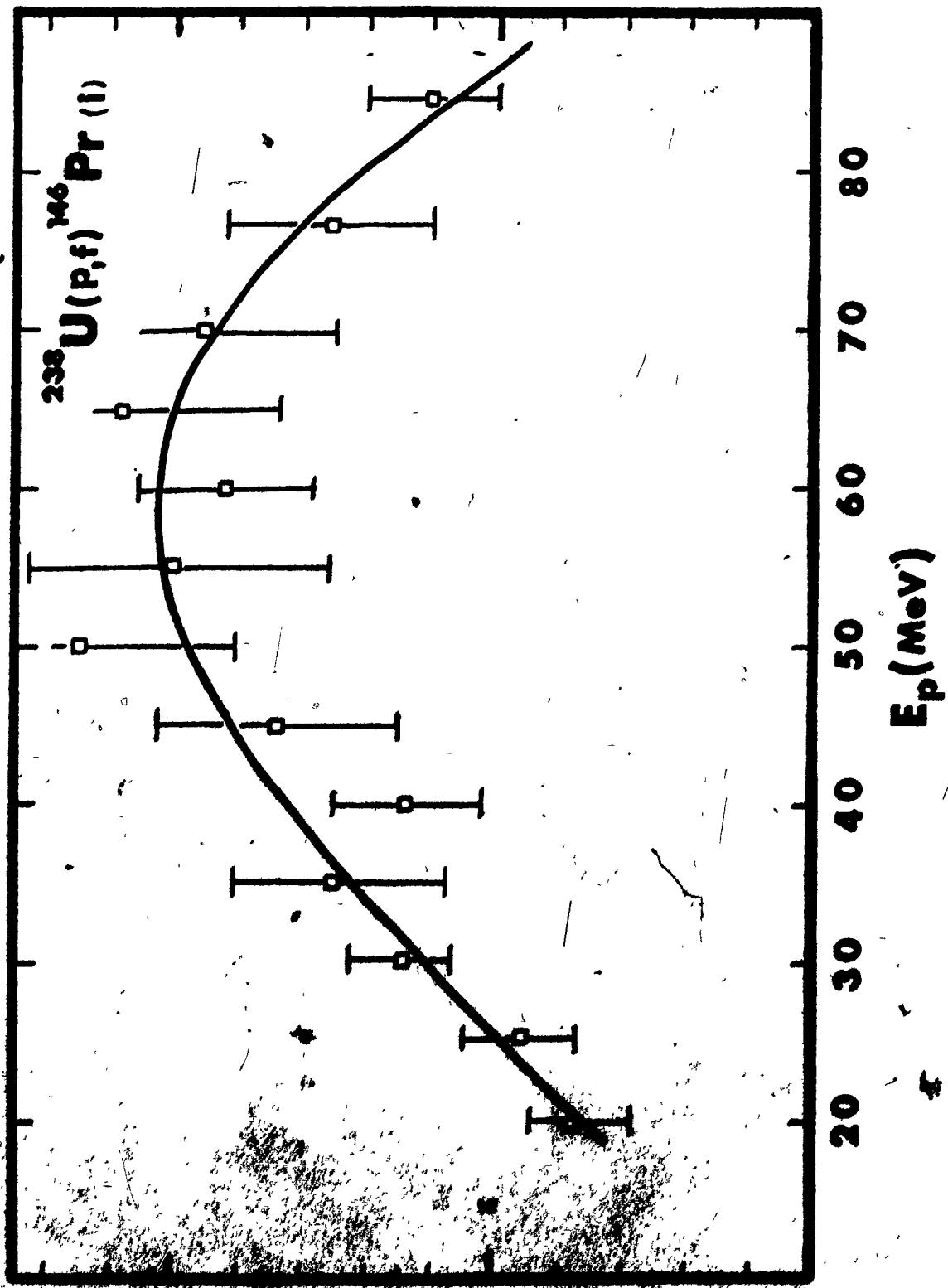


FIGURE 28: Excitation function for the independent formation of ^{151}Pm .

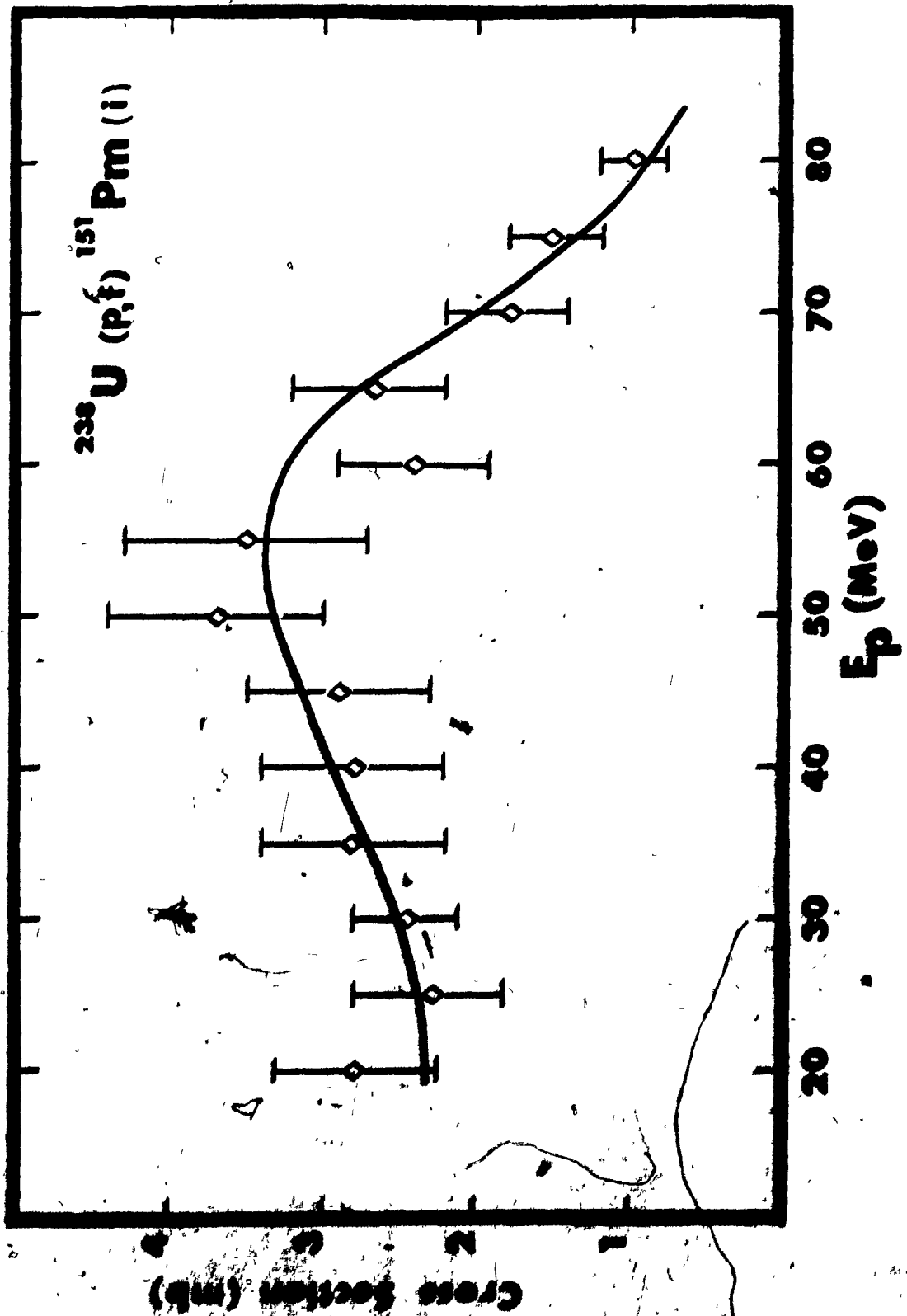
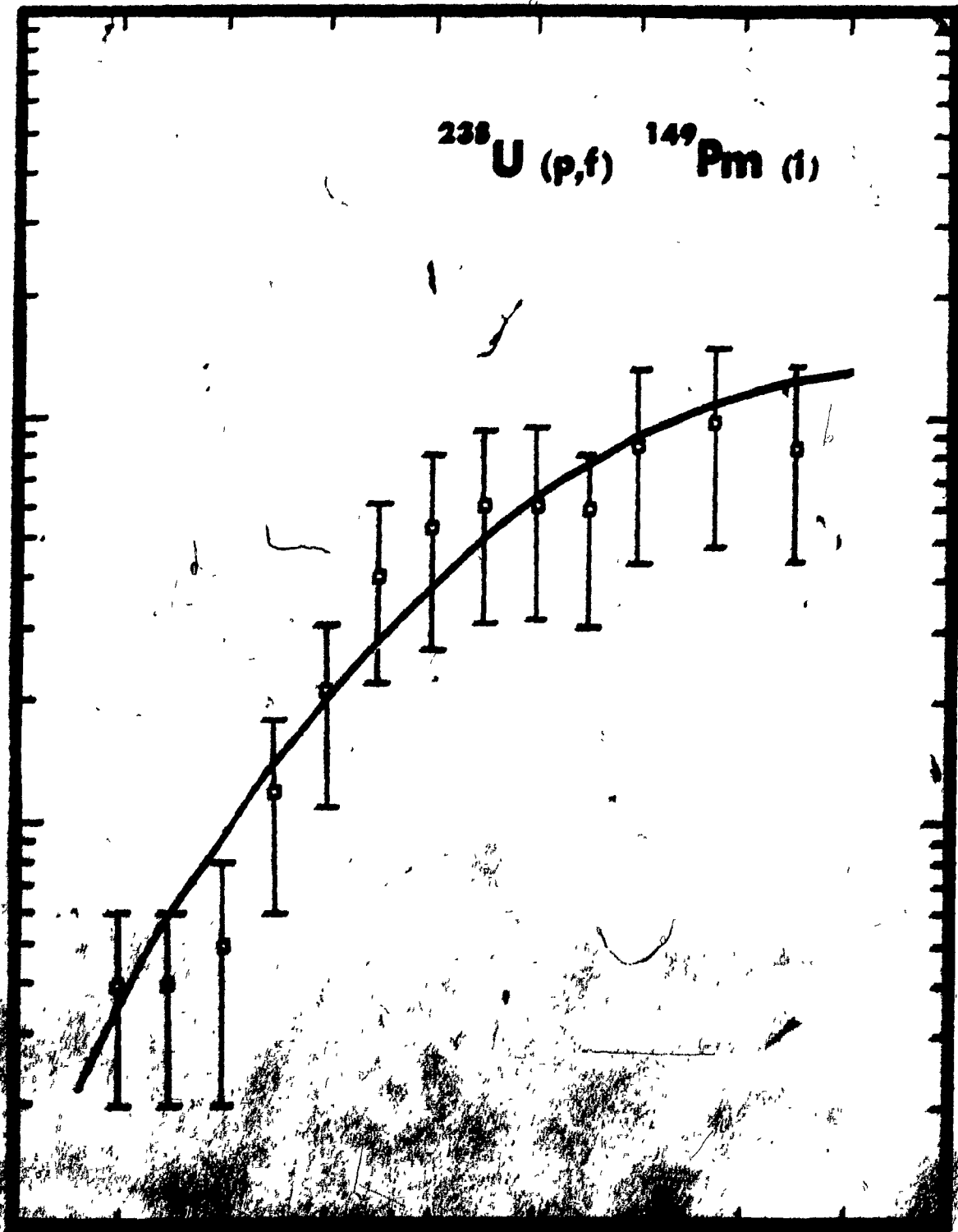


FIGURE 29: Excitation function for the independent formation
of ^{149}Pm .

Cross Section (mb)

^{238}U (p,f) ^{149}Pm (f)



the mass distribution, the corresponding total chain yield and the half-width at half-maximum (HWHM) of the assumed Gaussian distribution are listed in columns 2 to 4. The last column shows the values at each energy of a fit parameter defined as: $\sqrt{W*(O-C)^2/(NO-NV)}$

where: O = observed value NO = number of observation
 C = calculated value NV = number of variables
 W = statistical weight of the data points taken as the inverse of the uncertainties on the experimental determinations.

The values of total chain yields inferred from the Gaussian fit and used in subsequent independent fractional yields calculations are shown in Table X. The mass distribution curves appear on Figures 30 through 42 inclusively.

IV. FRACTIONAL INDEPENDENT YIELDS

The fractional independent yields were computed by dividing the experimentally determined independent cross sections by the total chain yields obtained as described above. An average additional error of 10% arising from the uncertainty in total chain yields values was added to the existing error bars on independent cross sections.

In the case of ^{148}Pm , the independent cross section had to be corrected for the contribution of ^{148}Pm to the overall yield of formation of this nuclide. (it was not possible to detect ^{148}Pm in the course of the experiments

TABLE IX: Parameters for the heavy side of the mass distribution

E_p (MeV)	A_p	NRMM (λ units)	σ_{max} (mb)	χ^2
20	136.7	11.5	36.4	0.562
25	135.9	11.0	47.6	0.669
30	135.8	11.0	49.5	0.759
35	134.9	12.0	57.2	0.964
40	133.2	12.5	56.6	0.712
45	132.3	12.0	67.2	0.403
50	132.4	11.0	69.8	0.392
55	132.2	12.5	66.4	0.809
60	130.2	12.5	65.8	1.159
65	130.4	12.0	75.1	1.007
70	131.0	13.0	68.4	0.625
77	126.6	13.0	77.8	0.706
85	127.8	11.0	70.8	0.702

$$\chi^2 \text{ fit factor} = \chi = \sqrt{\sum W(O-C)^2 / (NO-NV)}$$

O = observed value

NO = number of observations

C = calculated value

NV = number of variables

W = statistical weight

Table 2. Total chain yields used in fractional chain yield calculations

Chain Number	146	147	148	149	150	151
20	17.51	14.84	12.36	10.11	8.14	6.44
21	20.29	16.99	13.99	11.33	9.03	7.07
22	21.29	17.90	14.81	12.05	9.64	7.60
23	22.51	18.88	15.66	12.69	10.17	8.03
24	20.06	16.95	14.14	11.64	9.47	7.61
25	21.07	17.73	14.75	12.12	9.83	7.88
26	22.61	19.04	15.84	13.02	10.57	8.48
27	21.23	17.89	14.90	12.26	9.97	8.01
28	17.67	14.87	12.39	10.22	8.34	6.74
29	19.66	16.28	13.47	11.02	8.91	7.13
30	17.73	14.72	12.07	9.78	7.83	6.20
31	14.59	12.22	10.15	8.35	6.81	5.51
32	13.01	10.75	8.78	7.10	5.69	4.51

FIGURE 30: Heavy side of the mass distribution resulting from proton fission of natural uranium at 20MeV.

● This work

▲ Smith et al. (Pa 67)

■ Smith et al. (Pa 71) (interpolated)

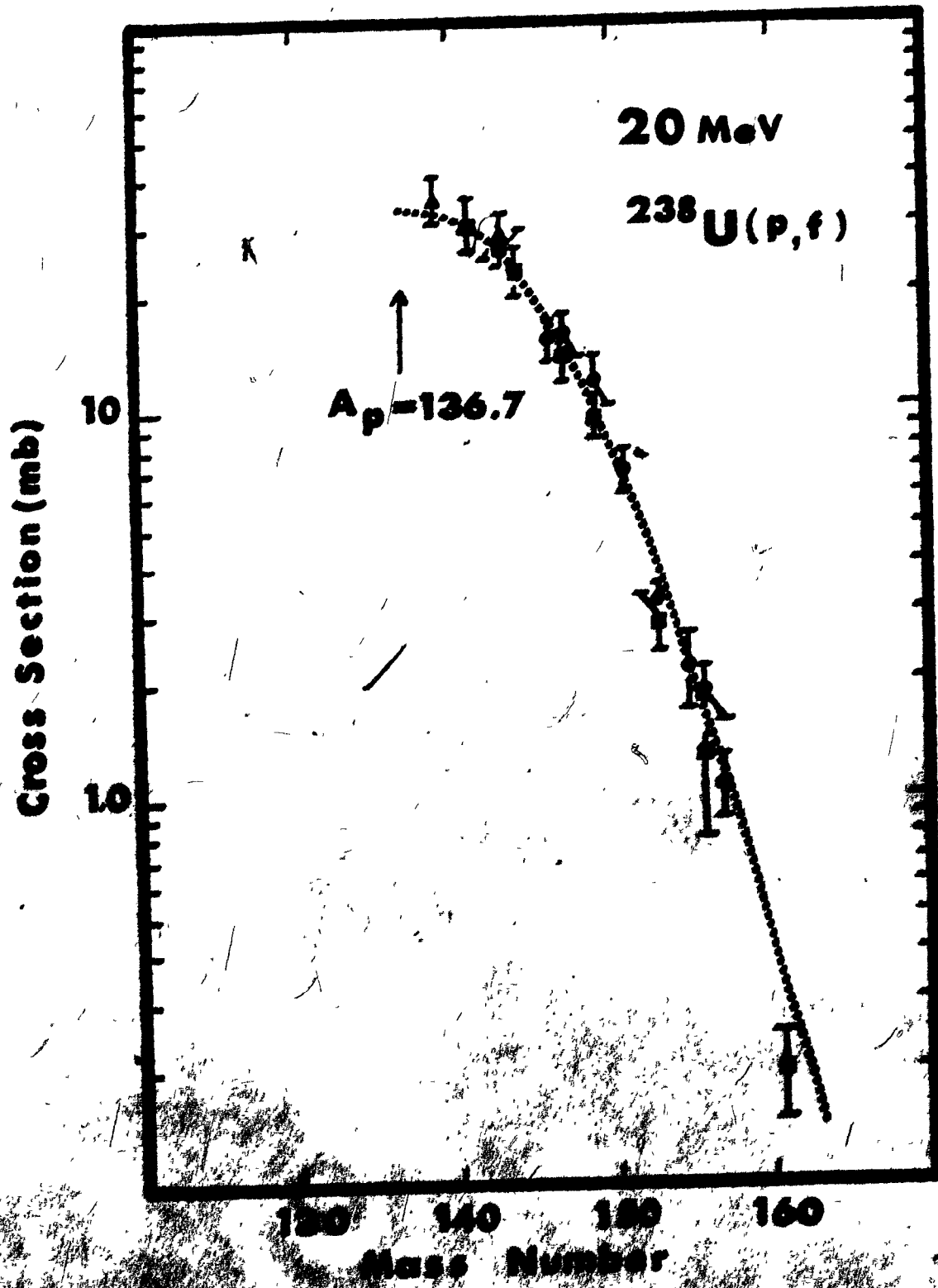


FIGURE 21: Heavy side of the mass distribution resulting from proton fission of natural uranium at 25 MeV.

- This work
- Raba et al. (1971)

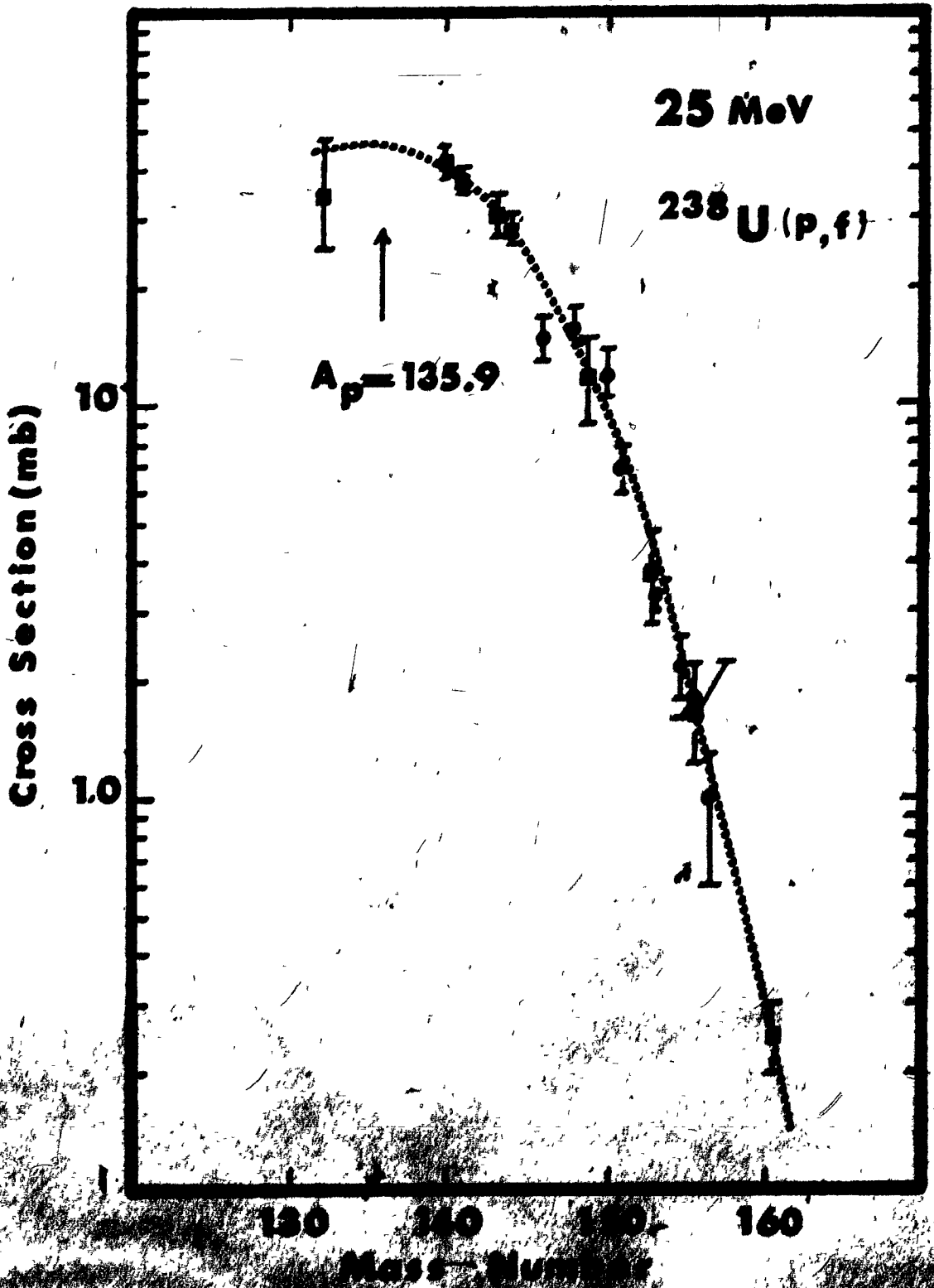


FIGURE 22: Heavy side of the mass distribution resulting from proton fission of natural uranium at 30 MeV.

- This work
- Dikšić et al. (Di 74)
- ▲ Parikh et al. (Pa 67)
- ◇ Stevenson et al. (St 58)
- Baba et al. (Ba 71)

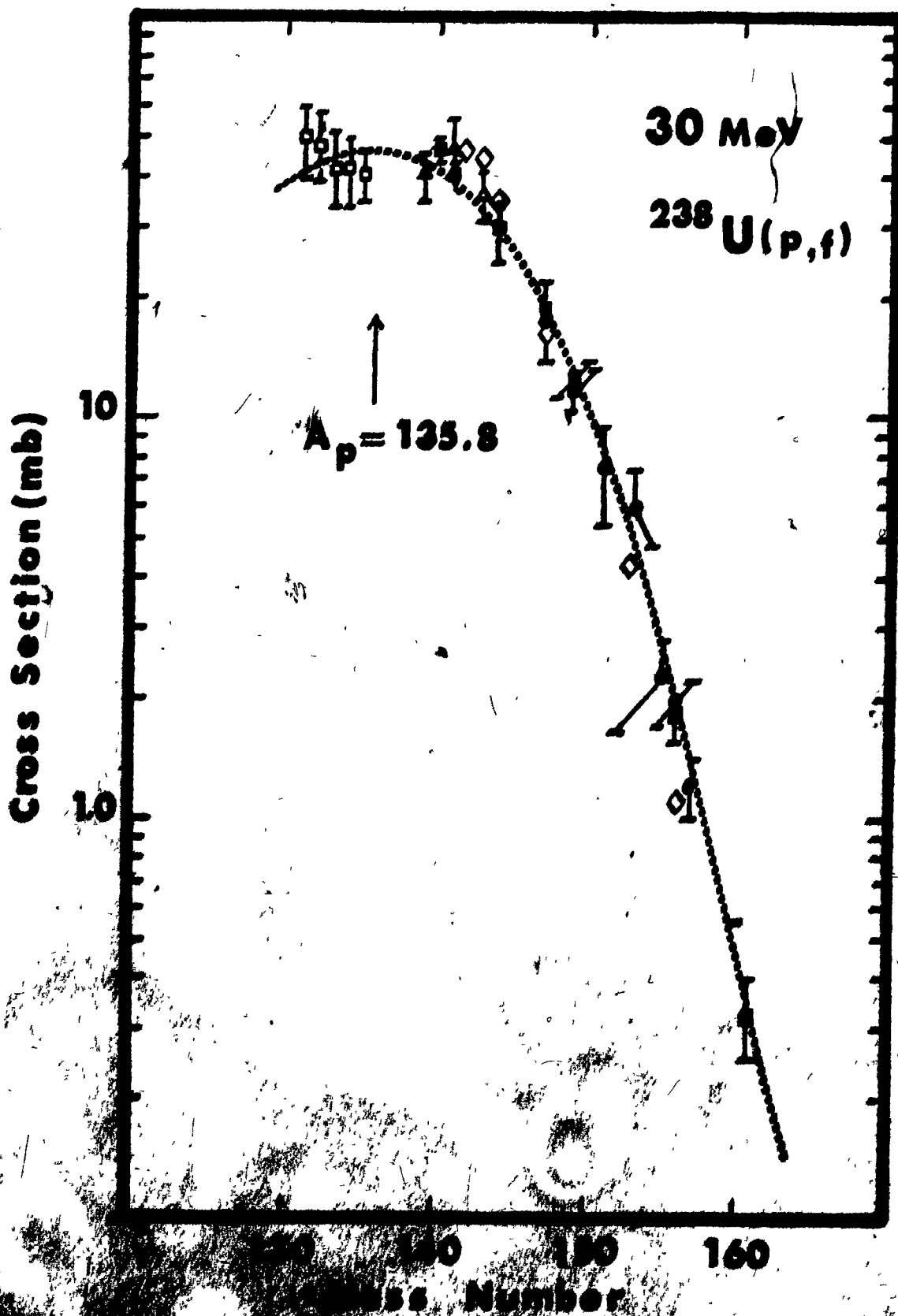


FIGURE 33: Heavy side of the mass distribution of natural uranium resulting from proton fission of natural uranium at 35 MeV.

- **This work**
- **Dikšić et al. (D1 74) (interpolated)**
- **Umezawa et al. (Um 71)**
- **Saba et al. Sa 71)**

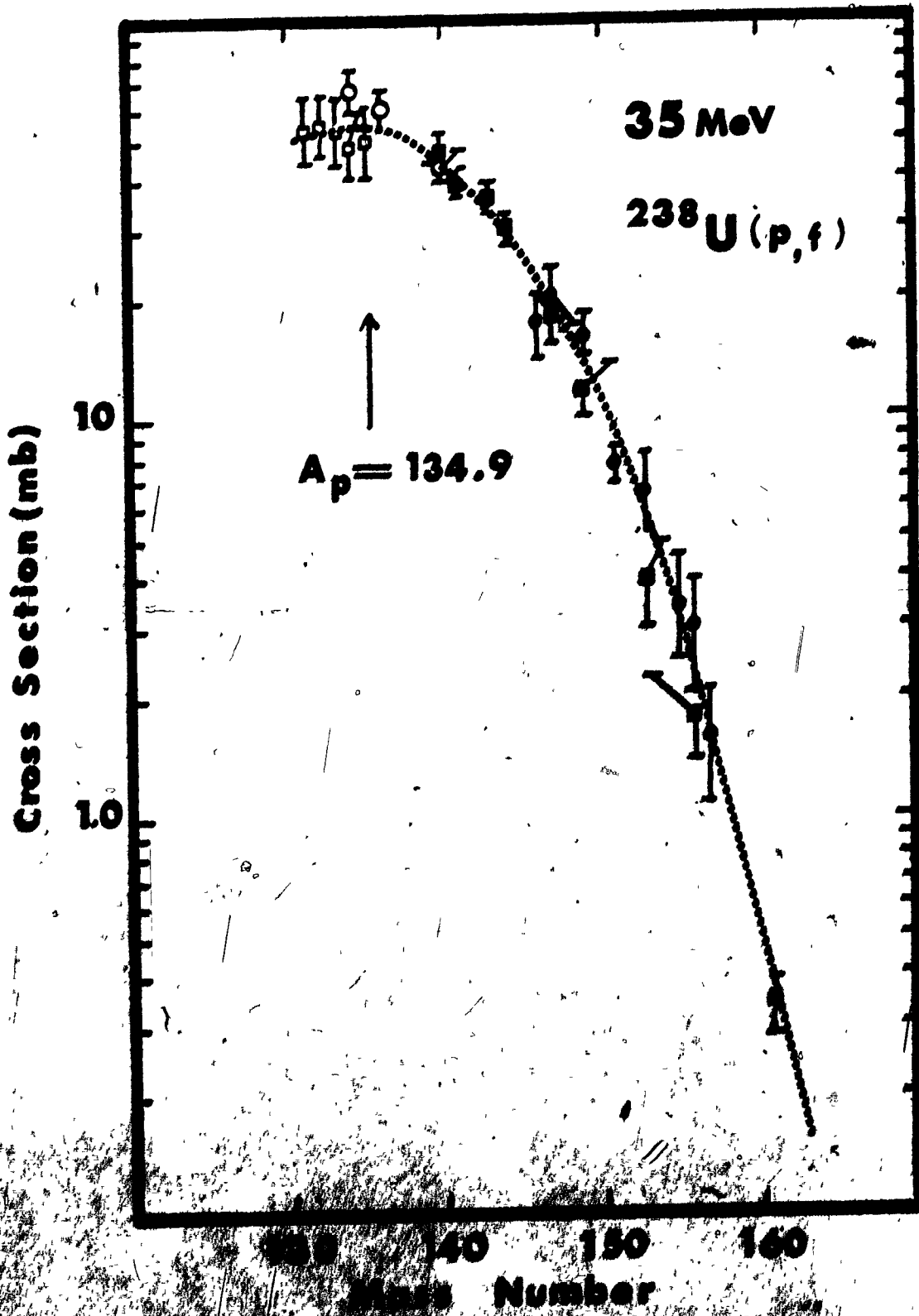


FIGURE 34: Heavy side of the mass distribution resulting from proton fission of natural uranium at 40 MeV.

- This work
- Dikić et al. (Di 74)
- ▲ Parikh et al. (Pa 67)
- Umezawa et al. (Um 71)
- Baba et al. (Ba 71)

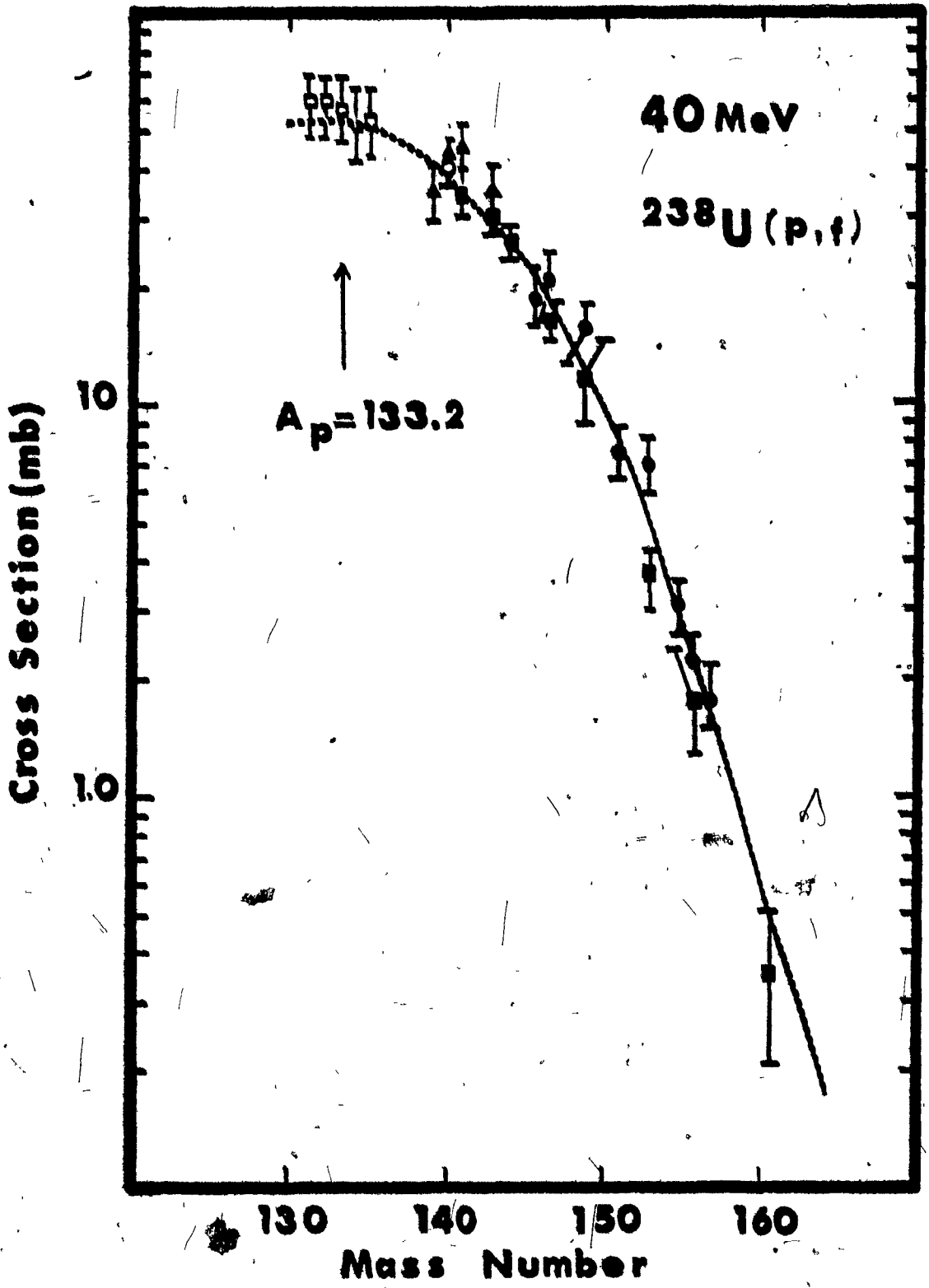


FIGURE 35: Heavy side of the mass distribution resulting from proton fission of natural uranium at 45 MeV.

- This work
- Dikić et al. (Di 74) (interpolated)
- Umazawa et al. (Um 71)
- Baba et al. (Ba 71)

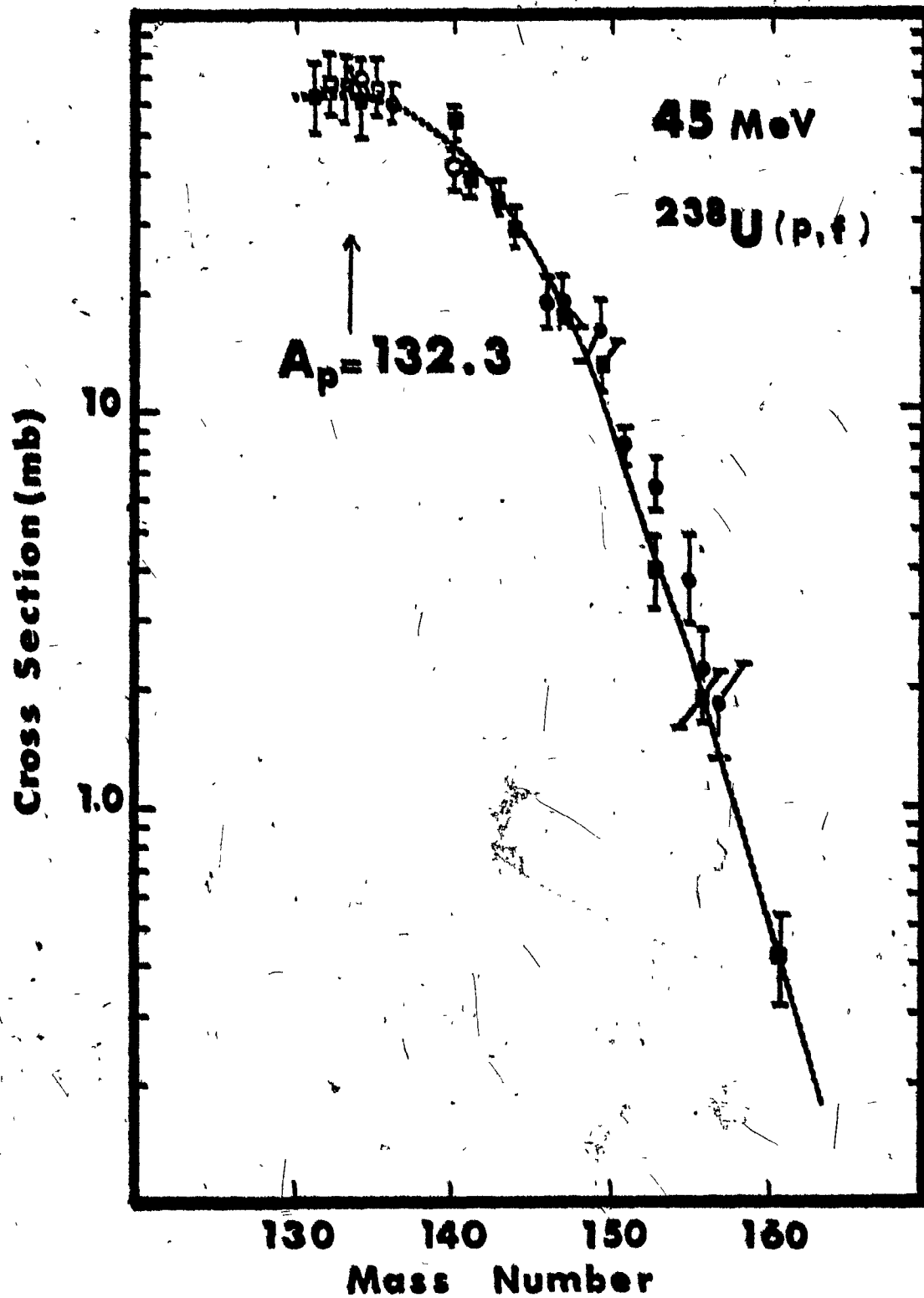


FIGURE 16: Heavy side of the mass distribution resulting from proton fission of material uranium at 50 MeV.

- This work
- Dikić et al. (Di 74)
- ▲ Parikh et al. (Pa 67)
- Baba et al. (Ba 71)

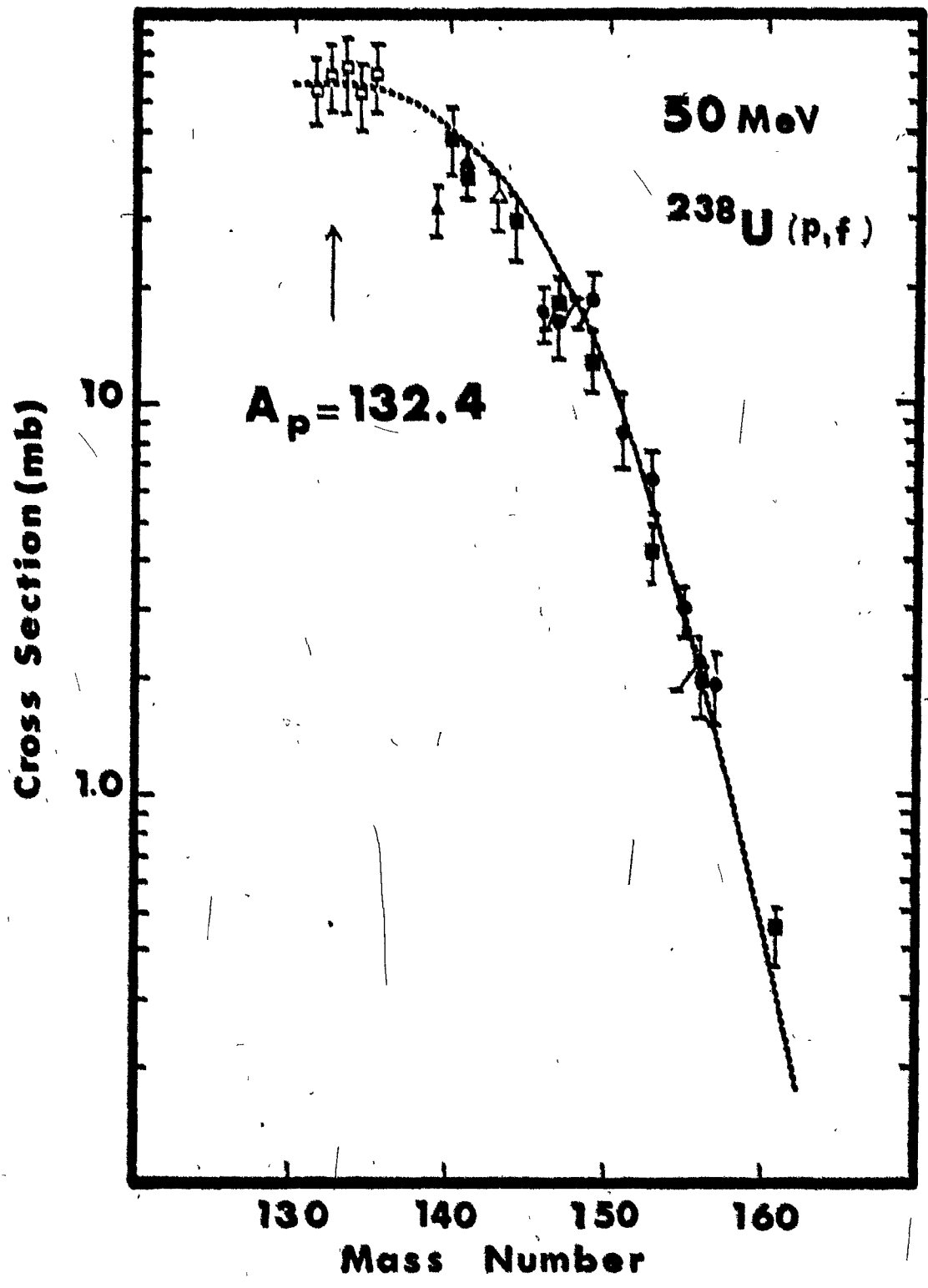


FIGURE 37: Heavy side of the mass distribution resulting from proton fission of natural uranium at 55 MeV.

- This work
- Dikić et al. (Di 74) (interpolated)
- Umezawa et al. (Um 71)
- Baba et al. (Ba 71)

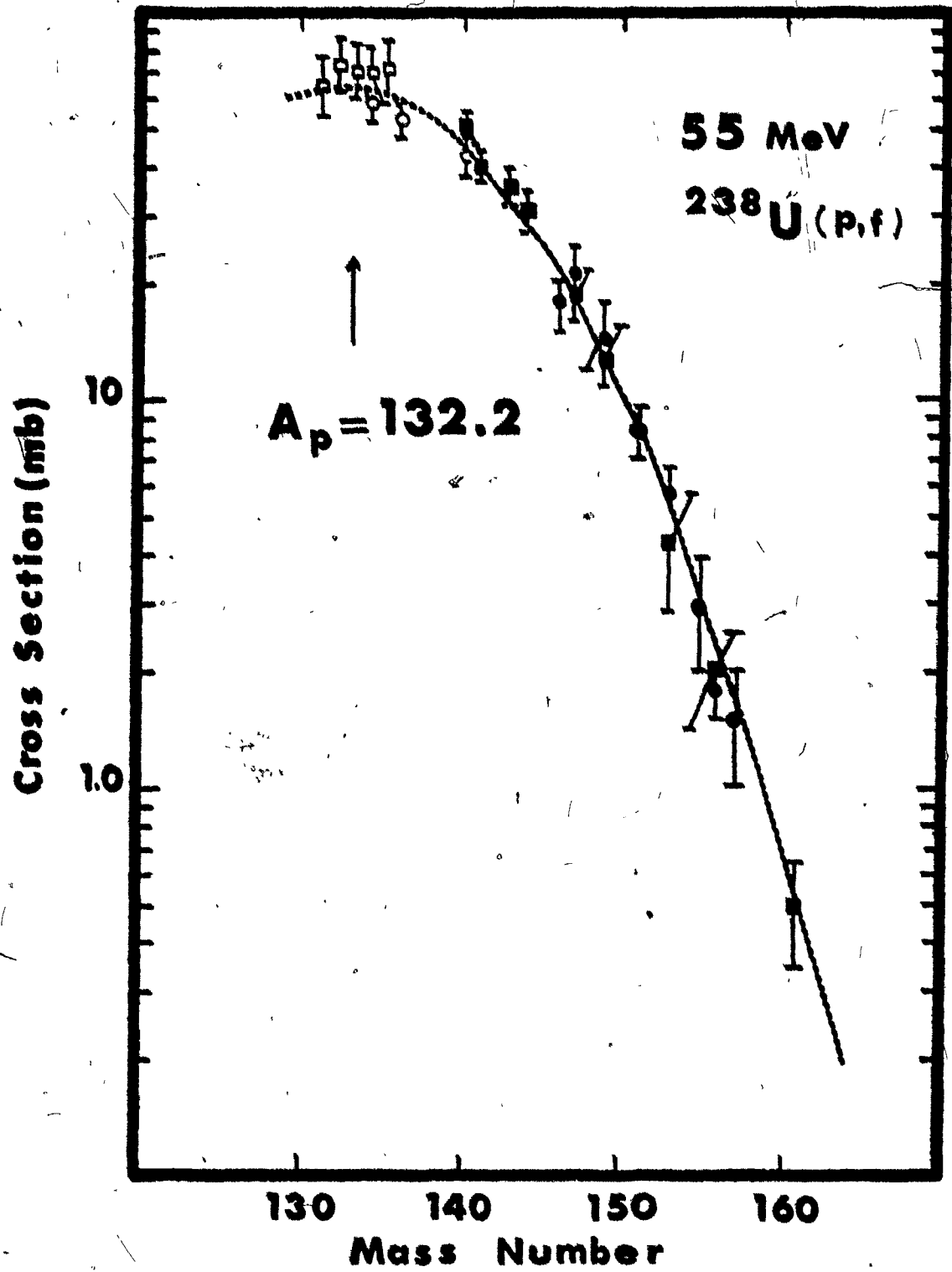


FIGURE 38: Heavy side of the mass distribution resulting from proton fission of natural uranium at 60 MeV.

- This work
- Dikšić et al. (Di 74)
- ▲ Parikh et al. (Pa 67)
- Umezawa et al. (Um 71)

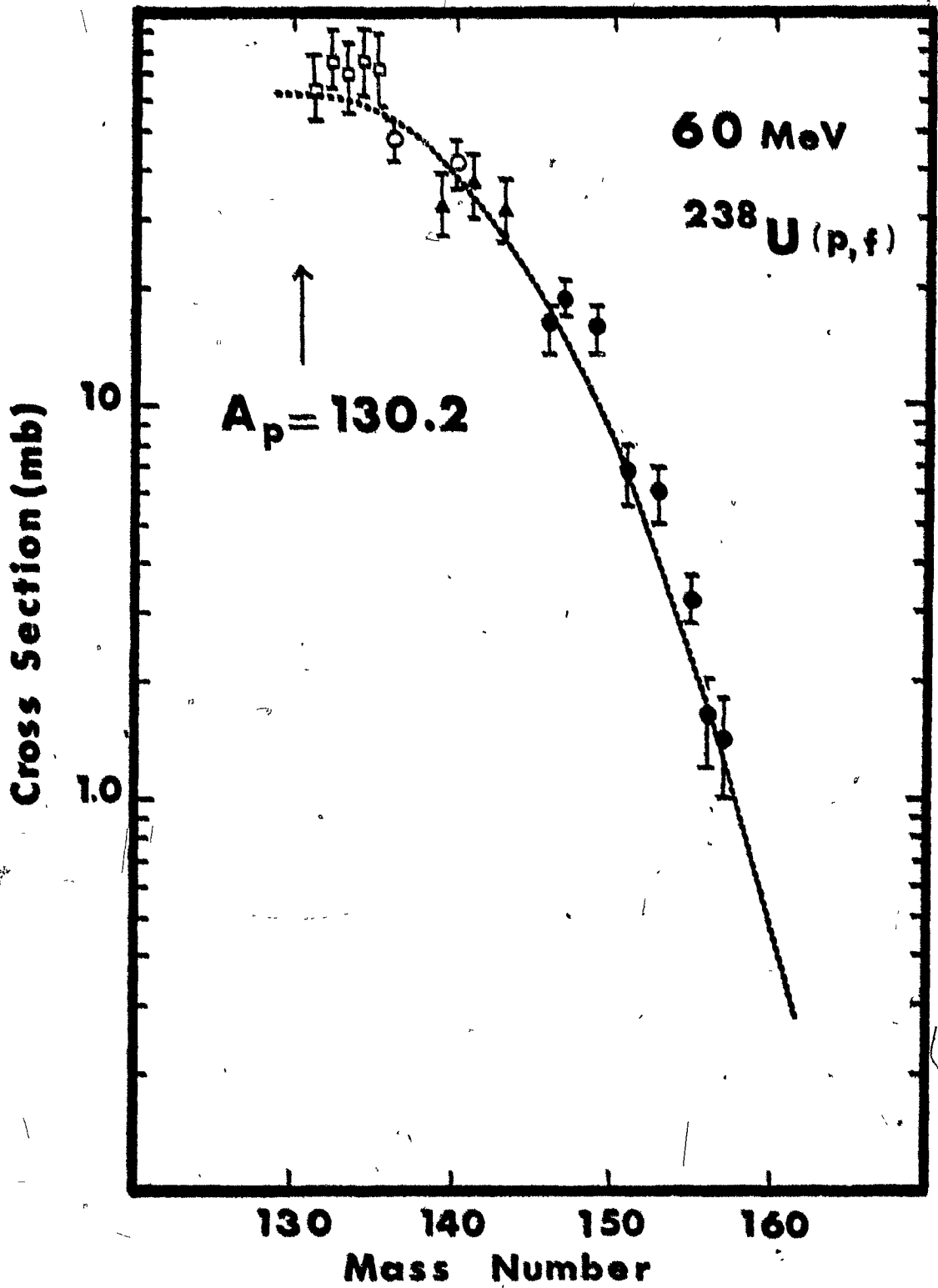


FIGURE 39: Heavy side of the mass distribution resulting from proton fission of natural uranium at 65 MeV.

- This work
- Dikšić et al. (Di 74) interpolated

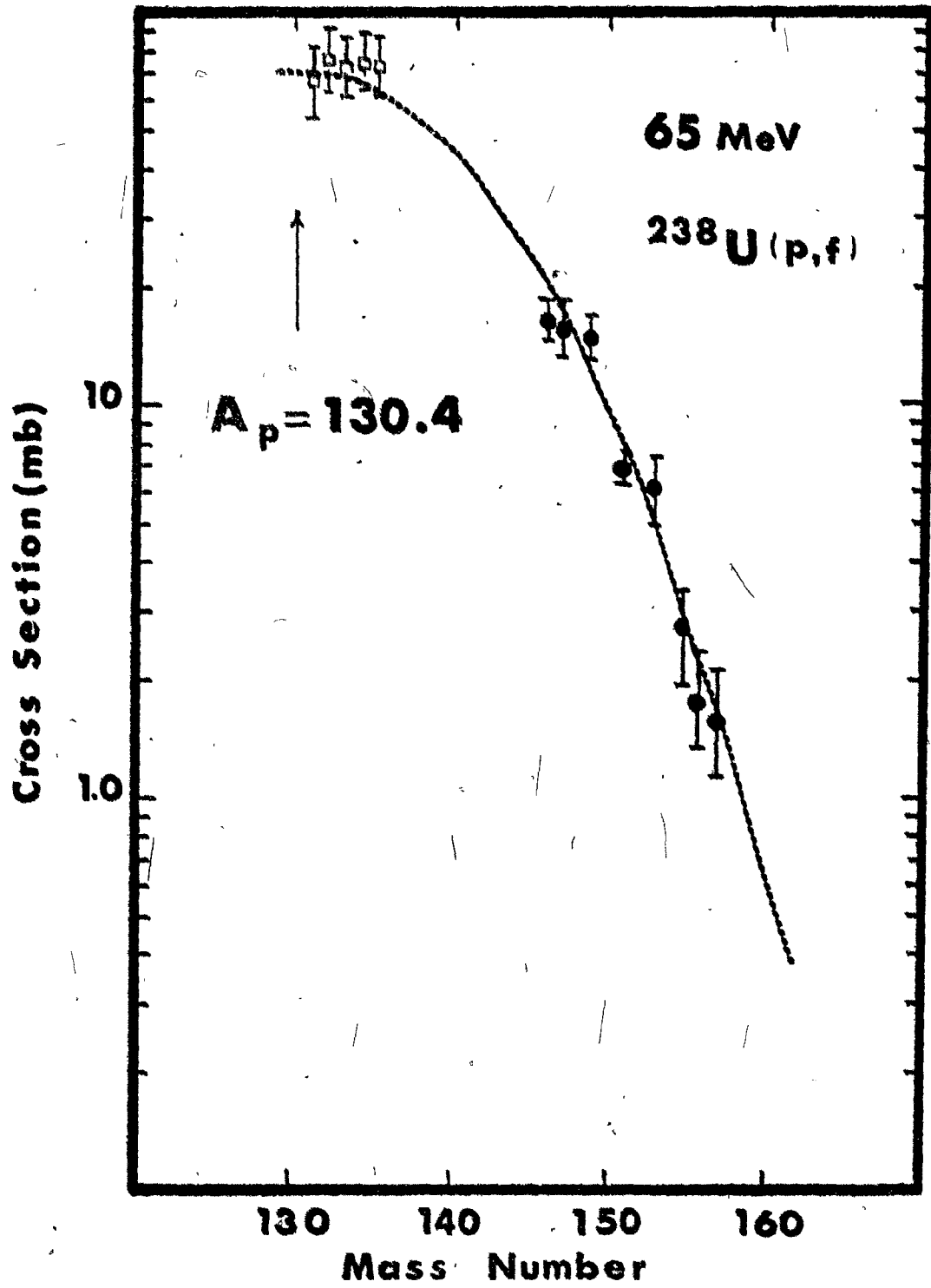


FIGURE 40: Heavy side of the mass distribution resulting from proton fission of natural uranium at 70 MeV.

- This work
- Dikić et al. (Di 74)
- ◇ Stevenson et al. (St 58)
- ▲ Parikh et al. (Pa 67)

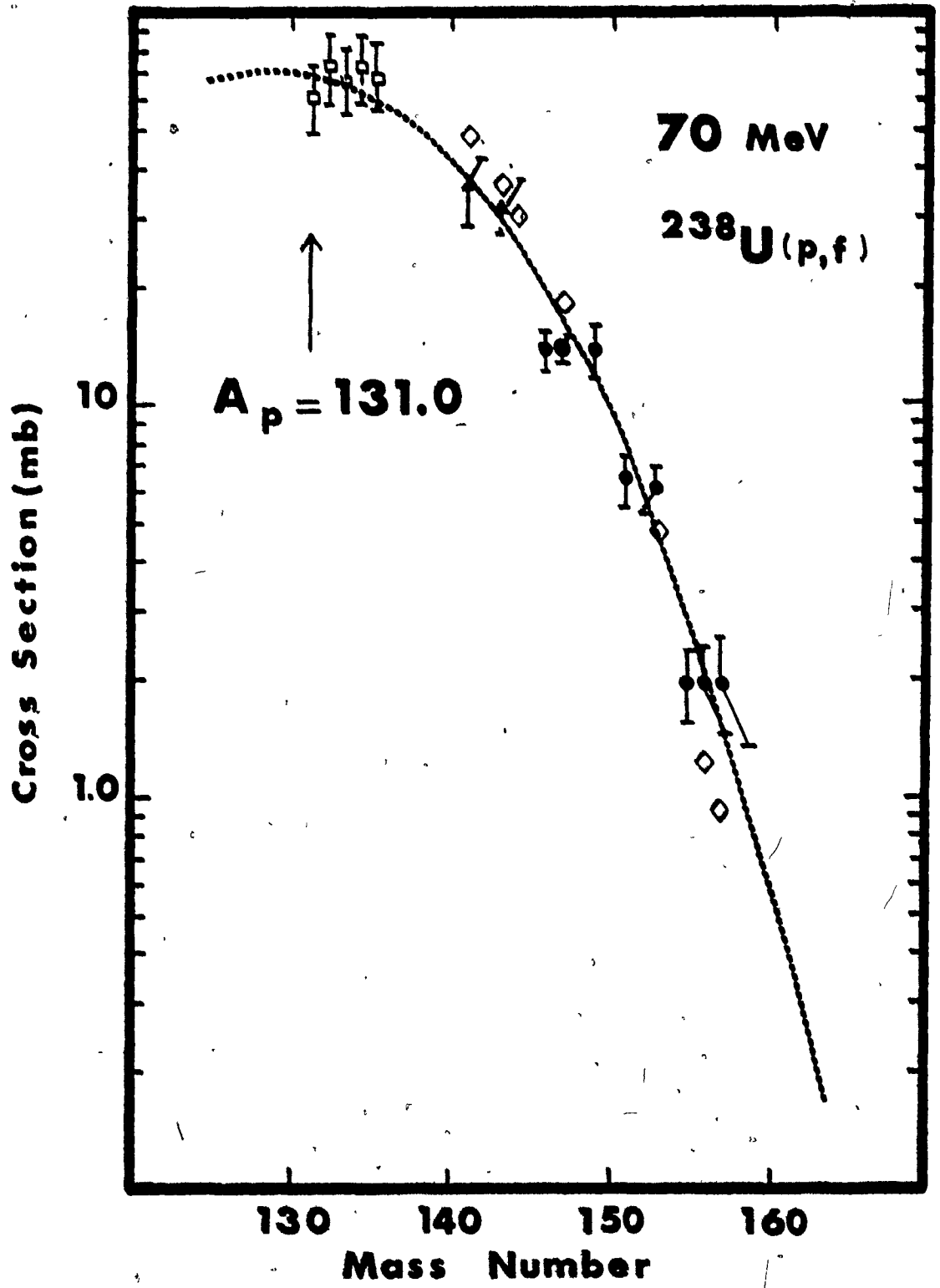


FIGURE 41: Heavy side of the mass distribution resulting from proton fission of natural uranium at 77 MeV.

- This work
- Dikšić et al. (Di 74) (interpolated)
- ▲ Parikh et al. (Pa 67)

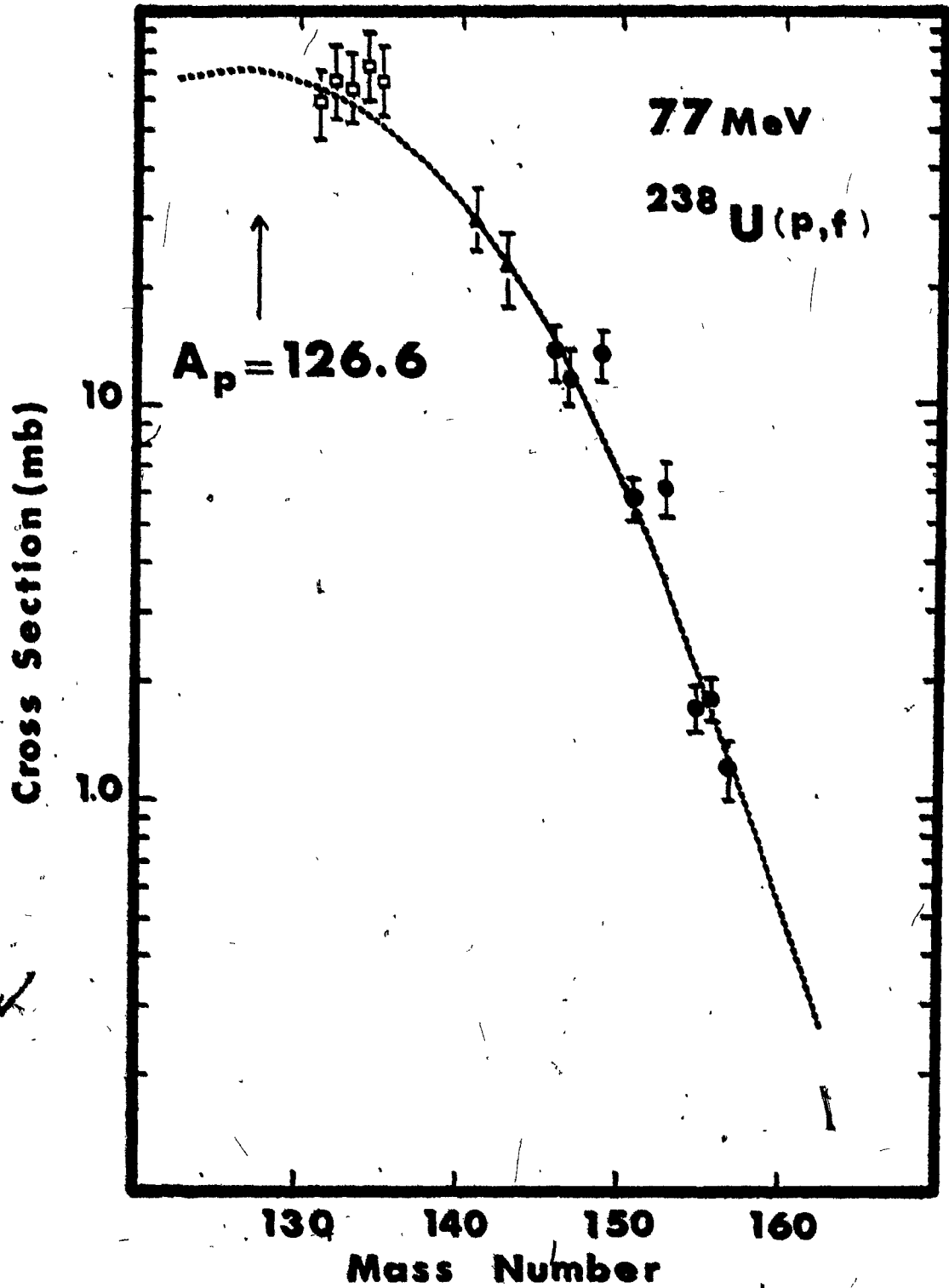
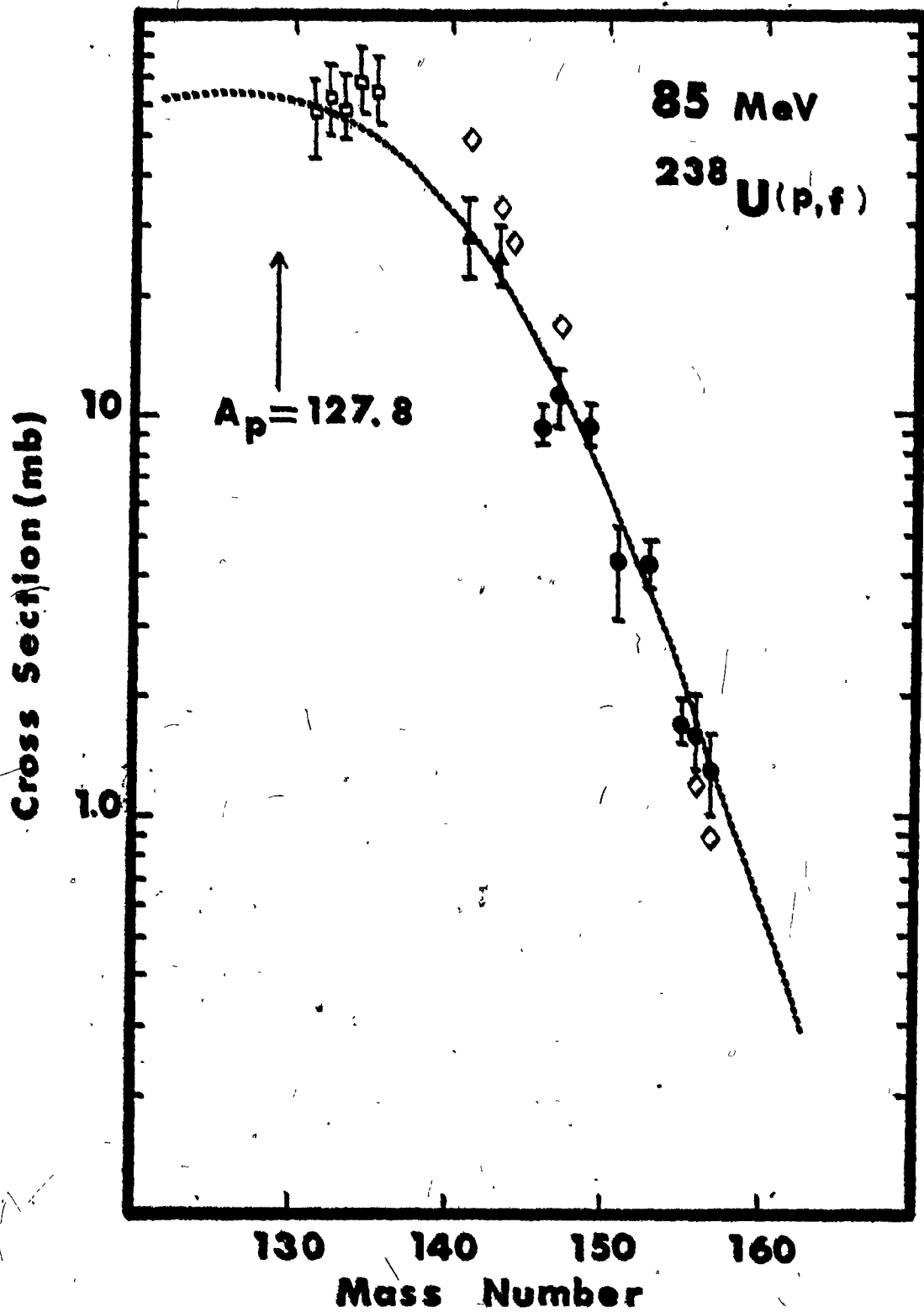


FIGURE 42: Heavy side of the mass distribution resulting from proton fission of natural uranium at 85 MeV.

- This work
- Dikšić et al. (Di 74)
- ◇ Stevenson et al. (St 58)
- ▲ Parikh et al. (Pa 67)



because of its extremely low production cross section in the energy range (20-85 MeV). Umezawa (Um 73) has measured the isomeric ratio $\frac{\sigma_m}{\sigma_m + \sigma_g}$ for ^{148m}Pm and ^{148g}Pm produced in thermal-neutron fission of ^{233}U and found a value of 0.88. On the basis of this result, one may reasonably expect this ratio to be higher in 20-85 MeV proton fission of ^{238}U since the higher the energy of the incident particle, the higher the angular momentum transferred to the target nucleus (at least in an energy range where, as in the present case, the compound nucleus mechanism predominates), a fact which should favour the formation of the high spin state (6-) ^{148m}Pm over that of the low spin state (1-) ^{148g}Pm . A 10% correction to the ^{148m}Pm cross sections was nonetheless applied for the purpose of fractional independent yields calculations.

The values of the fractional independent yields used in the construction of the final charge dispersion curves are shown in Table XI and Figures 43 to 45.

V. ERROR ANALYSIS

Errors involved in the experimental part of this work are of two types:

- systematic errors, due to an imprecise knowledge of certain constants of the reactions studied. They affect all experimental results in the same way once a set of constants has been adopted.
- random errors which arise from imprecision in the

TABLE XI: Fractional independent yields used in charge dispersion curves

σ_{nb} E_p (MeV)	$^{148}_{Pm}$ ^a N/Z=1.4262	$^{149}_{Pm}$ N/Z=1.4426	$^{150}_{Pm}$ N/Z=1.4590	$^{146}_{Pr}$ N/Z=1.4746	$^{151}_{Pm}$ N/Z=1.4754
20	^b 0.0001 ± 0.00001	0.0040 ± 0.0024	0.019 ± 0.005	0.20 ± 0.07	0.44 ± 0.18
25	^b 0.0002 ± 0.00003	0.0035 ± 0.0021	0.024 ± 0.008	0.22 ± 0.07	0.32 ± 0.15
30	^b 0.0004 ± 0.0001	0.0041 ± 0.0024	0.032 ± 0.007	0.30 ± 0.06	0.33 ± 0.12
35	^b 0.0009 ± 0.0001	0.0095 ± 0.0057	0.046 ± 0.016	0.33 ± 0.10	0.35 ± 0.16
40	^b 0.0019 ± 0.0002	0.0180 ± 0.0108	0.084 ± 0.032	0.32 ± 0.08	0.37 ± 0.17
45	^b 0.0035 ± 0.0004	0.0347 ± 0.0208	0.122 ± 0.043	0.40 ± 0.12	0.37 ± 0.14
50	0.0105 ± 0.0035	0.0415 ± 0.0249	0.160 ± 0.055	0.51 ± 0.16	0.44 ± 0.20
55	0.0089 ± 0.0027	0.0506 ± 0.0336	0.150 ± 0.030	0.48 ± 0.15	0.44 ± 0.22
60	0.0142 ± 0.048	0.0626 ± 0.0376	0.184 ± 0.044	0.53 ± 0.13	0.36 ± 0.16
65	0.0214 ± 0.063	0.0554 ± 0.0332	0.167 ± 0.037	0.56 ± 0.20	0.39 ± 0.18
70	0.0303 ± 0.066	0.0900 ± 0.0540	0.224 ± 0.041	0.53 ± 0.16	0.29 ± 0.17
77	0.0468 ± 0.138	0.1160 ± 0.0696	0.312 ± 0.057	0.52 ± 0.12	0.27 ± 0.12
85	0.0614 ± 0.148	0.1240 ± 0.0744	0.446 ± 0.084	0.46 ± 0.12	0.22 ± 0.10

a = corrected $^{148m}_{Pm}$ data (see text for details)

b = data from Umezawa et al. (Um 70)

FIGURE 43: Fractional independent yields of ^{148}Pm , ^{149}Pm ,
and ^{150}Pm .

- ▲ ^{150}Pm
- △ ^{149}Pm
- ^{148}Pm (This work)
- ^{148}Pm (Umazawa et al. (Um 70))

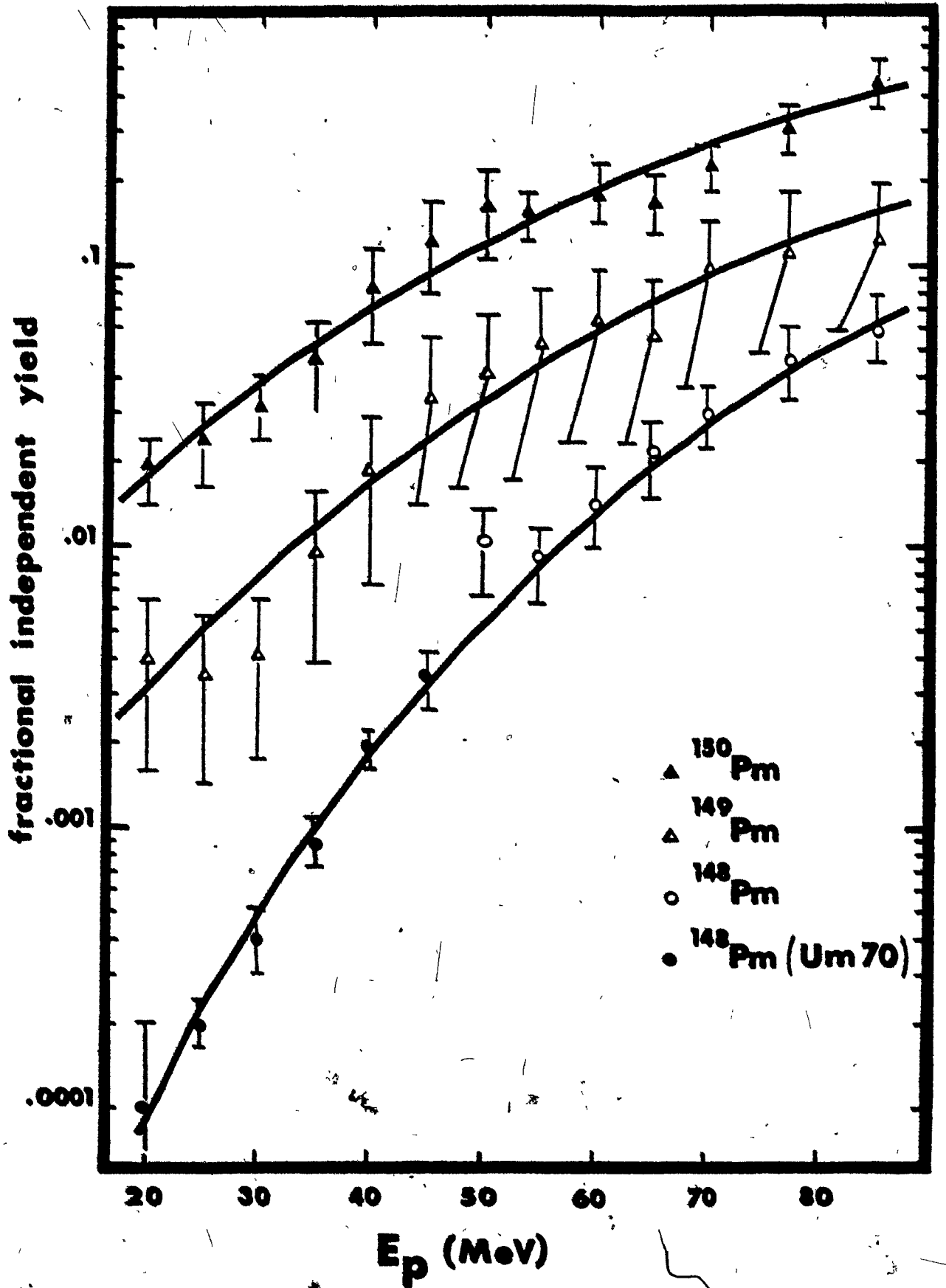


FIGURE 44: Fractional independent yields of ^{146}Pr .

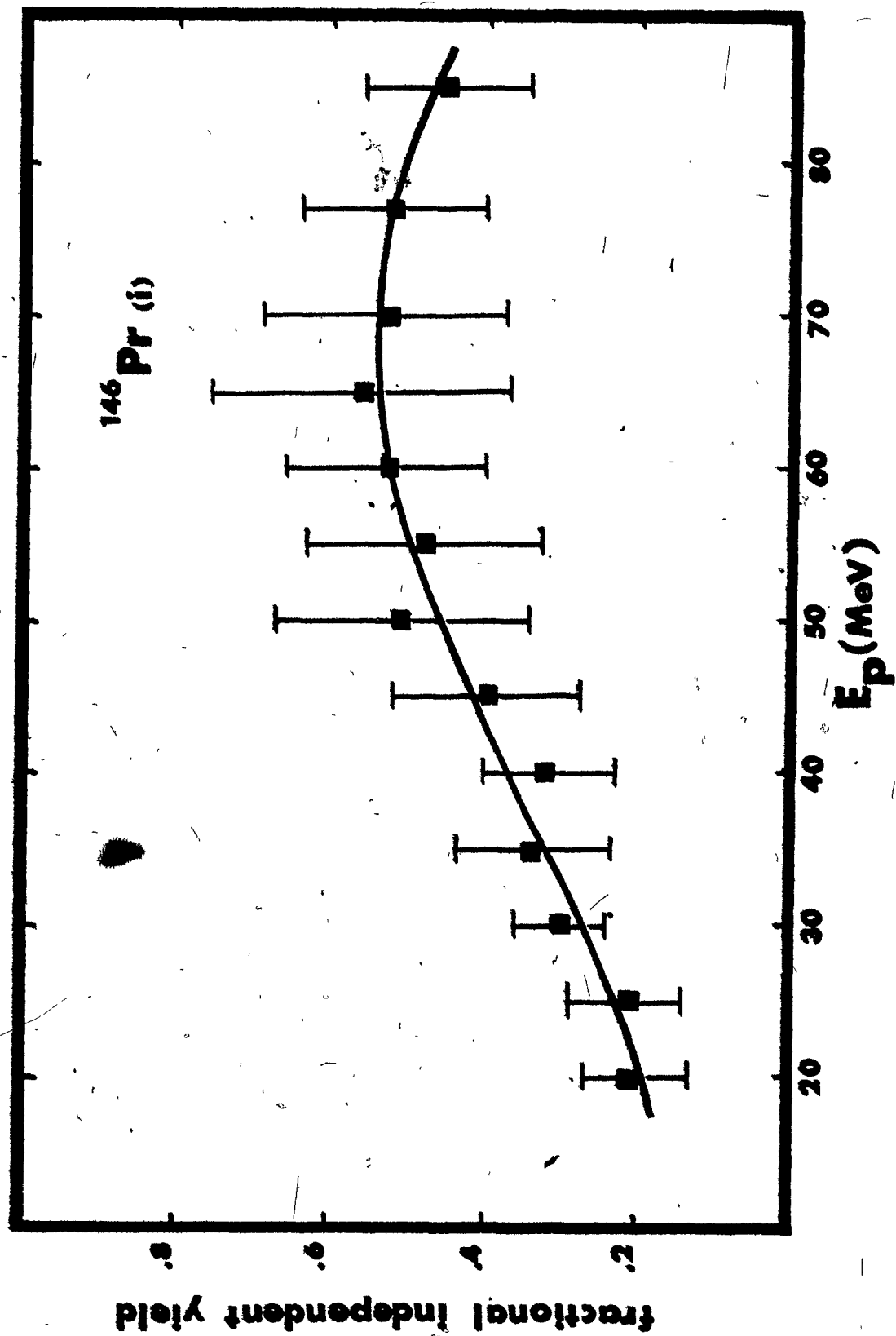
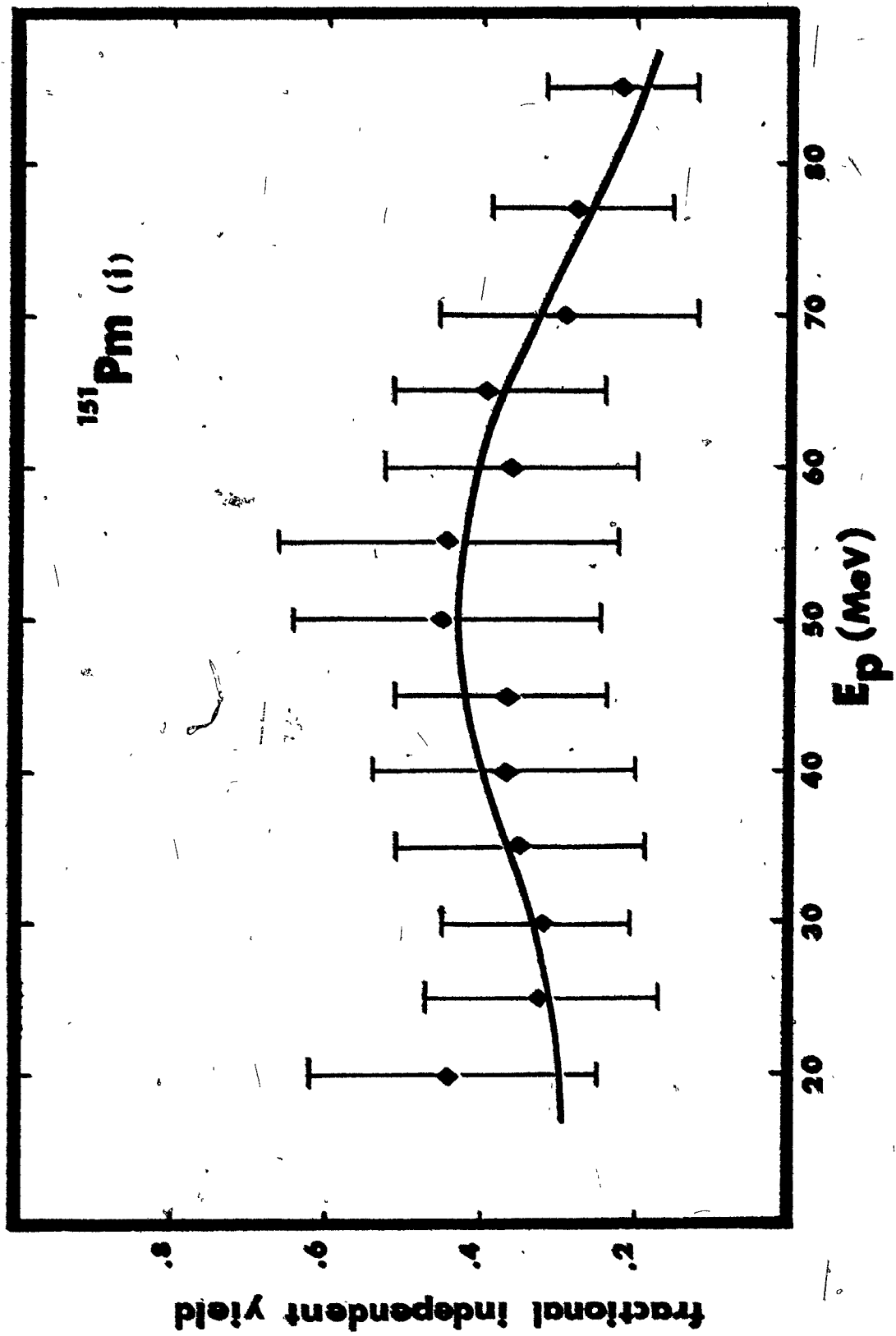


FIGURE 45: Fractional independent yields of ^{151}Pm .



actual measurements.

Errors in the decay characteristics of the nuclides studied (i.e. branching ratios and half-lives), errors in detector efficiencies and monitor cross sections belong to the first category. Uncertainties in the decay schemes can be important in the case of a weak peak. Most of the γ -rays selected for activity measurement purposes in this work were rather inverse peaks (see Table II), except for the 286.0 keV γ -line of ^{149}Pm . As mentioned previously, the observed discrepancy between ^{149}Pm experimental cross sections and those calculated from charge dispersion systematics may be accounted for by a 30% error in decay characteristics. In all other cases, no errors have been assigned to branching ratios taken from the literature. The half-lives found as a result of CLSQ analysis of the decay curves were in good agreement with the published values and the latter have been used to calculate the decay constants.

An error of $\pm 3\%$ was allowed for detector efficiencies, in accord with the recommendation of Fowler (Fo 72). An uncertainty of 5.9%, quoted by Newton et al. (Ne 73) in their monitor work, was adopted for the $^{65}\text{Cu}(p,pn)^{64}\text{Cu}$ cross section used for beam intensity determination. In the case of ^{151}Nd measurements, where ^{149}Nd acted as an internal monitor, an additional 5% error was added.

Random errors arise from the determination of disintegration rates, chemical yields, superficial densities

of the target and monitor foils, the reproducibility of sample geometry, volume measurements etc... An estimated error for each of these factors is given below.

The main source of error in cross-section values lies in the determination of the photopeak areas. This error was estimated to be $\pm 6\%$, except for ^{148m}Pm where an error of $\pm 8\%$ was assumed because of its low yields. The analysis of the decay curves introduces an additional error. For short lived-nuclides (i.e. half-lives less than a day), where the collection of data was carried out automatically, the error did not exceed 3% , due to the large number of points defining the decay curves. For longer lived nuclides, the uncertainty was estimated to be $\pm 5\%$.

The chemical yields were determined by gravimetric methods, using an analytical balance which gives a precision of ± 0.01 mg. The weight of the solid samples ranged from 10 to 15 mg and the imprecision in the weighings has therefore been neglected. The errors due to pipetting were minimized by using calibrated volumetric glassware and do not exceed $\pm 1\%$.

Sample geometry reproducibility did not introduce significant errors for short-lived nuclides where activity measurements have been carried out at distances from the detector greater than 75.0 mm. At a 20.7 mm distance, errors are believed not to be in excess of $\pm 2\%$ for solid samples.

E. DISCUSSION

I. EXCITATION FUNCTIONS

The independently-formed nuclides ^{148m}Pm , ^{150}Pm , and ^{149}Pm show the classical behaviour of neutron-deficient species formed in fission, namely a sharp rise in the excitation functions with increasing incident energy, as can be seen in Figures 26 and 29, whereas ^{146}Pr and ^{151}Pm which are further away from the stability line have excitation functions which reach a maximum located at 55 MeV for both curves (Figs. 27 and 28). Friedlander et al. (Fr 63) have pointed out that there is a definite correlation between neutron-to-proton ratio of fission products and the energy at which their excitation functions reach a maximum with the peak moving to higher energies with decreasing neutron-proton ratio. Such a conclusion was drawn from cesium data obtained in the fission of ^{238}U in the 0.1-6.2 GeV range, and was consequently confirmed by various other workers. This is illustrated in Figure 46. Whether this curve will represent the data for nuclides other than cesium is not clear. However, Parikh et al. (Pa 67) found that excitation functions for barium, lanthanum, and cerium agreed with the cesium data. Miller (Mi 73) observed a similar agreement in the case of antimony isotopes. According to the Friedlander systematics, ^{146}Pr and ^{151}Pm (which have almost identical N/Z ratios) should exhibit a maximum yield around 45 MeV, and our data confirm rather well this prediction. However, caution should be

exercised when such an analysis is performed on the basis of excitation functions constructed using formation cross sections, since one of the assumptions inherent in this approach is that the existence of a peak in the excitation function of an independent product is related to the energetics of the fission act leading to this particular product, and not to its probability of occurrence. In other words, that the maximum observed is due mostly to a preferential formation of this nuclide with respect to its adjacent isobars, rather than to an overall increase in the yield of the mass chain to which it belongs. Fractional independent yields are therefore more suitable for this type of analysis. The fractional independent yields of ^{146}Pr and ^{151}Pm determined in this work are affected by large uncertainties and the determination of a peak on their plot versus energy is somewhat dubious (see Figures 44,45). However, the peak energy values for these two nuclides have been plotted on Figure 46, as determined from fractional independent yields. They appear to be in accord with the peak-energy-versus neutron-proton ratio systematics of Friedlander et al. In the case of ^{148m}Pm , ^{149}Pm and ^{150}Pm , it was not possible to observe the maximum because it certainly occurs beyond the available range of bombarding energy (Fig. 43). Nevertheless, it was possible to extrapolate the excitation function of ^{150}Pm beyond the maximum with the aid of the cross section value at 170 MeV of Pappas and Alstad (Pa 61). The curve shown in Figure 26

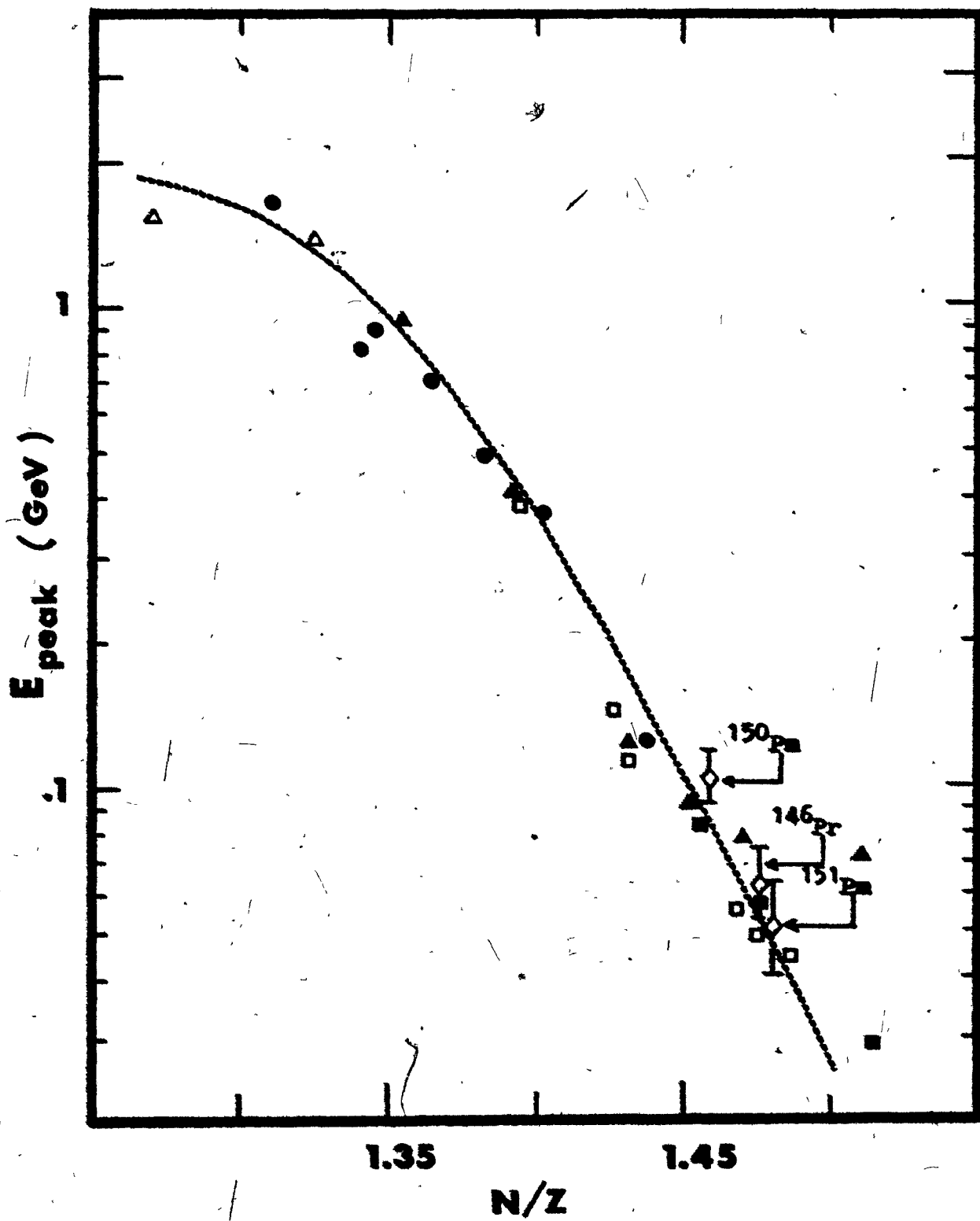
exhibits a maximum which is approximately located around 100 MeV, with a possible uncertainty of ± 10 MeV. The Friedlander systematics on maxima of excitation functions would predict a peak at 80-MeV incident energy, a value which lies just outside the range of error bars (see Fig. 46).

The general shape of the excitation functions of independently-formed nuclides can be explained qualitatively by invoking the same mechanism responsible for spallation reactions. The products with lower N/Z require more energy to be formed, the reason being that an increased number of neutrons has to be removed. The formation cross sections will be low at low incident energy and will increase with increasing energy until the formation of those products requiring even more energy becomes more probable, causing a decrease in the excitation function of elements with higher N/Z . For neutron-rich nuclides produced in medium-energy fission, the cross sections decrease monotonically with increasing bombarding energy, like for example ^{136}Cs and ^{134}Cs (Fr 63) and ^{128}Sb (Mi 73). In this work, no such variation has been observed for ^{146}Pr and ^{151}Pm .

The excitation functions of cumulatively-formed nuclides exhibit a broad peak in the case of the most neutron-deficient species observed like ^{147}Nd ($N/Z=1.4500$) and ^{153}Sm ($N/Z=1.4677$) (Figs. 17 and 22) as a result of what has been discussed above. Neutron-excess nuclides do not exhibit such a feature. For instance, the excitation function

FIGURE 46: Incident energies at which the excitation functions of the fission products of ^{238}U reach their maximum.

- FFGY (Cs) (Fr 63)
- △ FFGY (Rb) (Fr 63)
- ▲ Miller and Yaffe (Sb) (Ni 73)
- Parikh et al. (La, Ce, Pr) (Pa 67)
- Davies and Yaffe (Cs) (Da 63)
- ◇ This work



of ^{151}Nd ($N/Z=1.5172$) appears to be almost flat within experimental uncertainties (Fig. 20). This behaviour is strikingly different from that of lighter products with comparable neutron-to-proton ratio, like for example ^{141}Ba ($N/Z=1.5179$) produced under identical conditions, whose formation cross section decreases sharply from 43.5 mb at 20 MeV down to 8.6 mb at 85 MeV (Pa 67). This comparison may be taken as an indication of a less prominent role played by the displacement of the most probable charge along heavy isobaric chains in the decrease of cumulative cross sections with increasing bombarding energy. This is compatible with the low-energy formation hypothesis of heavy products.

II. HEAVY WING OF THE MASS DISTRIBUTION

The portion of the mass-yield curve of relevance to this work has been shown in Figures 30 to 42. Over the bombarding energy range studied, the heavy-mass peak is found to shift towards the lighter-mass side while the yields at the maximum increase monotonically by approximately a factor of 2. The half-width-at-half-maximum of this side of the distribution undergoes a slight increase from ~ 11 to ~ 13 mass units (see Table IX). Both variation of peak position and HWHM are consistent with the onset of symmetric fission and the filling up of the valley of the total mass distribution curve which causes a broadening in the upper part of the

curve. Baba et al, (Ba 71) have obtained so far the most extensive body of data pertaining to mass distributions in the fission of ^{238}U by protons of energy 13 to 55 MeV. From a decomposition of the overall curve into three Gaussian components corresponding to the two wings and a symmetric component centered on the valley based on the method of Ford (Fo 60), these authors were able to assess the relative importance of the two modes in the final result. By integration of yields over the theoretical Gaussian distributions, they obtained the total fission cross-sections. They consequently observed a steep rise in total fission yield from 0.22 to 1.45 barn between 18.2 MeV to 35.2 MeV, followed by a slower increase up to 55 MeV. A similar analysis performed with the aid of the data of Stevenson et al. in the 10-340 MeV bombarding energy range reveals a levelling off of the total fission cross section versus energy curve, the value reached at the plateau being ~ 1.5 barn. This result, combined with the fact that the yields around mass 130 increase constantly in the 20-85 MeV range, as shown here, and also that the contribution of the symmetric component goes from 0.055 barn at 20 MeV to 0.43 barn at 45.1 MeV, according to the method of Baba et al., is consistent with the decrease observed in higher mass yields above 50-MeV bombarding energy.

On the other hand, the increase in our total chain yields below this energy may be attributed to the general

increase of the asymmetric component, before the opening of new channels, among which symmetric fission is one, leading to the depression of this mode. Such an increase does not appear so markedly in the data of Stevenson et al. between 20 and 50 MeV. This discrepancy seems difficult to explain since at higher energies, our data and theirs agree well within experimental uncertainties.

III. CHARGE DISTRIBUTION

a) Construction of the charge dispersion curves

Charge dispersion curves for the mass region 146-151 were constructed by fitting Gaussian curves to the fractional independent yields given in Table XI. The method was based on the assumption that the dispersion of fission yields along isobaric chains was well represented by a normal Gaussian equation in the form given by Wahl (Wa 62) and described in chapter A (eq., A.8). In the present case, due to a lack of charge distribution data for chains heavier than $A = 151$, it was necessary to assume also that, in the mass range covered, the most probable charge and the charge dispersion (which is related to the full-width at half-maximum of the charge distribution curves) are essentially constant so that the various fractional independent yields listed in Table XI fall on a unique curve at a given incident energy.

These yields were plotted versus their neutron-to-proton ratios of the various nuclides to which they correspond

and computer fitted by a least-squares procedure identical to that utilized in the fitting of the heavy wing of the mass distribution (see preceding chapter). An additional constraint was also added: the fractional cumulative yields of ^{146}Ce , ^{149}Nd , and ^{151}Nd determined by summation on the theoretical charge-dispersion curves by determining the yields at the appropriate N/Z of the isobaric chains were required to agree with the experimentally-determined values. Friedlander et al. (Fr 63) have shown that this requirement provides a means of determining rather accurately the width of the distributions. In our study, we have limited our choice of cumulative yields to those of nuclides belonging to the mass range of the independently-formed nuclides investigated here. The use of the cumulative data for heavier masses reported in this thesis might introduce distortions in the determination of Z_p and full-width at half-maximum, since the variation of both quantities with the mass of the fission chain is not known.

The charge distribution curves thus determined are shown on Figures 47 to 59 inclusively.

The parameters of importance associated with the charge distribution curves are, as already mentioned, the position of the peak, expressed as N/Z_p or Z_p of a given mass chain and the width of the curves, which gives a measure of the charge dispersion along the isobaric chain and from which one can derive, at least qualitatively, information regarding the energetic aspect of specific mass divisions

occurring during the fission process. These parameters are displayed in Table XII in units of N/Z and Z . In the case of the peak position, the data have been also expressed in terms of the displacement of the most probable charge, Z_p , with respect to the line of β -stability. The most probable mass A_p was chosen as that of the Promethium isotope closest to the peak and the corresponding most stable charge, Z_A , has been taken from Coryell (Co 53).

The error bars on N/Z_p and the full-width at half-maximum have been calculated at 20, 50 and 85 MeV by generating for each of these incident energies a set of charge distribution curves obtained by successively taking the minimum and the maximum of one of the independent yields involved, while keeping the other equal to the values quoted in Table XI. In the least-squares-fit procedure used, these independent yields were equally weighted, whereas they were weighted by the inverse of their standard deviations in the original calculation of the charge dispersion parameters. The deviation on N/Z_p and FWHM was found to be essentially the same at the three energies above mentioned, ± 0.08 and ± 0.10 Z unit respectively. The total amplitude of these uncertainties is shown on Figures 60a and 60b and has been assumed to be valid over the whole bombarding energy range.

TABLE XII: Parameters of charge dispersion curves

E_p (MeV)	Peak position				Full-width at half-maximum		
	N/Z	A_p^a	Z_A^b	$Z_A - Z_p$	N/Z	Z	χ^c
20	1.517	153.5	63.65	2.65	0.044	1.06	1.412
25	1.515	153.4	63.61	2.61	0.044	1.06	1.427
30	1.517	153.5	63.65	2.65	0.047	1.13	1.587
35	1.512	153.2	63.54	2.54	0.046	1.12	1.536
40	1.507	152.9	63.43	2.43	0.048	1.16	1.068
45	1.498	152.4	63.25	2.25	0.046	1.12	1.280
50	1.498	152.4	63.25	2.25	0.051	1.25	1.286
55	1.500	152.5	63.29	2.29	0.051	1.25	1.283
60	1.498	152.4	63.25	2.25	0.053	1.30	1.186
65	1.500	152.5	63.29	2.29	0.057	1.40	1.248
70	1.498	152.3	63.22	2.22	0.061	1.60	1.151
77	1.496	152.2	63.18	2.18	0.063	1.55	1.098
85	1.492	152.0	63.11	2.11	0.063	1.53	1.677

a = calculated from Promethium isotopic distribution

b = from Coryell (Co 53)

c = fit parameter: $\chi = \sqrt{\sum W \cdot (O-C)^2 / (NO-NV)}$

W = statistical weight

NO = number of observations

O = observed value

NV = number of variables

C = calculated value

FIGURE 47: Charge distribution in the fission of ^{238}U
by protons of energy 20 MeV.

A = 146-151

○ This work

● Umezawa et al. (Um 70)

0

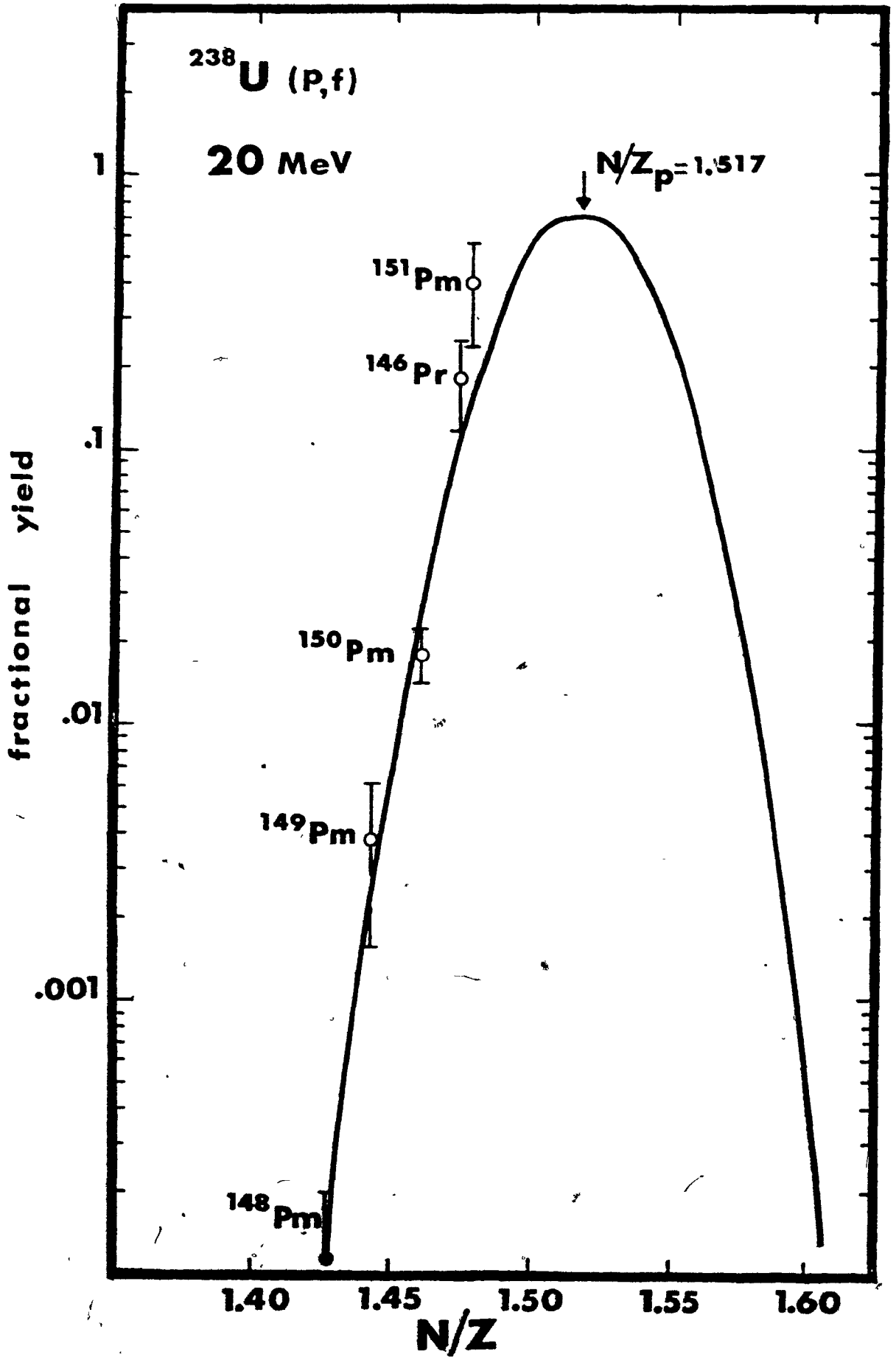


FIGURE 48: Charge distribution in the fission of ^{238}U
by protons of energy 25 MeV.

A = 146-151

○ This work

● Umazawa et al. (Um 70)

0

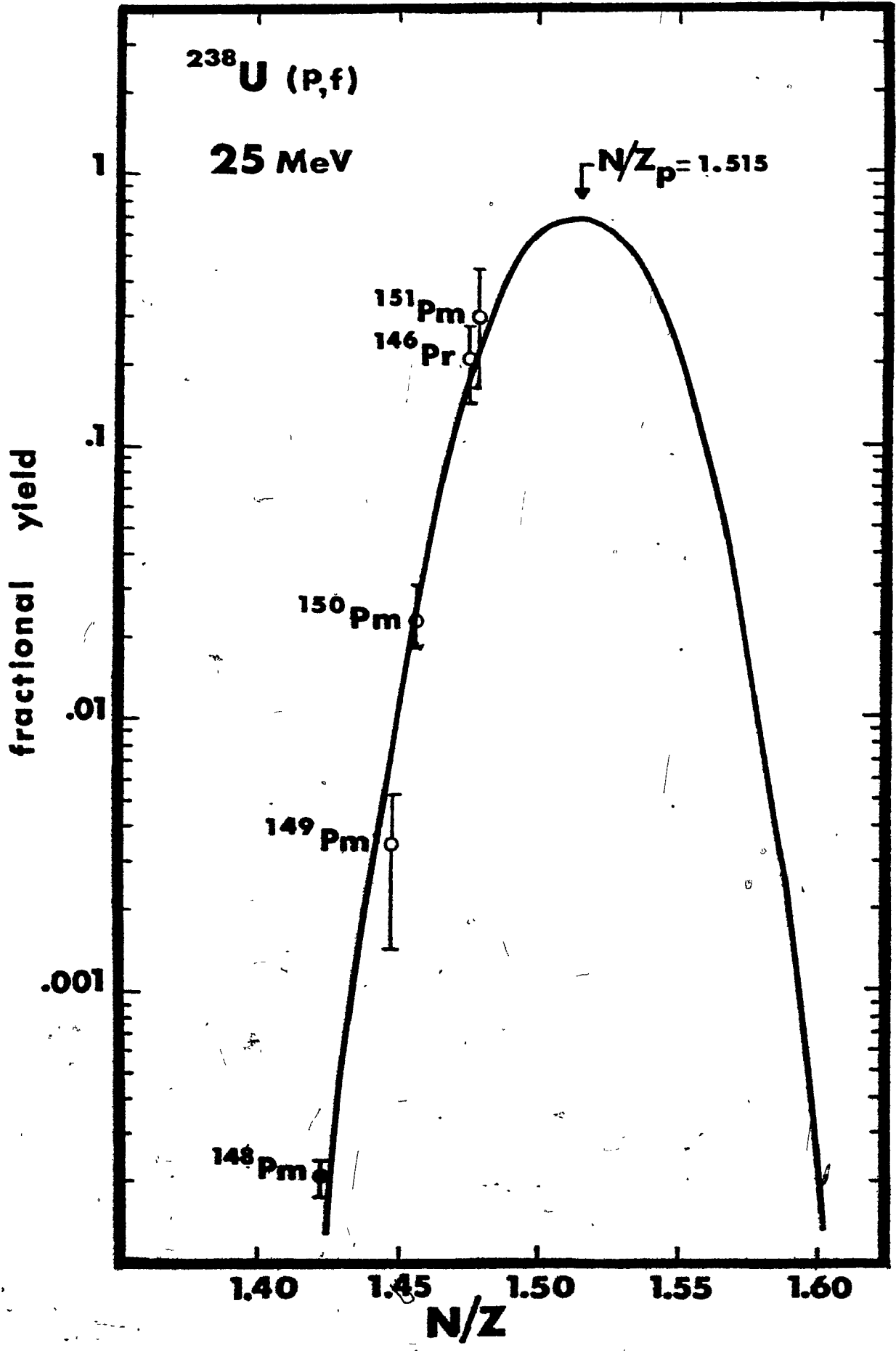


FIGURE 49: Charge distribution in the fission of ^{238}U
by protons of energy 30 MeV.

A = 146-151

- This work
- Umezawa et al. (Um 70)

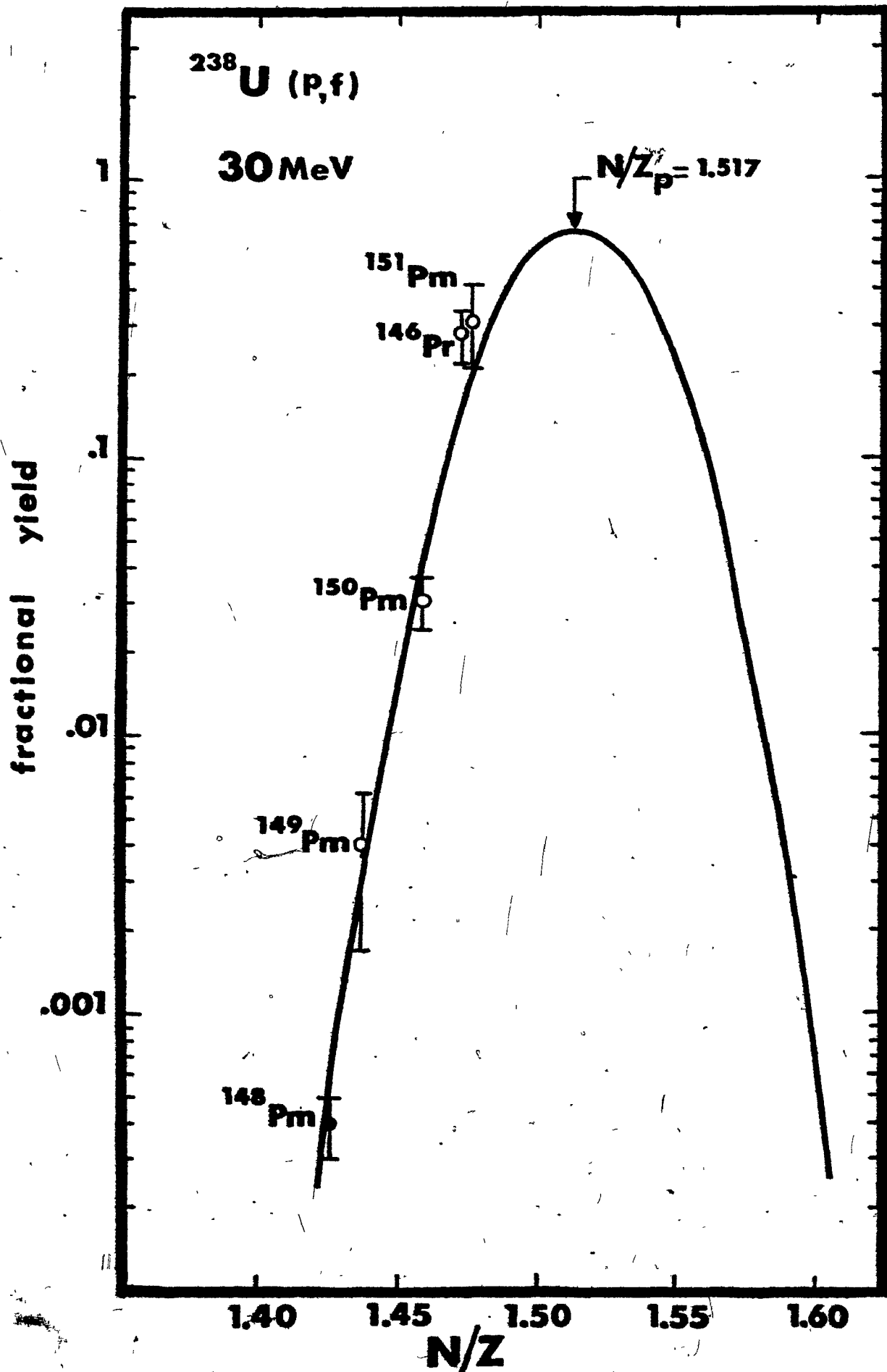


FIGURE 50: Charge distribution in the fission of ^{238}U
by protons of energy 35 MeV.

A = 146-151

○ This work

● Umezawa et al. (Un 70)

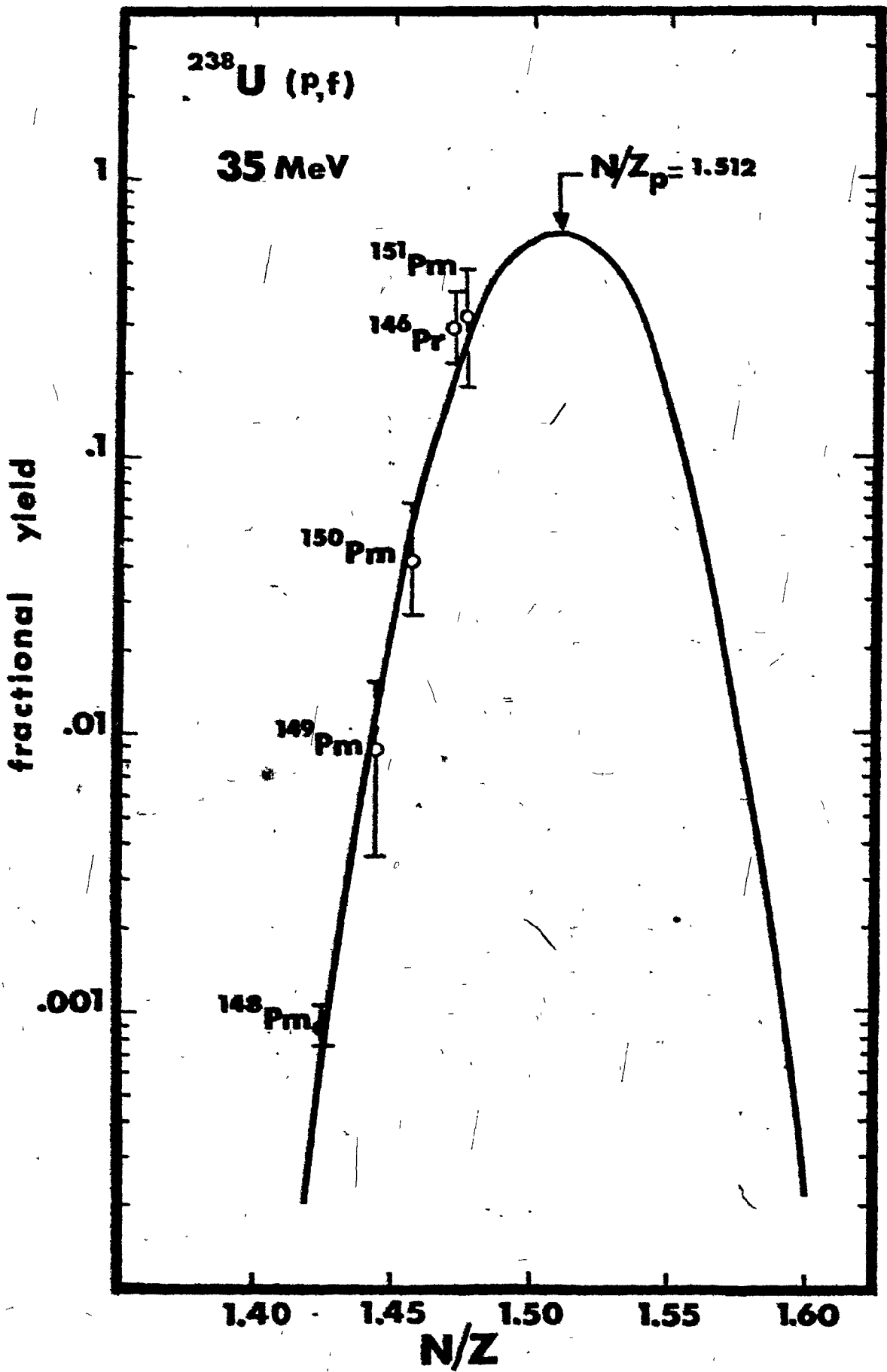


FIGURE 51: Charge distribution in the fission of ^{238}U
by protons of energy 40 MeV.

A = 146-151

○ This work

● Umezawa et al. (Um 70)

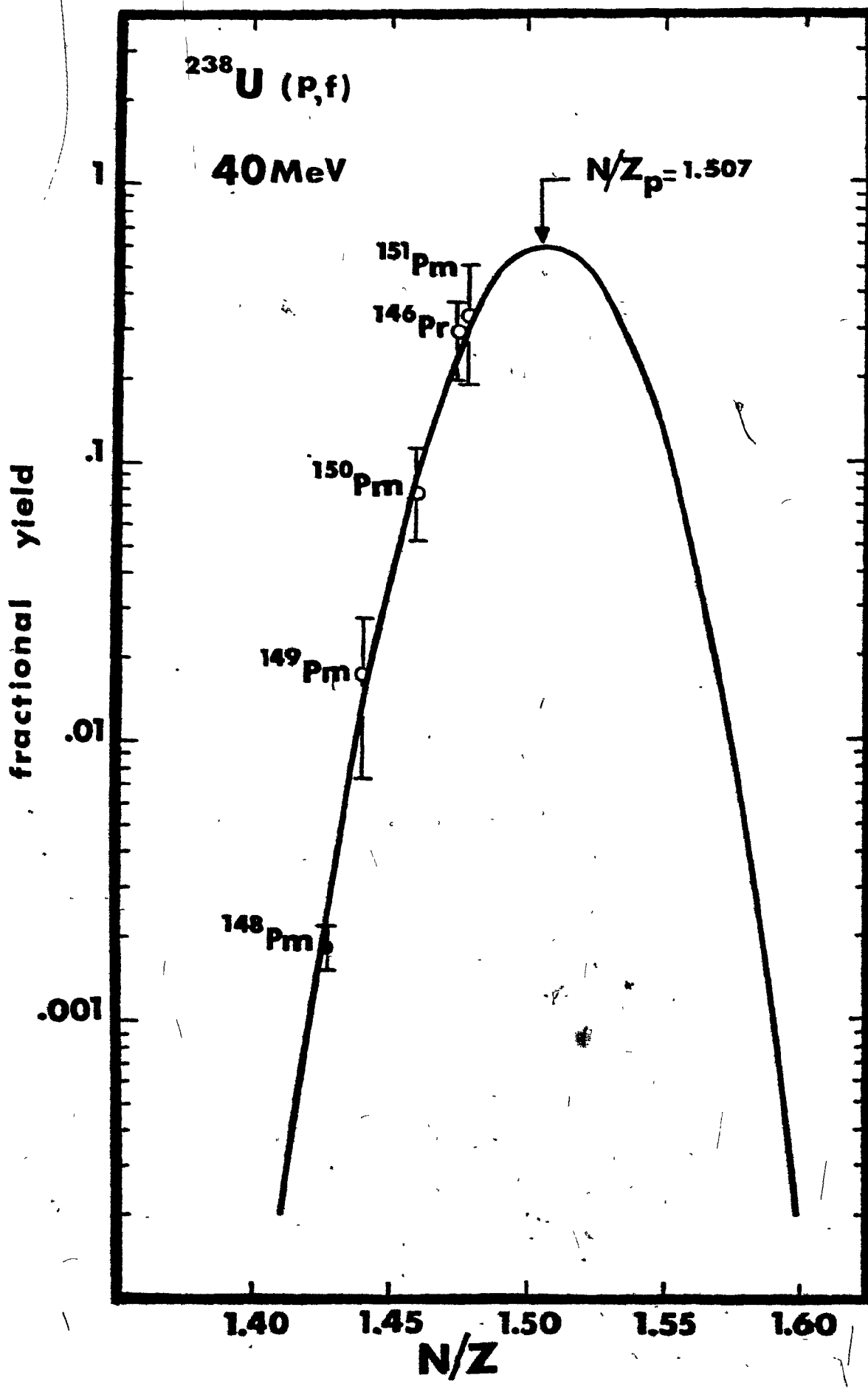


FIGURE 52: Charge distribution in the fission of ^{238}U
by protons of energy 45 MeV.

A = 146-151

○ This work

● Umezawa et al. (Um 70)

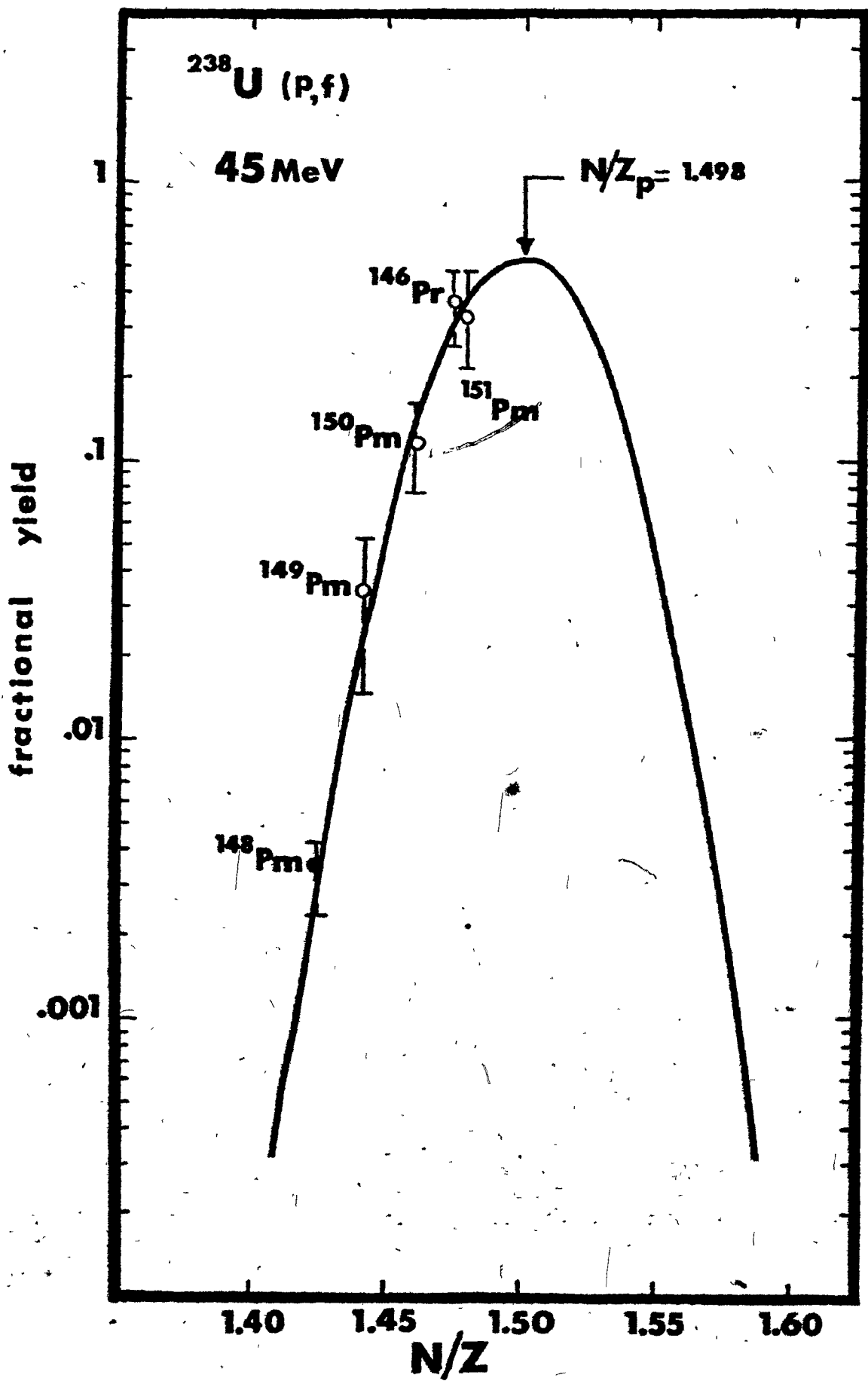


FIGURE 53: Charge distribution in the fission of ^{238}U
by protons of energy 50 MeV.

A = 146-151

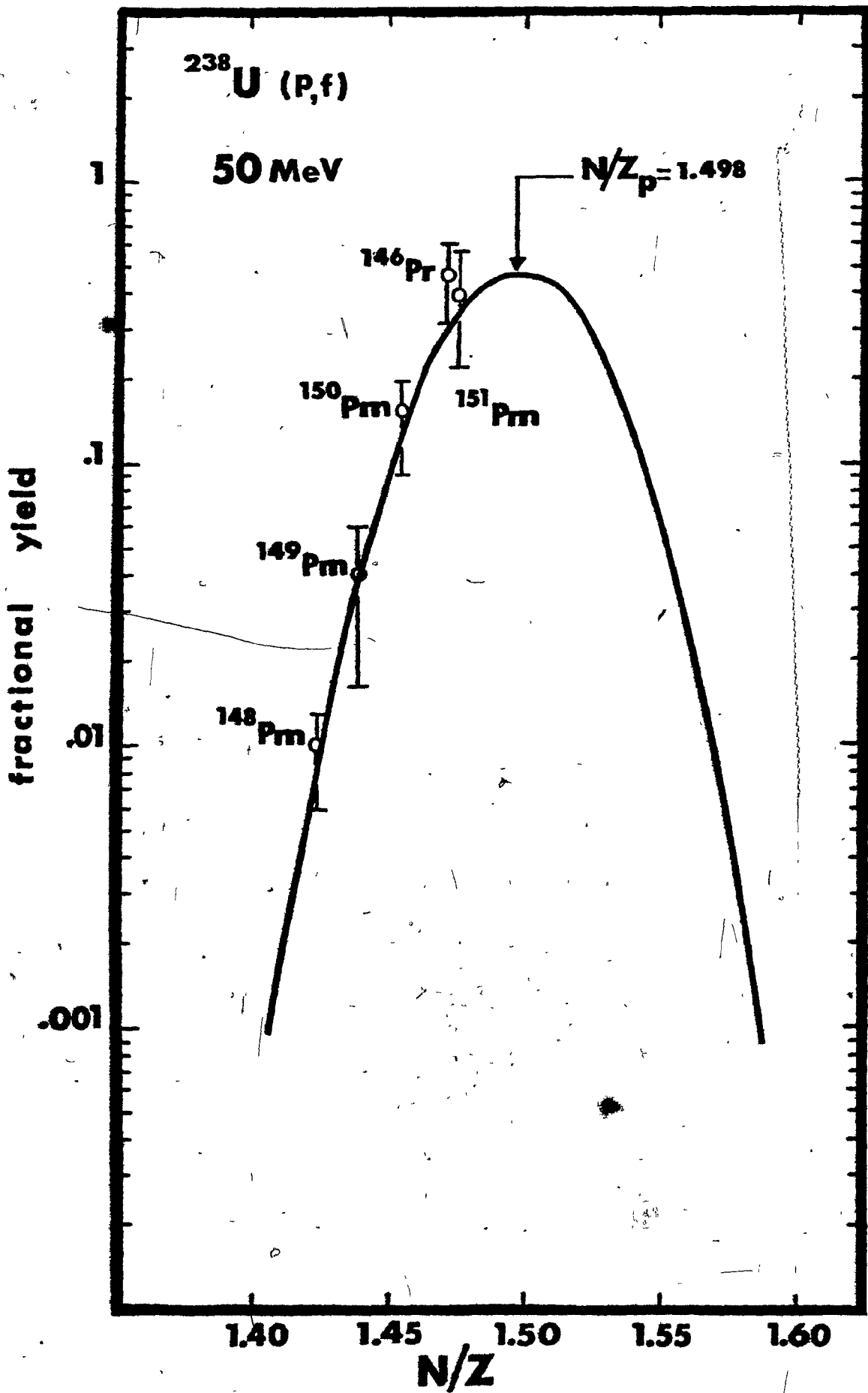


FIGURE 54: Charge distribution in the fission of ^{238}U
by protons of energy 55 MeV.

A = 146-151

0

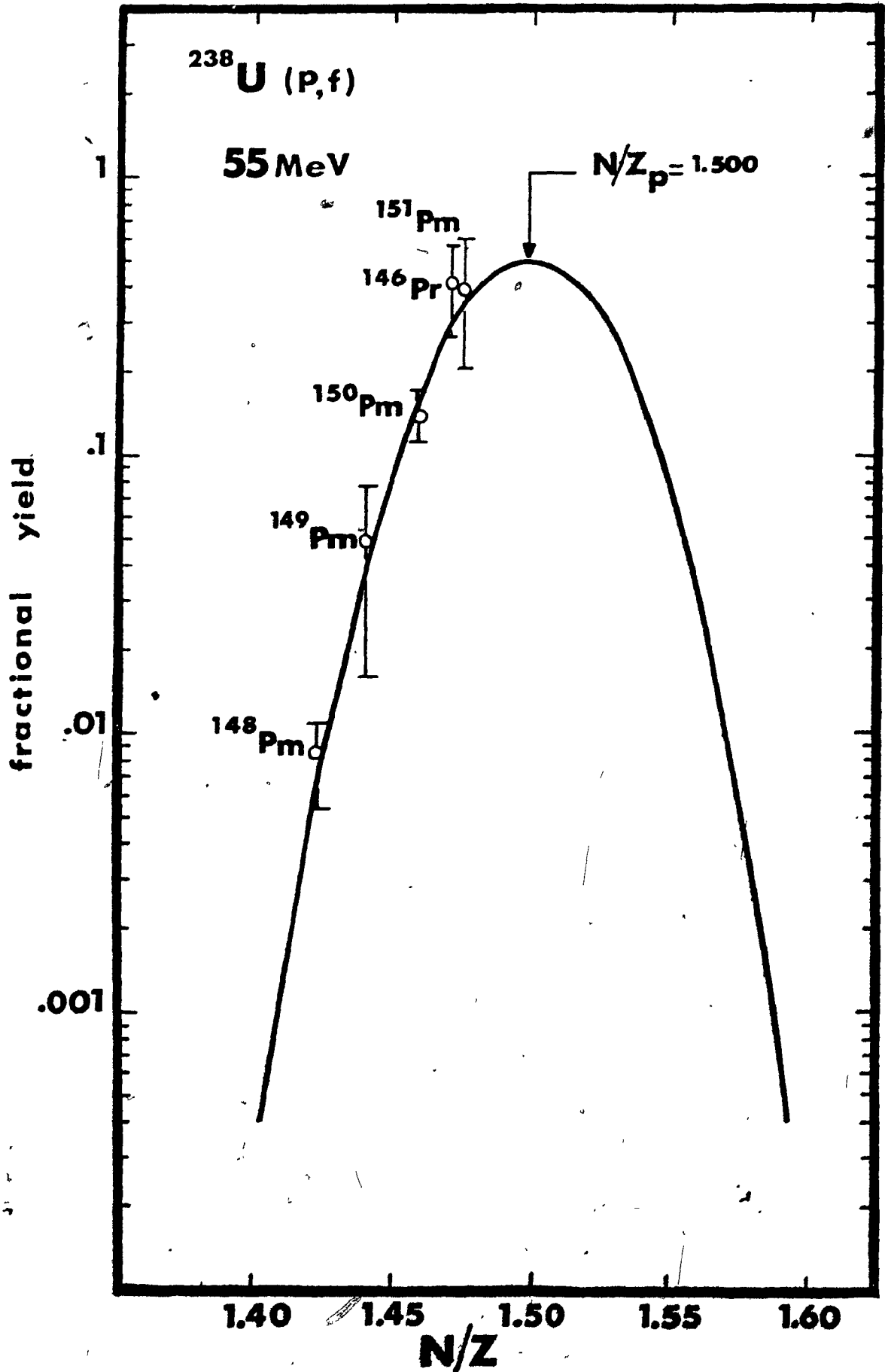


FIGURE 55: Charge distribution in the fission of ^{238}U
by protons of energy 60 MeV.

A = 146-151

^{238}U (p,f)

60 MeV

$N/Z_p = 1.498$

fractional yield

.001

.01

.1

1

^{148}Pm

^{149}Pm

^{150}Pm

^{151}Pm

^{146}Pr

1.40

1.45

1.50

1.55

1.60

N/Z

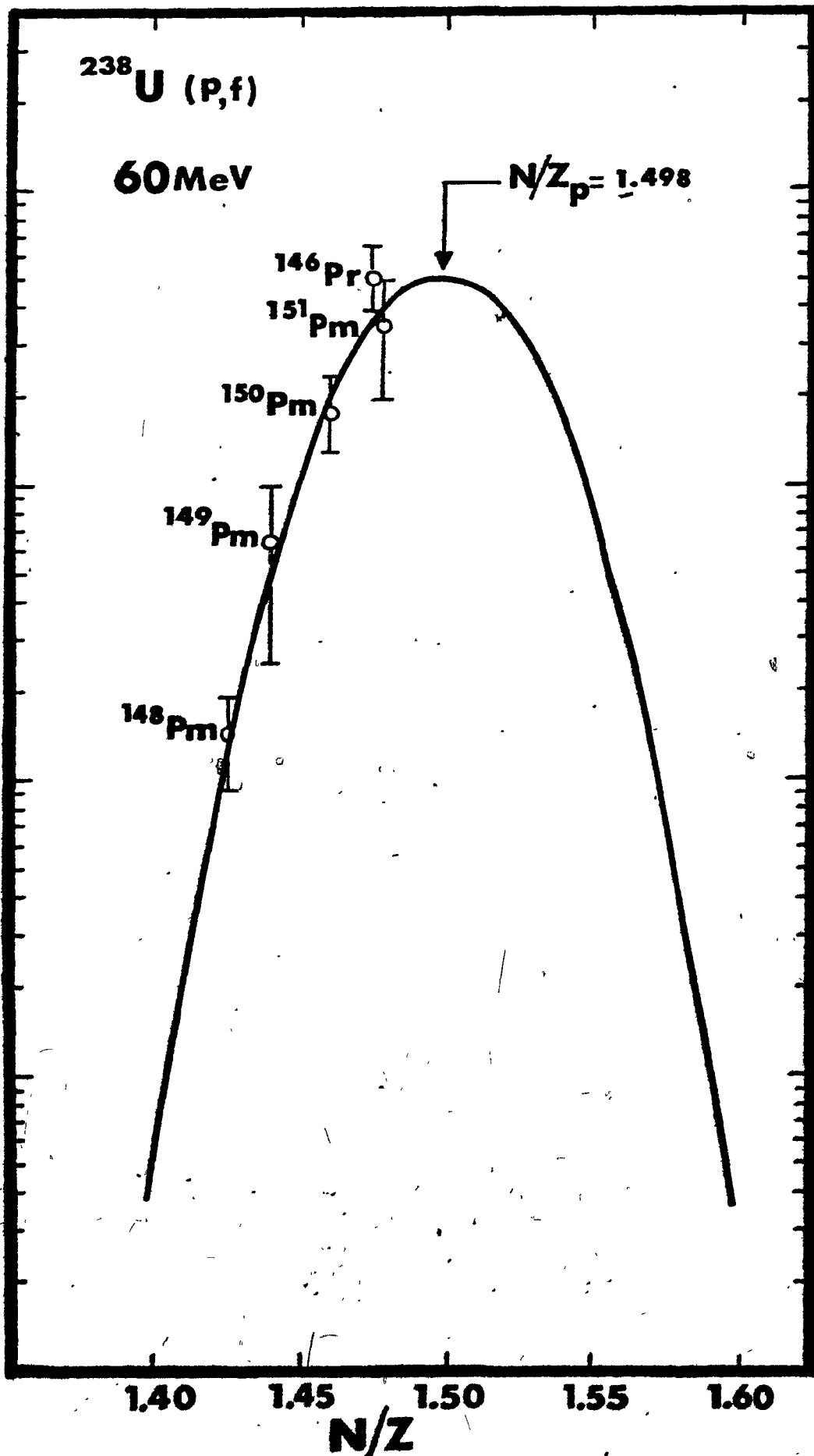


FIGURE 56: Charge distribution in the fission of ^{238}U
by protons of energy 65 MeV.

A = 146-151

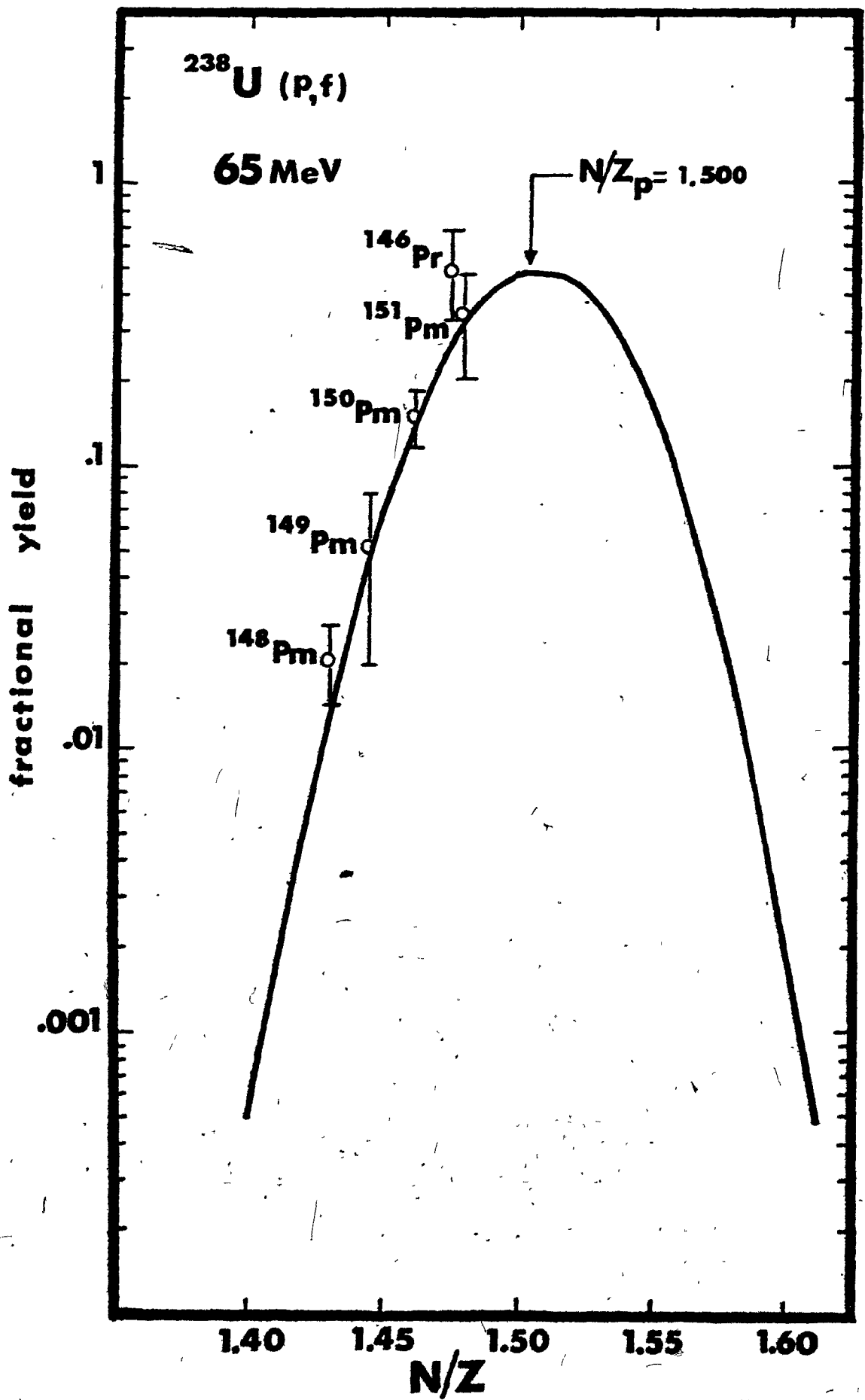


FIGURE 57: Charge distribution in the fission of ^{238}U
by protons of energy 70 MeV.

A = 146-151

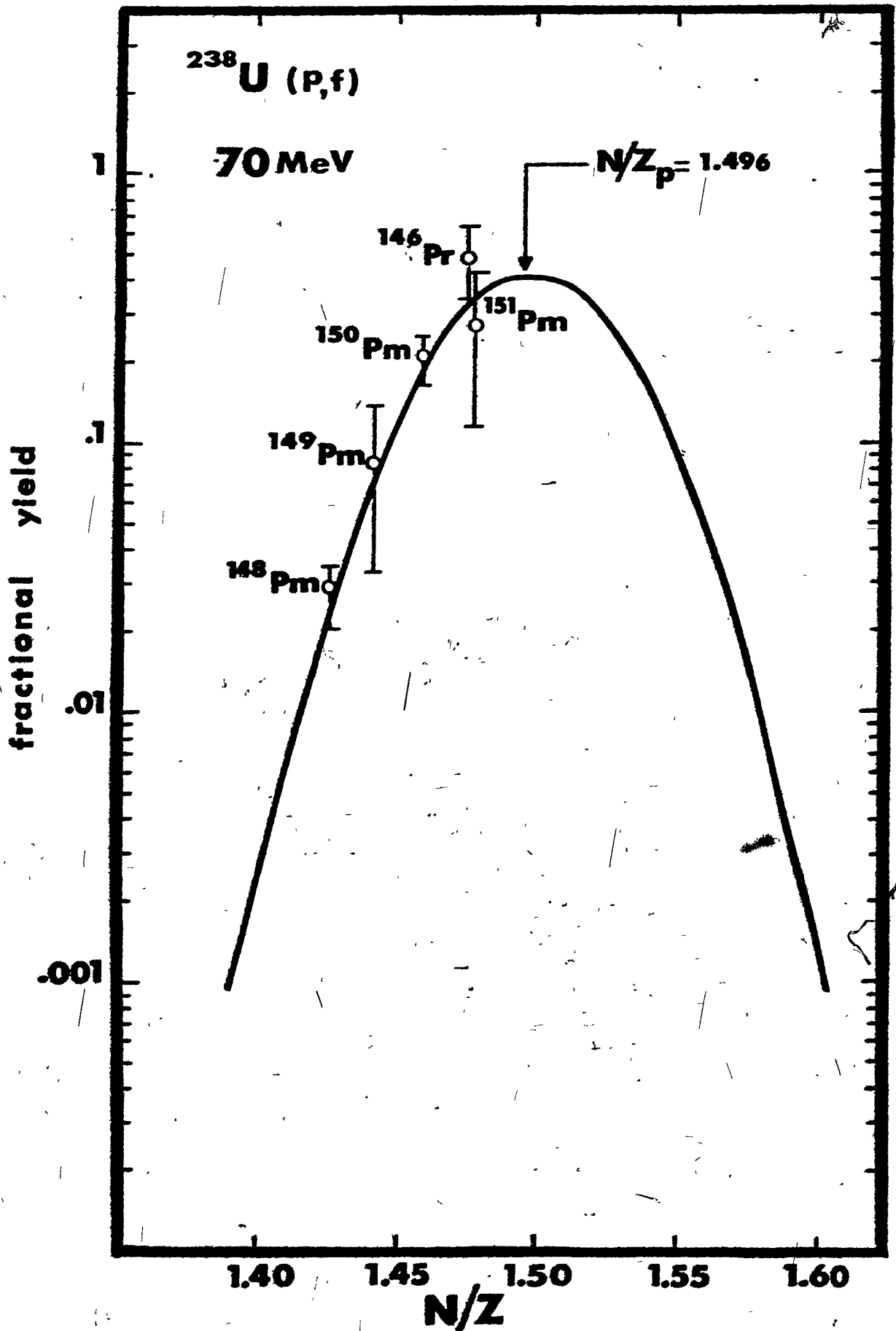


FIGURE 58: Charge distribution in the fission of ^{238}U
by protons of energy 77 MeV.

A = 146-151

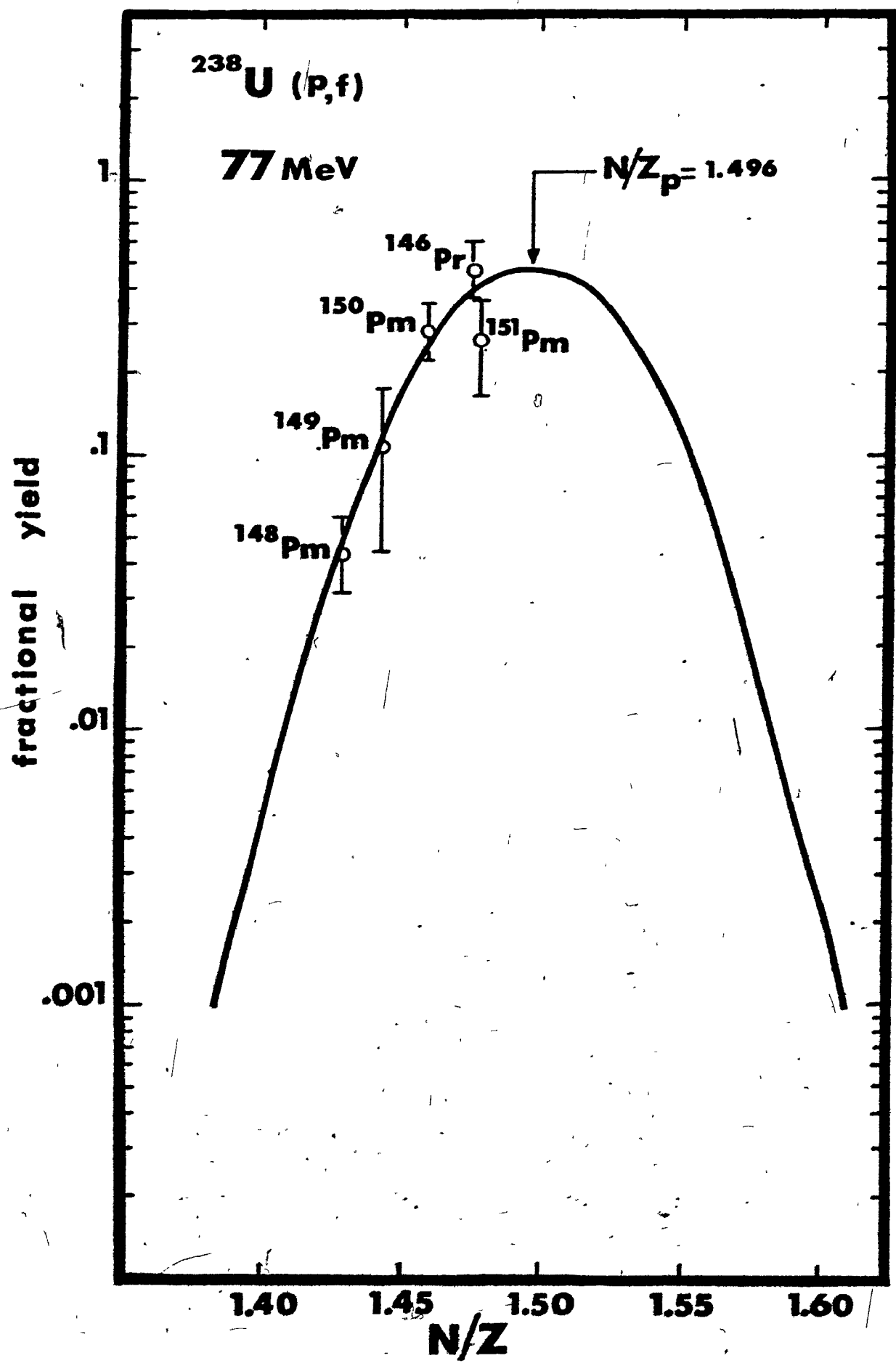
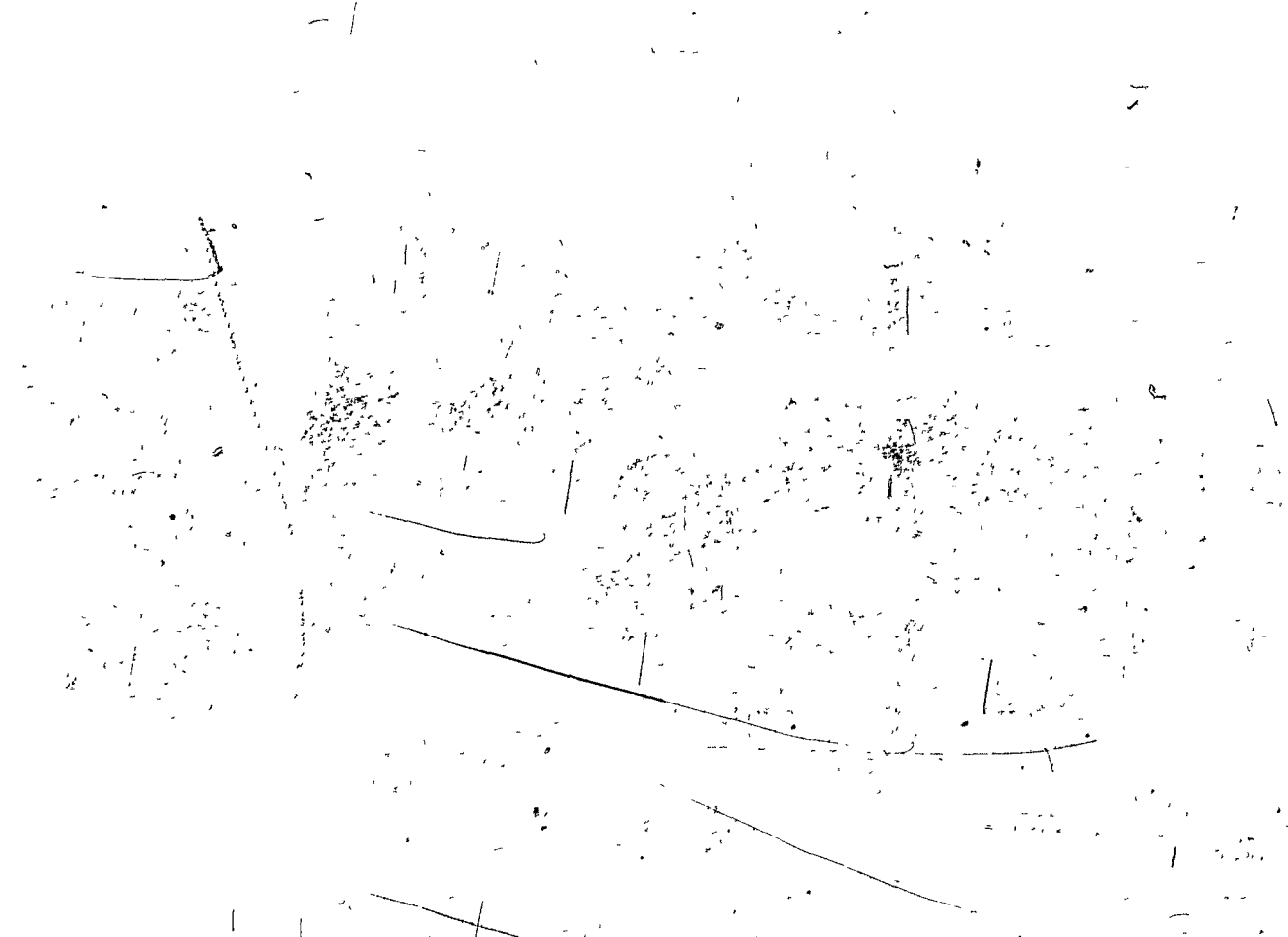
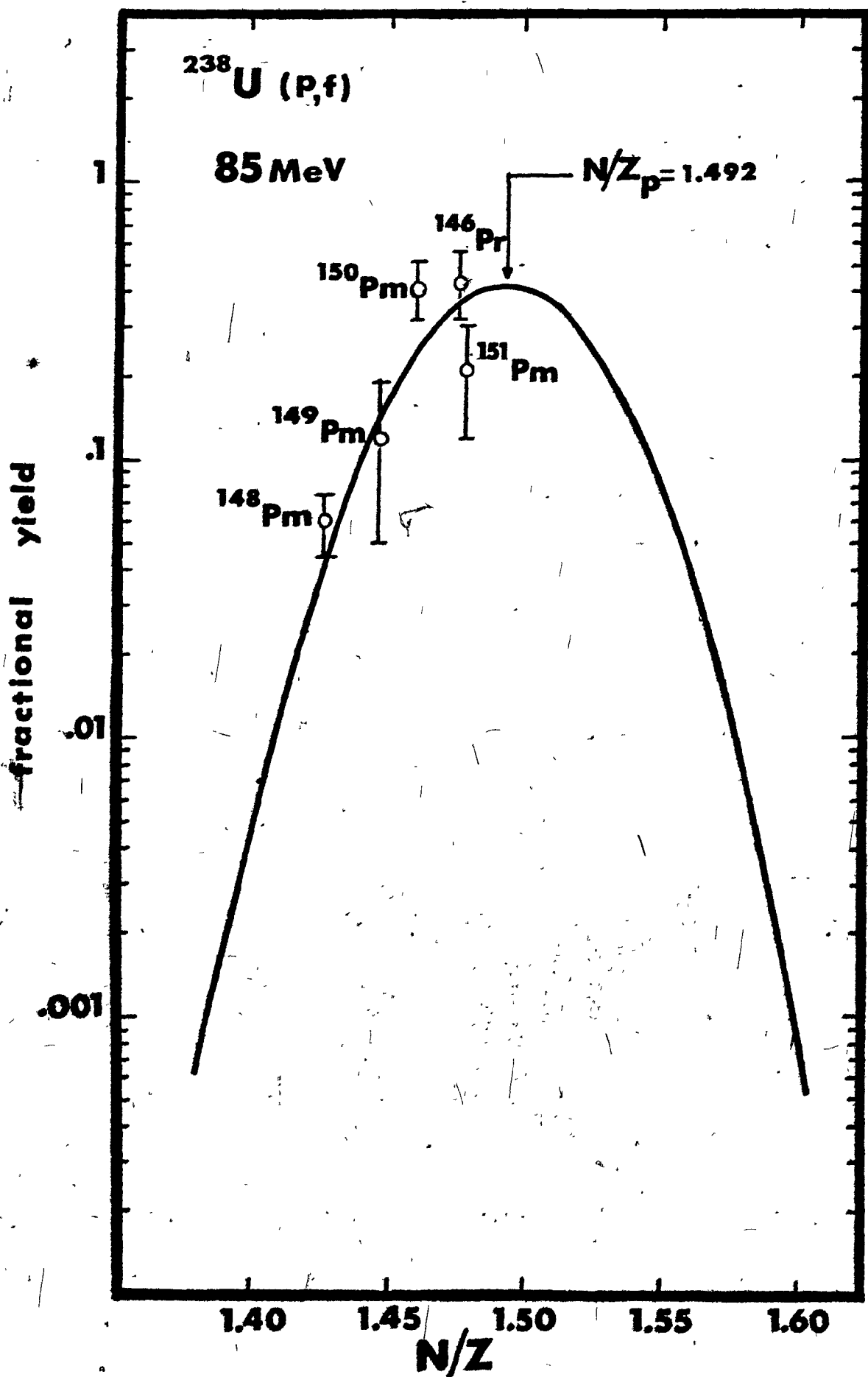


FIGURE 59: Charge distribution in the fission of ^{238}U
by protons of energy 85 MeV.

A = 146-151





b) Charge dispersion parameters and their correlation

i) Most probable charge as a function of incident energy

The shift of Z_p towards the stability line with increasing proton energy is clearly seen, as illustrated in Figure 60b, and this trend agrees at least qualitatively well with those already noticed by other workers in neighbouring mass regions (Da 63, Pa 67, Di 74). However, our data differ significantly from those obtained in lighter heavy-mass chains, in that Z_p varies with a smaller rate of charge (0.54 Z units in the 20-85 MeV range, as compared to 0.83 Z unit for mass 130 (Di 74), 1.142 unit for mass 136 (Da 63) and 1.02 Z unit for mass 141 (Pa 67)). Secondly, in the mass region 146-151, Z_p , within experimental error, varies linearly over the whole bombarding energy range, whereas in the case of the three chains above mentioned, the rate of movement of Z_p is seen to diminish beyond 50 MeV (Fig. 60b). This discontinuity in the $(Z_A - Z_p)$ versus bombarding energy curve has generally been attributed to the onset of the direct interaction mechanism which allows the formation of fissioning species with higher N/Z and/or the fact that, with increasing bombarding energy, the fraction of incident energy which remains as deposition energy in the fissioning nucleus decreases.

The linear decrease of $(Z_A - Z_p)$ for $A = 146-151$ suggests as a first approximation that the same mechanism is

FIGURE 60:

a) Variation of the full-width-at-half-maximum with incident energy:

A = 96 Khan et al. (Kh 70)[†]

A = 136 Davies and Yaffe (Da 63)[‡]

A = 152 This work

b) Displacement of the most probable charge with increasing bombarding energy

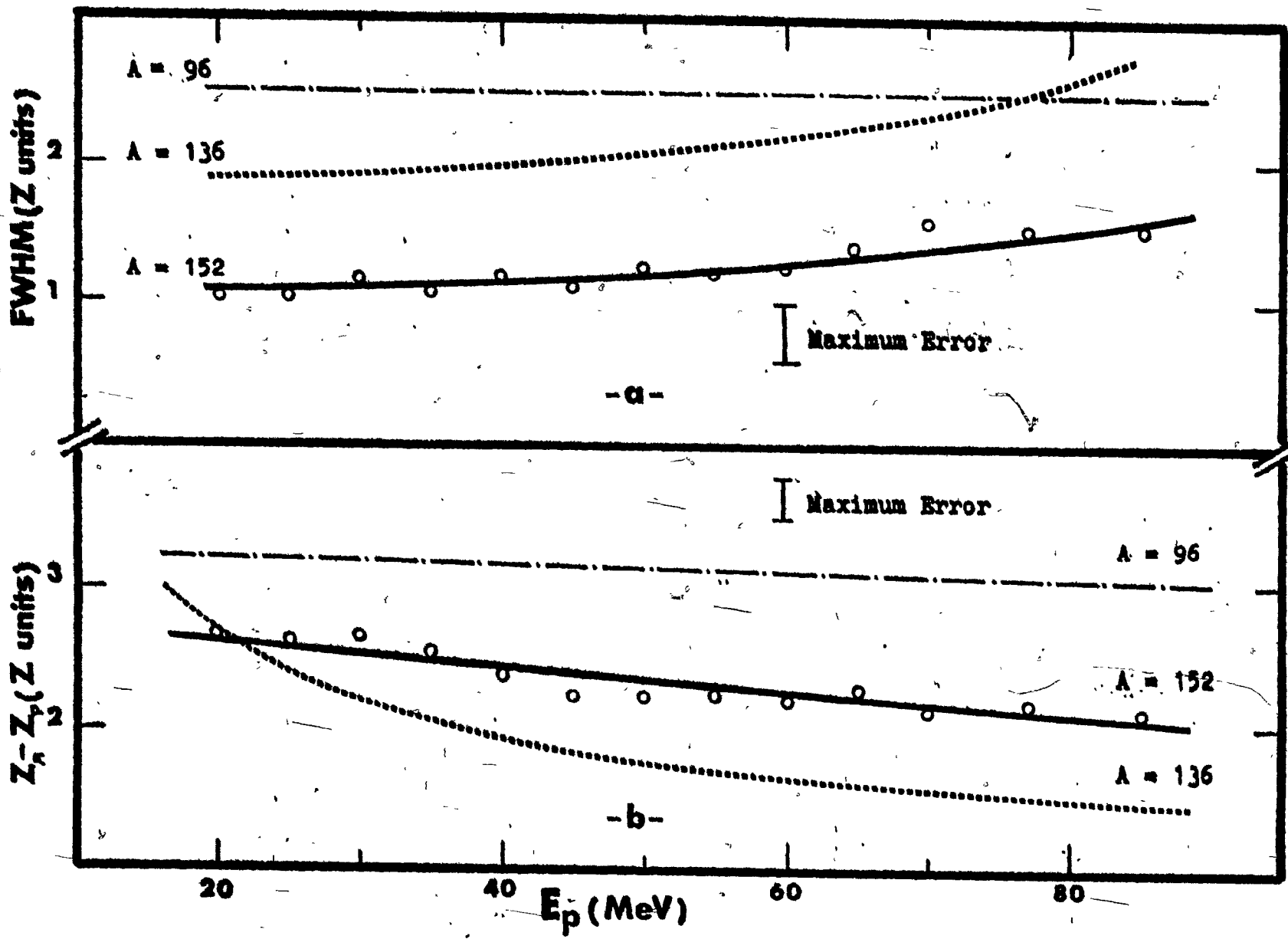
A = 96 Khan et al. (Kh 70)[†]

A = 136 Davies and Yaffe (Da 63)[‡]

A = 152 This work

† = normalized values shown in Table A-I

‡ = normalized values shown in Table A-II



responsible for the production of these mass chains in the 20-85 MeV energy range. On the other hand, the fissioning species from which the products studied originate should carry less excitation energy than those giving rise to less asymmetric mass splits, so that the primary fragments will emit fewer neutrons. This is incompatible with the assumption of a unique mechanism, namely a compound nucleus process in the present energy range. On the contrary, it would appear that very asymmetric mass divisions such as those encountered in the present work would be the result of well defined low-energy-deposition events arising from a compound-nucleus mechanism at low bombarding energies and direct interaction reactions above 50 MeV. This is consistent with the observed decrease in total chain yields above ~ 50 MeV which has been pointed out in the preceding section.

This proposition seems to be in contradiction with predictions made on the basis of the data obtained in the light-mass region of fission products. For $A \sim 96$, the measurements which have been carried out on ^{238}U and ^{235}U (Kh 70), ^{233}U (Ma 73), and ^{272}Th (Mc 72) show that Z_p is almost independent of both the incident energy and the nature of the target, thus suggesting that the variations introduced by these two factors are absorbed by the heavy complementary fission fragment. It should be noted however that the complementary mass region is centered around $A \sim 140$ and that, consequently, the heavier products investigated in

this work do not exhibit an identical behaviour. It would appear that, within a few mass units (~ 6 A units), the mechanism of production becomes more selective as far as excitation energy is concerned.

The dual energetic aspect of fission has been clearly demonstrated at higher energy. In mass regions below $A = 140$, the charge dispersion studies of Friedlander et al. (Fr 63) on cesium isotopic distributions up to 2.9 GeV, Yu et al. (Yu 73a) on xenon isotopic distribution at 11.5 GeV, Yu and Porile (Yu 73b) for mass chain $A = 131$ at the same energy have revealed the existence of double-humped charge dispersion curves. The neutron-excess species appeared to have all the characteristics of low-deposition energy fission products, whereas the neutron-deficient products have been attributed to events with higher deposition energies, possibly different from binary fission, such as deep spallation. The extension of these studies to higher masses by Chu et al. (Ch 71) at 11.5 GeV and Bächmann (Bä 70) at 28 GeV has shown that the charge dispersion curves change from a double hump with a shallow valley in between (peak-to-valley ratio ~ 2) at $A \approx 131$ to a distinct separation of the two maxima (peak-to-valley ratio ~ 8) at $A \approx 147$ and to a single peak on the neutron-deficient side at $A \approx 170$. This very important result was to confirm the previous conclusion that different mechanisms predominate in high-energy fission and also that these mechanisms become increasingly separable with increasing asymmetry of the process.

Our data indicate that this conclusion may be extended to the medium-energy range, where the only peak observed appears to be more stationary than for lighter heavy products.

Recoil studies have strengthened this conclusion at high energy. The ranges of neutron-deficient nuclides decrease by approximately a factor of 2 compared to their values at lower energies, while those of neutron-excess nuclides remain essentially independent of bombarding energy (Al 63), Su 56, Be 71). The change in range between these two classes of nuclides occurs rather sharply over ~ 2 charge units on the neutron-deficient side of stability (Br 65). This relative range behaviour was used by Starzyk and Sugarman (St 73) to decompose isobaric charge dispersion curves into three individual charge-dispersion components corresponding to two fission mechanisms (one at low energy and one at high energy) and a non-fission process tentatively assigned to a spallation-like mechanism. The introduction of the high-energy component of fission was rendered necessary by the fact that the midpoint of the sharp drop in ranges versus $(Z_A - Z)$ of the corresponding products occurs $\sim 2 Z$ units higher than the minimum in the double-humped charge dispersion curves. The relative contributions of the two fission modes to the overall isobaric yields, as calculated by Starzyk and Sugarman at 11.5 Gev, reveal a sharp decrease of the low-energy contribution between mass 131 and mass 147, the estimated values being 70% and 35% respectively. This result is compati-

ble with our previous conclusion. The increase in bombarding energy, which causes a shift of the energy spectrum of residual cascade nuclei towards higher values, therefore depletes the probability of occurrence of low-energy deposition events and consequently the production of the heavier neutron-excess products. One should note however that neutron-excess products of masses around $A \sim 131$, which are also the result of asymmetric events and as such are generally associated with "low-energy fission" are less affected in their production by an increase in bombarding energy than their heavier homologues. This is an indication that the term "low-energy fission" has to be taken in a broad sense as meaning fission consecutive to energy deposition events leading to excitation energies substantially lower than the incident energy, but not necessarily low in an absolute sense.

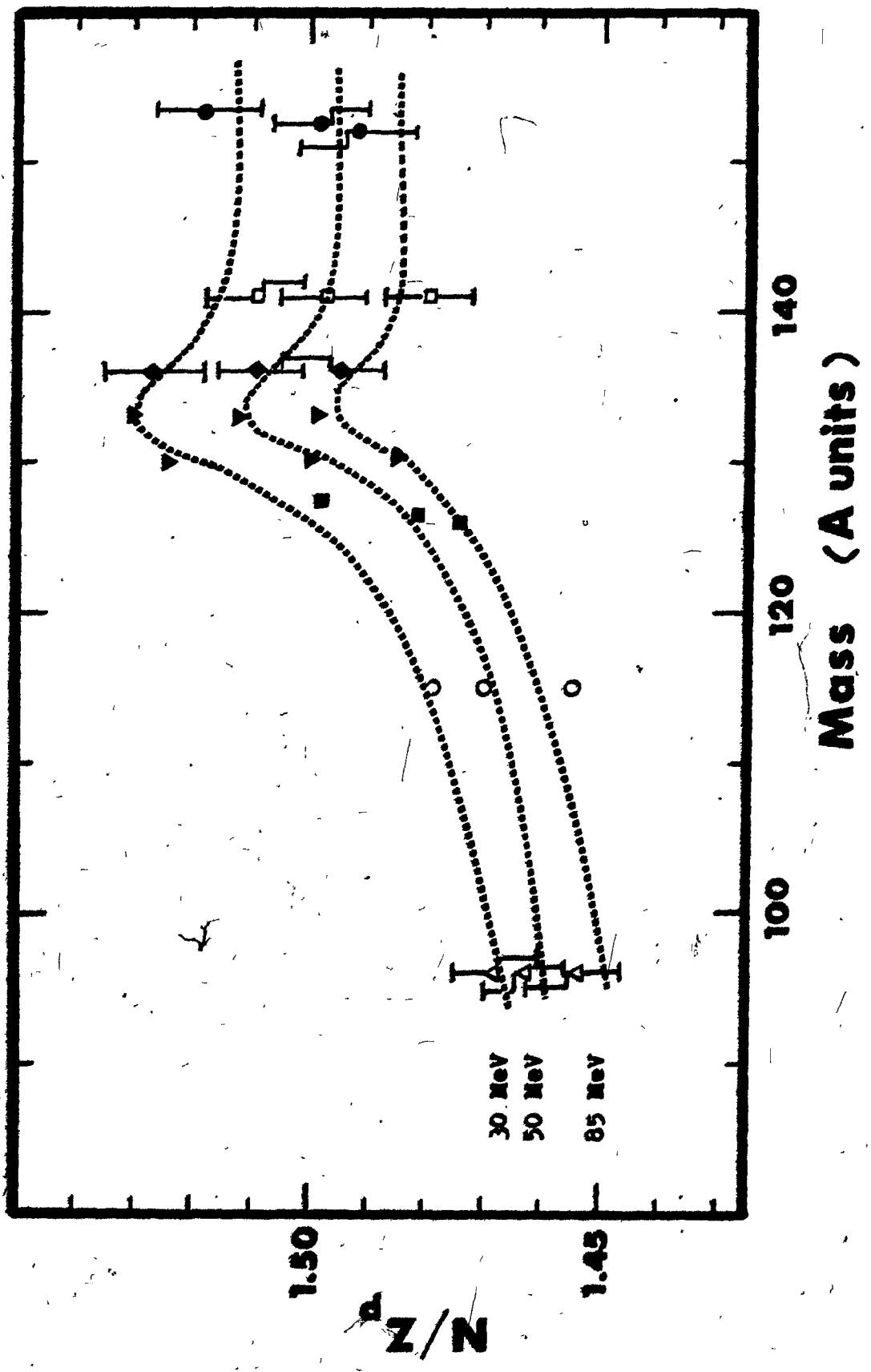
ii) N/Z_p as a function of mass

The variation of N/Z_p versus the mass number of the fission chains is shown in Figure 61 at 30, 50, and 85 MeV. The curves have been constructed with the help of the results of Sarkar (Sa 75), Miller and Yaffe (Mi 73), Dikšić et al. (Di 74), and the normalized values displayed in Tables A-I to A-III, in addition to our own data. At these three energies, the curves exhibit essentially the same features, i.e. a gradual increase in N/Z_p between $A = 96$ and $A \sim 127$, followed

FIGURE 61: Variation of N/Z_p with mass of the fission chain at 30, 50, and 85-MeV incident energy.

- Δ Khan et al. (Kh 70)[†]
- \circ Sarkar (Sa 75)
- \blacksquare Miller and Yaffe (Mi 75)
- \blacktriangledown Dikić et al (Di 74)
- \blacklozenge Davies and Yaffe (Da 63)[†]
- \square Parikh et al. (Pa 67)[†]
- \bullet This work

[†] = normalized values (Appendix A)



by a sharp rise up to mass 133. Beyond that point, a slow decrease takes place, with possibly a leveling-off of the curves for masses higher than $A = 141$.

The last part of the curves is certainly the most interesting aspect of the variation of N/Z_p . The decrease of N/Z_p with mass suggests, as a first approximation, that the average deposition energy increases with increasing asymmetry. This conclusion is contrary to those previously derived. However, this is not incompatible with fission acts taking place after the compound or cascade nucleus has evaporated a substantial number of neutrons. The decrease in N/Z_p beyond $A = 133$, for a given incident energy, would therefore reflect the evaporation of pre-fission neutrons rather than the emission of neutrons from highly excited fragments.

A similar remark has been made by Hagebø et al. (Ha 64) in their study of charge distribution in the light-fragment region ($A = 64-98$) of the fission products of ^{238}U by 170-MeV protons. The low N/Z_p values, together with the low width of the charge distribution encountered in this mass region led these authors to the conclusion that these results could be attributed either to very high and well defined energy depositions, i.e. the observed nuclides originate from a narrow spectrum of fissioning nuclei, followed by fission acts which are much faster than those occurring in thermal and low-energy induced fission, or to a late fission act which takes place at some intermediate stage of the evaporation chain which follows the primary nucleonic cascade. Hagebø

et al. (Ha 64) make also the additional assumption that in the latter case, the lighter fragments should carry an excitation energy higher than that received by the heavy complementary fragment in order to explain the low N/Z_p values obtained in the $A = 64-76$ mass region and inversely the high N/Z_p observed in the complementary mass region.

iii) Variation of the full-width at half maximum

The various values of FWHM reported in this work are plotted in Figure 60a, along with those for mass $A = 96$ and $A = 136$ given in Appendix A. An increasing FWHM with incident energy trend is apparent, although the standard deviations of these values are sufficiently large to make some arguments possible for a constant FWHM-versus-energy relationship. The charge dispersion at all energies appears to be much narrower than the values obtained for lighter mass chains, like for example for mass 136 where the FWHM varies from 1.88 Z at 20 MeV to 2.56 Z at 85 MeV (Da 63). This trend of decreasing FWHM with increasing mass number of the isobaric chain for a given incident energy had already been pointed out by Parikh et al. (Pa 67). A similar observation has also been made by Pappas and Alstad (Pa 61) for fission products of mass greater than $A = 140$ produced in the fission of ^{238}U by protons of energy 170 MeV. The latter found that only a narrower curve with a width of 2.2 charge units is compatible with their data as compared to 2.8 Z units in the

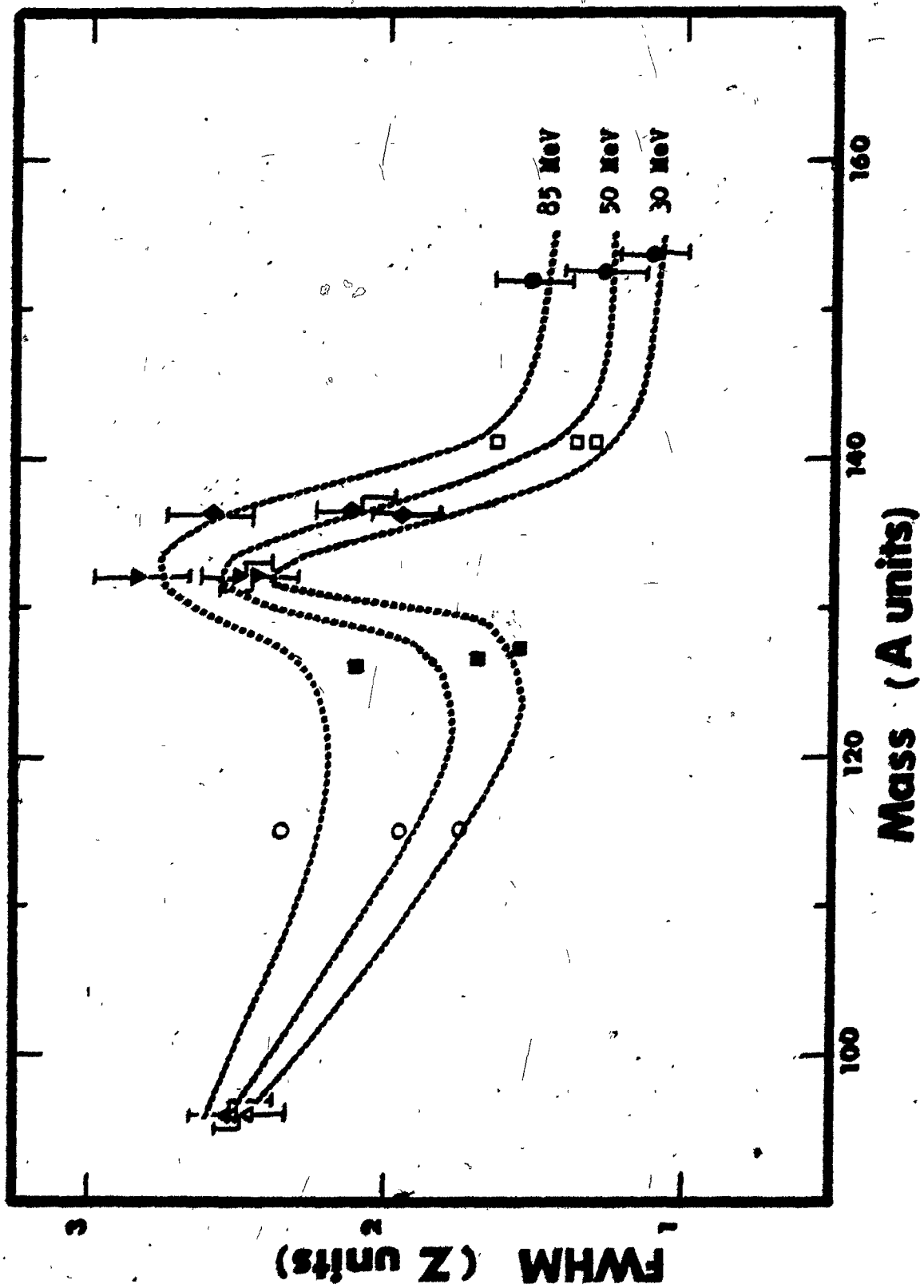
100 < A < 140 mass range. This finding received further support from the fact that this curve fits also the charge distributions observed for light mass products (A = 64-98) covering the complementary mass region (Ha 64). Khan et al. (Kh 70) however report much larger FWHM in the 20-85 MeV range for isobaric chains A = 90-92 (FWHM = 3.14-3.06 Z units). The variation of FWHM as a function of mass at three incident energies is shown on Figure 62. The values have been taken from the results published by the McGill team. In some instances, the charge dispersion curves have been redrawn by subjecting the independent yield to a treatment similar to that described in section I of this chapter. The results are given in Appendix A.

From Figure 60, it is evident that FWHM of charge dispersion curves are dependent upon mass, their maximum being located around mass 132. Pate et al. (Pa 58) have attributed the variation of widths with incident energy to the competition between neutron evaporation and fission competing at each step of the de-excitation chain, the widening being due to the Maxwellian distribution of neutrons evaporated from the excited fragments. Holub and Yaffe (Ho 73) have invoked the notion of an elementary charge distribution as that arising from the fission of only one kind of nucleus. As multichance fission occurs at moderate energies, the resulting charge dispersion curves would then be a sum of the elementary charge dispersions, an extreme case being that of

FIGURE 62: Variation of the full-width-at-half-maximum
as a function of mass at 30, 50 and 85 MeV incident energy:

- Δ Khan et al (Kh 70)[†]
- \circ Sarkar (Sa 75)
- \blacksquare Miller and Yaffe (Mi 73)
- \blacktriangledown Dikšić et al. (Di 74)
- \blacklozenge Davies and Yaffe (Da 63)[†]
- \square Parikh et al. (Pa 67)[†]
- \bullet This work

[†] = normalized values (Appendix A)



the double-humped charge distribution curves reported at high energies.

Such an argument might also be useful to explain the variation of FWHM with mass. The low widths observed for products beyond $A = 140$ would then be caused by a narrow spectrum of fissioning nuclei. The peak at mass 132 seems then difficult to explain since the directing influence of the 82-neutron shell in the nucleus is believed to be particularly felt in this mass region.

IV. CALCULATION OF THE TOTAL NUMBER OF NEUTRONS EMITTED

From the observation of the variation of Z_p of the products formed in ^{232}Th fission by α -particles at excitation energies ranging from 20 to 57 MeV, McHugh and Michel (Mc 68) have concluded that this quantity parallels Z_A , at a given energy, in the region of heavy-mass chains ($A = 126$ to $A = 150$). They have consequently proposed a method relating the rate of change in neutron emission with excitation energy, to the rate of change of Z_p , by which one can derive the total number of post-fission neutrons emitted during the fission act leading to the observed products. This treatment is summarized as follows. The rate of change of Z_p is expressed by:

$$\left(\frac{\partial Z_p}{\partial E}\right)_A = -\left(\frac{\partial Z_p}{\partial A}\right)_E \left(\frac{\partial A}{\partial E}\right)_{Z_p} \quad (\text{E.1})$$

$$\text{with: } (\partial A / \partial E)_{Z_P} = -(\partial v / \partial E)_{Z_P} \quad (\text{E.2})$$

$$\text{then: } (\partial v / \partial E)_{Z_P} = (\partial Z_P / \partial E)_A / (\partial Z_P / \partial A)_E \quad (\text{E.3})$$

$$\text{with: } (\partial Z_P / \partial A)_E = (\partial Z_A / \partial A)_E \quad (\text{E.4})$$

as mentioned above.

In one instance, the variation of Z_P as a function of mass has been directly evaluated from isobaric distribution studies (Di 74) in the mass range 131-135. This variation was found to be linear with increasing mass number over the bombarding energy range used in this work, with a slope of 0.38 ± 0.02 . This value was subsequently used in the estimation of $(\partial v_h / \partial E)_{Z_P}$.

$(\partial Z_P / \partial E)_A$ was obtained by linear-least-squares fit of our Z_P data normalized to mass $A = 152$. The excitation energies of the average fissioning nuclei have been calculated by Dikić et al. (Di 74) using the Vegas STEPNO code (Ch 68) followed by Monte Carlo evaporation (Do 58, Do 59) for the same target nucleus, from 30 to 85 MeV bombarding energy. Intermediate values of $\langle E^* \rangle$ have been estimated by interpolation. This would yield a value of $(\partial Z_P / \partial E)_A = 0.0208 \text{ MeV}^{-1}$. This result is substantially lower than the value of 0.027 MeV^{-1} found in the $A = 131-135$ mass region (Di 74) and 0.048 MeV^{-1} in the $A = 111-117$ mass region (Sa 75). Satisfactory agreement is obtained with the value of 0.0195 reported by Nethaway (Ne 74) from a compilation of data in the region of mass $A = 148-160$, for excitation energies up to 21.5 MeV and

fissioning nuclei whose mass ranges from 233 to 254. This fact shows, in particular, that the charge behaviour of fission products in the region of $A \sim 150$ seems to be independent of the nature of the target in the low and medium excitation energy range. The number of postfission neutrons has been calculated with the assumption that:

$$\partial v_T / \partial E = \partial v_h / \partial E + \partial v_l / \partial E \quad (E.5)$$

where h and l refer to heavy and light fragments respectively and $\frac{v_h}{v_l} = 2$. The latter assumption is supported by the results of Cheifetz et al. (Ch 70) who report an experimentally measured v_h/v_l ratio of 2.2 for the mass split 1.5 in the 155-MeV proton-induced fission of ^{238}U . Bishop et al. (Bi 70) have reported v_h/v_l ratios from 1.12 to 1.34 for similar mass splits in the same system in the 11.5 MeV-22 MeV proton energy region, with an increasing v_h/v_l ratio with energy trend. The value chosen in our case therefore appears reasonable.

The total number of neutrons thus estimated by adding to the post fission neutron the prefission neutrons (cascade neutrons v_c and evaporated neutrons v_e) calculated with the aid of the codes previously mentioned (Di 74). Our results are displayed in Table XIII, along with those of Dikšić et al. (Di 74) for $A = 131-135$ and Sarkar (Sa 75) for $A = 111-117$. It appears that an increase in the asymmetry translates into a decrease in the total number of neutrons emitted. This result was already predictable from the slower

TABLE XIII: Total number of neutrons emitted in the asymmetric fission of ^{238}U

E_p (MeV)	30	40	50	60	70	85
$\langle E^* \rangle$ (MeV)	26.7	32.1	35.8	43.4	45.4	53.9
a_{ν_c}	0.29	0.45	0.59	0.61	0.74	0.81
b_{ν_E}	1.12	1.63	2.16	2.60	3.09	3.63
c_{ν_p}						
$A=152$ ($\nu_h/\nu_l=2$)	2.19	2.64	2.94	3.56	3.73	4.43
d_{ν_T} $A=152$	3.60	4.72	5.69	6.77	7.56	8.87
e $A=131-135$	4.26	5.50	6.56	7.83	8.68	10.19
f $A=111-117$	3.90	5.10		6.70 ^g	8.20	9.60

a = pre-fission cascade neutrons

b = pre-fission evaporated neutrons

c = post-fission neutrons

d = total number of neutrons

e = after Dikšić et al. (Di 74)

f = after Sarkar (Sa 75)

g = $E_p = 55$ MeV, $\langle E^* \rangle = 39.6$ MeV

rate of change of Z_p with increasing bombarding energy and is in accord with the hypothesis of highly asymmetric mass splits as being induced by low-deposition energy cascades. However, the exactness of this calculation might be questioned also on the basis of this same hypothesis, that is the average excitation energies used in the calculation of the number of post-fission neutrons might not be representative of the average fissioning nuclei leading to the products observed in this work. In any case, this calculation will result in an over-estimation of the number of emitted neutrons, a fact which does not modify the conclusions drawn from the observed variation of Z_p versus incident energy.

SUGGESTIONS FOR FUTURE WORK

An obvious continuation of this work would consist in the investigation of the complementary mass region, where thorough charge dispersion studies, in the energy range used in this dissertation, remain to be done. Such studies would involve the isolation of elements like Gallium, Germanium, and Arsenic, where half-lives suitable for a radiochemical method can be found.

A second approach might consist in performing thick target-thick catcher recoil studies on the same nuclides investigated in this work. This would enable the estimation of the excitation energies of the precursors of the fissioning nuclei leading to the production of heavy fragments. Such a method might, in principle, answer the question as to which of the two mechanisms invoked in Section III-2 of the Discussion predominates in highly asymmetric mass divisions induced at medium energy. However, recoil studies in this energy range might prove to be a rather delicate problem since the differences in excitation energies involved in the production of measurable amounts of independently-formed nuclides are necessarily small and the overall range of possible excitation energies narrow, as compared to fission at high energies, a situation to which the method has, so far, almost exclusively been applied.

SUMMARY AND
CONTRIBUTION TO KNOWLEDGE

The independent formation cross sections of ^{148}Pm and ^{150}Pm , and the cumulative formation cross sections of ^{146}Ce , ^{146}Pr , ^{147}Nd , ^{149}Nd , ^{149}Pm , ^{151}Nd , ^{151}Pm , ^{153}Sm , ^{155}Sm , ^{156}Sm , and ^{157}Eu produced in the fission of ^{238}U by protons of energy 20-85 MeV have been measured radiochemically. The independent cross sections of ^{146}Pr , ^{149}Pm , and ^{151}Pm have been estimated from the cumulative yields. Excitation functions were constructed and the energy at which their maxima was reached was observed to decrease with proton energy when compared to increasing neutron-to-proton ratio of the products.

The charge distribution curves in the region $A = 146-151$ of the products of the fission of ^{238}U by protons of energy 20-85 MeV have been determined. The most probable charge deduced shows an energy dependence qualitatively similar to that observed for neighbouring lower masses, i.e. a displacement towards stability with increasing incident energy. However, it has been shown clearly that this displacement is less pronounced than in the $A = 130-136$ mass region. The full-widths at half-maximum are narrower than those reported for lighter fission chains. These two features appear to be compatible with the hypothesis of an increasing asymmetry of mass division as being favoured by either low-

energy deposition events due to direct interaction, or long pre-fission-neutron evaporation chains. In the second case, it becomes necessary to assume that the complementary light fragments carry more excitation energy than they should on the basis of a uniform distribution, in order to explain the high $(Z_A - Z_P)$ values observed in the mass region investigated in this work.

The incident energies corresponding to the peak of the excitation functions of independently-formed ^{146}Pr , ^{150}Pm , and ^{151}Pm have been found to be in good agreement with the systematics proposed in order to correlate similar quantities for heavy products of lower mass.

The cumulative formation cross sections of 11 nuclides ranging in mass from $A = 146-157$ have been used, along with the information derived from charge distribution, to estimate total chain yields. These have proved useful in providing a better definition of the heavy side of the mass-yield curve resulting from the fission of ^{238}U in the 20-85 MeV range of bombarding energy. The behaviour of this portion of the mass distribution with increasing incident energy, i.e. a decrease in total chain yields beyond 50-MeV incident energy accompanied by a shift of the most probable mass towards lower values, has also been found to be compatible with the hypothesis invoked in the preceding paragraph.

The estimated total number of neutrons emitted in the asymmetric mode of fission is lower than in less asym-

metric processes, when the same calculation procedure is used. This might also indicate that highly asymmetric mass divisions originate from fission events taking place in excited nuclei carrying less energy than those leading to processes less removed from symmetry.

APPENDIX A:

Results for charge dispersion in mass chains 96, 136 and 141 are presented in Tables AI to AIII respectively. The cross sections have been taken from the work of Davies and Yaffe (Da 63), Khan, Saha and Yaffe (Kh 70) and Parikh, Marsden, Porile and Yaffe (Pa 67). The normalization procedure was identical to that used in section E. The charge distribution curves were fitted to Gaussians with the help of the ORGLS program. The primary charge dispersion parameters were used to calculate the most probable charge and the full-width at half-maximum corresponding to the most probable isotope at the peak of each distribution. The results displayed here have been normalized to the masses above mentioned. The last column in the tables corresponds to a fit parameter with the same definition as given in section D. The normalized values have served for intercomparison between charge dispersion data belonging to various fission chains, as described in the discussion section.

TABLE AI: Charge dispersion data for $A = 96$ (Kh 70)
(normalized)

E_p (MeV)	Peak position			Full-width at half-maximum		
	N/Z	Z_p	$Z_A - Z_p$	N/Z	Z	χ^*
20	1.460	39.03	3.14	0.176	2.80	0.777
30	1.463	38.90	3.27	0.159	2.51	0.465
40	1.458	39.06	3.11	0.150	2.38	0.384
50	1.462	39.00	3.17	0.156	2.47	0.406
60	1.453	39.14	3.03	0.141	2.25	0.397
70	1.454	39.11	3.06	0.154	2.45	0.380
77	1.453	39.10	3.07	0.154	2.46	0.308
85	1.454	39.11	3.06	0.157	2.50	0.386

* χ = as defined in section D

TABLE AII: Charge dispersion data for $A = 136$ (Da 63)
(normalized)

E_p (MeV)	Peak position			Full-width at half-maximum		
	N/Z	Z_p	$Z_A - Z_p$	N/Z	Z	χ^*
20	1.549	53.35	2.65	0.090	1.88	0.619
30	1.526	53.84	2.16	0.092	1.96	1.067
50	1.509	54.21	1.79	0.098	2.12	1.047
65	1.505	54.29	1.71	0.102	2.21	1.154
80	1.496	54.49	1.51	0.117	2.56	1.092

* χ = as defined in section D

TABLE AIII: Charge dispersion data for $A = 141$ (Pa 67)
(normalized)

E_p (MeV)	Peak position			Full-width at half-maximum		
	N/Z	Z_p	$Z_A - Z_p$	N/Z	Z	χ^2
20	1.524	55.86	2.97	0.070	1.55	0.366
30	1.509	56.20	2.63	0.061	1.37	0.456
40	1.499	56.42	2.41	0.055	1.24	0.724
50	1.498	56.45	2.38	0.057	1.29	1.134
60	1.493	56.56	2.27	0.058	1.32	0.622
70	1.488	56.67	2.16	0.064	1.46	0.732
77	1.483	56.79	2.04	0.072	1.65	1.882
85	1.479	56.88	1.95	0.071	1.63	0.807

* χ^2 = as defined in section D

REFERENCES

- Ad 71: G.D. Adcev, P.A. Cherdantsev, and I.A. Gamalya, Phys. Lett. B35, 125 (1971).
- Al 63: J.M. Alexander, C. Baltzinger, and M.F. Gazdik, Phys. Rev. 129, 1826 (1963).
- Am 68a: I. Amarel, R. Bernas, J. Chaumont, R. Foucher, J. Jastrzebski, A. Johnson, R. Klapisch, and J. Teillac, Ark. Fys. 36, 77 (1968).
- Am 68b: S. Amiel, in "Nuclear Chemistry", edited by L. Yaffe (Academic Press Inc., New-York, 1968), Vol. II, p. 251.
- Am 74: S. Amiel and H. Feldstein, Proceedings of the 3rd Symposium on Physics and Chemistry of Fission, Rochester 1973 (International Atomic Energy Agency, Vienna 1974), Vol. II, p. 65.
- An 69: K.D. Androsenko, Proceedings of the 2nd Symposium on Physics and Chemistry of Fission, Vienna 1969 (International Atomic Energy Agency, Vienna 1969), p. 419.
- Ar 64: P. Armbruster, D. Hovestadt, H. Meister, and H.J. Specht, Nucl. Phys. 54, 586 (1964).
- Ar 70: P. Armbruster, Nucl. Phys. A140, 385 (1970).
- BÄ 70: K. Bächmann, J. Inorg. Nucl. Chem. 32, 1 (1970).
- Ba 71: S. Baba, H. Umezawa, and H. Baba, Nucl. Phys. A175, 177 (1971).
- Be 59: S.T. Belyaev, Kgl. Dansk. Vidensk. Selsk. Mat. Fys. Medd. 11, 31 (1959).

- Ba 71: K. Beg and N.T. Porile, Phys. Rev. C3, 1631 (1971).
- Bi 70: C.J. Bishop, R. Vandenbosch, R. Alcy, R.W. Shaw Jr, and I. Halpern, Nucl. Phys. A150, 129 (1970).
- Bo 39: N. Bohr and J.A. Wheeler, Phys. Rev. 56, 426 (1939).
- Bo 51: W.F. Boldridge and D.N. Hume, in "Radiochemical Studies: The Fission Products", edited by C.D. Coryell and N. Sugarman (McGraw Hill Book Company, Inc., New York, 1951), paper 294.
- Bo 56: A. Bohr, in Proceedings of the 1st International Conference on the Peaceful Uses of Atomic Energy (United Nations, New York, 1956), Vol. 2, p. 151.
- Bo 73: A. Bohr and B.R. Mottelson, Ann. Rev. Nucl. Sci. 23, 363 (1973).
- Br 63: H.C. Britt, H.E. Wegner, and J.C. Gursky, Phys. Rev. 129, 2239 (1963).
- Br 65: R. Brandt, in "Physics and Chemistry of Fission" (International Atomic Energy Agency, Vienna, 1965), Vol. II, p. 329.
- Br 71: J.C. Brodovitch, private communication (1971).
- Br 72: M. Brack, J. Damgaard, A.S. Jensen, H.C. Pauli, V.M. Strutinsky, and C.Y. Wong, Rev. Mod. Phys. 44, 2, 320 (1972).
- Bu 62: L.A. Busing and H.A. Levy, Oak Ridge National Laboratory Report No. ORNL-TM-271, unpublished (1962).
- Bu 71: S.C. Burnett, R.L. Ferguson, F. Plasil, and H.W. Schmitt, Phys. Rev. C1, 2034 (1971).

- Ch 66: G.R. Choppin and E.F. Meyer Jr., *J. Inorg. Nucl. Chem.* 28, 1509 (1966).
- Ch 68: K. Chen, Z. Fraenkel, G. Friedlander, J.R. Grover, J.M. Miller, and Y. Shimamoto, *Phys. Rev.* 166, 949 (1968).
- Ch 70a: J. Chaumont, *Thesis, Faculté des Sciences d'Orsay, Université de Paris* (1970).
- Ch 70b: E. Cheifetz and Z. Fraenkel, and J. Galin, M. LeFort, J. Peter, and X. Tarrago, *Phys. Rev.* C2, 256 (1970).
- Ch 70c: Y.Y. Chu, E.M. Franz, and G. Friedlander, *Phys. Rev.* C1, 1826 (1970).
- Ch 71: Y.Y. Chu, E.M. Franz, G. Friedlander, and P.J. Karol, *Phys. Rev.* C4, 2202 (1971).
- Co 53: C.D. Coryell, *Ann. Rev. Nucl. Sci.* 2, 305 (1953).
- Co 62: S. Cohen and W.J. Swiatecki, *Ann. Phys. (New York)* 19, 67 (1962).
- Co 63: S. Cohen and W.J. Swiatecki, *Ann. Phys. (New York)* 22, 406 (1963).
- Cr 69: I.F. Croall and J.B. Cuninghame, *Nucl. Phys.* A125, 402 (1969).
- Cu 63: J.B. Cumming, *U.S. Atomic Energy Report Number NAS-NS-3107*, 25 (1963).
- Da 63: J.H. Davies and L. Yaffe, *Can. J. Phys.* 41, 762 (1963).
- Di 74: M. Dikšić, D.K. McMillan, and L. Yaffe, *J. Inorg. Nucl. Chem.* 36, 7 (1974).

- Do 58: I. Dostrovsky, Z. Fraenkel, and P. Rabinowitz,
Proceedings of the 2nd International Conference
on the Peaceful Uses of Atomic Energy (United Nations,
Geneva, 1958) Vol. 15, p. 301.
- Do 59: I. Dostrovsky, Z. Fraenkel, and G. Friedlander,
Phys. Rev. 116, 683 (1959).
- Er 63: E. Erba, U. Facchini, E. Saetta-Menichella, L.
Severgnin, and F. Tonolini, Phys. Lett. 6, 294 (1963).
- Er 64: E. Erba, U. Facchini, E. Saetta-Menichella, and F.
Tonolini, Phys. Lett. 12, 109 (1964).
- Fa 62: H. Farrar and R.H. Tomlinson, Nucl. Phys. 34, 367
(1962).
- Fe 34: E. Fermi, Nature 133, 898 (1934).
- Fi 59: R.H. Fickel and R.H. Tomlinson, Can. J. Phys. 37,
916 (1959).
- Fi 54: W.H. Fleming, R.H. Tomlinson and H.G. Thode, Can. J.
Phys. 32, 522 (1954).
- Fi 72: K.F. Flynn, E.P. Horwitz, C.A. Bloomquist, R.F. Barnes,
R.K. Sjoblom, P.R. Fields, and L.E. Glendenin, Phys.
Rev. C5, 1725 (1972).
- Fo 53: P. Fong, Ph.D. Thesis, Department of Physics, University
of Chicago (1953).
- Fo 56: P. Fong, Phys. Rev. 102, 434 (1956).
- Fo 60: G.P. Ford, Phys. Rev. 118, 1261 (1960).
- Fo 63: P. Fong, Phys. Rev. Lett. 11, 375 (1963).
- Fo 64: P. Fong, Phys. Rev. 135B, 1338 (1964).

- Fo 70: P. Fong, Phys. Rev. C2, 735 (1970).
- Fo 71: P. Fong, Phys. Rev. C3, 2025 (1971).
- Fo 72: N.N. Fowler, private communication (1972).
- Fo 74a: P. Fong, Phys. Rev. C10, 1152 (1974).
- Fo 74b: N.N. Fowler and A.C. Wahl, J. Inorg. Nucl. Chem.,
36, 1201 (1974).
- Fr 54: J.S. Fraser and J.C.D. Milton, Phys. Rev. 93, 818
(1954).
- Fr 63: G. Friedlander, L. Friedman, B. Gordon, and L. Yaffe,
Phys. Rev. 129, 1809 (1963).
- Fr 66: J.S. Fraser and J.C.D. Milton, Ann. Rev. Nucl. Sci.
16, 379 (1966).
- Fr 68a: S.R. Fried, J.L. Anderson, and G.R. Choppin, J. Inorg.
Nucl. Chem. 30, 3155 (1968).
- Fr 68b: S.R. Fried, J.L. Anderson, and G.R. Choppin, J. Inorg.
Nucl. Chem. 30, 3167 (1968).
- Ga 67: J. Galin, Thesis, Faculté des Sciences d'Orsay, Univer-
sité de Paris (1967).
- Gl 51: L.E. Glendenin, C.D. Coryell, and R.R. Edwards, in
"Radiochemical Studies: The Fission Products",
edited by C.D. Coryell and N. Sugarman (McGraw Hill
Book Company, Inc., New York, 1951), paper 52.
- Gl 55: L.E. Glendenin, R.F. Flynn, R.E. Buchanan, and E.P.
Steinberg, Anal. Chem., 27, 59 (1955).
- Gl 65: L.E. Glendenin and J.P. Unik, Phys. Rev. B140, 1301
(1965).

- Go 49: R.H. Goekerman and I. Perlman, Phys. Rev. 76, 628 (1949).
- Gr 54: R.E.S. Green, Phys. Rev. 93, 1006 (1954).
- Gr 59: J.J. Griffin, Phys. Rev. 116, 107 (1959).
- Gr 62: J.J. Griffin, Phys. Rev. 127, 1248 (1962).
- Gu 68: C. Gustafson, I.L. Lamm, B. Nilsson, and S.G. Nilsson, Ark. Fys. 36, 613 (1968).
- Ha 39: O. Hahn and F. Straßmann, Naturwiss. 27, 11 (1939).
- Ha 49: O Hahn, J. Chem. Soc., Suppl. No. 2, 8259 (1949).
- Ha 58: I. Halpern and V.M. Strutinsky, in Proceedings of the 2nd International Conference on the Peaceful Uses of Atomic Energy (United Nations, Geneva, 1958), Vol. 13, p. 408.
- Ha 59: I. Halpern, Ann. Rev. Nucl. Sci., 9, 245 (1959).
- Ha-64: E. Hagebø, A.C. Pappas and P. Aagaard, J. Inorg. Nucl. Chem. 26, 1639 (1964).
- Ha 67: E. Hagebø, J. Inorg. Nucl. Chem. 29, 2515 (1967).
- Ha 68: R.W. Nasse, R. Ebert, and G. Süssmann, Nucl. Phys. A106, 117 (1968).
- Ha 74: I. Haldorsen, A.C. Pappas, and N. Skarestad, J. Inorg. Nucl. Chem. 36, 245 (1974).
- He 69: G.H. Herrmann and H.O. Denschlag, Ann. Rev. Nucl. Sci. 19, 1 (1969).
- Hi 55: H.G. Nicks and R.S. Gilbert, Phys. Rev. 100, 1286 (1955).
- Hi 62: H.G. Nicks, H.B. Levy, W.E. Nervik, P.C. Stevenson, J.B. Niday, and J.C. Armstrong Jr., Phys. Rev. 128, 700 (1962).

- No 69: J.J. Hogan and N. Sugarman, Phys. Rev. 182, 1210 (1969).
- No 72: N.E. Holden and F.W. Walker, "Chart of the Nuclides", Knolls Atomic Power Laboratory, U.S. Atomic Energy Commission, Eleventh Edition, April 1972.
- No 73: R. Holub and L. Yaffe, J. Inorg. Nucl. Chem. 35, 3991 (1973).
- No 74: D.C. Hoffman and M.N. Hoffman, Ann. Rev. Nucl. Sci. 24, 151 (1974).
- Nu 51: D.N. Hume and R.I. Martens, in "Radiochemical Studies: The Fission Products", edited by C.D. Coryell and N. Sugarman (McGraw Hill Book Company, Inc., New York, 1951), paper 304.
- Nu 62: J.R. Huizenga and R. Vandenbosch, in "Nuclear Reactions", edited by P.M. Endt and P.B. Smith (North Holland Publishing Co., Amsterdam, 1962).
- Ny 60: E.K. Hyde, "A Review of Nuclear Fission", Lawrence Radiation Laboratory, University of California, Berkeley, report UCRL 9036 (1960).
- Jo 61: S.A.E. Johansson, Nucl. Phys. 22, 529, (1961)
- Jo 70: T. Johansson, S.G. Nilsson, and E. Szymanski, Ann. Phys. (Paris) 5, 377 (1970).
- Rh 70: A.M. Khan, G.B. Saha, and L. Yaffe, Can. J. Chem. 48, 1924 (1970).
- Rl 67: R. Klapisch, J. Chaumont, C. Philippe, I. Amarel, R. Fergeau, M. Salome and R. Bernas, Nucl. Instr. Methods 33, 216 (1967).

- Kl 68: R. Klapisch, J. Chaumont, J. Jastrzebski, R. Bernas, G. Simonoff, and M. Lagarde, Phys. Rev. Lett. 20, 743, (1968).
- Kl 69: R. Klapisch, Ann. Rev. Nucl. Sci. 19, 33 (1969).
- Ko 69: J. Korkisch, "Modern Methods for the Separation of Rare Metal Ions" (Pergamon Press, 1969), p. 197.
- Kr 53: K.A. Kraus and G.E. Moore, J. Am. Chem. Soc. 75, 1460 (1953).
- La 61: M. Lefort, G.N. Simonoff, and X. Tarrago, Nucl. Phys. 25, 216 (1961).
- La 67: C.N. Lederer, J.N. Hollander, and I. Perlman, "Table of Isotopes", Sixth Edition, John Wiley and Sons, New York (1967).
- La 75: J.K.P. Lee, G. Pilar, B.L. Tracy, and L. Yaffe, J. Inorg. Nucl. Chem. 37, 2035 (1973).
- Li 56: M. Lindner and R.N. Osborne, Phys. Rev. 103, 378 (1956).
- Li 60: M. Lindner and A. Turkevitch, Phys. Rev. 119, 1632 (1960).
- Na 48: M.G. Mayer, Phys. Rev. 74, 235 (1948).
- Na 49: M.G. Mayer, Phys. Rev. 75, 1969 (1949).
- Na 73: H. Marshall and L. Yaffe, J. Inorg. Nucl. Chem. 35, 1797 (1973).
- Ne 66: J.A. McHugh, J. Inorg. Nucl. Chem. 20, 1787 (1966).
- Ne 68: J.A. McHugh and M.C. Michel, Phys. Rev. 172, 1160 (1968).
- Ne 71: T. McGee, C.L. Rao, and L. Yaffe, Nucl. Phys. A173, 395 (1971).

- Mc 72: T. McGee, C.L. Rao, and L. Yaffe, 'J. Inorg. Nucl. Chem. 34, 3323 (1972).
- Me 39: L. Meitner and O.R. Frisch, Nature 143, 239 (1939).
- Me 58: N. Metropolis, R. Bivins, M. Storm, A. Turkevitch, J.M. Miller, and G. Friedlander, Phys. Rev. 110, 185, 204 (1958).
- Me 62: S. Meghir, Ph.D. Thesis, Department of Chemistry, McGill University (1962).
- Mi 59: J.M. Miller and J. Hudis, Ann. Rev. Nucl. Sci. 9, 159 (1959).
- Mi 62: J.C.D. Milton and J.S. Fraser, Can. J. Phys. 40, 1626 (1962).
- Mi 70: L.D. Miller, Ph.D. Thesis, Department of Chemistry, McGill University (1970).
- Mi 73: L.D. Miller and L. Yaffe, J. Inorg. Nucl. Chem. 35, 1805 (1973).
- Mo 59: B.R. Mottelson and S.G. Nilsson, Kgl. Sensk. Vidensk. Selsk. Nat. Fys. Skr. 1, No. 8 (1959).
- Mo 70a: U. Mosel and D. Scharnweber, Phys. Rev. Lett. 25, 678 (1970).
- Mo 70b: P. Möller and S.G. Nilsson, Phys. Lett. 331, 171 (1970).
- Mo 71: U. Mosel and H.W. Schmitt, Nucl. Phys. A165, 73 (1971).
- Mo 71: P. Möller and S.G. Nilsson, Private communication to R. Vandenbosch and J.R. Huizenga, p. 317 (Va 73).
- Mu 72: M.G. Mustapha, U. Mosel, and H.W. Schmitt, Phys. Rev. Lett. 28, 1536 (1972).
- Mu 73: M.G. Mustapha, U. Mosel, and H.W. Schmitt, Phys. Rev. C7, 1519 (1973).
- My 66: W.D. Myers and W.J. Swiatecki, Nucl. Phys. 81, 1 (1966).
- My 67: W.D. Myers and W.J. Swiatecki, Ark. Fys. 36, 343 (1967).

- Ne 61: H.W. Newson, Phys. Rev. 122, 1224 (1961).
- Ne 73: D. Newton, S. Sarkar, L. Yaffe, and R.B. Moore, J. Inorg. Nucl. Chem. 35, 361 (1973).
- Ne 74: D.R. Nethaway, University of California Lawrence Livermore Laboratory, Report UCRL-51538 (1974).
- Ni 55: S.G. Nilsson, Kgl. Dansk. Vidensk. Selsk. Mat. Fys. Medd. 29, No. 16 (1955).
- Ni 65: J.R. Nix and W.J. Swiatecki, Nucl. Phys. 71, 1 (1965).
- Ni 67: J.R. Nix, Ann. Phys. (New York) 41, 52 (1967).
- Ni 69: S.G. Nilsson, C.F. Tsang, and A. Sobierewski, E. Szymanski, S. Wycech, and C. Gustafson, I.L. Lamm, P. Moller, S. Nilsson, Nucl. Phys. A131, 1 (1969).
- Ni 72: J.R. Nix, Ann. Rev. Nucl. Sci. 22, 65 (1972).
- No 66: W. Norenberg, Z. Physik 197, 246 (1966).
- Pa 55: A.C. Pappas, Proceedings of the 1st International Conference on Peaceful Uses of Atomic Energy, Geneva 1955 (United Nations, New York, 1956), Vol. VII, p. 19.
- Pa 58a: B.D. Pate, J.S. Foster, and L. Yaffe, Can. J. Chem. 36, 1691 (1958).
- Pa 58b: B.D. Pate, Can. J. Chem. 36, 1707 (1958).
- Pa 61a: B.D. Pate and M. Postkanzer, Phys. Rev. 123, 647 (1961).
- Pa 61b: A.C. Pappas and J. Alstad, J. Inorg. Nucl. Chem. 17, 195 (1961).
- Pa 66: A.C. Pappas and E. Hagebø, J. Inorg. Nucl. Chem. 28, 1769 (1966).

- Pa 67: S.S. Parikh, D.A. Marsden, N.T. Porile, and L. Yaffe, Can. J. Chem. 45, 1863 (1967).
- Pa 71: V.V. Pashkevitch, Nucl. Phys. A169, 275 (1971).
- Pe 71: D.G. Perry and A.W. Fairhall, Phys. Rev. C4, 977 (1971).
- Po 62: S.M. Polikanov, V.A. Druin, V.A. Karnaukhov, V.L. Mikheev, A.A. Pleva, N.K. Sobolev, V.G. Subbotin, G.M. Ter-Akop'yan, and V.A. Formichev, Sov. Phys. JETP 15, 1016 (1962).
- Po 64: P.N. Portner, Foster Radiation Laboratory Report, McGill University, January 1964, unpublished.
- Pr 47: R.D. Present, Phys. Rev. 72, 7 (1947).
- Ra 72: S.A. Rao Phys. Rev. C5, 171 (1972).
- Re 68: W. Reisdorf, Z. Physik 209, 77 (1968).
- Re 71: W. Reisdorf, J.P. Unik, N.C. Griffin, and L.E. Glendenin, Nucl. Phys. A177, 337 (1971).
- Ru 63: G. Rudstam, in "Physics and Chemistry of Fission" (International Atomic Energy Agency, Vienna, 1963), Vol. II, p. 323.
- Sa 70: G.B. Saha and L. Yaffe, J. Inorg. Nucl. Chem. 32, 745 (1970).
- Sa 71: G.B. Saha, I. Tomita, and L. Yaffe, Can. J. Chem. 49, 2205 (1971).
- Sa 73: S. Sarkar, Ph.D. Thesis, Department of Chemistry, McGill University (1973).
- Se 47: R. Serber, Phys. Rev. 72, 1114 (1947).

- St 58: P.C. Stevenson, N.G. Hicks, W.E. Nervik, and D.R. Nethaway, Phys. Rev. 111, 886 (1958).
- St 61a: V.M. Strutinsky, Soviet Phys. JETP 12, 546 (1961).
- St 61b: P.C. Stevenson and W.E. Nervik, "The Radiochemistry of Rare Earths, Scandium, Yttrium and Actinium", U.S. Atomic Energy Report Number NAS-NS-3020 (1961).
- St 64: V.N. Strutinsky, Sov. Phys. JETP 18, 1298 (1964).
- St 65: P.C. Stevenson, "Processing of Counting Data", U.S. Atomic Energy Report Number NAS-NS-3109 (1965).
- St 67: V.N. Strutinsky, Nucl. Phys. A95, 420 (1967).
- St 73: P.M. Starsyk and N. Sugarman, Phys. Rev. C8, 1448 (1973).
- Su 47: N. Sugarman, J. Chem. Phys. 15, 544 (1947).
- Su 56: N. Sugarman, M. Campos, and K. Wielgos, Phys. Rev. 101, 388 (1956).
- Sw 56: W.J. Swiatecki, Phys. Rev. 104, 993 (1956).
- Sw 58: W.J. Swiatecki, Proceedings of the 2nd International Conference on Peaceful Uses of Atomic Energy (United Nations, Geneva, 1958) Vol. 15, p. 248.
- Sw 65: W.J. Swiatecki, in "Physics and Chemistry of Fission" (International Atomic Energy Agency, Vienna, 1965) Vol. I, p. 3.
- Te 62: J. Terrell, Phys. Rev. 127, 880 (1962).
- Te 65: J. Terrell, in "Physics and Chemistry of Fission" (International Atomic Energy Agency, Vienna, 1965) Vol. II, p. 3.

- Th 47: H.G. Thode and R.L. Graham, *Can. J. Research* 25A,
1 (1947).
- Th 60: H.G. Thode, C.C. McNullen, and K. Fritse, *Adv. Inorg.
Chem. Radiochem.* 2, (1960).
- Th 64: T.D. Thomas and R. Vandenbosch, *Phys. Rev.* 133B, 976
(1964).
- To 69: I. Tomita and L. Yaffe, *Can. J. Chem.* 47, 2921 (1969).
- Tr 72: B.L. Tracy, J. Chaumont, R. Klapisch, J.M. Nitschke,
A.M. Poskanzer, E. Roeckl, and C. Thibault, *Phys.
Rev.* C5, 222 (1972).
- Tu 51: A. Turkevitch and J.B. Niday, *Phys. Rev.* 84, 52 (1951).
- Um 70: H. Umesawa, S. Baba and N. Baba, *Nucl. Phys.* A160,
65 (1970).
- Um 71: H. Umesawa, *J. Inorg. Nucl. Chem.* 33, 2731 (1971).
- Um 73: H. Umesawa, *J. Inorg. Nucl. Chem.* 35, 353 (1973).
- Un 64: J.P. Unik and J.R. Huizenga, *Phys. Rev.* 134B, 90 (1964).
- Un 74: J.P. Unik, J.E. Gindler, L.E. Glendenin, K.F. Flynn,
A. Gorski, and R.K. Sjoblom, *Proceedings of the 3rd
Symposium on the Physics and Chemistry of Fission,
Rochester 1973 (International Atomic Energy Agency,
Vienna, 1974) Vol. II, p. 19.*
- Va 73: R. Vandenbosch and J.R. Huizenga, "Nuclear Fission",
(Academic Press, New York, 1973).
- Vo 59: J. Von Holdt, *Proceedings of the Western Computer
Conference (1959)*, p. 256, as quoted in U.S. Atomic
Energy Report NAS-NS-3109 (1966).

- Vo 67: N.R. Von Gunten, K.F. Flynn, and L.E. Glendenin, Phys. Rev. 161, 1192 (1967).
- Wa 55: R.K. Wanless and N.G. Thode, Can. J. Phys. 33, 341 (1955).
- Wa 58: A.C. Wahl, J. Inorg. Nucl. Chem. 6, 263 (1958).
- Wa 62: A.C. Wahl, R.L. Ferguson, D.R. Nethaway, and K. Wolfsberg, Phys. Rev. 126, 1192 (1962).
- Wa 65: A.C. Wahl, in "Physics and Chemistry of Fission" (International Atomic Energy Agency, Vienna 1965), Vol. I, p. 317.
- Wa 69: A.C. Wahl; A.E. Norris, R.A. Rouse and J.C. Williams, Proceedings of the 2nd Symposium on Physics and Chemistry of Fission, Vienna 1969 (International Atomic Energy Agency, Vienna 1969), p. 813.
- Wa 70: R.L. Watson, R.C. Jared and S.G. Thompson, Phys. Rev. C1, 1886 (1970).
- We 35: C.F. von Weizsäcker, Z. Phys. 96, 431 (1935).
- Wi 62: C. Williamson and J.P. Boujot, "Tables of Range and Rate of Energy Loss of Charged Particles of Energy 0.5 to 150 MeV", Commissariat à l'Énergie Atomique, CEA report No. 2189 (1962).
- Wi 64: L. Wilets, "Theories of Nuclear Fission" (Oxford University Press, London, 1964).
- Wi 67: J. Wing and P. Fong, Phys. Rev. 157, 1038 (1967).
- Wo 69: C.Y. Wong, Phys. Lett. B10, 61 (1969).
- Ya 69: L. Yaffe, Proceedings of the 2nd Symposium on Physics and Chemistry of Fission (International Atomic Energy Agency, Vienna 1969), p. 701.

Yu 73a: Y.W. Yu and N.T. Porile, and R. Narasila and O.A.
Schaeffer, Phys. Rev. C8, 1091 (1973).

Yu 73b: Y.W. Yu and N.T. Porile, Phys. Rev. C7, 1897 (1973).